NIST Technical Note
NIST TN 2235

Structure Separation Experiments: Shed Burns without Wind

Alexander Maranghides
Shonali Nazare
Faraz Hedayati
Daniel Gorham
Eric Link
Matthew Hoehler
Matthew Bundy
Xareni Monroy
Murray Morrison
William (Ruddy) Mell
Anthony Bova
Derek McNamara
Thomas Milac
Steven Hawks
Frank Bigelow
Bob Raymer
Frank Frievalt
William Walton

This publication is available free of charge from:
https://doi.org/10.6028/NIST.TN.2235

NIST NATIONAL INSTITUTE OF STANDARDS AND TECHNOLOGY
U.S. DEPARTMENT OF COMMERCE

NIST Technical Note
NIST TN 2235

Structure Separation Experiments: Shed Burns without Wind

Alexander Maranghides
Shonali Nazare
Eric Link
Matthew Hoehler
Matthew Bundy
Fire Research Division
Engineering Laboratory

Faraz Hedayati
Daniel Gorham
Xareni Monroy
Murray Morrison
Insurance Institute for Businesses & Home Safety

William (Ruddy) Mell
Anthony Bova

Thomas Milac
Derek McNamara
United States Forest Service

Steven Hawks
Frank Bigelow
Office of the State Fire Marshal
California Department of Forestry and Fire Protection

Bob Raymer
California Building Industry Association

Frank Frievalt
Mammoth Lakes Fire Protection District

William Walton
University of Maryland

This publication is available free of charge from:
https://doi.org/10.6028/NIST.TN.2235

September 2022

U.S. Department of Commerce
Gina M. Raimondo, Secretary

National Institute of Standards and Technology
Laurie E. Locascio, NIST Director and Under Secretary of Commerce for Standards and Technology

NIST TN 2235
September 2022

Publication History
Approved by the NIST Editorial Review Board on 2022-19-14

How to Cite this NIST Technical Series Publication
Maranghides A, Nazare S, Link E, Hoehler M, Bundy M, Hedayati F, Gorham D, Monroy X, Morrison M, Mell W, Bova A, Milac T, McNamara D, Hawks S, Bigelow F, Raymer B, Frievalt F, Walton W (2022) Structure Separation Experiments: Shed Burns without Wind. (National Institute of Standards and Technology, Gaithersburg, MD), NIST Technical Note (TN) NIST TN 2235. https://doi.org/10.6028/NIST.TN.2235

NIST Author ORCID iDs
Alex Maranghides: 0000-0002-3545-2475
Shonali Nazare: 0000-0002-0407-5849
Eric Link: 0000-0002-7784-5023
Matthew Hoehler: 0000-0002-6049-7560
Matthew Bundy: 0000-0002-1138-0307

Contact Information
alexander.maranghides@nist.gov
shonali.nazare@nist.gov

Abstract

This report describes the experiments conducted during the first phase of a multi-phase project designed to assess structure-to-structure fire spread in the Wildland-Urban Interface (WUI). The experiments focused on quantifying thermal exposures from auxiliary structures, e.g., storage sheds. The effects of shed size, construction material, fuel loading, and separation distance on the ignition of primary structures (residential dwellings) with no wind were studied.

Preliminary structure separation experiments using natural gas burners and an instrumented target structure were conducted to optimize instrumentation and experimental design for subsequent shed burn experiments. Full-scale fire experiments were conducted in which various sizes and types of sheds were used to generate typical radiative and convective heat exposures. Experiments were conducted indoors at the National Institute of Standards and Technology (NIST) to quantify exposures from small source structures (sheds) in terms of mass loss rate (MLR) and heat release rate (HRR). HRR was measured using oxygen consumption calorimetry. Large ($\leq$ 120 ft^2) and Very Large ($>$ 250 ft^2) sheds were tested outdoors at the Insurance Institute for Business & Home Safety (IBHS) test facility. The mass loss method was employed to estimate the HRR for the outdoor shed burns. In addition, indoor shed burn experiments with a target structure were conducted to assess target performance against exposures from varying sheds (construction, size, fuel loading) and separation distances. All experiments were performed without an artificially generated wind field.

The preliminary experiments helped troubleshoot and provided insights into the airflow effects within the indoor test facility. The indoor shed burn experiments demonstrated that the mass loss measurements can be used to infer HRR measurements. The peak HRR (PHRR), which is related to the fire hazard, was a function of shed construction materials, shed size, and fuel loading inside the shed. Heat fluxes were measured, and the effects of the burning shed on the target structure were documented under no-wind conditions as a function of separation distance, construction materials, shed size, fuel loading, and shed openings.

The mass loss method was used to infer HRR from very large auxiliary structures tested outdoors at the IBHS test facility. Generally, for a given shed size and fuel loading, the PHRR depended on the shed construction material. Combustible shed source structures with fuel loading inside generated a greater PHRR than noncombustible sheds with similar fuel loading, almost by a factor of 4. The exposures quantified in this study demonstrate that any auxiliary structures made from combustible materials can pose a significant fire hazard when placed next to the primary structure. For noncombustible source structures with fuel loading inside, the shed orientation with respect to the primary structure and the size of the shed door opening are critical factors.

Sheds and auxiliary structures exceeding 120 ft^2 (11 m^2) floor area are subject to placement requirements with respect to residential structure(s) on the same lot through Chapter 7A of the California Building Code; the location and spacing of smaller sheds (e.g., under 120 ft^2) may or may not be regulated depending on local requirements. The findings from this study can provide technical input to national, state, and local building codes to alleviate fire spread from auxiliary structures within WUI communities.

Keywords

Heat release rate; heat flux measurements; mass loss rate; radiant and convective heat exposure; structure separation distance; sheds; wildland-urban interface.

Table of Contents

List of Tables

List of Figures

Acknowledgments

The authors are grateful to Lauren DeLauter, Philip Deardorff, Marco Fernandez, and Michael Selepak for outstanding technical support, and Edward Hnetkovsky for excellent administrative support.

The SSE project was not possible without the collaboration and financial support of CAL FIRE. Appreciation is also extended to Thomas Milac and Willian (Ruddy) Mell of the USFS for the modelling work that was crucial in designing the experiments described in this report.

Executive Summary

Growing WUI Fire Problem

The rapidly developing nature of wildland-urban interface (WUI) fires and their sensitivity to several contributing factors (e.g., fuel, topography, and weather) presents challenges on various fronts including wildfire suppression, community evacuation, structure protection, and resource management. Once a wildfire approaches the WUI, structural ignition and fire spread within WUI communities can occur by direct flame impingement, ember exposure, thermal radiation, and combinations thereof. Post-fire case studies in WUI settings have identified that defensive actions including fuel displacement, fire suppression, fire containment, and exposure protection by first responders have a significant impact on structure survivability. Fire exposures from a fully involved single-family residence often result in fire propagation that is very difficult to stop in the presence of wind, especially in high density communities. Structure survivability is the result of the relationship between the structure construction and local intensity and duration of fire and ember exposures. Flaming embers generated by an intensely burning structure are capable of igniting structures that are hundreds of meters away, while intense radiant heat from a burning structure can easily ignite a structure that is several meters away. Thus, structure separation distance is extremely crucial in controlling structure-to-structure fire spread. Communities should assess both components, hardening for ember and fire exposures in the process of cost-effective structure and community hardening.

The Hazard Mitigation Methodology (HMM) provides an implementable path forward by considering the spatial relationships between fuels, exposures, and hardening at the structure and parcel levels. The HMM also demonstrates the complexity of structure hardening for both fire and ember exposures. While all structures must be hardened for ember exposures, this project specifically addresses radiative and convective exposures to characterize the spacing requirements outlined in the HMM. As documented in the HMM, there exists a direct relationship between exposure and the structure hardening required for survival, and cost-effective mitigation is a tuned balance between the two components.

Project Rationale and Description

National Institute of Standards and Technology (NIST) WUI fire case studies have identified multiple parcel-level attributes (sources) that can directly cause residential structure ignitions. The parcel-level attributes include, but are not limited to, combustible fences, wood piles, combustible landscaping elements, storage sheds, auxiliary structures, parked vehicles, and recreational vehicles (RVs). A three-phase research program was developed to specifically address structure-to-structure fire spread in WUI communities. This project is a collaboration among the California Department of Forestry and Fire Protection (CAL FIRE), California Building Industry Association (CBIA), United States Forest Service (USFS), Insurance Institute for Business & Home Safety (IBHS), United States Fire Administration (USFA), International Wildland-Urban Interface Code (IWUIC), and NIST. The project is divided into three phases: Phase 1 quantified thermal exposure from sheds (15 ft^2 to 288 ft^2) as fire sources; Phase 2 will assess thermal exposures from accessory dwelling units (400 ft^2 to 600 ft^2), also known as “in-law suites” (small accommodation structures frequently built close to a primary residential

structure); and Phase 3 will evaluate fire exposures from RVs and parked non-commercial vehicles.

The primary objective of Phase 1 was to quantify the effects of shed size, construction type, fuel loading, and separation distance on the ignition of primary structures with and without an applied wind. This manuscript reports the shed burn experiments with no wind. The smaller sized sheds were tested indoors in the National Fire Research Laboratory (NFRL) at NIST to quantify thermal exposures in terms of heat release rate (HRR) and mass loss rate (MLR) while larger sized sheds were tested outdoors at the IBHS test facility in Richburg, SC. The shed burn experiments with applied wind will be reported in subsequent manuscripts. The test plans detailing the experimental design, instrumentation, source (shed) and target structure specifications, and data acquisition have been previously reported while the modeling efforts associated with Phase 1 SSE will be documented in a separate publication.

Five experimental series are described in this report. The first four series were conducted at NIST and the fifth at the IBHS test facility. All experimental series were designed to be conducted without applied wind. The series were: 1) preliminary structure separation experiments (SSE) conducted to optimize instrumentation and experimental design for shed burn experiments, 2) verification experiments to confirm the system operations including the calorimetry, mass loss, and heat flux measurements within its performance tolerances, 3) shed burn experiments conducted indoors at the NIST test facility to quantify exposures from small source structures (Closets and Very Small sheds) in terms of HRR and MLR, 4) shed and target experiments conducted to assess target performance against exposures from varying sheds (construction, size, fuel loading) and separation distances, and 5) outdoor shed (Medium, Large and Very Large sheds) burn experiments with no wind loading at the IBHS test facility.

Design of the Preliminary Structure Separation Experiments

The preliminary structure separation experiments were conducted using a natural gas burner and an instrumented target structure (roof-wall assembly) to quantify radiant and convective heat transfer. Initial experimental design called for a 13 ft tall target wall; however, safety concerns of handling heavy steel plates used to characterize 2D thermal conduction resulted in a reduction of the target wall height from 13 ft to 6 ft. The reduction of the target wall height also eliminated the need to raise the gas burner 6 ft from the ground. While the realism of a full single-story facade was lost by reducing the target wall height, the quantification of heat transfer was not impacted.

Three experiments were performed to generate heat transfer data and quantify thermal exposure to the “eaves” and the “window” from a known source. This information will be used for the validation and verification of Fire Dynamics Simulator (FDS). Model performance will be documented in a future publication. The experiments also served as a shakedown for the subsequent free burn experiments and shed and target experiments.

Design of Weighing Platform and Measurement Verification Experiments

One of the main objectives of the indoor shed burn experiments was to assess the feasibility of the mass loss method for estimating HRR from a burning shed. A weighing platform was designed and fabricated to collect the mass loss rate data. The platform needed to be large enough (20 ft × 20 ft × 1 ft) to accommodate any debris from the burning sheds while at the same time fit within the structural columns of the NFRL and under the 9 m × 12 m calorimeter. The platform needed to be placed under the calorimeter in such a way that the target structure could also be built for the shed and target experiments (see Section 5 on shed and target experiments). The platform and load cells needed to accommodate experimental configurations with the shed placed near the middle of the platform (for the shed burns) as well as the shed placed at the edge of the platform (for the shed with target experiments). A larger weighing platform (24 ft × 36 ft × 2 ft) was designed and fabricated for the outdoor shed burn experiments at IBHS.

The measurement verification burns were performed as a part of the routine procedure at the NFRL. Two experiments were performed using a natural gas burner with heat output of 8 MW and 4 MW to generate the full range of heat release rates anticipated for the experimental series. These experiments confirmed good agreement between fuel consumption (mass loss) and oxygen consumption calorimetry, heat flux gauges, and the thermal sensitivity of the load cells in the weighing platform.

Indoor Shed Burn Experiments at NIST

The primary purpose of the indoor burn experiments (shed only burns) was to quantify thermal exposures from small source structures (sheds) in terms of MLR and HRR using oxygen consumption calorimetry.

Thermal exposures were quantified for sheds of different sizes, construction materials, and with different fuel loadings. A total of nine shed burn experiments were conducted, including one repeat experiment to establish reproducibility of shed burns. The reproducibility of peak HRR (PHRR) was found to be within 7 %. Closet and Very Small sheds made from wood, plastic, and steel, each with low and high fuel loadings were tested. The fire hazard assessed in terms of PHRR was found to be higher for combustible wood and plastic sheds when compared to the noncombustible steel sheds. The construction material for wood and plastic sheds (Closets and Very Small sheds) contributed approximately 40 % towards the total combustible mass and a 60 % increase in fuel load compared to the steel shed, therefore producing the higher PHRR corresponding to higher fire hazard. Non-flame retarded plastic sheds burned with higher intensity compared to wooden sheds.

The effects of shed size and fuel loading indicated that the lower fuel loading density allows for re-radiation and higher oxygen availability and hence faster flame spread over the combustible fuel. The PHRR was not affected by the fuel loading; however, the time to reach peak was delayed for higher fuel loadings. As expected, the total heat release increased linearly with the shed size and with increased fuel loading. Measurements of heat fluxes above and away from the source fire indicated that the lower positioned heat flux gauges (HFGs) recorded higher heat fluxes compared to the upper HFGs. This was due to their relative proximity to the burning fuel

(source) compared to the upper flux gauges that were exposed to intermittent flames/plume. As expected, the relative magnitudes of heat flux decreased with distance from the source fire. For noncombustible sheds that maintained structural integrity throughout the burn, the heat flux measurements in front of the door opening were largely affected by the size of door opening and the arrangement of wood cribs within the shed. A cursory examination of correlation between the PHRR and peak heat flux measured above and from across the source structure revealed that a linear correlation exists between the peak heat flux and the PHRR values, and a reasonable estimate of the heat flux for a given PHRR at a given separation distance was possible.

Indoor Shed Burn Experiments with Target Structure at NIST

The primary purpose of the shed and target experiments was to assess target performance for exposures from different sheds (construction, size, fuel loading) at different separation distances. The primary challenge in the design of these experiments was the size and placement of the target structure (assembly of exterior wall, roof, and a window) under the 9 m × 12 m calorimeter. The design considerations for the target structure included:

Height and width of the target structure

The target structure height selected was that of a tall single-story residence. This was selected as a realistic worst-case scenario for Phase 1 when accounting for the thermal exposures generated from burning sheds ranging 4 ft to 8 ft in height.

Components of the target structure

The target structure comprised of a wall-roof assembly with a double pane window and a vented attic. The wall was constructed with nominal 2-in × 4-in studs with 1-in-thick mineral fiber cavity insulation. A drywall was used as an interior layer, and the exterior wall had three layers; a noncombustible gypsum board sandwiched between oriented strand board (OSB) and an exterior layer of noncombustible cement board. Typically, an exterior noncombustible layer in the wall assembly would meet the requirements of WUI building codes (e.g., SFM-12-7A-1). The main objective of this project was to assess the performance of eaves but not the wall. In order to achieve the main experimental objective and to prevent any potential ignition of the wall, an additional insulating layer of noncombustible gypsum panel lined with fiberglass mats was used in the construction of the target wall for this project. This extra insulation layer was used for all but the last experiment where the wall performance was evaluated.

The asphalt shingle roof had a pitch of 5:12 and an open-eave configuration. A fire-resistant eave vent with an intumescent coating was installed in the central rafter bay. The selected eave vent conformed with the ASTM E2886 and is commonly used for residential construction in WUI areas.

A horizontal sliding, double-pane window with a vinyl frame was used. Annealed glass (non-tempered) was used in the construction of the windows, typical of existing building stock that may be part of a retrofit hazard mitigation program. Window screens, typically required for WUI construction compliance, were also used. Metal or fiberglass screens are used to resist ember entry, and they are also known to reduce the amount of radiant heat transmitted to the glass.

Placement of target structure under the calorimeter

This issue required coordination with the modeling effort of the SSE project to assess potential interactions between the target structure and the calorimeter hood, the north wall adjacent to the calorimeter, and air flow in the NFRL. Placement of the target wall was further coordinated with the weighing platform design and placement as mentioned above. The modeling activities associated with Phase 1 SSE will be documented in a separate publication.

Orientation of target under the calorimeter

Preliminary modeling and initial design suggested placement of the target structure at the western side of the 9 m × 12 m hood with the "exterior" of the facade facing east. This was selected as a desired location given the air flow dynamics in the NFRL; however, safety considerations regarding fire suppression and egress dictated a 180º rotation with the target structure placement at the eastern side of the calorimeter.

A total of six experiments were conducted, including one repeat experiment to confirm the ignition of the target structure in a given configuration. Generally, the thermal exposure from the sheds to the target structure in the absence of wind was a function of:

1. Construction material of the shed,
2. Fuel loading in the shed,
3. Shed orientation (i.e., door opening position), and
4. Structure separation distance (SSD).

The target structure performances are discussed in terms of ignition of eaves/rafters, damage to the exterior layer of the target wall, window performance (frame melting and/or ignition, and breakage of the windowpane), and vent performance (ember and/or flame penetration through the vent, temperature measurements using thermocouples located in the vent, and efficiency of intumescent coating in closing the vent cells).

For combustible wood Closet, following the ignition of the contents, fire spread to the Closet wall and roof and consumed the Closet. The fire spread to the eaves and roof of target structure depended on the fuel content of the Closet and its location with respect to the target structure. A noncombustible steel Closet with similar size and fuel loading contained the fire within the source structure, and the damage to the target structure was negligible because the door opening was facing away from the target structure.

The following observations were made from the data in this experimental series:

1. Heat fluxes of approximately 15 kW/m² for at least 5 min resulted in the ignition of open eaves made from combustible wood. These conditions were observed with:
    a. A noncombustible Very Small shed with high fuel loading. The door opening of this shed was facing the target structure separated by a distance of 5 ft.
    b. A combustible wood Closet with low fuel loading and structure separation distance of 0 ft.
2. Local thermal damage to the exterior layer (cement board) of the target wall was observed, and the intensity of cracking and/or spalling was a function of shed

construction material, fuel loading, shed orientation, and SSD. The extra layer of sheathing included in the exterior wall construction was necessary to prevent the ignition of OSB given the exposures from the source structures with combustible fuel in the SSD configuration evaluated (i.e., SSD = 0).

3. Thermal damage of windows were observed in experiments with wood Closets with zero structure separation distance (SSD = 0) and for a Very Small steel shed with an SSD = 5 ft with the door opening facing the target structure. The broken annealed glass would likely be displaced in the presence of wind, thereby forming an opening for embers and flames to enter the structure. No visible damage to the windows was observed for noncombustible sheds where the door opening, and hence the flames from burning fuel, was facing away from the target structure.
4. For combustible wood Closets the radiant and convective heat exposure was sufficient to activate the intumescent coating on the honeycomb core of the vent. The intumescent coating was not effective to block the heat, and temperatures exceeding 380 ºC were recorded on the unexposed side of the vent suggesting vent failures per ASTM E2886. Nonetheless, the performance of these vents cannot be interpreted as failures with respect to the standard test method (ASTM E2886) as the thermal exposures to the vents were significantly different than those specified in the standard.
5. A non-flame retardant caulking failed once the eaves and rafters ignited, forming an opening for flame penetration. Replacement of a non-flame retardant caulking with a flame retardant caulking prevented flame penetration in subsequent tests. The longevity and outdoor performance of fire caulking was not investigated.

Outdoor Shed Burn Experiments at IBHS

The main objective of the outdoor shed burn experiments was to estimate HRR of larger sheds that could not be tested under the 10 MW calorimeter at the NFRL. The HRR of burning Medium (M), Large (L), and Very Large (VL) sheds was estimated from the mass loss rate using a large weighing platform specifically designed and constructed for this project. Similar to the indoor shed burn experiments, the outdoor shed burn experiments measuring mass loss rate were performed without an artificially generated wind field. Ambient wind conditions < 3 m/s (7 mi/h) were recorded during the shed burn experiments. In addition to the estimation of HRR, thermal exposures from the source structure (shed) to potential nearby target structures were quantified by measuring heat fluxes at heights, orientations, and distances representative of components of a target structure (i.e., single-family residence). The locations of the heat flux sensors represented the fascia board, under-eave, and window on the surrogate target structure.

A total of six outdoor shed burn experiments were conducted, including one repeat experiment to establish reproducibility of the measured data. The overall results of the outdoor shed burn experiments demonstrated that:

1. The mass loss method for estimating HRR of the Medium, Large and Very Large sheds was feasible. The wind, the turbulence of hot gases during flashover, and the collapse of the structural components during the fire affected mass loss measurements. The derived HRR was generally noisy due to significant fluctuations in mass loss data and the presence and fluctuation of low (under 10 mi/h) ambient wind.

2. Considering the scale of shed burns, the reproducibility of outdoor shed experiments in terms of PHRR was found to be within 20 %.
3. Measurement and comparison of heat flux data enabled the characterization of the effects of shed construction materials and shed sizes on the fire hazard. The results indicated the following:
    a. The noncombustible steel sheds were much more capable of protecting surrounding target structures or fuels from radiant and convective heating. For a given shed size, heat fluxes from the plastic shed were significantly higher than those from the steel shed. The surrogate target structures were exposed to radiant and convective heat from burning wood cribs after the plastic melted, while the fire was contained within the steel shed resulting in a reduced amount of radiant heat at the surrogate targets.
    b. The duration of heat exposure from steel sheds was much longer compared to combustible plastic and wood sheds with similar fuel loads as energy release was limited by the size of door opening.

Overall Findings

The results of this limited experimental series in Phase 1 of the SSE project have highlighted significant fire hazard from storage sheds to nearby residential structures under no wind or low, ambient wind conditions. The experiments provide information on relative hazard associated with sheds of different construction materials, sizes, and fuel loadings. The minimum SSD is defined as the shortest distance between the source and target structures to prevent ignition and flame spread. The experimental series identified the structure separation distance (SSD) for no wind scenarios and the effects of slope were not considered. The findings of this study apply for hardened construction as described in Section 5.2.1; SSDs will need to be increased for non-hardened constructions. The target structure performance for the exposures tested in this experimental series identified component performances under no wind conditions, and the results highlight the potential gap between existing test methods and realistic exposures during WUI fires.

In addition to the technical findings listed above, the overall outcomes from SSE Phase 1 are as listed below:

1. The lessons learned from the experimental design and execution, instrumentation, data acquisition, and data processing will be useful in planning and execution of experiments in Phase 2 and Phase 3 of the SSE project.
2. NIST is not a regulatory agency. The purpose of this work is to provide AHJs with the technical information on hazard quantification and thermal exposures from auxiliary structures on the parcel. This information can be used at the national, state, county, and/or community level to mitigate fire hazards from auxiliary structures and enhance life and property safety in the WUI.
3. The information generated here, together with additional SSE work, may also be used in the future by the fire protection community to enhance test methods to better capture the relationships between realistic exposures and home hardening.

The experimental results are subject to uncertainties associated with parameters such as temperature, heat flux, HRR, distance, mass, and time measurements. Despite these uncertainties the results demonstrate that the thermal exposure varies with the type and size of sheds, the SSD, and fuel loadings. Additional factors that would be expected to affect thermal exposure but were not varied in this study include fuel moisture, wind, and topography. Considering the experimental uncertainties and additional factors that could affect the thermal exposure from the source structures, it is possible to provide some general guidance with regard to fire hazard of a storage shed, SSD, thermal exposures and expected ignition behaviors of target structures.

While not representative of worst-case conditions, the data from these experiments should be useful for assessing the fire hazard of the storage sheds, SSD, and likelihood of ignition of target structure subjected to conditions similar to those investigated here.

Recommendations

Shed Usage

- ✓ Consider Remove, Relocate, Reduce (RRR) as specified in HMM to reduce fire exposures.
  - Minimum SSD[1,2] = 10 ft for Closet and Very Small sheds (< 26 ft^2).
  - Minimum SSD = 20 ft for Large and Very Large sheds (< 288 ft^2).
- ✓ Choose shed construction materials to reduce exposures; however, this alone cannot substitute for RRR and SSD
  - Consider relative position of neighboring residence for door orientation of noncombustible steel shed.
  - Keep shed doors closed.
  - Avoid placing plastic sheds on sloped terrain, on elevated decks, and/or where resulting pool fires can spread and ignite nearby combustibles.

Target Hardening

- ✓ Replace annealed glass windows with tempered glass where fire exposures are expected on the structure. This should be done in conjunction with window screens and other necessary structure hardening for embers and fire (HMM).
- ✓ Use flame-retardant caulking around eave boxing, eave vents, and windows.
- ✓ Additional gypsum panel sheathing may be used to prevent ignition of combustible layers of the exterior wall assembly under noncombustible cladding.

Further Research

- ✓ The standard test method for assessing performance of eave vents needs to be further assessed for realistic thermal exposures. **N**IST **E**ave **V**ent **E**xperiments (NEVE) have been planned to assess vent performance exposed to flaming fires.

[1] Minimum SSD applies for hardened construction as described in Section 5.2.1; SSD will need to be increased for non-hardened constructions.
[2] Minimum SSD does not account for effects of wind and/or slope.

- ✓ Assess the performance of fire caulking for extended exterior use. Work is planned at NIST to assess the fire performance of flame retarded caulking that has been exposed to accelerated weathering.

1. Introduction

Structure-to-structure fire spread occurs in wildland-urban interface (WUI) areas with short structure separation distance (SSD) due to multiple structure ignitions from a wildland fire outpacing suppression capabilities. Since, in many cases, the structural fuel load is larger than that of adjacent ornamental vegetation surrounding a structure or the wildland fuel load, these initial ignitions can result in numerous other structure ignitions. These ignitions can be challenging to contain until there is a reduction or change in exposure conditions (e.g., wind, humidity, SSD, or other factors), enabling containment of the fire by first responders.

Typically, authorities having jurisdiction (AHJ) prescribe minimum SSD depending on building height, type, presence of sprinklers, and/or prescribed structure hardening requirements for outdoor fire exposures. For example, in addition to regulating primary residential structures, the California Building Code regulates auxiliary structures with more than 120 ft^2 (11 m^2) floor area. However, the SSD requirements for auxiliary structures are only considered with respect to residential structure(s) on the same lot (Fig. 1a); there is no placement requirement or guidance for the placement of auxiliary structures with respect to structures on neighboring parcels. Fig. 1 illustrates an example of how code compliance is typically interpreted/applied for the placement of an auxiliary structure. When property lines are considered as a limit of code application, the hazard imposed from the auxiliary structure to the neighboring residence in Fig. 1a is unmitigated. When two residences are located on the same lot, as shown in Fig. 1b, both structures are subjected to the SSD.

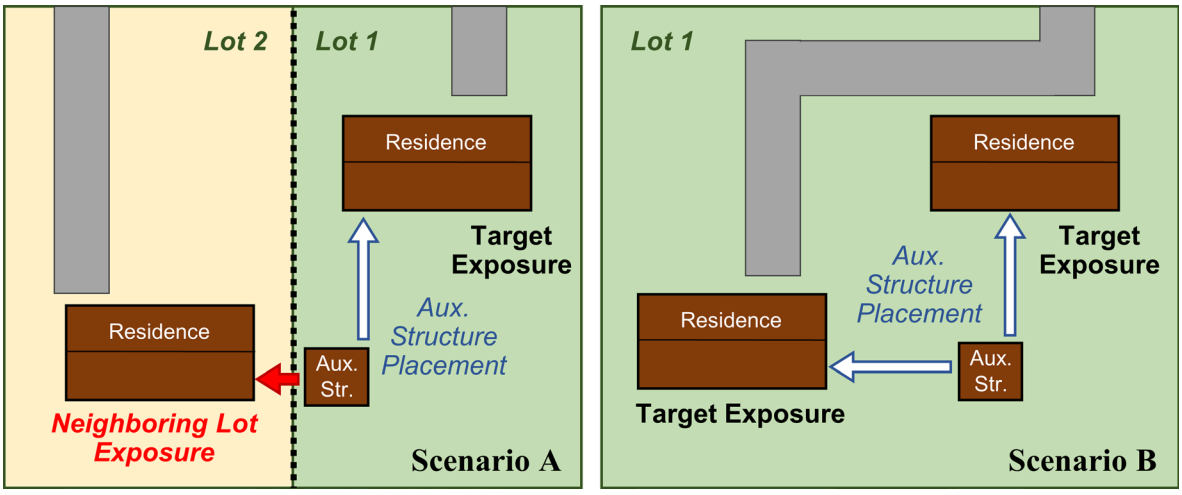

Fig. 1. Shed placement on (A) Two properties, (B) One property (Fig. not to scale).

Many jurisdictions do not provide guidance for the placement of sheds or auxiliary structures with floor area < 120 ft^2 (11 m^2). Frequently used by homeowners for additional storage space, sheds of this size are frequently designed with a single pitch roof (without a ridge) and are typically placed against or next to residential structures. In cases of two-story buildings, these sheds may be located under second-floor windows.

Vulnerabilities related to the construction and placement of auxiliary structures and their role in structure-to-structure fire spread in the WUI was highlighted in NIST's case study of the Camp Fire [1]. Small auxiliary storage sheds can be ignited from flaming fire exposures and/or by

embers. Fire can reach both the shed and its contents relatively easily as many storage sheds do not have flooring, more easily allowing surface fire to get under the shed and causing ignition of the contents. Combustible shed materials, shed contents, and accumulated windblown debris adjacent to sheds are readily ignited by surface fire and embers. Burning sheds can readily become a source of additional fire which may ignite adjacent residential structures resulting in a cascade of ignitions, especially under high-wind conditions. Such structure-to-structure fire spread can outpace first responders, making it difficult to contain fires within high density housing communities. Understanding SSD with the support of experimental measurements can improve community resilience to WUI and structure-to-structure fire exposures through implementation in best practice guidelines, such as described in the NIST WUI Structure/Parcel/Community Fire Hazard Mitigation Methodology (HMM) [2].

The primary objective of this project is to quantify the effects of shed sizes, construction types, fuel content inside the shed, and separation distance on the ignition of primary structures. This project is a collaboration among the California Department of Forestry and Fire Protection (CAL FIRE), California Building Industry Association (CBIA), United States Forest Service (USFS), Insurance Institute for Business & Home Safety (IBHS), U.S. Fire Administration (USFA), International Wildland-Urban Interface Code (IWUIC), and the National Institute of Standards and Technology (NIST).

Full-scale fire experiments were conducted at the NIST National Fire Research Laboratory (NFRL) and outside the IBHS wind-loading test cell. The experiments used construction materials and structural assemblies compliant with building codes in the State of California. Numerical modeling aided in developing the experiment design [3].

This manuscript is the second of four planned reports on experiments assessing shed-to-structure fire spread within WUI communities. The first report [3] described the test plan for the proposed experiments. The current manuscript describes the results of the full-scale shed burn experiments with no wind loading. The third report will describe the results of the outdoor Closet, Very Small and Small shed burn experiments with wind. The fourth report will describe the Large and Very Large shed burn experiments at the IBHS test facility with applied wind field.

The experiments described in the current manuscript are divided into five sections. The preliminary structure separation experiments (SSE) conducted to optimize instrumentation and experimental design for shed burn experiments are described in Section 2, while the verification experiments that provide confirmation of the system operations within its performance tolerances are described in Section 3. Section 4 provides a detailed description of shed burn experiments conducted indoors at the NIST test facility to quantify exposures from small source structures (sheds) in terms of mass loss rate and heat release rate (HRR), and Section 5 discusses shed and target experiments conducted to assess target performance against exposures from varying sheds (construction, size, fuel loading) and separation distances. The final Section 6 provides a detailed description of outdoor shed burn experiments at the IBHS test facility. Each section describes the test objectives, detailed experimental configurations including data acquisition instrumentation, test matrix, and test procedures. The test results are provided with a summary of technical findings.

The policy of NIST is to use SI units in its published materials. Because this report is primarily directed to communities and the building construction industry in the U.S., which uses British imperial units, it is more practical and less confusing to use British imperial units, in some cases,

rather than the SI units. However, most engineering drawings, experimental specifications, and dimensions are presented in SI units. In most cases, units are presented in both systems.

2. Preliminary Structure Separation Experiments

The preliminary structure separation experiments (SSE) were conducted using a natural gas burner and an instrumented target structure (roof-wall assembly) to quantify radiant and convective heat transfer. The experimental design was derived from the standard test method for assessing resistance to wildfire penetration of eaves, soffits, and other projections described in ASTM E 2957 [4].

2.1. Test Objectives

The objectives of the preliminary SSE were to:

1. Generate heat transfer data using steel plates with thermocouples and heat flux gauges (HFG) for model validation. The steel plates represent the eaves and window of the target structure.
2. Investigate "eaves" and "window" response to convective and radiant heat exposure from natural gas burner.
3. Provide insights into the design and construction of a target structure for subsequent shed and target experiments.

These objectives were accomplished by performing the following three experiments:

1. **Experiment 1 (SSEGasBurner1):** The steel plates used in place of the eaves (SPE) and the window (SPW) were exposed to fire from the natural gas burner at 200 kW, 400 kW, and 600 kW. Temperature and heat flux data was recorded during exposure to the natural gas burner and during the cooling period. The natural gas burner was situated 5 ft (1.5 m) away from the target structure, representing a SSD of 5 ft (1.5 m).
2. **Experiment 2 (SSEGasBurner2):** Experiment 1 was repeated with the natural gas burner placed against the target structure with an SSD of 0 ft.
3. **Experiment 3 (SSEGasBurner3):** The SPE and the SPW were exposed to the natural gas burner with an SSD of 0 ft, and the output of the gas burner was increased until intermittent flame contact with the SPE was observed. The maximum heat output of the natural gas burner for this experiment was 1 MW.

2.2. Experimental Configuration

The preliminary structure separation experiments with the gas burner were conducted under the 27.6 ft × 40.7 ft (8.4 m × 12.4 m) calorimetry hood at the NFRL. The top view of the experimental setup under the exhaust hood is shown in Fig. 2. The placement of the natural gas burner with respect to the target structure (noncombustible wall and roof assembly) used in the preliminary SSE is shown in Fig. 3. The gas burner was placed on the test platform with approximately 6 ft (1.8 m) between the top of the burner and the eaves. A heat flux gauge rig was used as a surrogate for the target structure to measure radiative heat fluxes at pre-determined locations. The placement of the heat flux gauge rig with respect to the gas burner and the instrumented target structure is shown by the blue dots in Fig. 2.

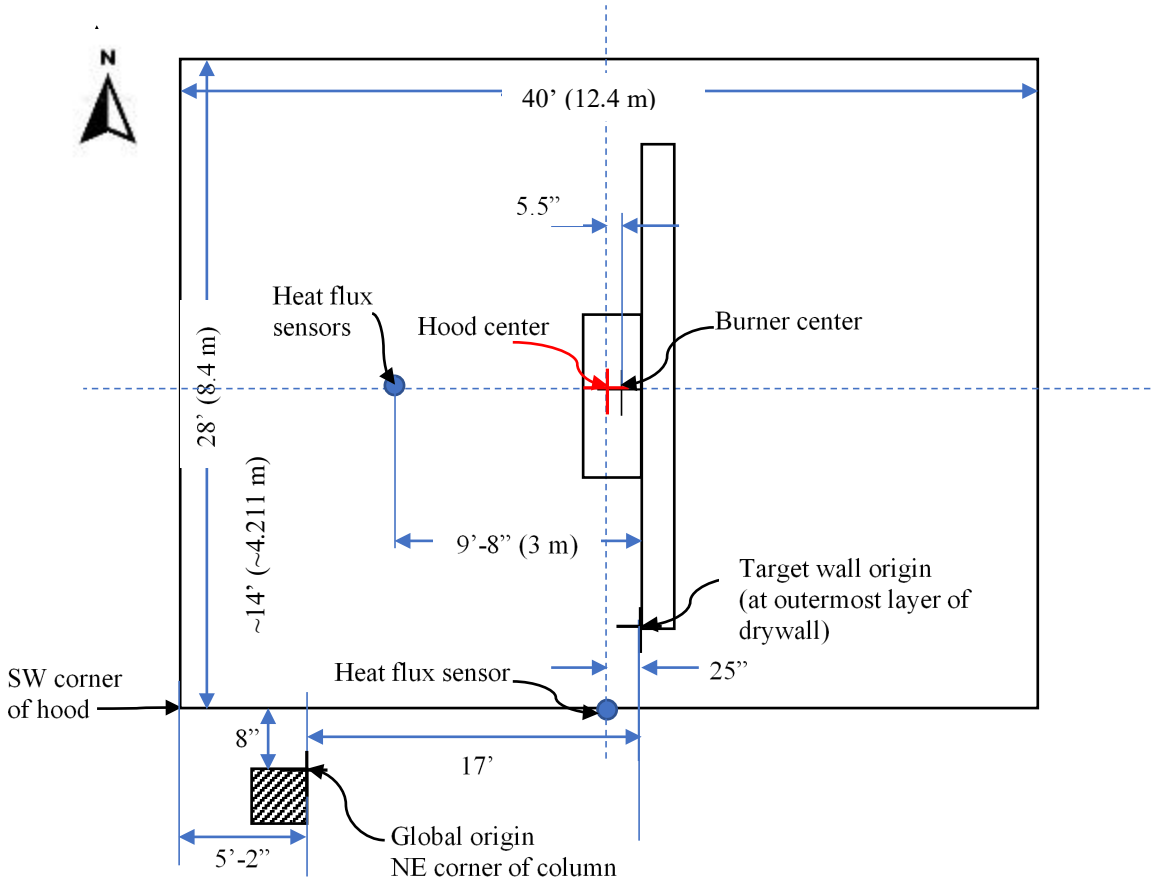

Fig. 2. Top view of experimental setup for preliminary burns with natural gas burner and target structure under the hood.

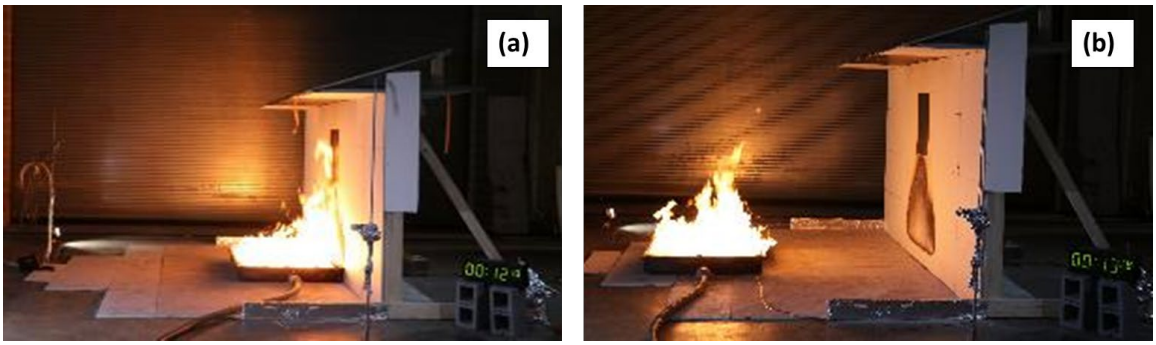

Fig. 3. Instrumented target structure exposed to gas burner (a) located next to the target wall and (b) located 5 ft (1.5 m) from the target structure.

The front and top view of the instrumented target structure is shown in Fig. 4. The positions of the sensors and the thermocouples on the steel plates in Cartesian coordinates (x, y, z), where the origin O is the wall origin and z is the distance up from the floor, are provided in Table 1. The uncertainties in distance measurements are generally less than ½ inch (1.2 cm). Longer distances over 4 ft have slightly higher uncertainty of 1 in (2.54 cm), as discussed in Appendix C.

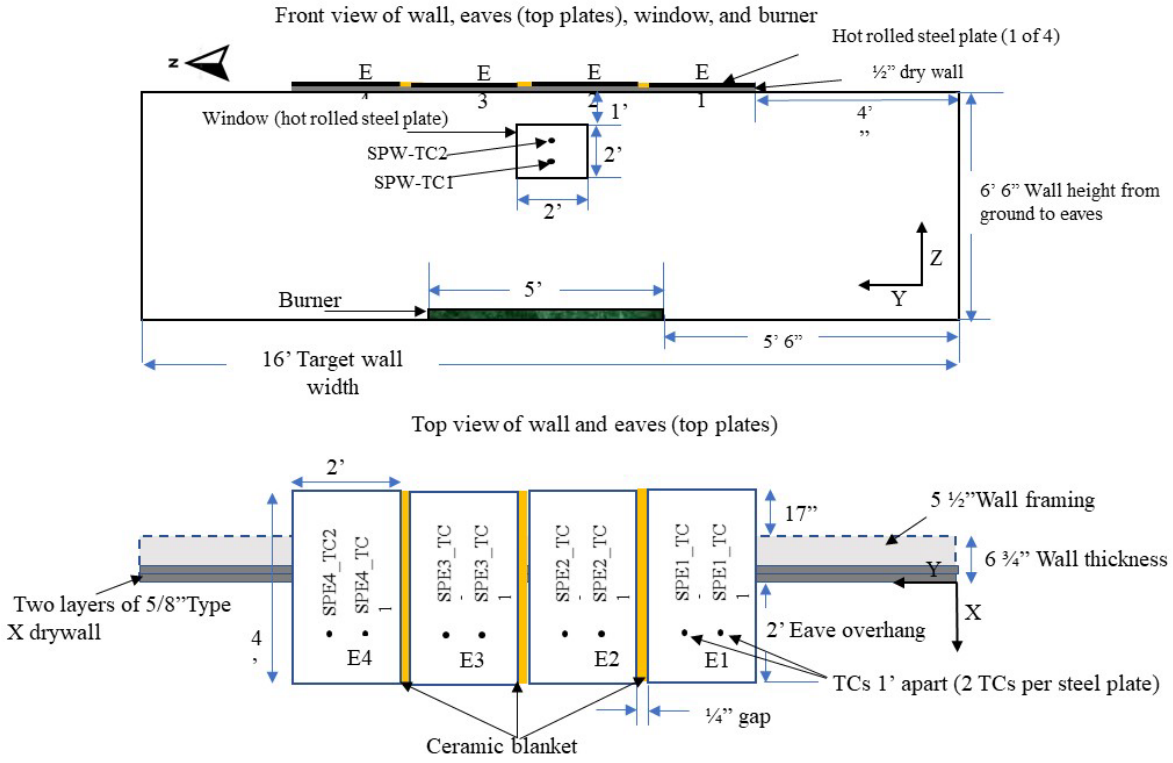

Fig. 4. Front and top view of the instrumented target structure used in preliminary burns (Fig. not to scale).

Table 1. Location of instrumentation for preliminary SSE with reference to the target structure origin.

Device	ID	X, cm (East+)	Y, cm (North+)	Z, cm (Up+)
Ambient Temperature at DAQ	TCAmb	—	—	—
Steel Plate Window Bottom	SPW_TC1	0	96	48
Steel Plate Window Top	SPW_TC2	0	96	60
Steel Plate Eave 1 (south) TC south	SPE1_TC1	−12	54	78
Steel Plate Eave 1 (south) TC north	SPE1_TC2	−12	66	78
Steel Plate Eave 2 (middle south) TC south	SPE2_TC1	−12	78	78
Steel Plate Eave 2 (middle south) TC north	SPE2_TC2	−12	90	78
Steel Plate Eave 3 (middle north) TC south	SPE3_TC1	−12	103	78
Steel Plate Eave 3 (middle north) TC north	SPE3_TC2	−12	115	78
Steel Plate Eave 4 (north) TC south	SPE4_TC1	−12	127	78
Steel Plate Eave 4 (north) TC north	SPE4_TC2	−12	139	78
Plate thermocouple facing wall front	PTC1	−118	96	56
Plate thermocouple gas temperature	PTC1g	−118	96	56
HFG1 facing wall front	HFG1	−118	96	54
HFG2 (radiometer) facing wall front	HFG2	−118	96	52

2.2.1. Data Acquisition and Instrumentation

A National Instruments (NI) cDAQ-9184 data acquisition (DAQ) chassis populated with NI-9213 I/O-Modules for thermocouples and NI-9215 modules for sensors with voltage outputs were used to sample the output from the heat flux sensors and thermocouples at a frequency of 1 Hz. The HRR measurements were made on an independent data collection system called the Modular In-situ Data Acquisition System (MIDAS). The I/O-Modules had at least 16-bit precision, resulting in uncertainties from the DAQ that were orders of magnitude lower than those from other sources in the measurements reported. A channel list was prepared to incorporate the measurements, including HRR, heat flux, and temperature.

2.2.1.1. Fire Calorimetry

The calorimetry measurement system at the NFRL measures heat release based on the principle of oxygen consumption calorimetry and the principle of fuel consumption calorimetry (consumption of natural gas). The NFRL utilizes large canopy exhaust hoods to capture fire effluents to quantify the heat release as a function of time. The system includes an emissions control system (ECS) to treat smoke particulates and combustion gases to comply with local

environmental requirements. Uncertainty in the HRR measurement using oxygen consumption calorimetry was 8.7% [5].

These structure separation experiments using instrumented target wall and natural gas burner utilized only oxygen consumption calorimetry. Verification (confirmation) of the oxygen consumption calorimeter using fuel consumption calorimetry as a reference was conducted immediately prior to this test series. The verification burn experiments are described in Section 3.

The heat release data and videos from the NFRL experiments will be published in the fire calorimetry database [6].

2.2.1.2. Temperature Measurements

Type K thermocouples were peened to the steel plates by drilling small holes in the steel plates. The thermocouples had a full range value of 1250 °C, and the standard relative uncertainty in temperature measurements reported by the manufacturer was ± 0.75 %.

A forward-looking infrared (FLIR) camera measured effective radiation temperatures. A high-speed mid-wavelength infrared camera (FLIR SC8300HD) recorded thermal images of the target structure for qualitative monitoring.

2.2.1.3. Heat Flux Measurements

The heat flux sensors and plate thermometer are shown in Fig. 5.

Fig. 5. Photograph showing plate thermometer (PTC) and heat flux sensors.

HFG1 is a water-cooled Schmidt-Boelter total heat flux transducer, and HFG2 is a water-cooled Schmidt-Boelter transducer with a zinc selenide window radiometer with a view angle of 150°. The plate thermometer was made and calibrated as described in Ref. [7].

The incident heat flux on a plate thermometer ($\dot{q}''_{inc}$, in W/m^2) can be calculated using the measured temperature of the plate thermometer (T_{PT}, in K) and the gas temperature near the plate thermometer (T_{gas}, in K), using the following relation, a rearrangement of Eq. 18 from Ingason and Wickstrom [8]:

$$\dot{q}''_{inc} = \sigma \cdot T_{PT}^4 + \frac{(h_{PT} + k_{PT})(T_{PT} - T_{gas})}{\varepsilon_{PT}} + \frac{\rho_{ST} \cdot C_{ST} \cdot \delta \cdot \left(\frac{\Delta T_{PT}}{\Delta t}\right)}{\varepsilon_{PT}} \quad \text{Eq. (1)}$$

where the time (t) is in seconds, the Stefan Boltzmann constant (σ) is 5.670E-8 W/(m^2·K^4), the convective heat transfer coefficient (h_{PT}) is taken to be 10 W/(m^2·K) [7], the conduction correction factor determined from NIST cone calorimeter data (k_{PT}) is 4 W/(m^2·K), ρ_{ST} is the alloy plate density, 8470 kg/m^3 from the alloy manufacturer, C_{ST} is the alloy plate heat capacity, 502 J/(kg·K) at 300 °C from the alloy manufacturer, δ is the alloy plate thickness, 0.79 mm, and the emissivity of the plate thermometer (ε_{PT}) is taken to be 0.85 at 480 °C. The expanded uncertainty in steady-state heat flux under ideal conditions measured by the plate thermometers is 5 % at 75 kW/m^2 [7].

2.2.1.4. Visual Characterization

Visual cameras were used to record the experiments.

2.2.1.5. Airflow Measurements

A handheld anemometer was used to measure the airflow at various locations under the exhaust hood and along the target structure. The airflow measurements and the locations are given in Table 2.

Table 2. Locations and airflow measurements during the preliminary structure separation experiments.

Location		Airflow speed, m/s					
		ECS* on but no fire		200 kW	400 kW	600 kW	1000 kW
		Parallel to wall	Perpendicular to wall	Parallel to wall	Parallel to wall	Parallel to wall	Parallel to wall
	Anemometer opening facing	North	East	North	North	North	North
South end	low (~300 mm above ground)	0.0	—	0.2 to 0.6	0.0 to 0.3	—	—
	~1 m above ground	0.0	—	0.0 to 0.2	0.0 to 0.2	—	—
	high (~300 mm below eave)	0.0	—	0.2 to 0.4	0.0 to 0.1	—	—
Middle	low (~300 mm above ground)	0.0	0.2	—	—	—	—
	~1 m above ground	0.0	0.0	—	—	—	—
	high (~300 mm below eave)	0.0	0.0	—	—	—	—
North end	low (~300 mm above ground)	0.0	—	—	0.5 to 0.7	—	—
	~1 m above ground	0.0	—	—	0.3 to 0.4	—	—
	high (~300 mm below eave)	0.0	—	—	0.0 to 0.2	—	—

*Emission Control System

2.3. Data Analysis and Results

The main objective of the preliminary structure separation experiments was to quantify convective and radiative heat fluxes from the natural gas burner with known heat outputs. Measurements from the preliminary SSE provided insights into radiative heat exposures to the eaves, window, and the nearby target structure in the subsequent experiments. The gas burner output or the fuel consumption and the corresponding HRR data from the oxygen calorimetry for the three preliminary SSE are plotted in Fig. 6. The heat fluxes for each experiment recorded at HFG1 and HFG2 and the calculated heat fluxes from the plate thermometer (PTC1) are plotted as a function of time in Fig. 7. Comparison with the corresponding HRR curve for a given experiment shows that the curves had similar time dependencies.

Thermocouples have been extensively used to measure temperature in fire environments. However, it is important to note that the temperature recorded by a thermocouple is not necessarily representative of the media immediately surrounding the sensor. In the absence of temporal variations, the temperature of the thermocouple sensor is controlled by a balance of convection, conduction, and radiation to and from the sensor. In addition, due to its thermal inertia, a thermocouple has a finite time response that varies depending on the same heat transfer processes. Consequently, it is unlikely that the temperatures recorded by the thermocouple in these experiments corresponded to those of the surrounding media. All reported temperatures are uncorrected for these factors. The standard relative uncertainty in thermocouple measurements is ± 0.75 %. Appendix C provides discussion on temperature measurement uncertainties.

However, the time-temperature profiles for the lower and upper TCs in the window and for the PTC1 shown in Fig. 8 do reflect changes corresponding to the heat output stages during these experiments. Fig. 9 shows the distribution of maximum temperatures recorded by the TCs in the steel plate eaves (SPE). The maximum temperatures recorded by TCs in the SPEs across the target structure are similar in the SSEGasBurner1 experiment. This uniformity in heating the SPEs can be attributed to the placement of the gas burner at an SSD of 5 ft. For the SSEGasBurner2 and SSEGasBurner3 experiments (SSD = 0 ft), the TCs in the central SPEs recorded higher temperatures compared to the SPEs on the ends. The parabolic shape of the trendline fitted to the plot of temperature data in Fig. 9 corresponds to the shape of scorching seen on the target wall in Fig. 10. The temperature variation in the eaves for the SSEGasBurner2 and SSEGasBurner3 experiments, with peak temperatures slightly left of center in Fig. 9, can be attributed to the observed plume lean toward the north side of the target wall (left).

Comparisons of temperature data measured using thermocouples and temperature data derived from FLIR measurements during SSEGasBurner1, SSEGasBurner2, and SSEGasBurner3 experiments are shown in Fig. 12, Fig. 13, and Fig. 14, respectively. The FLIR data extraction points are shown in Fig. 11. Temperature measurements from the FLIR camera are slightly lower than those measured by thermocouples and this behavior is consistent in all three experiments, except that the FLIR data drops at certain times during SSEGasBurner3 (see Fig. 14). This sudden drop in temperature estimated using the FLIR camera could be due to the noise in the data recorded by the camera. The plateau in the temperature profiles from the FLIR camera measurements could be attributed to the saturated image intensities for temperature above the maximum range of the camera when using a particular neutral density (ND) filter. The maximum temperature for the ND filter used in this study was around 375 ºC.

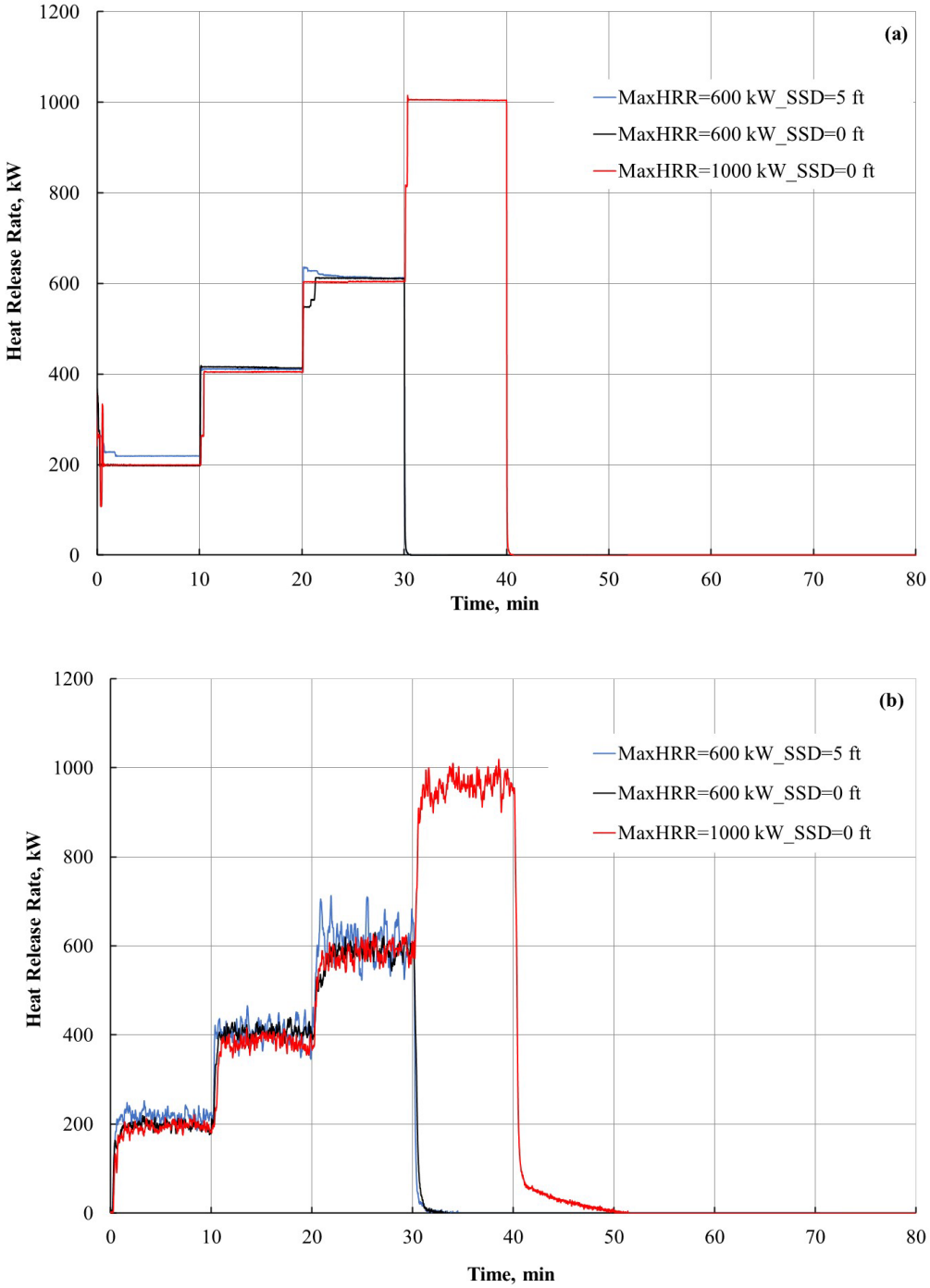

Fig. 6. Temporal plots of (a) gas burner output and (b) measured heat release rate for SSEGasBurner 1, SSEGasBurner 2, and SSEGasBurner 3 experiments. Uncertainties in HRR measurements are described in Appendix C.

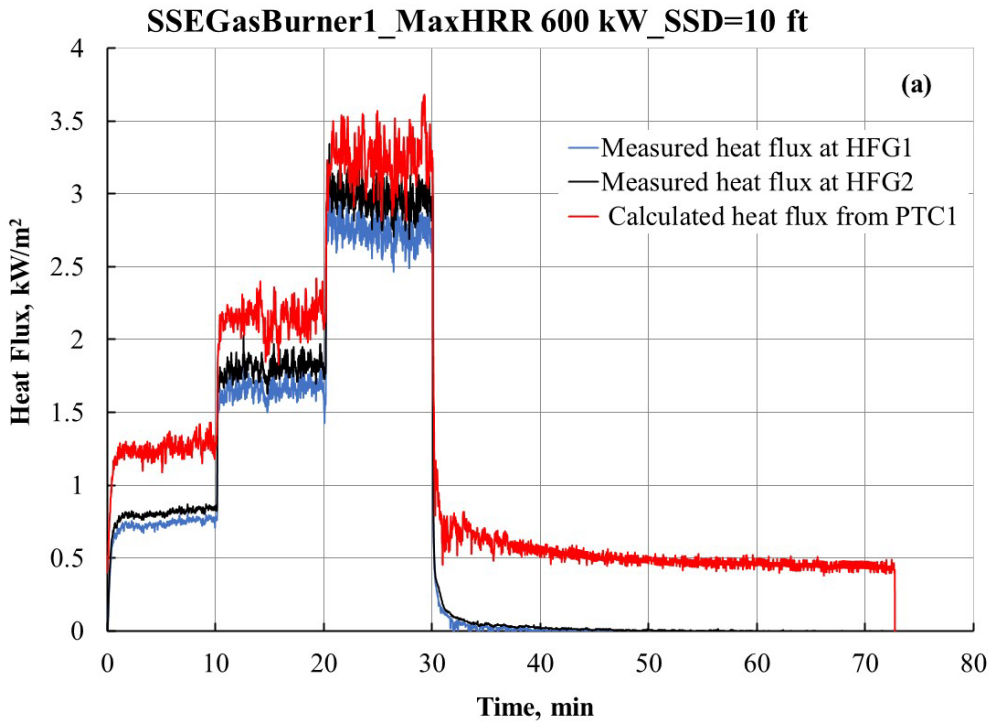
SSEGasBurner1_MaxHRR 600 kW_SSD=10 ft
(a)
Measured heat flux at HFG1
Measured heat flux at HFG2
Calculated heat flux from PTC1
Heat Flux, kW/m²
Time, min
0
0.5
1
1.5
2
2.5
3
3.5
4
0
10
20
30
40
50
60
70
80

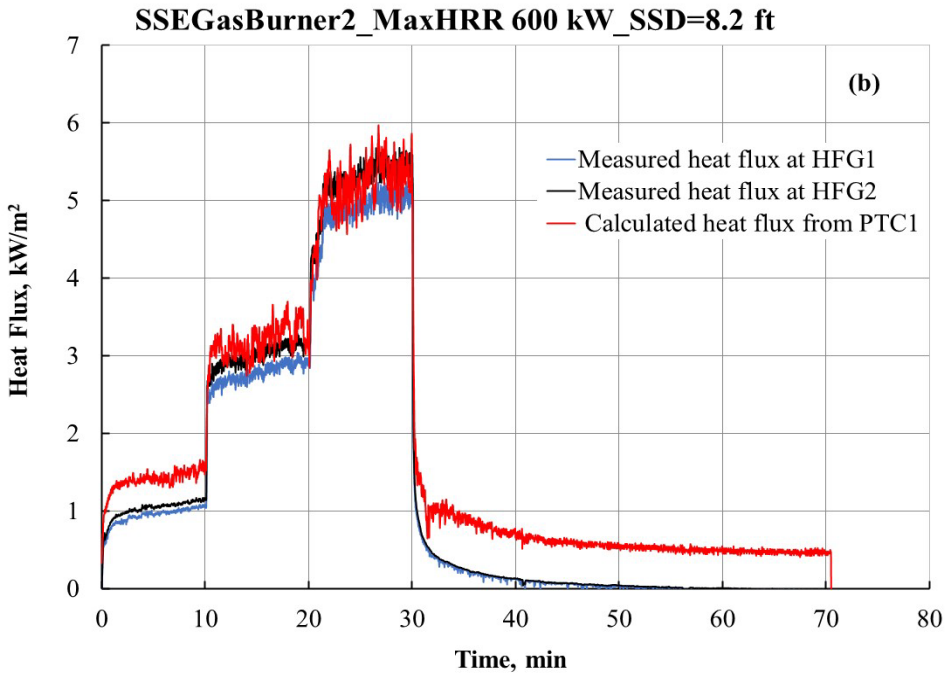
SSEGasBurner2_MaxHRR 600 kW_SSD=8.2 ft
(b)
Measured heat flux at HFG1
Measured heat flux at HFG2
Calculated heat flux from PTC1
Heat Flux, kW/m²
Time, min
0
1
2
3
4
5
6
7
0
10
20
30
40
50
60
70
80

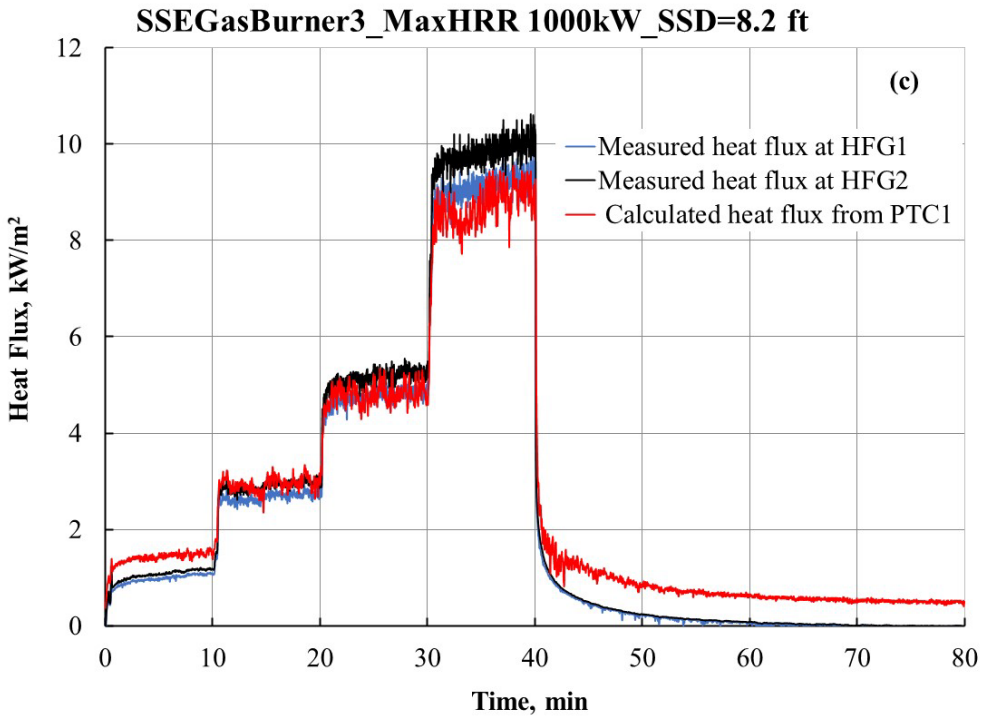

Fig. 7. Comparison of measured (HFG1and HFG2) and calculated (PTC1) heat fluxes during (a) SSEGasBurner 1, (b) SSEGasBurner 2, and (c) SSEGasBurner 3 experiments. Uncertainties in heat flux measurements are described in Appendix C.

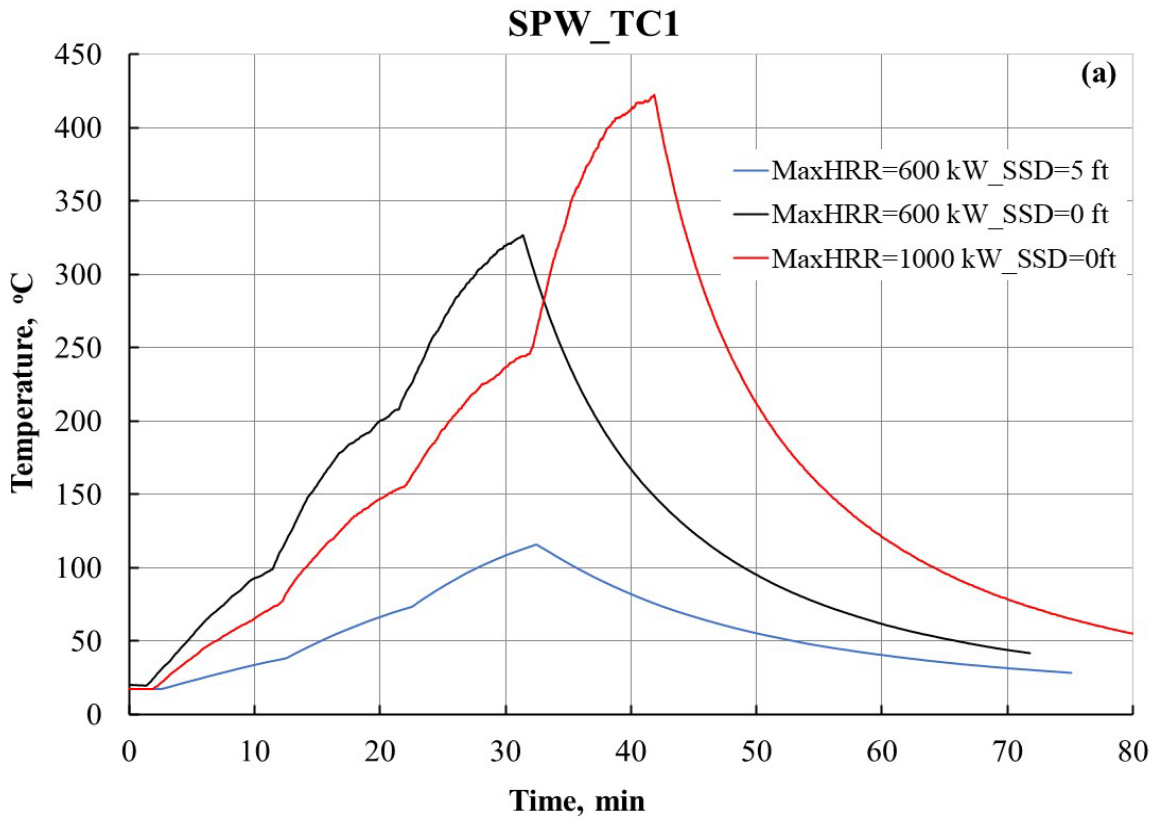
SPW_TC1
(a)
MaxHRR=600 kW_SSD=5 ft
MaxHRR=600 kW_SSD=0 ft
MaxHRR=1000 kW_SSD=0ft
Temperature, °C
Time, min
0
50
100
150
200
250
300
350
400
450
0
10
20
30
40
50
60
70
80

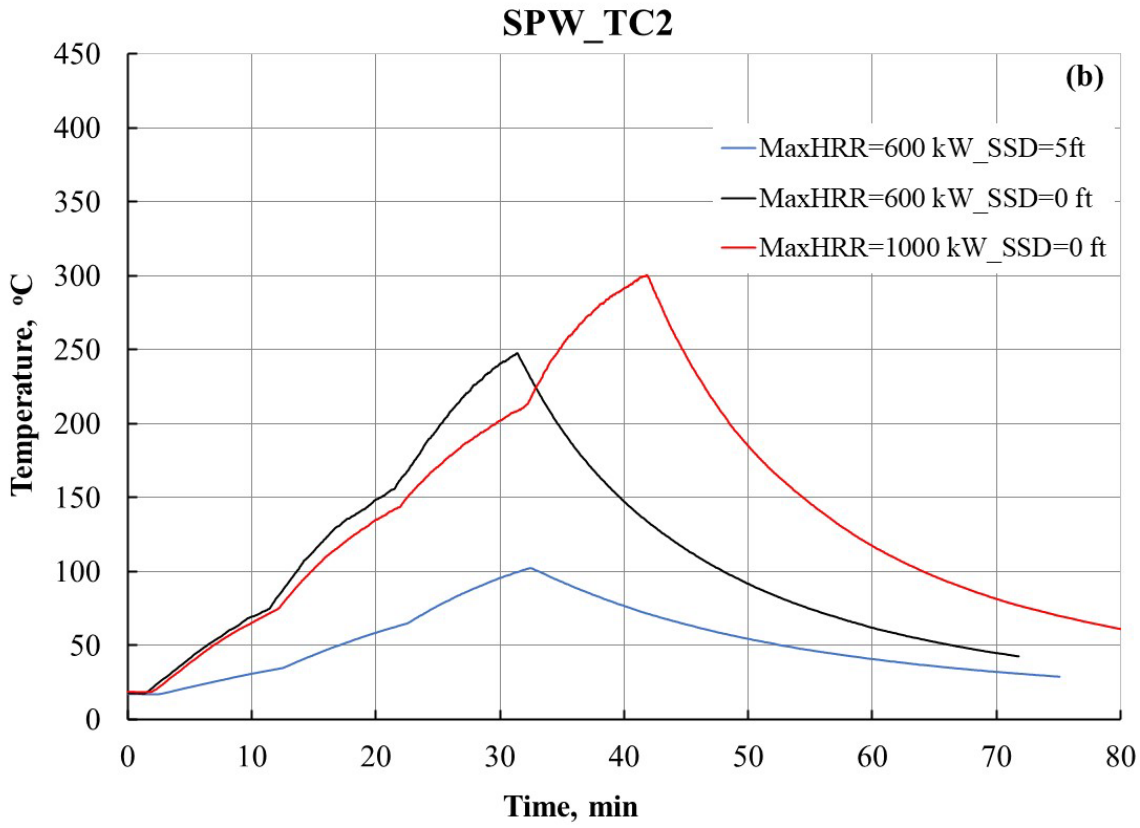
SPW_TC2
(b)
MaxHRR=600 kW_SSD=5ft
MaxHRR=600 kW_SSD=0 ft
MaxHRR=1000 kW_SSD=0 ft
Temperature, °C
Time, min
0
50
100
150
200
250
300
350
400
450
0
10
20
30
40
50
60
70
80

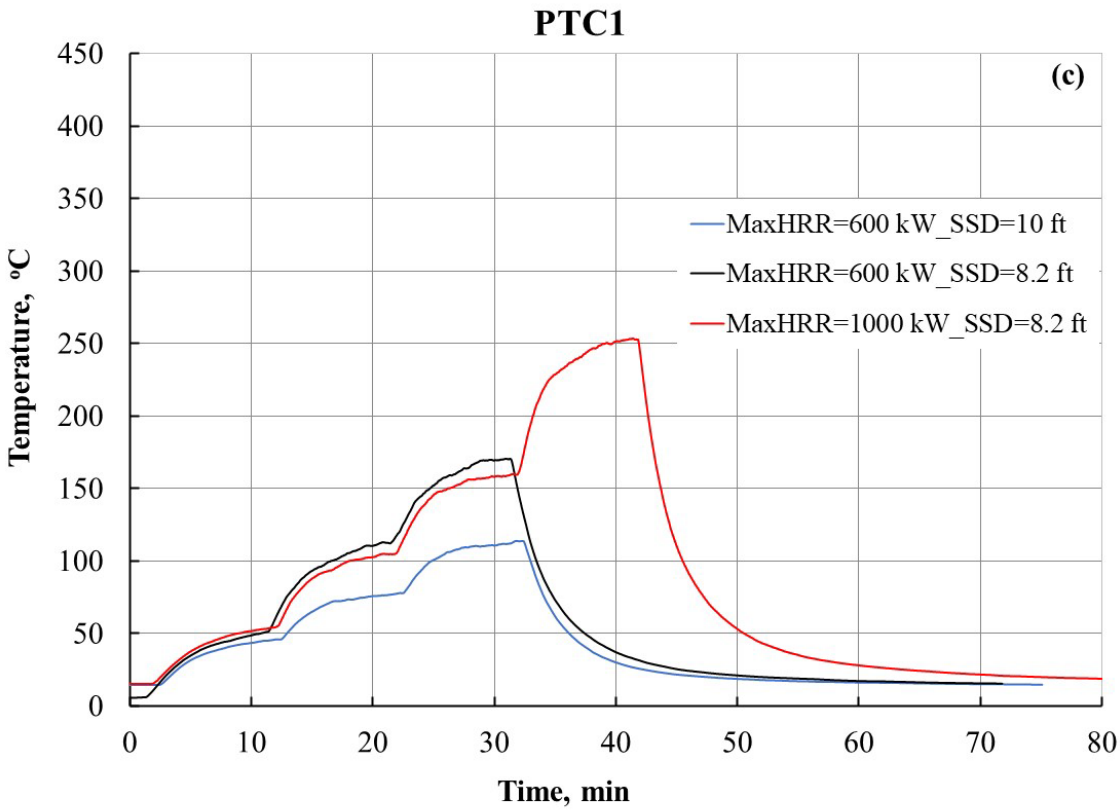

Fig. 8. Comparison of temperature-time profiles recorded at (a) lower, (b) upper thermocouple on the window steel plates (SPW_TC1 and SPW_TC2), and (c) PTC1. Standard relative uncertainty is ± 0.75 %.

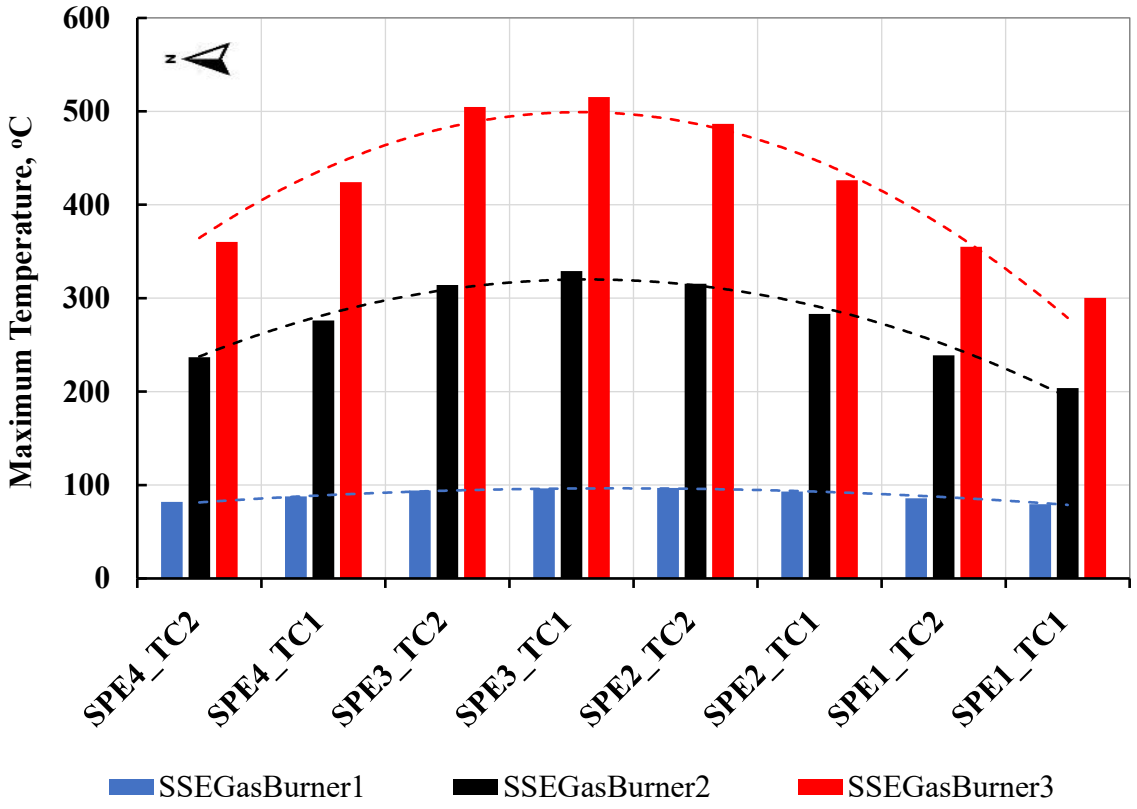

Fig. 9. Comparison of maximum temperatures measured in the eave steel plates (SPE) during SSEGasBurner1, SSEGasBurner2, and SSEGasBurner3 experiments. Standard relative uncertainty is ± 0.75 %. Note: N in the insert indicates north.

Fig. 10. Photograph showing scorching on the target wall.

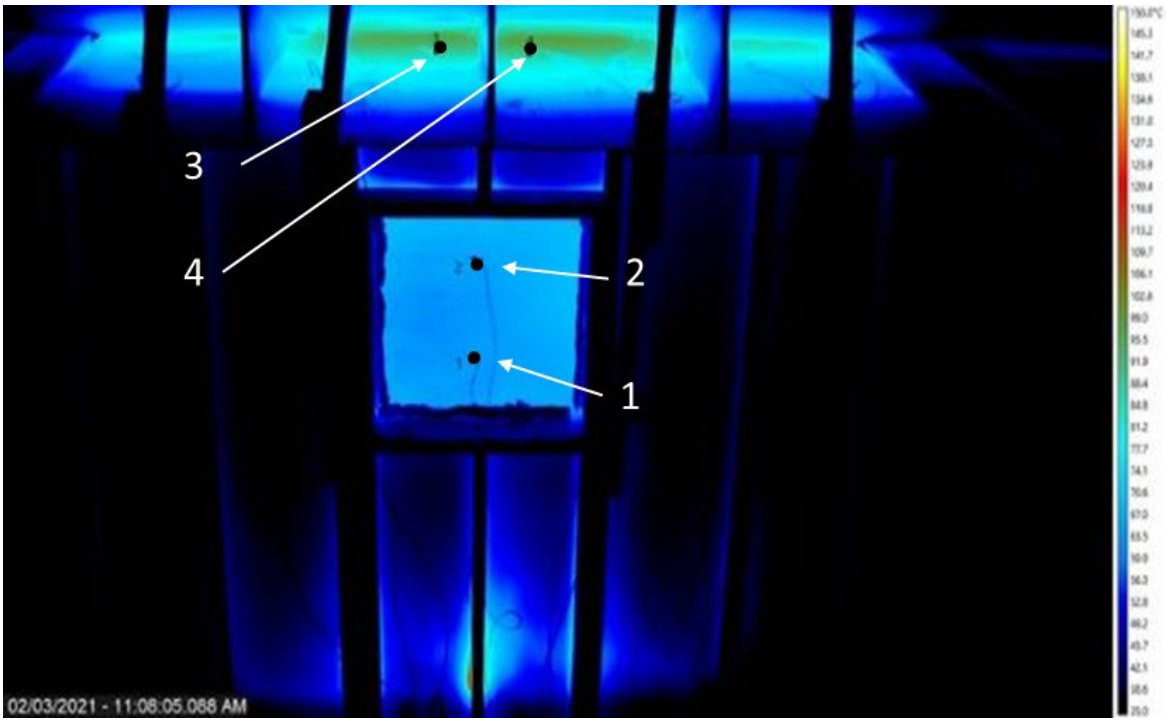

Fig. 11. Thermal image showing FLIR data extraction points.

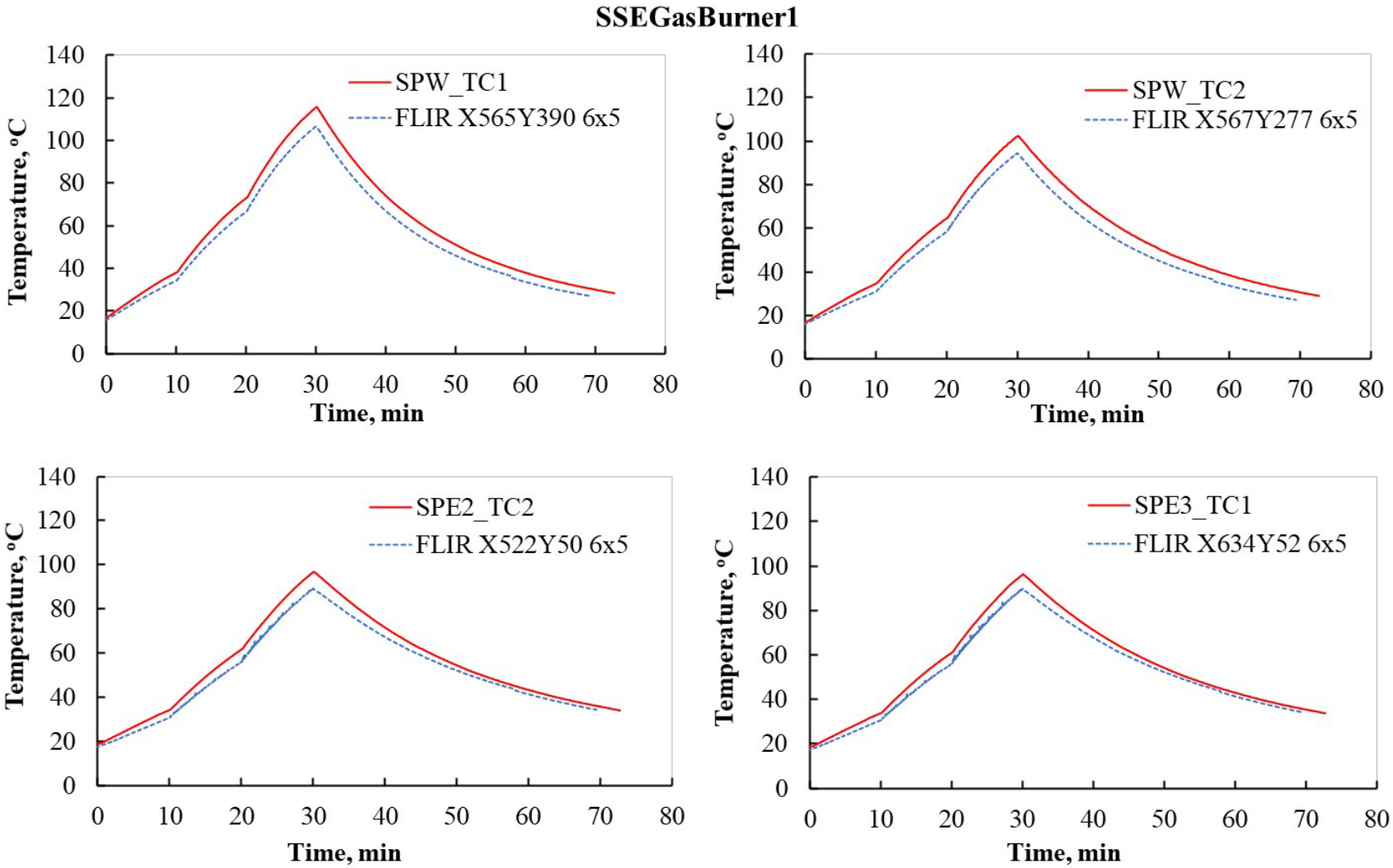

Fig. 12. Comparisons of temperature data measured using thermocouples and temperature data derived from FLIR measurements during SSEGasBurner1 experiment. Standard relative uncertainty for thermocouples is ± 0.75 %.

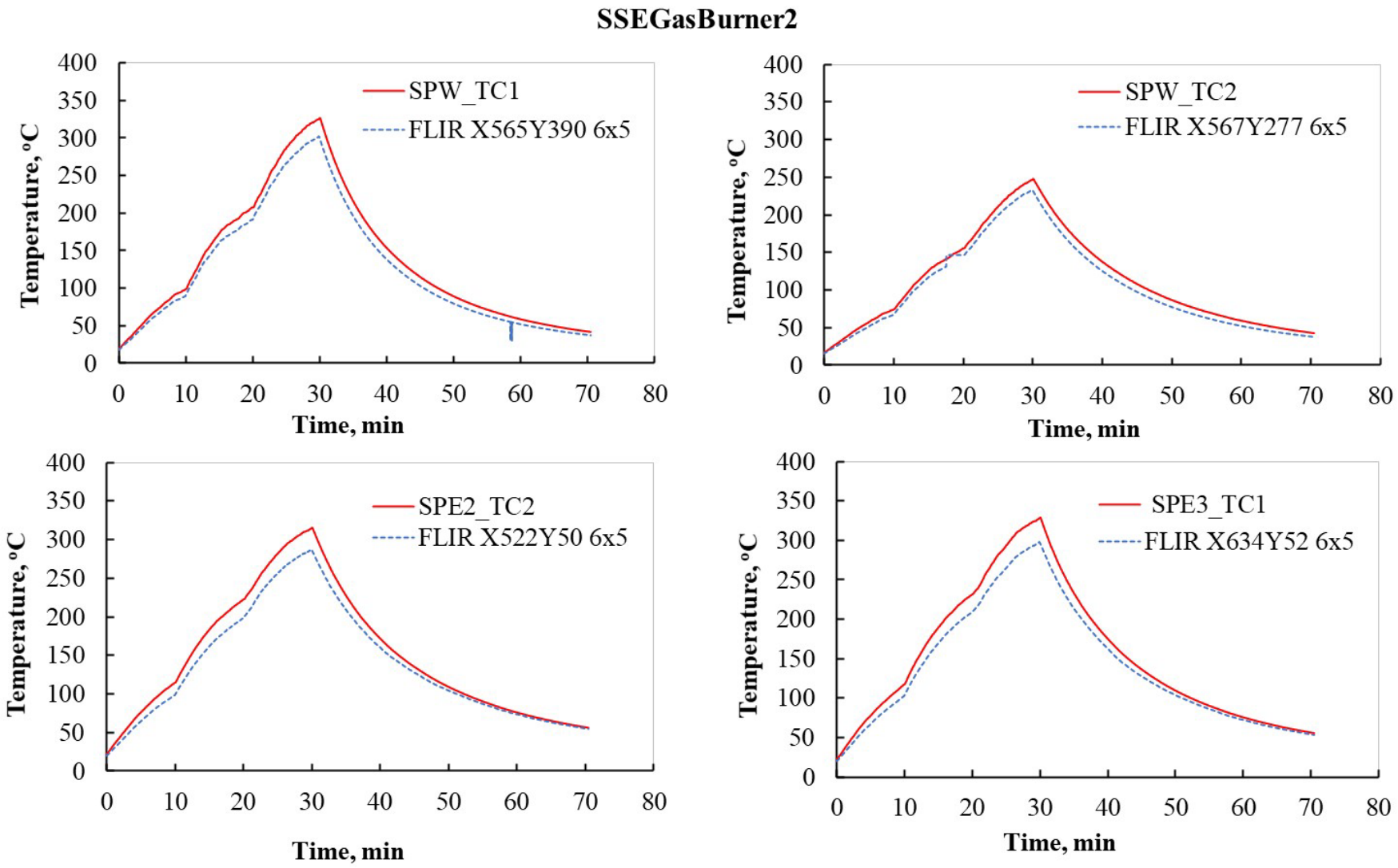

Fig. 13. Comparisons of temperature data measured using thermocouples and temperature data derived from FLIR measurements during SSEGasBurner2 experiment. Standard relative uncertainty for thermocouples is ± 0.75 % .

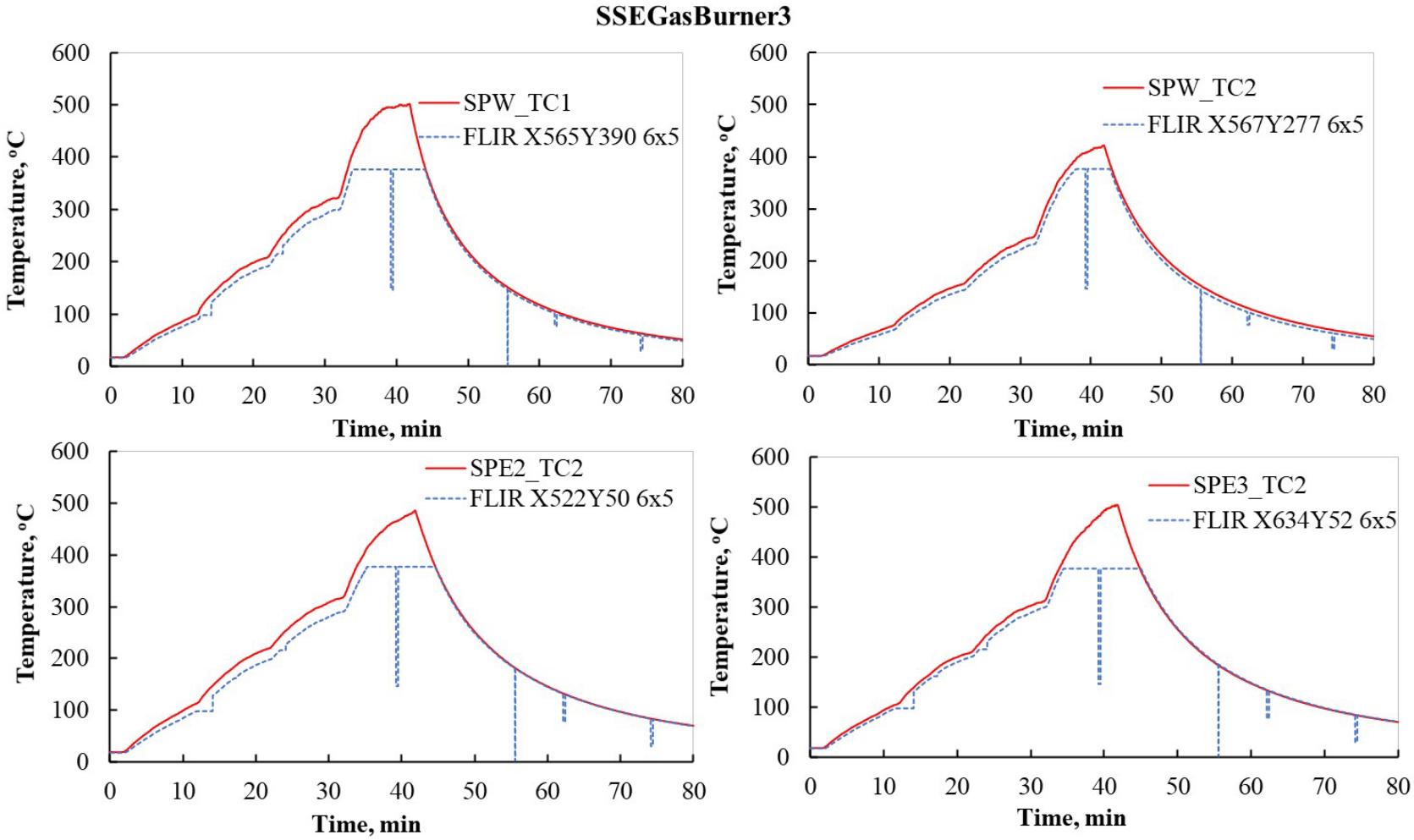

Fig. 14. Comparisons of temperature data measured using thermocouples and temperature data derived from FLIR measurements during SSEGasBurner3 experiment. Standard relative uncertainty for thermocouples is ± 0.75 % .

2.4. Technical Outcomes

The preliminary experiments using natural gas burners and an instrumented target structure have generated an extensive database that is available for the modeling community for validation and verification of the heat conduction subroutine/model within the Fire Dynamics Simulator (FDS). The cursory review of the data shows thermal propagation of heat in both horizontal (along the eaves) and vertical (on the window) configurations.

In addition to generating data helpful for modeling purposes, these experiments significantly helped troubleshoot and optimize the instrumentation and experimental design of the subsequent shed burn experiments. These experiments provided insights into the effects of the airflow bias within the NFRL as indicated by the observed plume lean toward the north.

3. Measurement Verification Experiments

Verification experiments, also referred to as 'confirmation burns', are part of the routine procedure at the NFRL [4]. These experiments are performed before starting a new experimental series using a natural gas burner to generate the full range of heat release rate anticipated for the experimental series. These natural gas burn experiments exercise all components of the calorimetry measurement and provide confirmation that the system is operating within its performance tolerances. The natural gas consumption system provides an accurate and precise source of chemical heat release rate as input into the facility's oxygen consumption calorimeters. Most importantly, the gas burners allow for a comparison of two independent measurements of heat release; one based on the principle of fuel consumption calorimetry and the other based on the principle of oxygen consumption calorimetry. This comparison is used for confirmation of both measurements and not as a 'calibration' of the oxygen consumption calorimetry [4].

In this experimental series, the verification burns also aided in confirming the heat flux gauges and examining the thermal sensitivity of the load cells in the weighing platform.

3.1. Experimental Configuration

Fig. 15 shows the experimental setup under the exhaust hood for the verification experiments. The natural gas burner was placed on the weighing platform and the heat flux gauge rigs were placed in front of the gas burner. In the final experiment only, plate thermometers were suspended facing downward at heights of 3 m (10 ft), 4 m (13 ft), and 5 m (16 ft) above the center of the burner. Table 3 provides the instrumentation location for the verification experiments with reference to the global origin.

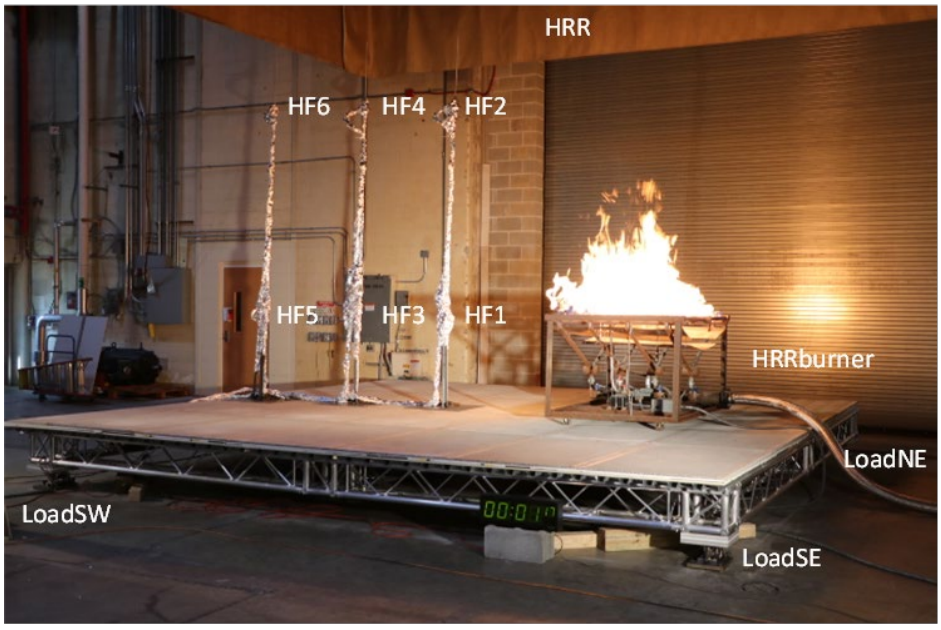

Fig. 15. Photograph showing experimental setup for the verification experiments. (Plate thermometers not shown in the photograph).

Table 3. Location of instrumentation for verification experiments with reference to the global origin.

Device	ID	X, cm (East +)	Y, cm (North +)	Z, cm (Up +)
Heat flux gauge on NS centerline facing burner (distance = 2 m; height = 1 m)	HF1	−200	20	100
Heat flux gauge on NS centerline facing burner (distance = 2 m; height = 3 m)	HF2	−200	20	300
Heat flux gauge on NS centerline facing burner (distance = 3 m; height = 1 m)	HF3	−300	0	100
Heat flux gauge on NS centerline facing burner (distance = 3 m; height = 3 m)	HF4	−300	0	300
Heat flux gauge on NS centerline facing burner (distance = 4 m; height = 1 m)	HF5	−400	−20	100
Heat flux gauge on NS centerline facing burner (distance = 4 m; height = 3 m)	HF6	−400	−20	300
Thermocouple on loadcell SW corner	TCSW	−33	152	0
Thermocouple gas temperature near loadcell SW corner	TCSWg	−33	152	0
Thermocouple on loadcell NW corner	TCNW	−33	740	0
Thermocouple gas temperature near loadcell NW corner	TCNWg	−33	740	0
Thermocouple on loadcell NE corner	TCNE	555	740	0
Thermocouple gas temperature near loadcell NE corner	TCNEg	555	740	0
Thermocouple on loadcell SE corner	TCSE	555	152	0
Thermocouple gas temperature near loadcell SE corner	TCSEg	555	152	0
Plate thermometer facing down 10 ft above center of burner	PTC1	0	0	305
Plate thermometer gas temperature 10 ft above center of burner	PTC1g	0	0	305
Plate thermometer facing down 13 ft above center of burner	PTC2	0	0	396
Plate thermometer gas temperature 13 ft above center of burner	PTC2g	0	0	396
Plate thermometer facing down 16 ft above center of burner	PTC3	0	0	488
Plate thermometer gas temperature 16 ft above center of burner	PTC3g	0	0	488
Weighting platform loadcell SW corner	LoadSW	−33	152	0
Weighting platform loadcell NW corner	LoadNW	−33	740	0
Weighting platform loadcell NE corner	LoadNE	555	740	0
Weighting platform loadcell SE corner	LoadSE	555	152	0

3.2. Data Acquisition and Instrumentation

The data acquisition system described in Section 2.2.1 was used for the confirmation burns. NI-9215 modules for sensors with voltage outputs were added to sample the output from the load cells at a frequency of 1 Hz. Since the load cells were sensitive to thermal exposures, Type K thermocouples were used to measure the change in temperature of the load cells. The mass measurements were added to the channel list including HRR, heat flux, and temperature measurements.

3.2.1. Weighing Platform

A rectangular platform constructed using lightweight aluminum modular trusses covered with fire-resistant decking layers, placed on 4 load cell weighing modules, was used to determine mass loss rate of the fire sources. Fig. 16 shows a schematic elevation view of the platform. The nominal dimensions of the platform were 19.26 ft × 19.26 ft x 1.22 ft (5.87 m × 5.87 m × 0.37 m); Fig. 15 shows an overview of the platform. The fixtures for the weighing modules located at each corner of the platform were designed to facilitate the expected rotation (due to bending) and translation (due to axial thermal expansion) of the platform during fire testing.

Initially, the load cells in the weighing modules were left exposed to ambient conditions in the laboratory (Fig. 17); however, a drift in the load measurements due to heating of the load cells was noted during the initial verification. In the subsequent tests, the load cells were thermally isolated by wrapping them in a thermal ceramic fiber blanket and aluminum foil, as shown in Fig. 18. The conceptual design and additional drawings for the weighing platform were provided in the first report of this series [3].

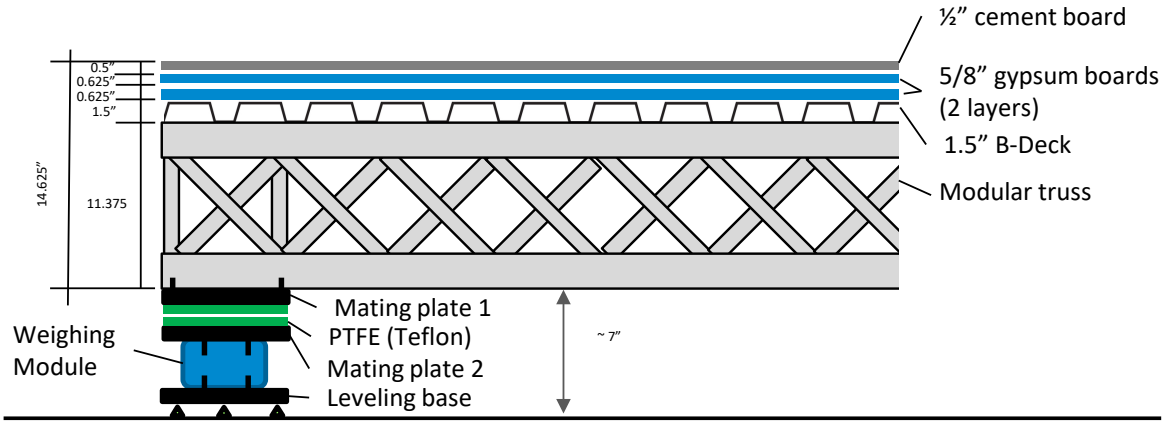

Fig. 16. Schematic illustration of the weighting platform elevation view.

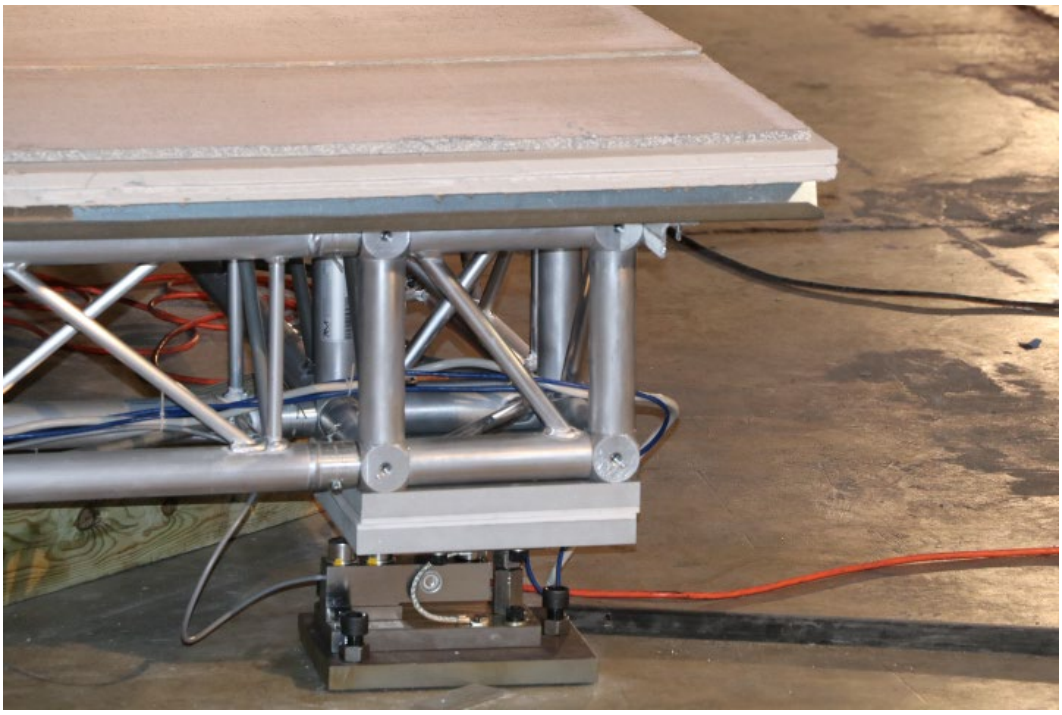

Fig. 17. Photograph showing weighing platform with load cells exposed to ambient laboratory conditions.

Fig. 18. Photograph showing weighing platform with load cells wrapped in thermal ceramic fiber blanket and aluminum foil.

3.2.2. Heat Flux Measurement

A total of six water-cooled Schmidt–Boelter heat flux gauges (manufactured by Medtherm) were used for heat flux measurements. Heat flux gauges were oriented perpendicular to the short axis of the gas burner as shown in Fig. 15. The locations and orientations of the heat flux gauges are provided in Table 3.

At the start of the experimental series, the heat flux gauges were cleaned, repainted using high temperature black paint of known absorptivity and emissivity, and calibrated by placing under a radiant cone heater. The calibration coefficient was determined by relating the voltage generated by the experimental gauge thermopile to the heat flux measured by the NIST reference gauge. Calibration curves and coefficients for all the heat flux gauges used in this experimental series are provided in Appendix A. The uncertainties in heat flux measurements are ± 3 % as discussed in Appendix C.

3.3. Results and Technical Outcomes

Temporal plots of both fuel consumption and oxygen consumption calorimetry HRR for the 8 MW and 4 MW natural gas outputs are shown in Fig. 19(a) and Fig. 19(b), respectively. These temporal plots confirm that the two independent measurements of heat release, fuel consumption and oxygen consumption calorimetry, agree within the estimated uncertainty limits. The plotted data also confirm that proper delay times have been applied in the heat release computation by oxygen consumption.

The heat fluxes for each experiment recorded at the three heat flux gauge rigs are plotted as a function of time in Fig. 20 and Fig. 21. Comparison with the corresponding HRR curve for a given experiment shows that the curves had similar time dependencies.

The verification experiments also confirmed the need for thermal insulation of the load cells, which was subsequently added to prevent the platform framing and weighing modules from heating above 50 °C.

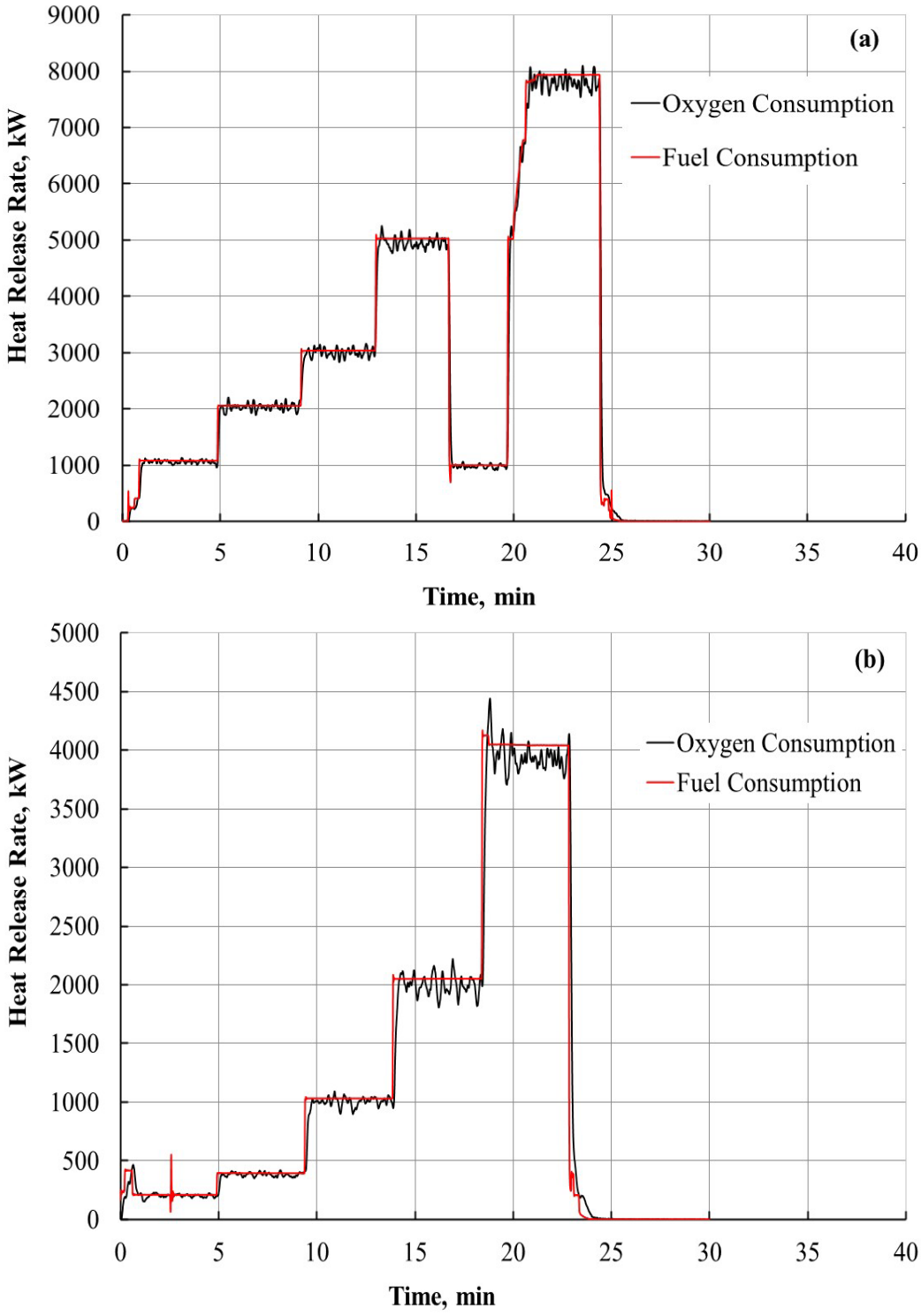

Fig. 19. Temporal profiles of HRR measured by oxygen consumption and fuel consumption calorimetry using (a) 8 MW and (b) 4 MW natural gas burners. Uncertainties in HRR measurements are described in Appendix C.

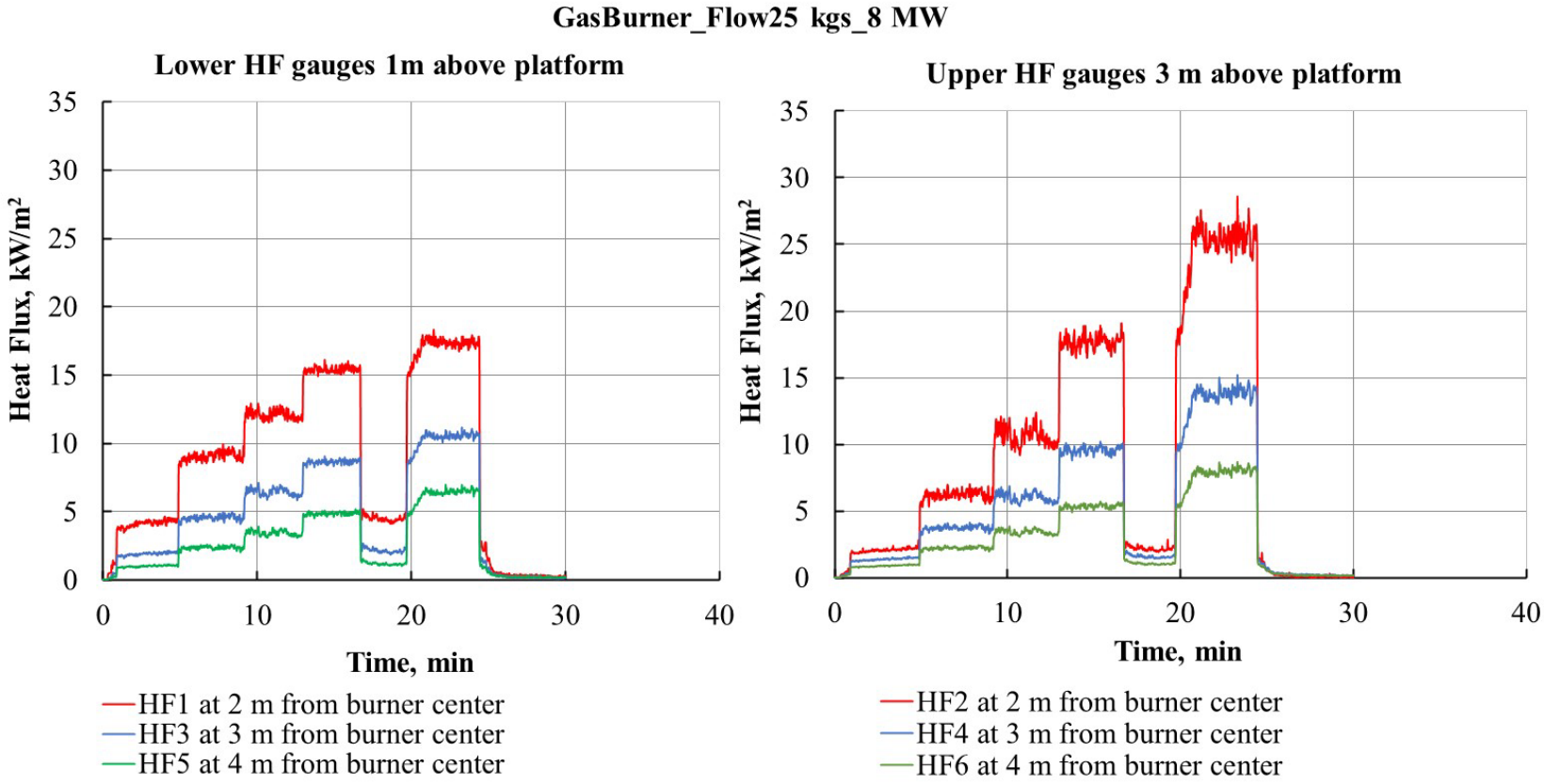

Fig. 20. Heat fluxes as a function of time recorded simultaneously by gauges located on the HFG Rig1, HFG Rig2, and HFG Rig3 placed in front of the natural gas burner (8 MW output). Standard relative uncertainty is ± 3 %.

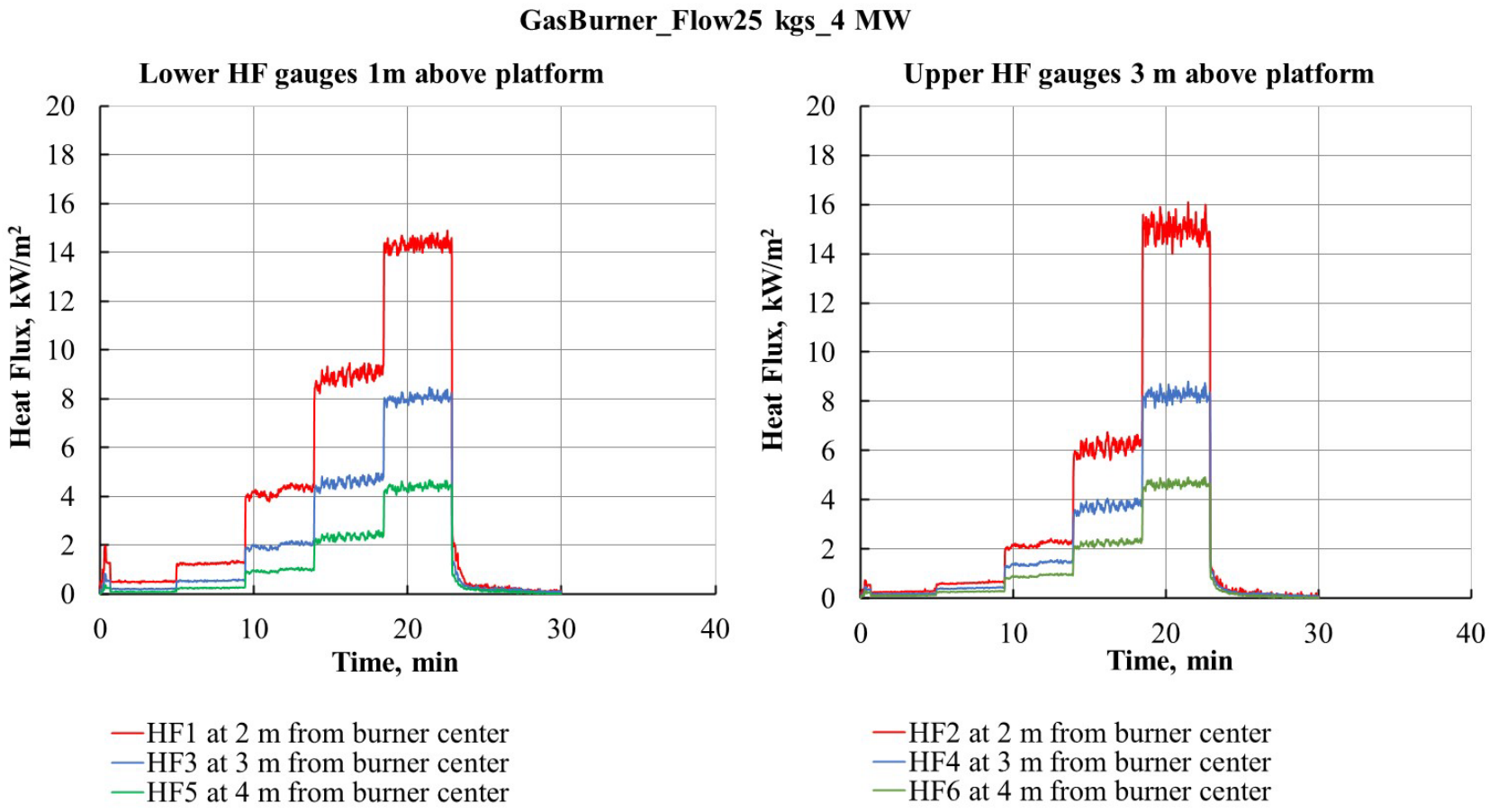

Fig. 21. Heat fluxes as a function of time recorded simultaneously by gauges located on the HFG Rig1, HFG Rig2, and HFG Rig3 placed in front of the natural gas burner (4 MW output). Standard relative uncertainty is ± 3 %.

4. Indoor Shed Burn Experiments without Wind

4.1. Test Objectives

The primary objective of the indoor free burning shed experiments was to quantify thermal exposures from small source structures (sheds) in terms of mass loss rate and HRR using oxygen calorimetry. Wood cribs based on ANSI/UL711 [9] design were placed within the source structures to simulate fuel loadings in storage sheds. High and low fuel loadings were considered in this study. Size 1-A cribs (12 layers of 6 members with approximate dimensions of 38 mm × 38 mm × 500 mm) had approximate dimensions of 500 mm × 500 mm × 456 mm for a given spacing of 54 mm between two members. The average mass of 1-A cribs was 19.4 kg ± 0.4 kg.

Heat fluxes were measured at predetermined locations to quantify thermal exposures to potential nearby target structures. To facilitate the mass loss measurement and avoid modification of flow dynamics, a nearby target wall was not present and the sources were burned alone. The burning behavior of sheds with different construction materials and sizes with two fuel loadings, high and low, were tested.

4.2. Experimental Configuration

A schematic of the general experimental setup for the shed burn experiments is shown in Fig. 22. Fig. 23 shows a photograph of the instrumentation and the wood Closet on the weighing platform.

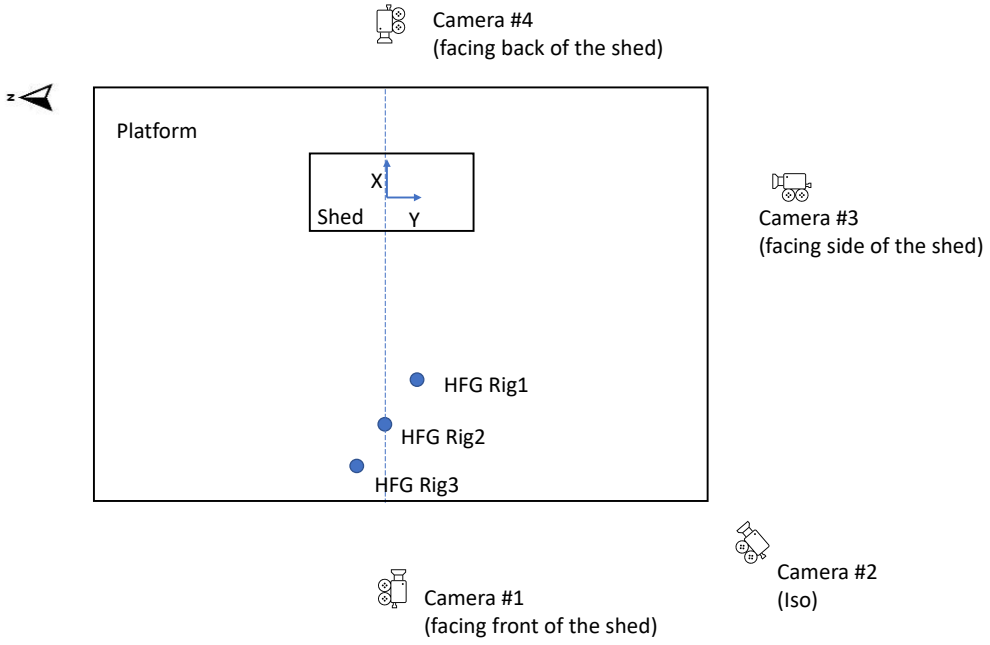

Fig. 22. Schematic showing experimental setup for free shed burn experiments.
Note: Plate thermometer rig is not shown in the schematic.

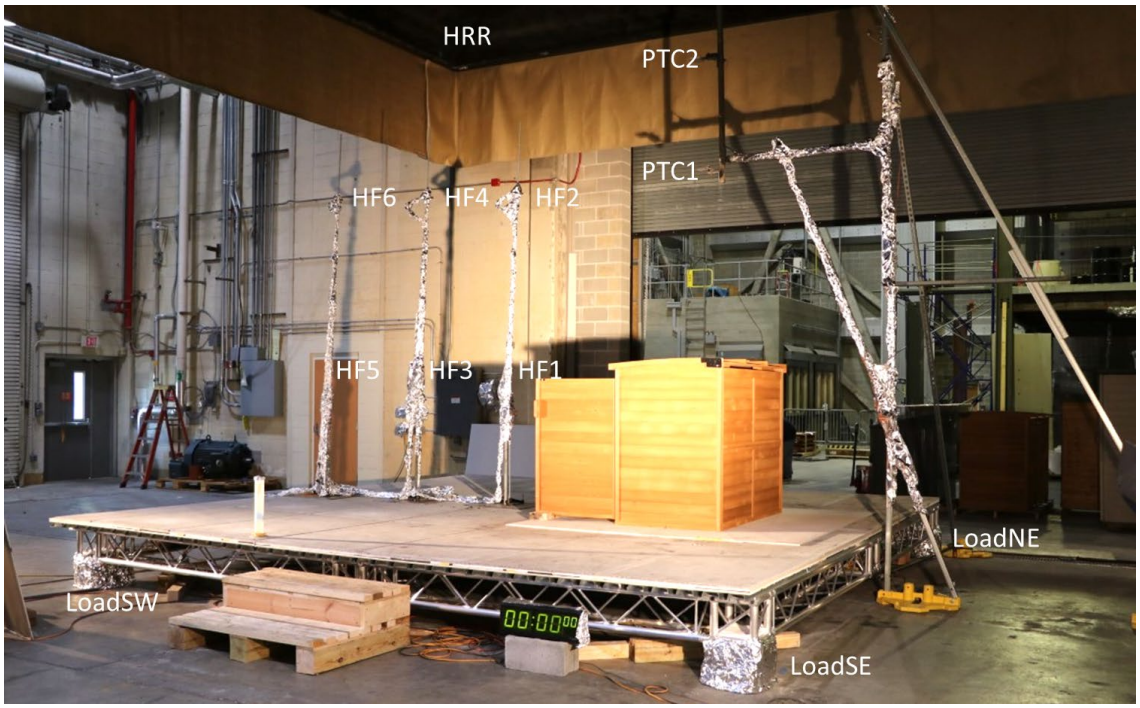

Fig. 23. Photograph showing experimental setup for shed burn experiments.
Note: not seen in the picture is PTC3.

4.2.1. Data Acquisition and Instrumentation

The data acquisition and instrumentation details are the same as provided in Sections 2.2.1 and 3.2.

Three sets of plate thermometers (facing down) and bare bead thermocouples were used to measure temperatures and estimate heat fluxes at three heights above the source (shed) center. The vertical location of the plate thermometers corresponded approximately to the location of the window (PTC1), eaves (PTC2), and roof peak (PTC3) of a single-story façade. This configuration enabled the estimation of heat fluxes at the window, eaves, and the roof when the target structure was exposed to radiant and convective heating from a burning source shed.

A video system consisting of four video cameras was used to record the burning of the shed. Synchronization of the video recordings was enabled through a central timing capability. The specific locations and orientation of the instrumentation for these experiments are provided in Table 4. The uncertainties in distance measurements are discussed in Appendix C.

Table 4. Location and orientation of instrumentation with reference to the shed origin (center of shed).

Device	ID	X (cm) (East +)	Y (cm) (North +)	Z (cm) (Up +)	Orientation
Heat flux gauge	HF1	−200	20	100	Facing shed
Heat flux gauge	HF2	−200	20	300	Facing shed
Heat flux gauge	HF3	−300	0	100	Facing shed
Heat flux gauge	HF4	−300	0	300	Facing shed
Heat flux gauge	HF5	−400	−20	100	Facing shed
Heat flux gauge	HF6	−400	−20	300	Facing shed
Plate thermometer	PTC1	10	−15	296	Above shed center, facing down
Plate thermometer	PTC1g	10	−15	296	Above shed center, facing down
Plate thermometer	PTC2	0	0	396	Above shed center, facing down
Plate thermometer	PTC2g	0	0	396	Above shed center, facing down
Plate thermometer	PTC3	10	15	496	Above shed center, facing down
Plate thermometer	PTC3g	10	15	496	Above shed center, facing down
HDMI Camera #1	Front	—	—	—	Facing shed
HDMI Camera #2	Iso	—	—	—	Isometrically facing shed
HDMI Camera #3	Side	—	—	—	Facing side of shed
HDMI Camera #4	Back	—	—	—	Facing rear side of shed

4.2.2. Test Procedure

Before starting a test, the shed and crib mass was measured and recorded. The moisture content of the wood cribs was measured on dry-basis using a hand-held moisture detector for solid wood. Measured moisture content for wood cribs was consistently < 5 %. The shed and wood cribs were placed on the weighing platform at pre-determined locations. In all the tests, the shed door was kept fully open to minimize complexities arising from reduced ventilation. The ventilation conditions significantly affect the fire hazard, such as HRR, fire growth rate, smoke, and CO production. Closed doors would significantly alter HRR and present a less critical scenario. When the test preparatory tasks were completed, the wood crib assembly inside the shed was ignited using 300 mL of heptane in an aluminum pan of nominal dimensions 90 mm × 130 mm × 30 mm (7.5 in × 5 in × 1.25 in). This method of wood crib ignition is known to be reproducible [10]. The heptane in the aluminum pan was ignited using a propane burner, and ignition was activated manually and recorded by the data acquisition system. At the same time, a digital display clock was started.

Once ignited, the shed was allowed to burn until it and the wood cribs had collapsed, and flames were no longer visible. At this point, the end of the experiment was announced and background data was collected. In the case of the noncombustible steel sheds, the experiment ended after the wood cribs had collapsed and flames were no longer visible. The data acquisition system was stopped after the background data was collected. The data was then transferred to the NFRL server.

Digital still cameras were used to record views from several directions and distances during an experiment.

4.2.3. Test Matrix

The primary test parameters for the indoor shed burn experiments were the construction materials, size, and fuel loading. The different values for each parameter are summarized in Table 5.

The test naming convention for NISSE experiments was as follows:

> *Phase* (1B) - *Material* [Wood (W), Steel (S), Plastic/Composite (P)] - *Size* [Closet (C), Very Small (VS)] - *Fuel Loading* (l, m, h) - *Wind speed* [w (mi/h)] – *structure separation distance (SSD)* [# (ft)].

The letter "R" followed by a number at the end of the test name indicates a test replicate. For example, the first repeat for a very small wooden shed with high fuel loading, no wind, and 10 ft SSD will have test number 1B-WVSh0-10-R1.

The shed dimensions and dimensions of the door openings are provided in Table 6,and the shed and fuel loading specifications are provided in Table 7. The uncertainties in distance measurements are discussed in Appendix C.

Table 5. Test parameters for the indoor shed burn experiments (1 ft = 0.305 m).

Source Structure Construction	**Source Structure Size**	**Fuel Loading**
Wood Steel Plastic/Composite	Closet (3 ft × 5 ft) < 75 ft^3 Very Small (4 ft × 4 ft) < 150 ft^3 Small (4 ft × 8 ft) < 300 ft^3 Medium (8 ft × 8 ft) > 300 ft^3	Low High

Table 6. Shed dimensions and storage capacity.

Shed Type	Measured shed dimensions, in			Measured door dimensions, in		Area of door opening, ft^2	Measured footprint, ft^2	Nominal shed storage capacity*, ft^3
	Height, minimum/ maximum	Width	Depth	Height	Width			
Wood Closet	52/53	63	36	47	60	20	16	75
Plastic Closet	66/72	70	30	63	31	14	15	55
Steel Closet	45/53	58	37	47	53	17	15	66
Wood Very Small Shed	60/64	67	56	52	63	23	26	70
Plastic Very Small Shed	48/50	56	51	43	48	14	21	106
Steel Very Small Shed	45/52	55	51	49	59	20	20	95

*Values provided by the manufacturer.

Table 7. Shed and fuel loading specifications for the sheds tested at NFRL.

Test #	Test ID	Material	Shed Type	Fuel Load*	Mass, kg			Fuel Density, MJ/ft^2
					Shed	Cribs	Total combustible	
1	1B-WCh0	Wood	Closet	High (4)	49	78	127	152
2	1B-WCh0-R1	Wood	Closet	High (4)	48	78	126	152
3	1B-WCh0-R2	Wood	Closet	High (4)	48	78	126	152
4	1B-PVSh0	Plastic	Very Small	High (6)	61	115	176	161
5	1B-WVSh0	Wood	Very Small	High (6)	75	117	192	142
6	1B-SVSh0	Steel	Very Small	High (6)	42	116	116	111
7	1B-WCl0	Wood	Closet	Low (2)	49	38	87	79
8	1B-PCl0	Plastic	Closet	Low (2)	38	39	67	104
9	1B-SCl0	Steel	Closet	Low (2)	24	38	38	49

*(number of 1-A cribs)

4.3. Data Analysis and Results

A variety of data can be used to characterize burning behavior of source structures. In this study, both visual observation and heat release rate (HRR) measurements were used to characterize fire growth. Images captured from various video cameras were used to provide an overview of each shed burn experiment.

The HRR of a source term is generally recognized as the most important parameter related to fire hazard. The temporal profile of the HRR of the source structure (shed) for the duration of the burn represents information on the fire behavior of the source structure. The total heat released (THR) during a fire test is calculated by integrating the HRR curve and thus represents the fire load of the test specimen. The temporal plots of mass loss and HRR for each of the source structures tested are provided in the following subsections. Mass loss data was also used to derive HRR, and comparisons of measured HRR and derived HRR are also provided for each experiment. The derived HRR was estimated as the product of mass loss rate and the effective heat of combustion. Considering the majority of fuel was wood cribs, an effective heat of combustion value of 16.2 MJ/kg was used. Comparison of measured and calculated HRR from combustible fuel in all the tests suggests that the HRR estimated from the mass loss rate was very similar to the HRR measured by oxygen consumption calorimetry. The observed differences are comparable to the uncertainty of 8.7% in HRR measurements by oxygen consumption calorimetry.

Additional measurements of radiative heat fluxes were designed such that supplemental characterization of shed burn experiments can be provided. Heat fluxes were recorded by six gauges located in front of the shed and are plotted as a function of time for each experiment. The peak heat flux values are tabulated for each shed burn experiment in Table 8. Generally, it was observed that the lower positioned HFGs recorded greater heat fluxes compared to the upper HFGs. The difference exceeds the uncertainties in heat flux measurements reported in Appendix C. This pattern is due to the relative proximity of the gauges to the source fire compared to the upper flux gauges. The viewing angles were similar for all gauges used.

Temporal plots of calculated heat fluxes derived from plate thermometers located above the shed are plotted, and the peak heat flux values calculated at approximate heights of window (PTC1), eaves (PTC2), and roof (PTC3) are presented for each experiment. The temporal plots of the measured and calculated heat fluxes had substantial high frequency fluctuations. The heat flux data presented in the subsections below is raw and was not smoothed.

A summary of heat release, heat flux, and temperature measurements for all shed burn experiments is provided in Table 8.

Table 8. Measured peak HRR, total heat released, maximum temperatures, and maximum heat flux values for the indoor shed burn experiments. Uncertainties in measured parameters are discussed in Appendix C.

Test ID	Material	Shed Size	Fuel Loading (1A cribs)	Total Combustible Mass, kg	THR, MJ	PHRR, MW	Calculated Peak Heat Flux above the Shed, kW/m²			Measured Peak Heat Flux from Shed Center, kW/m²					
							PTC1 3 m**	PTC2 4 m**	PTC3 5 m**	2 m*		3 m*		4 m*	
										1 m**	3 m**	1 m**	3 m**	1 m**	3 m**
1B-WCh0	Wood	C	High (4)	127	2104	4.2	76	48	21	47	27	21	15	10	9
1B-PVSh0	Plastic	VS	High (6)	176	4121	6.0	52	43	26	60	40	25	20	13	12
1B-WVSh0	Wood	VS	High (6)	192	3150	4.8	37	23	11	41	41	20	18	10	10
1B-SVSh0	Steel	VS	High (6)	116	1966	2.2	11	7	4	36	53	18	14	9	7
1B-WCl0	Wood	C	Low (2)	87	1457	4.0	38	19	9	57	30	24	15	11	9
1B-SCl0	Steel	C	Low (2)	39	684	0.9	4	2	1	16	7	6	2	3	2
1B-PCl0	Plastic	C	Low (2)	62	1542	3.2	35	12	6	28	11	12	8	7	6

*Distance from shed center, **height above the weighing platform.

1.1.1. Heptane Burn

As mentioned in Section 3.2.2, 300 mL of heptane was used as an ignition source for the wood cribs within the source structures. The HRR of the 300 mL heptane was measured in triplicate to determine the contribution of heat release from heptane during the shed burns. The temporal profiles of the HRR are shown in Fig. 24. The total heat released from 300 mL heptane was 9.2 MJ ± 0.2 MJ and the peak HRR was 54 kW ± 5 kW. On average, 300 mL of heptane burned for 5 min.

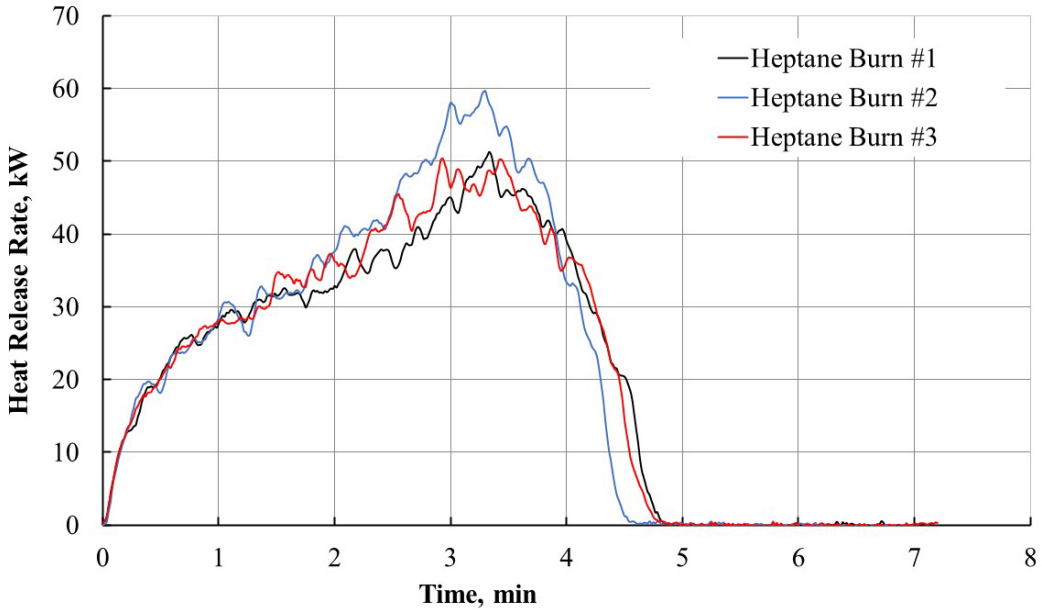

Fig. 24. Heat release rate for 300 mL of heptane.

4.3.1. Test: 1B-WCh0

4.3.1.1. Shed Specification

The source structure was a commercially available wood Closet with high fuel loading of four 1-A wood cribs. The Closet was made from cypress wood. A photograph of the wood Closet is shown in Fig. 25(a), and a photograph of the wood Closet with four wood cribs stacked in a 2 × 2 pattern is shown in Fig. 25(b). As seen in Fig. 25(b), the front door of the wood Closet was kept open, however, the top lid was placed in position without locking. The total mass of the four wood cribs was 78 kg and that of the wood Closet was 49 kg. The resulting total combustible mass for this source structure was 127 kg. The Closet had a height of 53 in and had a footprint of 16 ft^2.

This particular shed with high fuel loading was tested in triplicate to establish the reproducibility of the burning and of the measured data. The results of these reproducibility tests are discussed in Section 4.4.1.

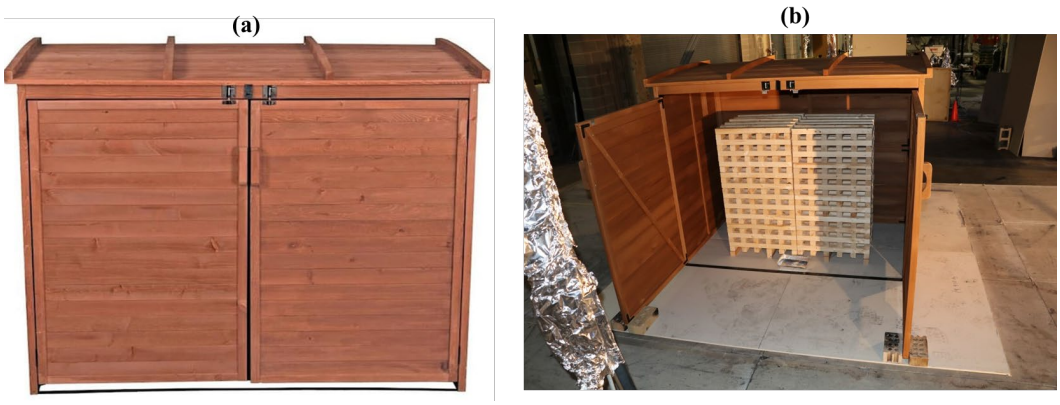

Fig. 25. Photograph of (a) wood Closet and (b) wood Closet with four 1-A cribs. Test 1B-WCh0.

4.3.1.2. Burn Overview

The flame spread in the wood Closet can be noted from the photographs in Fig. 26. The burning behavior of the wood Closet with high fuel loading can also be noted from the mass loss plot and the HRR plot shown in Fig. 27(a) and Fig. 27(b). The HRR curve for 1B-WCh0 has two peaks. Visual observations during the test and review of test videos suggest that the top lid of the Closet was lifted up due to the flames from burning of heptane and wood cribs. The first peak occurred during the initial burning of cribs, and the burning of shed side walls contributed to the second peak in the HRR profile. Intense burning of the source structure at the time of peak HRR at 8 min and 10 min from the ignition of wood cribs can be noted from Fig. 26(c) and Fig. 26(d), respectively. Fig. 26(e) shows the burning of wood cribs after the source structure was fully consumed in the fire and the wood cribs were exposed to excess oxygen.

Heat fluxes calculated from plate thermometer measurements above the shed are plotted in Fig. 28. Peak heat fluxes in the flame and plume above the shed were recorded at 10 min from the ignition of wood cribs. The highest heat fluxes were recorded at PTC1, which corresponded with the window height. Fig. 29 shows the comparison of measured heat fluxes horizontally from the shed. The lower heat flux gauges recorded high heat fluxes due to their proximity to the burning fuel, while upper gauges measured the flame heat flux. The high measured and calculated heat fluxes suggest that non-hardened structures or structural components would readily ignite under such exposure conditions.

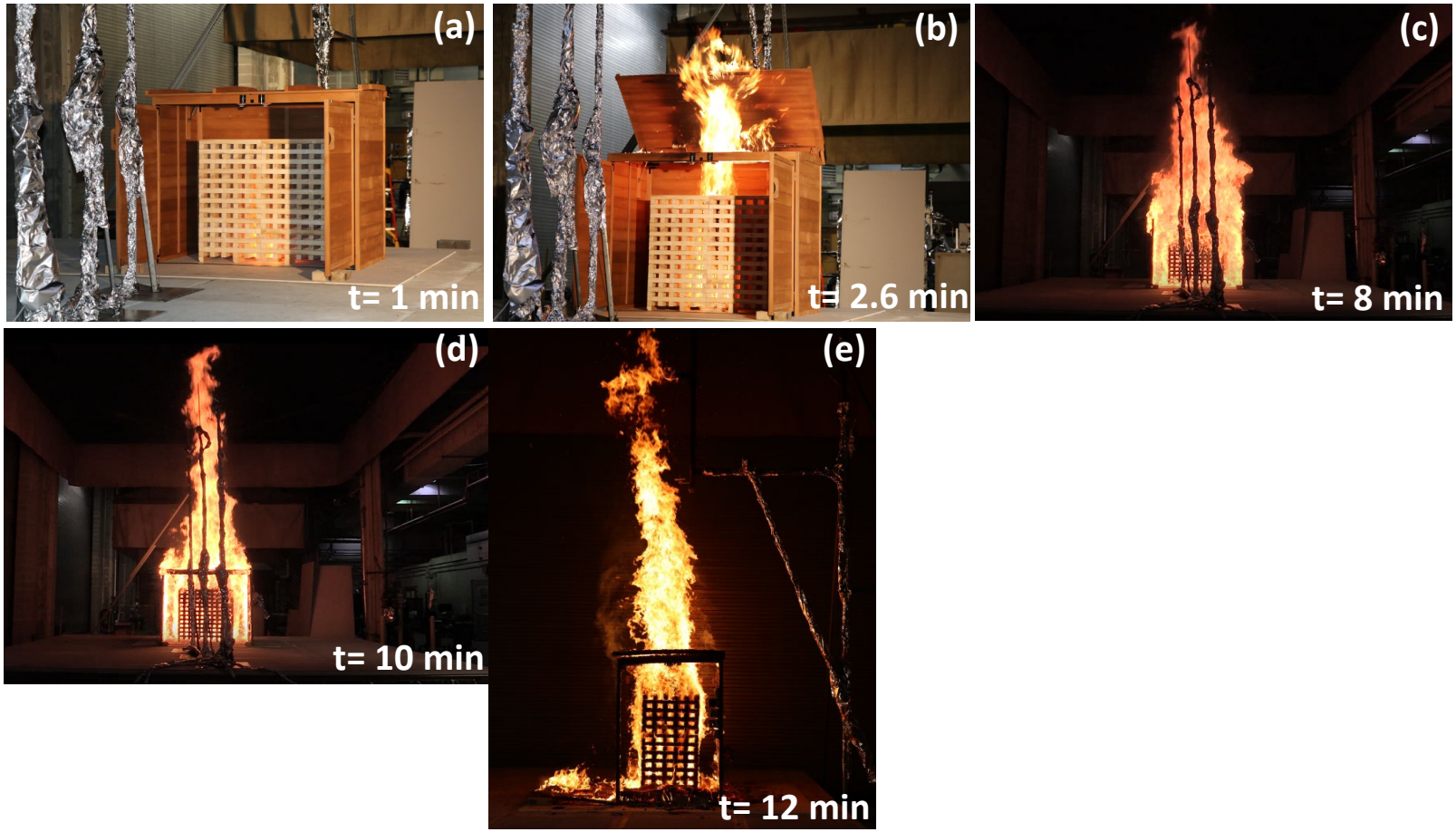

Fig. 26. Photographs captured from videos recorded by (a) and (b) Cameras #2, (c) and (d) Camera #1, and (e) Camera #3 showing ignition of cribs, the opening of the Closet top, flame heights at the time of PHRRs, and burning of wood cribs after the Closet was consumed in test1B-WCh0.

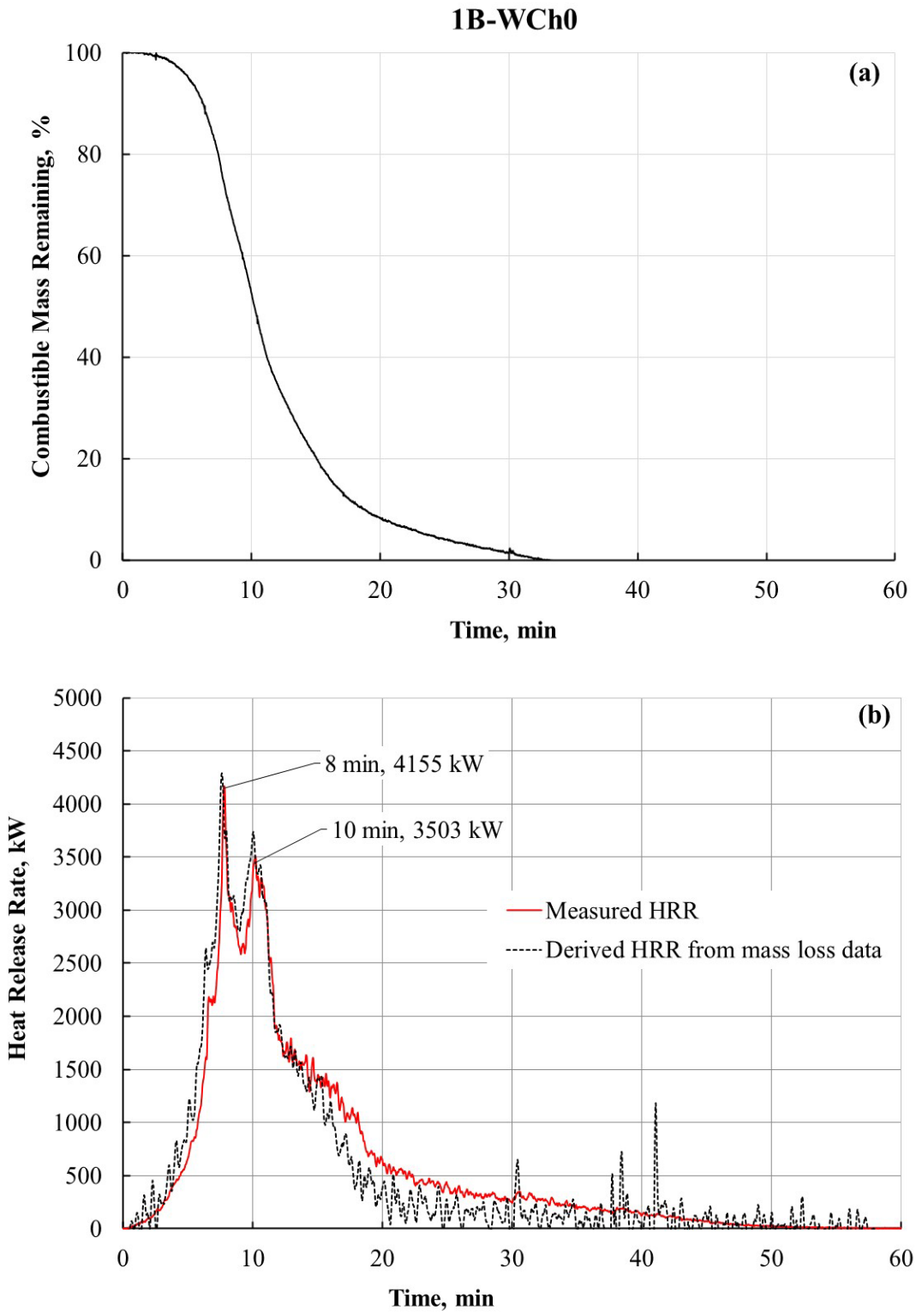

Fig. 27. Temporal plots of (a) percent mass of combustible fuel and (b) measured and calculated heat release from combustible fuel in test 1B-WCh0.

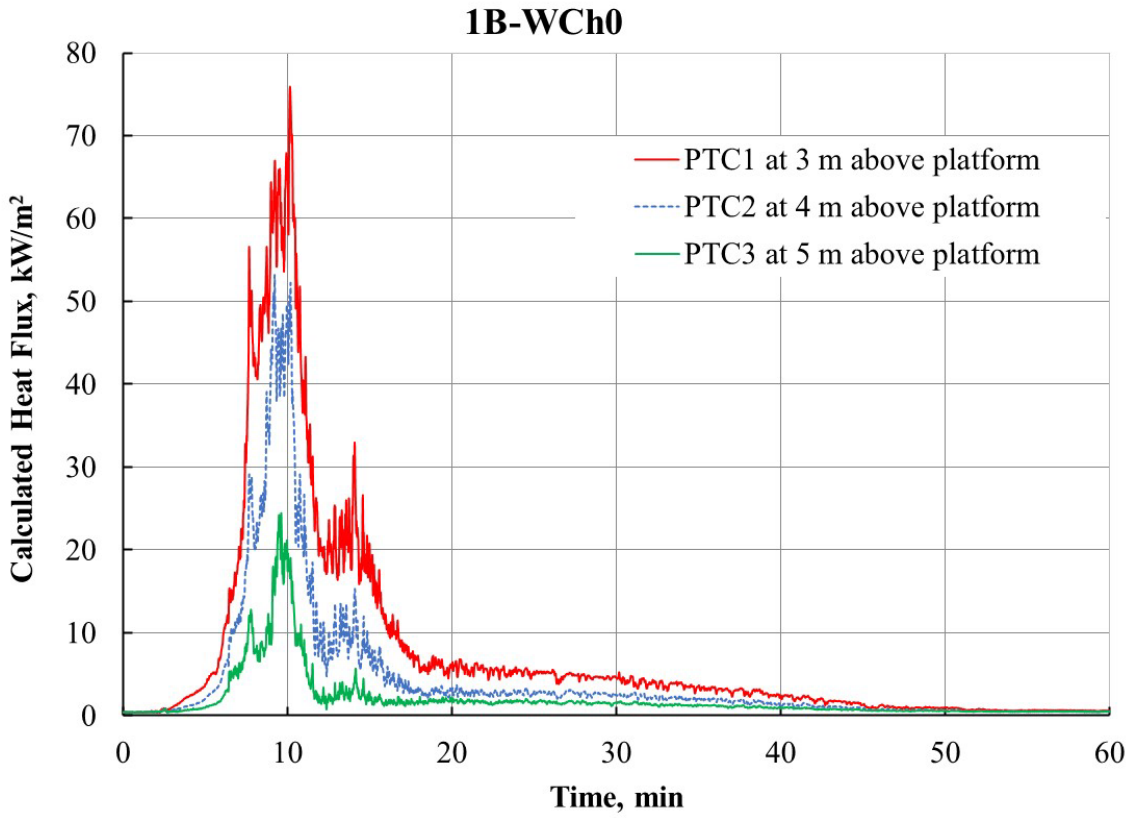

Fig. 28. Heat fluxes calculated from PTC1, PTC2, and PTC3 located above the Closet in test 1B-WCh0. Standard relative uncertainty is ± 5 %.

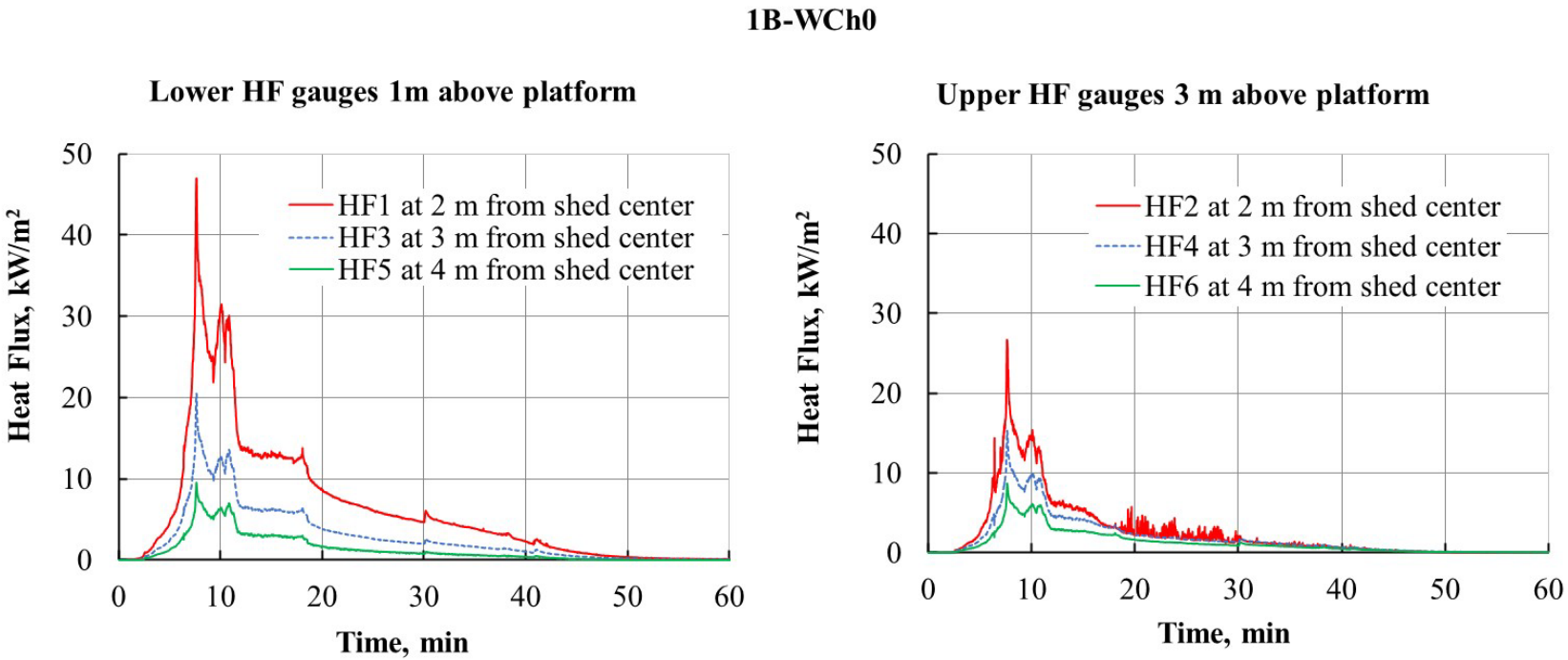

Fig. 29. Heat fluxes as a function of time recorded simultaneously by gauges located on the Rig1, Rig2, and Rig3 placed in the front of the Closet in test 1B-WCh0. Standard relative uncertainty is ± 3 %.

4.3.2. Test: 1B-PVSh0

4.3.2.1. Shed Specifications

A photograph of a plastic Very Small (VS) shed is shown in Fig. 30(a), and a photograph of a plastic VS shed loaded with six wood cribs is shown in Fig. 30(b). This shed was made from high density polyethylene (HDPE) and had a footprint of 15 ft^2. As seen in Fig. 30(b), the front door of the shed was kept open for the burn. The total mass of six wood cribs was 115 kg, and the mass of the plastic VS shed was 61 kg. The resulting total combustible mass for this source structure was 176 kg. In anticipation of a pool fire due to the melting of the HDPE, the plastic shed was placed in a sheet metal pan with nominal dimensions of 229 cm × 224 cm × 8 cm.

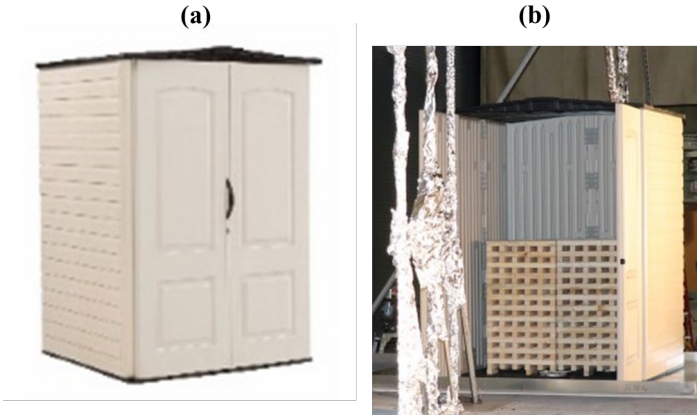

Fig. 30. Photograph of (a) plastic Very Small shed (b) with high fuel loading of six 1-A cribs. Test1B-PVSh0.

4.3.2.2. Burn Overview

The burning behavior of the plastic VS shed with six cribs is shown in Fig. 31. The shed roof melted and collapsed immediately after the ignition of the wood cribs. The door and the walls ignited and melted about 5 min after the ignition of the cribs, as shown in Fig. 31(c). After the shed melted and collapsed, the molten plastic burned as a pool fire in the metal pan with tall flames reaching as high as 16 ft, as shown in Fig. 31(d). The pool fire and the burning of the wood cribs generated a combined PHRR of 6 MW at 8 min. The mass loss profile and HRR profiles for 1B-PVSh0 are shown in Fig. 32. Following the collapse of the roof within 5 min of wood crib ignition, the plate thermometers above the shed were exposed to intermittent flame contact. High heat fluxes, in excess of 50 kW/m^2, were registered at the window height (PTC1) as shown in Fig. 33. Since the shed structure did not provide much protection from the burning fuel within the structure, the surrogate target components above the shed were exposed to significant heat fluxes throughout the burn. Heat fluxes measured by gauges located in front of the shed are plotted as a function of time in Fig. 34. Slight peak in the heat flux profile in Fig. 34(a) at 40 min corresponds with the peak in measured HRR in Fig. 32(b). The raking of embers from wood crib burning caused intense smoldering of embers in presence of freshly available ambient oxygen resulting in additional HRR.

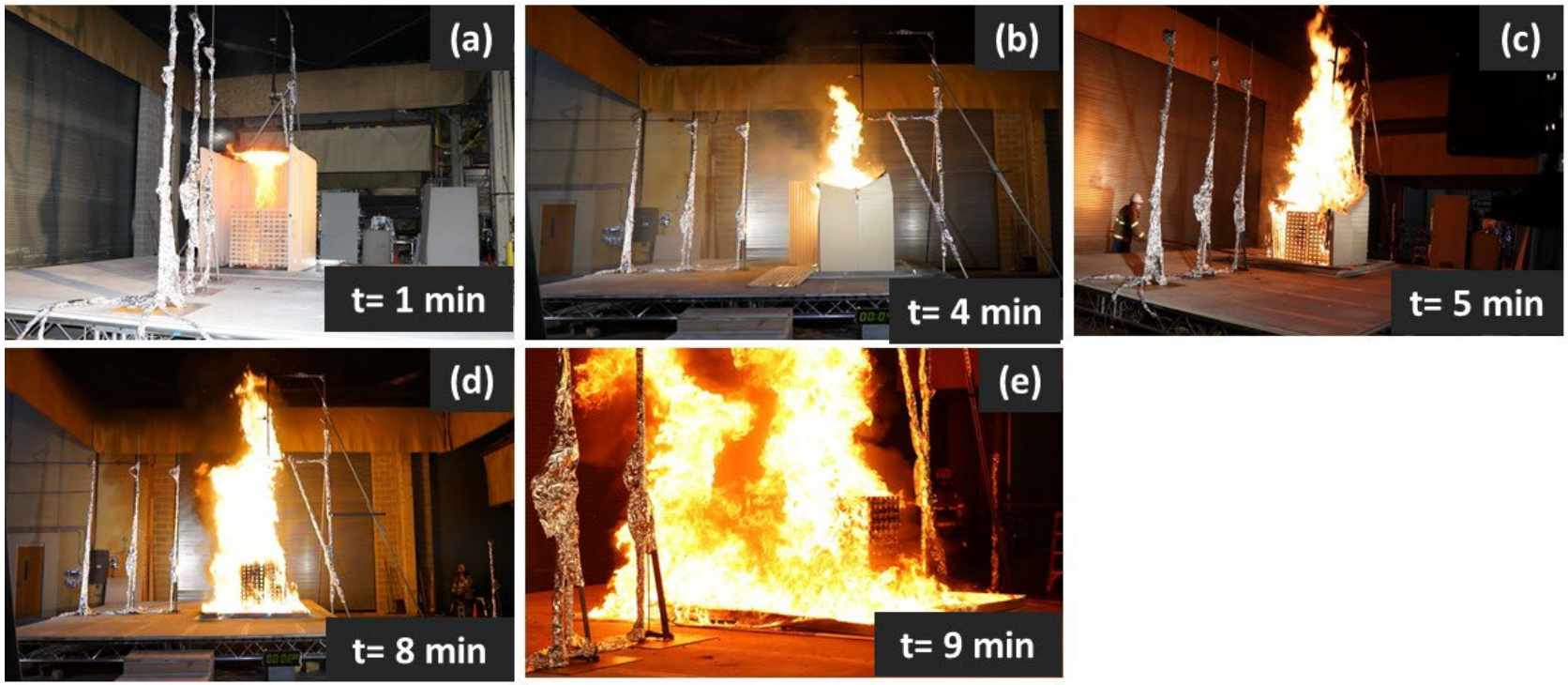

Fig. 31. Photographs captured from videos recorded by (a) Camera #1, (b) Cameras #3, (c) Camera #2, (d) Camera #3, and (e) Camera #2 showing flame spread to the roof, roof collapse, flame heights at the time of PHRRs, and pool fire due to burning of polymer melt and burning of wood cribs in test 1B-PVSh0.

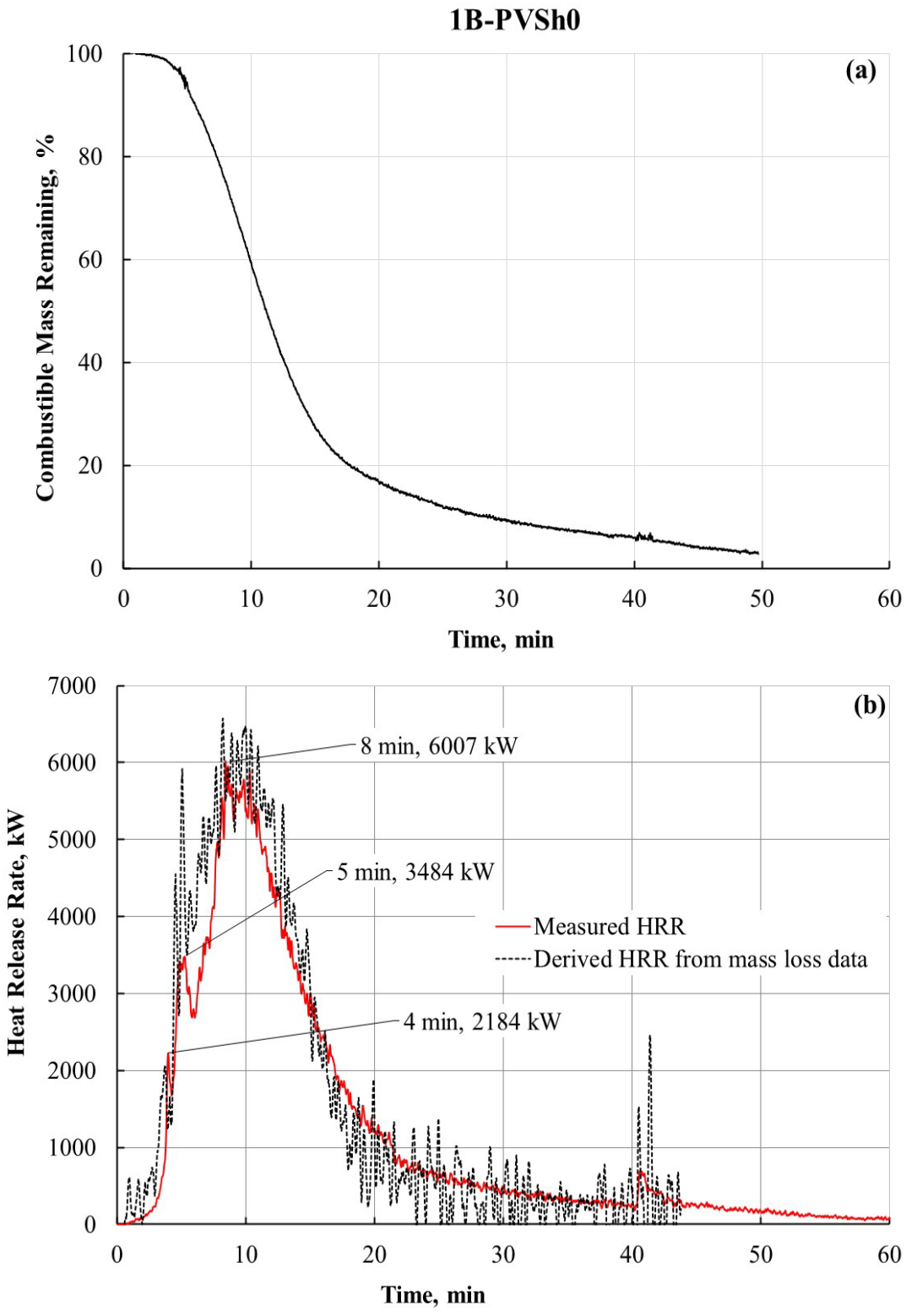

Fig. 32. Temporal plots of (a) percent mass of combustible fuel and (b) measured and calculated heat release from combustible fuel in test 1B-PVSh0.

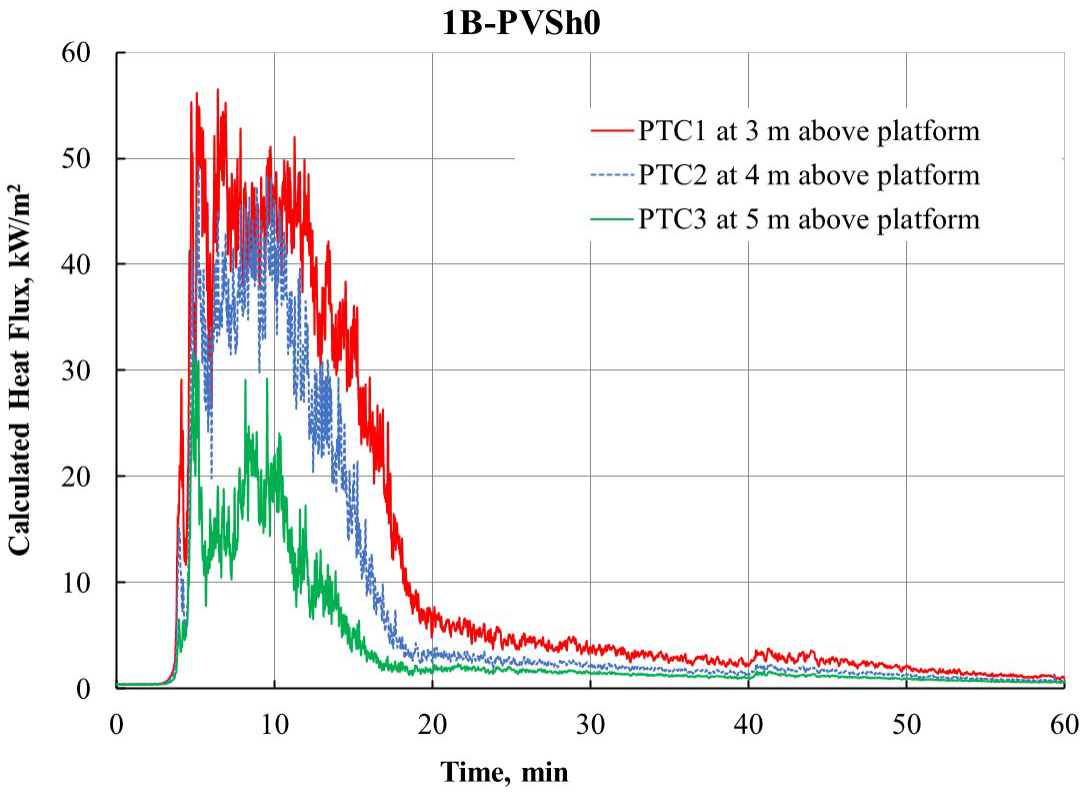

Fig. 33. Heat fluxes calculated from PTC1, PTC2, and PTC3 located above the Very Small shed in test1B-PVSh0. Standard relative uncertainty is ± 5 %.

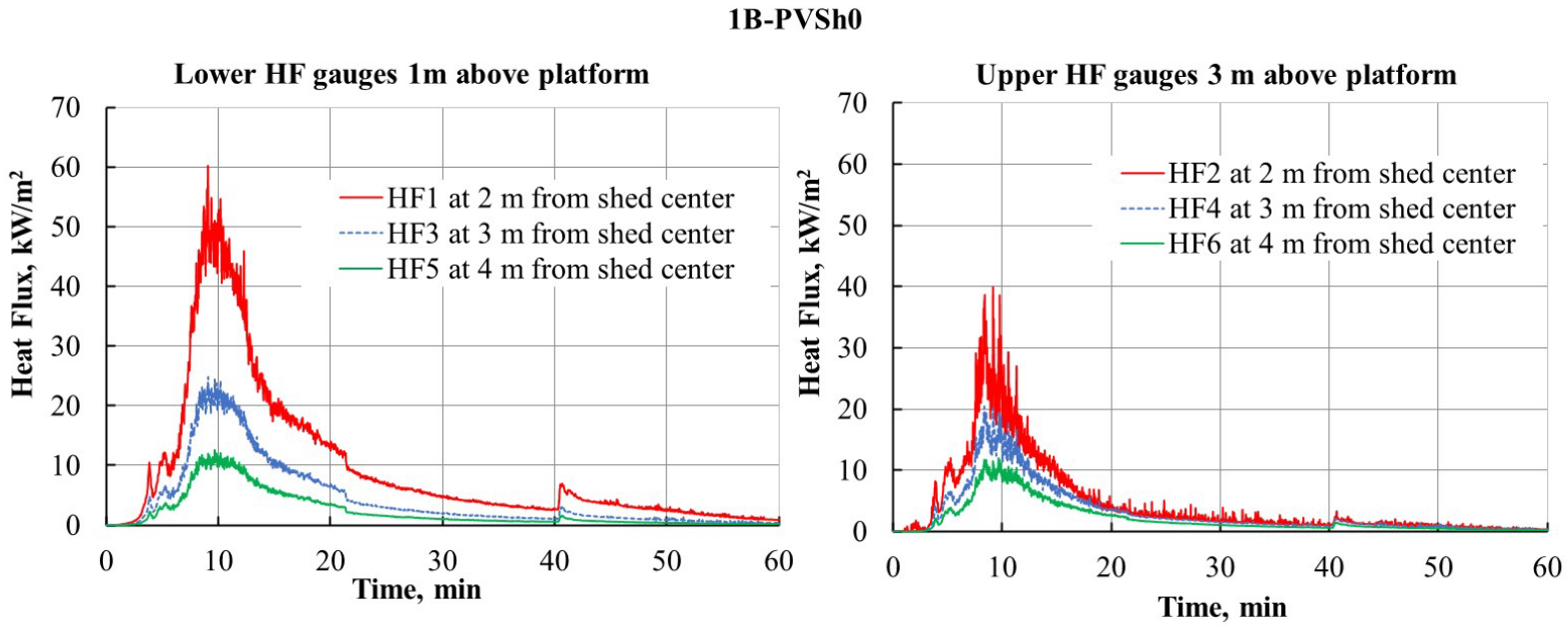

Fig. 34. Heat fluxes as a function of time recorded simultaneously by gauges located on Rig1, Rig2, and Rig3 placed in the front of the Very Small shed in test 1B-PVSh0. Standard relative uncertainty is ± 3 %.

4.3.3. Test: 1B-WVSh0

4.3.3.1. Shed Specification

The source structure was a commercially available wood Very Small shed with high fuel loading of six 1-A wood cribs. A photograph of a wood Very Small shed is shown in Fig. 35(a), and a photograph of a wood Very Small shed with six wood cribs stacked in a 3 × 2 pattern is shown in Fig. 35(b). As seen in Fig. 35(b), the front door of the shed was kept open. The total mass of six wood cribs was 117 kg and that of the shed was 75 kg. The resulting total combustible mass for this source structure was 192 kg. The shed was 64 in high and had a footprint of 26 ft^2.

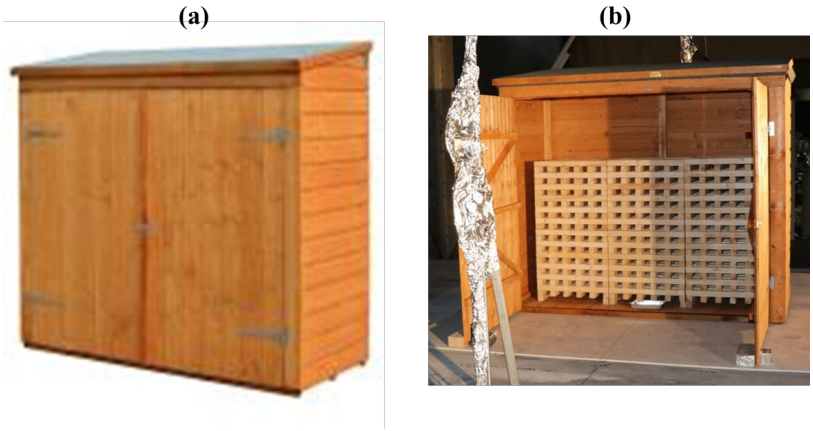

Fig. 35. Photograph of (a) wood Very Small shed (b) with high fuel loading of six 1-A cribs. Test 1B-WVSh0.

4.3.3.2. Burn Overview

The fire growth for a wood Very Small shed with six wood cribs is shown in Fig. 36. The corresponding mass loss and HRR profiles for the WVSh0 test are shown in Fig. 37. The PHRR of 4.7 MW was registered when the shed roof burned and exposed the burning wood cribs to excess ambient oxygen. The second peak in the HRR profile occurred at 9 min from ignition when the shed structure collapsed, making more oxygen available to the wood cribs to burn more vigorously. Corresponding images when the PHRR was registered are shown in Fig. 36(b) and Fig. 36(c).

The temporal profiles of heat fluxes calculated from plate thermometer measurements above the shed have two characteristic peaks, as shown in Fig. 38. The first sharp peak corresponds to the intense burning of the shed and the wood cribs, while the second, broader peak corresponds to the burning of wood cribs only. The comparison of heat flux profiles in Fig. 39 shows distinct differences in the heat flux measurements at the lower and upper heat flux gauges. The upper heat flux gauges are located above the shed and are exposed predominantly to radiation from flames. The heat flux profiles for the lower heat flux gauges are much broader and registered higher heat fluxes than the upper ones due to exposure from the burning wood cribs. The

prolonged high heat fluxes at low heights suggest that any nearby, low-lying combustible fuels may pyrolyze and are susceptible to a piloted ignition from landing embers.

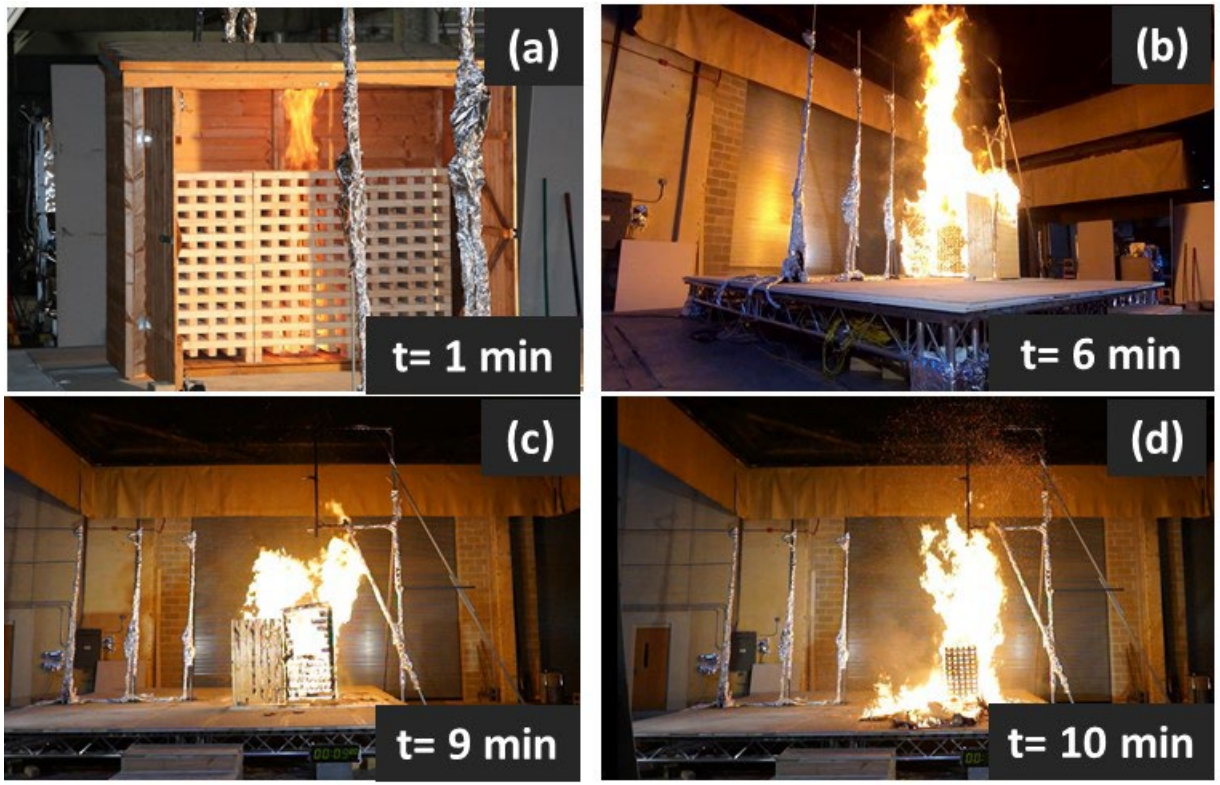

Fig. 36. Photographs captured from videos recorded by (a) Camera #1, (b) Cameras #2, (c) and (d) Camera #3 showing flame spread to the roof, roof collapse and flame heights at the time of 1st PHRR, 2nd PHRR after the side and back wall was consumed, and collapse of shed structure and generation of embers in test 1B-WVSh0.

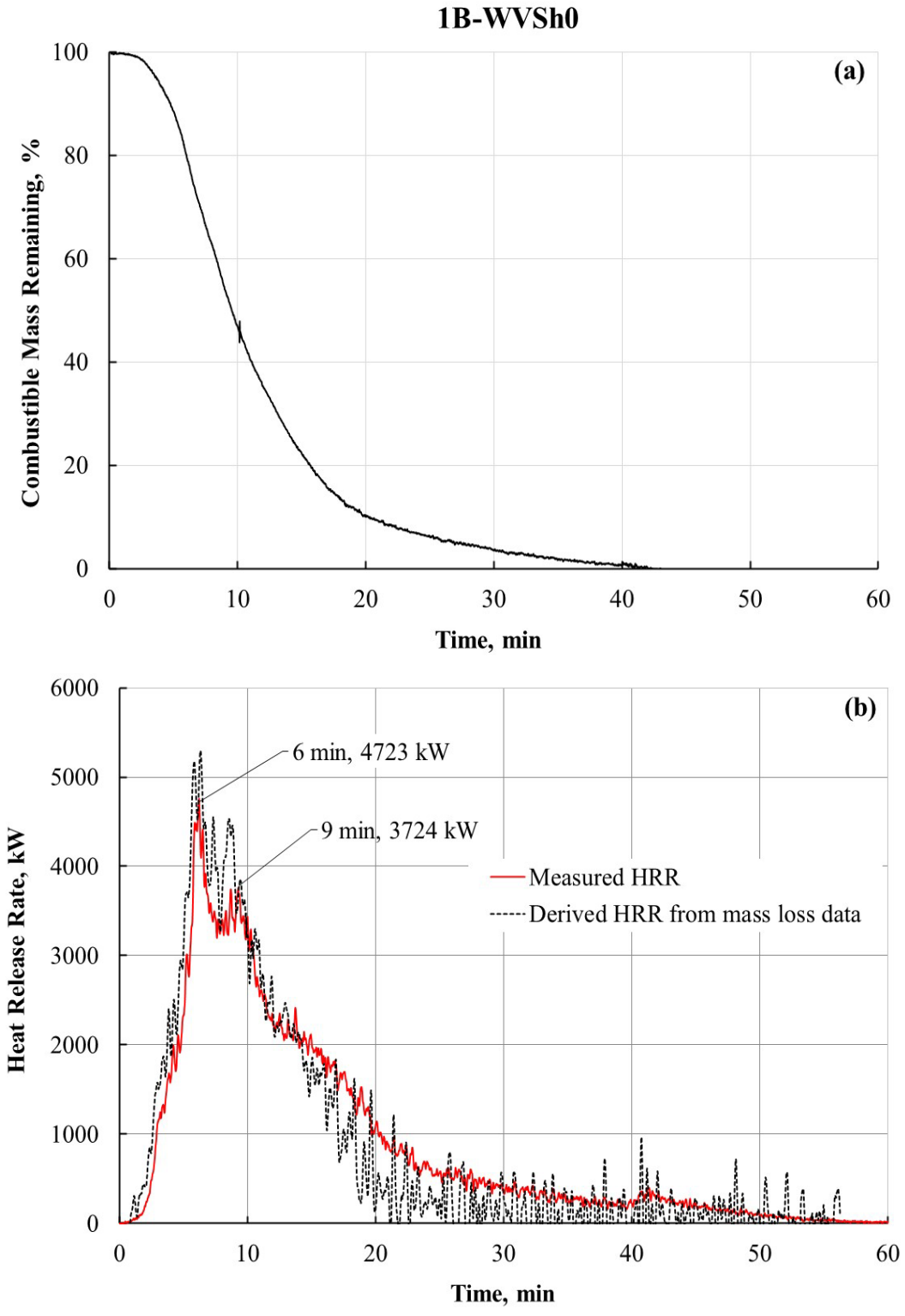

Fig. 37. Temporal plots of (a) percent mass of combustible fuel and (b) measured and calculated heat release from combustible fuel in test 1B-WVSh0.

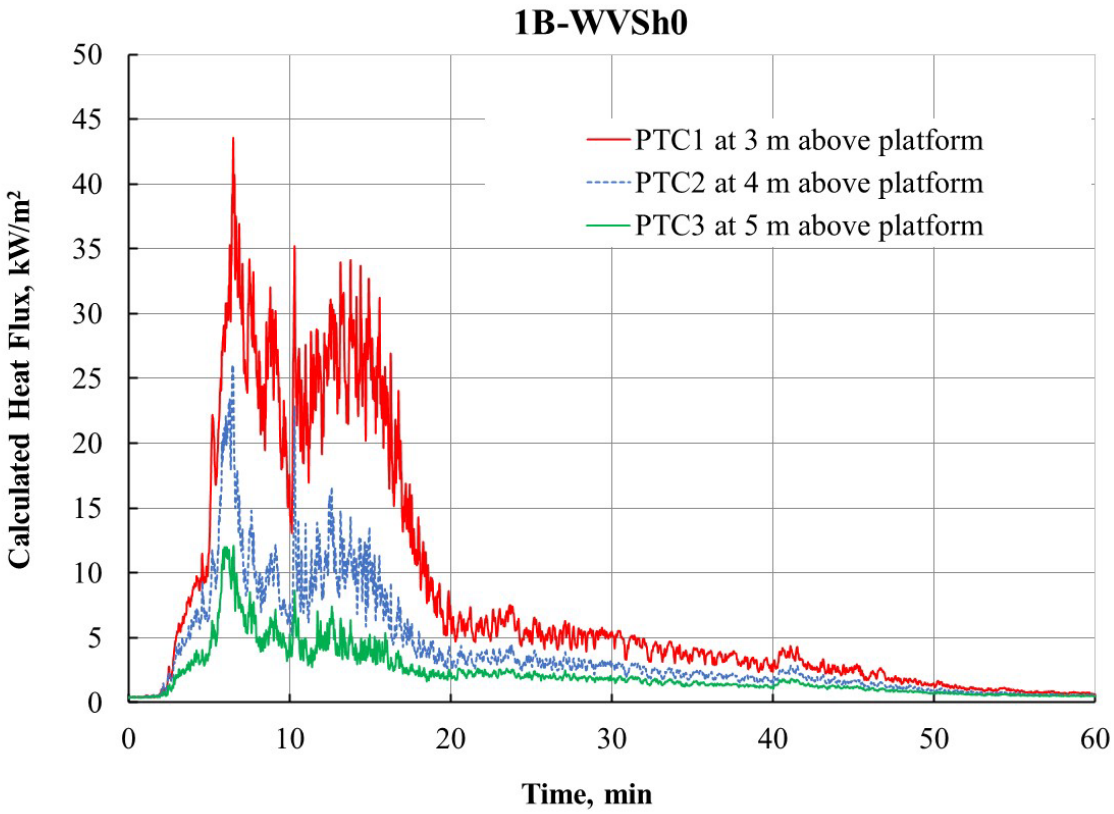

Fig. 38. Heat fluxes calculated from PTC1, PTC2, and PTC3 located above the Very Small shed in test1B-WVSh0. Standard relative uncertainty is ± 5 %.

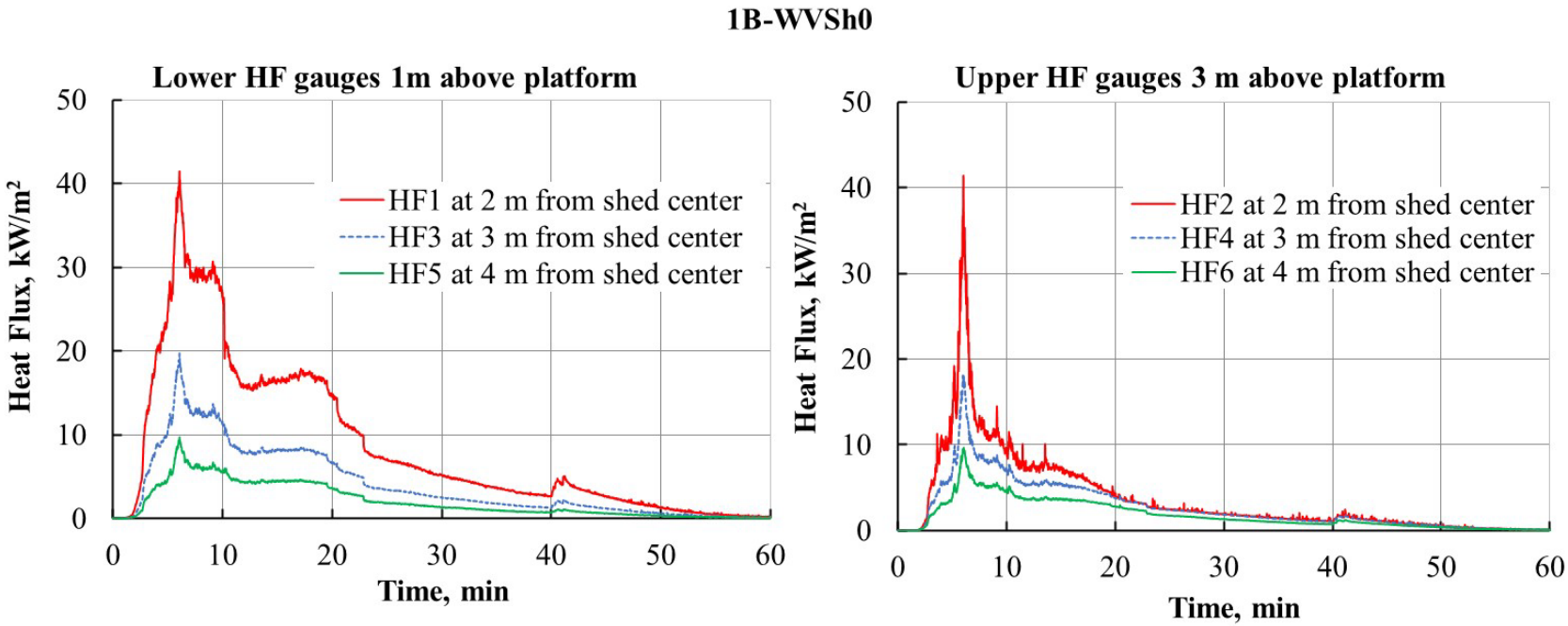

Fig. 39. Heat fluxes as a function of time recorded simultaneously by gauges located on the Rig1, Rig2, and Rig3 placed in the front of the Very Small shed in test 1B-WVSh0. Standard relative uncertainty is ±3 %.

4.3.4. Test: 1B-SVSh0

4.3.4.1. Shed Specification

The VS steel shed was a noncombustible shed made from galvanized steel and is shown in Fig. 40(a). The VS steel shed was 52 in high and had a footprint of 20 ft^2. Due to limited floor area available for this shed, six wood cribs were arranged in a triangular pattern, 3 × 2 (see Fig. 40(b)). The total combustible mass was 116 kgs.

Fig. 40. Photograph of (a) steel Very Small shed (b) with high fuel loading of six 1-A cribs. Test 1B-SVSh0.

4.3.4.2. Burn Overview

The photographs showing fire growth within the noncombustible steel Very Small shed are provided in Fig. 41. The temporal profiles of mass loss and HRR for 1B-SVSh0 are shown in Fig. 42(a) and Fig. 42(b). The HRR profile has two peaks; the initial steep rise in the HRR curve can be attributed to the burning of wood cribs giving the first peak (1.9 MW at 8 min) while the second peak (2.1 MW at 14 min) occurred when the cribs collapsed. This collapse produced intense burning of the remainder of the cribs due to exposure of fresh fuel to the ambient oxygen. This burning behavior was confirmed by visual observations and a review of video recordings. The shed remained intact through the burning of wood cribs. Visual observations also suggested that the burning of wood cribs inside the noncombustible steel shed was primarily influenced by the size of the door opening. The measured HRR for this shed burn shows delayed response compared to the derived HRR, and this could be attributed to the intact shed which altered the flow of combustion products to the exhaust hood.

The temporal profiles of heat fluxes calculated from plate thermometer measurements above the steel Very Small shed are shown in Fig. 43. Since the burning of the wood cribs essentially occurred inside the shed and the flames jetted away from the centerline out the door of the shed, the plate thermometers above the shed did not register a significant increase in temperatures, resulting in calculated heat fluxes less than 15 kW/m^2 (see Fig. 43). This is significantly lower than the heat fluxes reported for combustible sheds where the roof burned off, exposing the plate thermometers to the radiant and convective heat.

The size of the door opening, and arrangement of the wood cribs also affected the heat flux measurements by the gauges located next to the shed. Unlike the previous tests where lower heat flux gauges registered higher heat fluxes compared to the upper gauges, high heat fluxes were recorded by the upper gauges as compared to the lower gauges. The fire plume from the wood cribs stretched through the door opening to contact the upper heat flux gauges (see Fig. 41(b)) and registered higher heat flux values, while the lower gauges were exposed to the burning wood cribs but not exposed to significant flames. Measurements of heat flux values at the lower heat flux gauges were comparable to other shed burns. The comparison of measured heat fluxes across the shed is shown in Fig. 44.

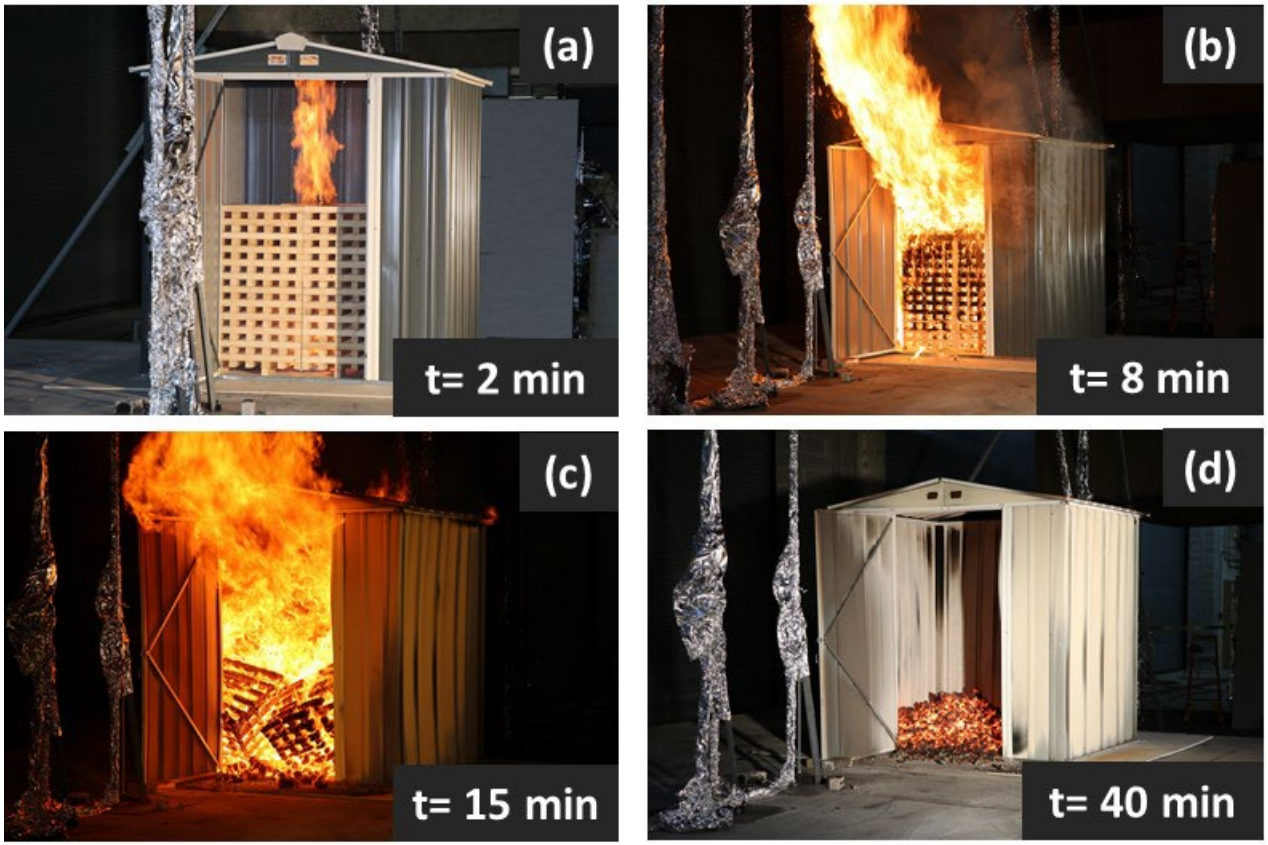

Fig. 41. Photographs captured from videos recorded by Camera #3 showing (a) flame spread to the roof top (b)flames emerging out from shed at the first PHRR, (c) wood cribs collapse at the second PHRR and (d) smoldering embers at the end of the test 1B-SVSh0.

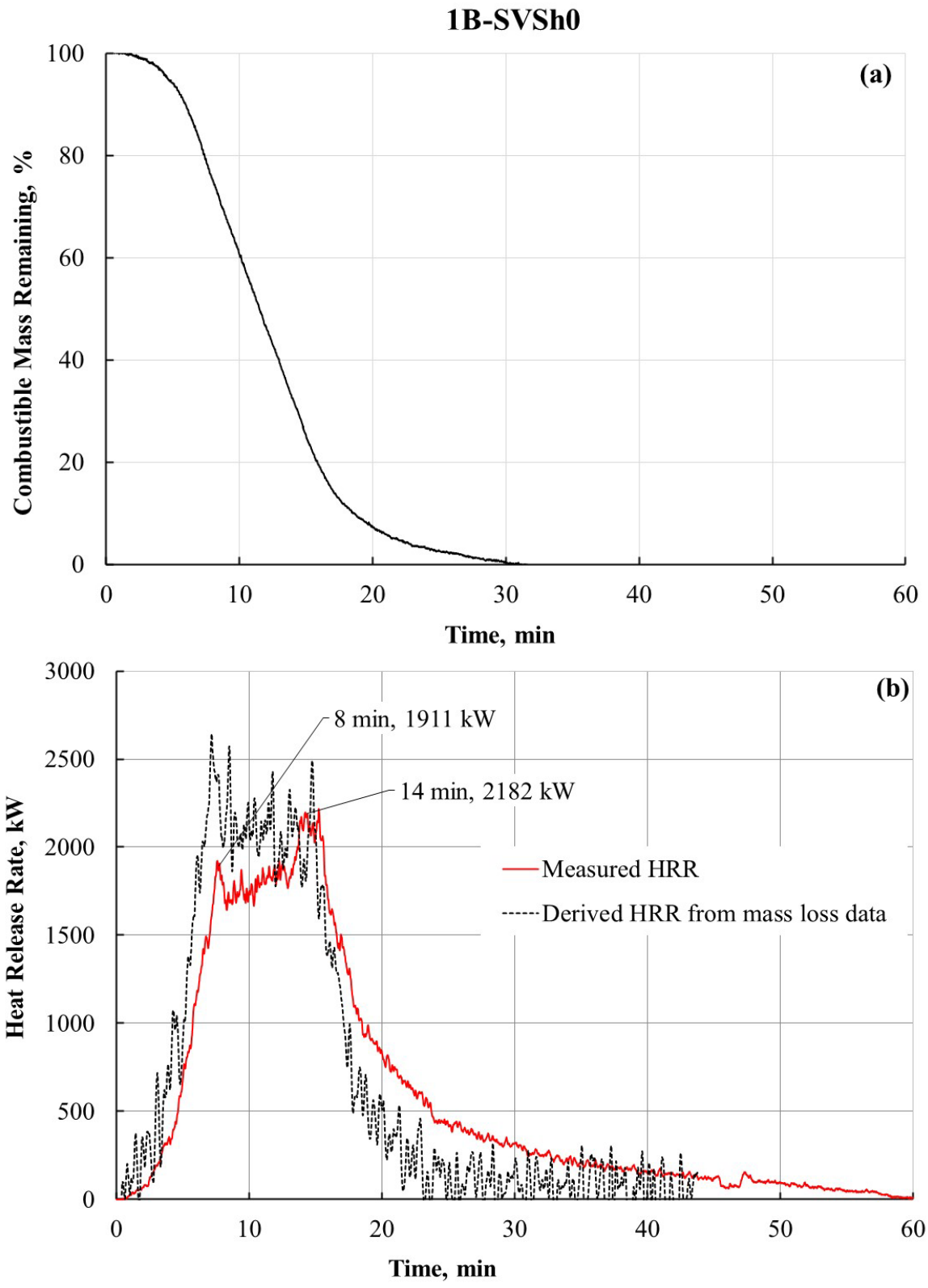

Fig. 42. Temporal plots of (a) percent mass of combustible fuel and (b) measured and calculated heat release from combustible fuel in test 1B-SVSh0.

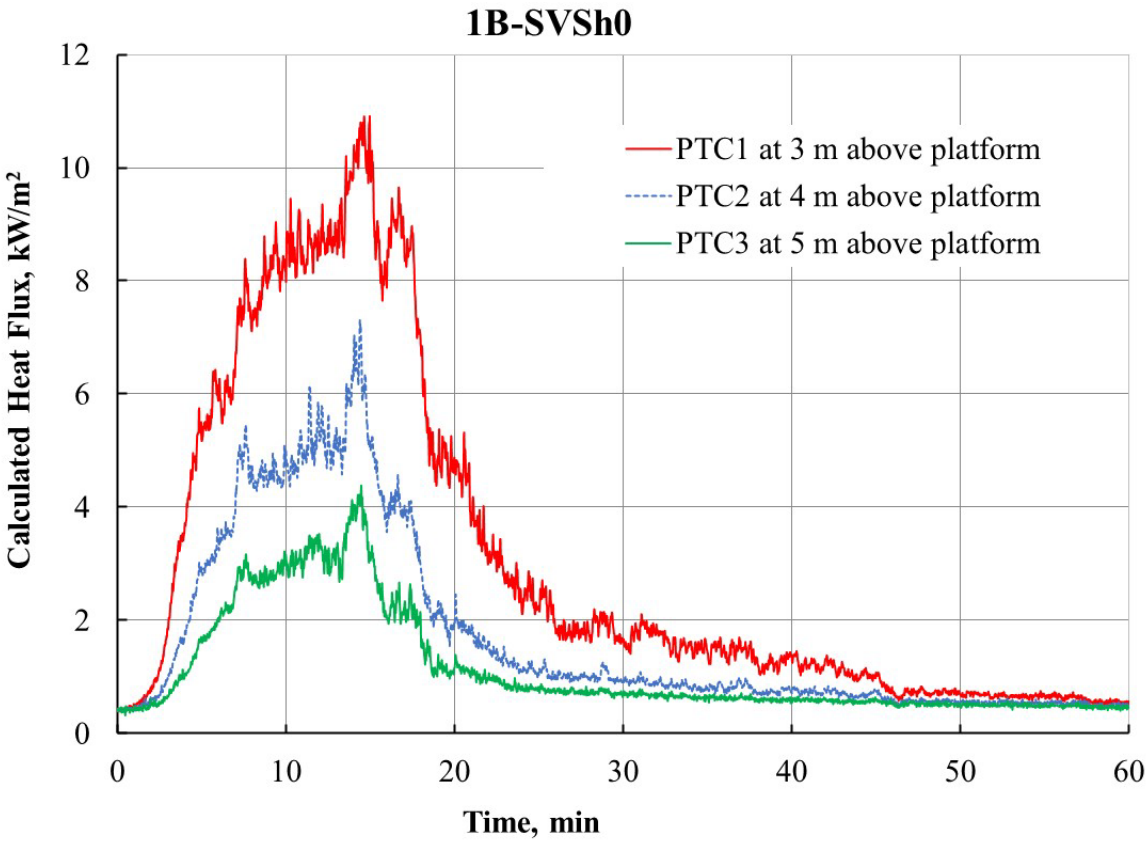

Fig. 43. Heat fluxes calculated from PTC1, PTC2, and PTC3 located above the Very Small shed in test 1B-SVSh0. Standard relative uncertainty is ± 5 %.

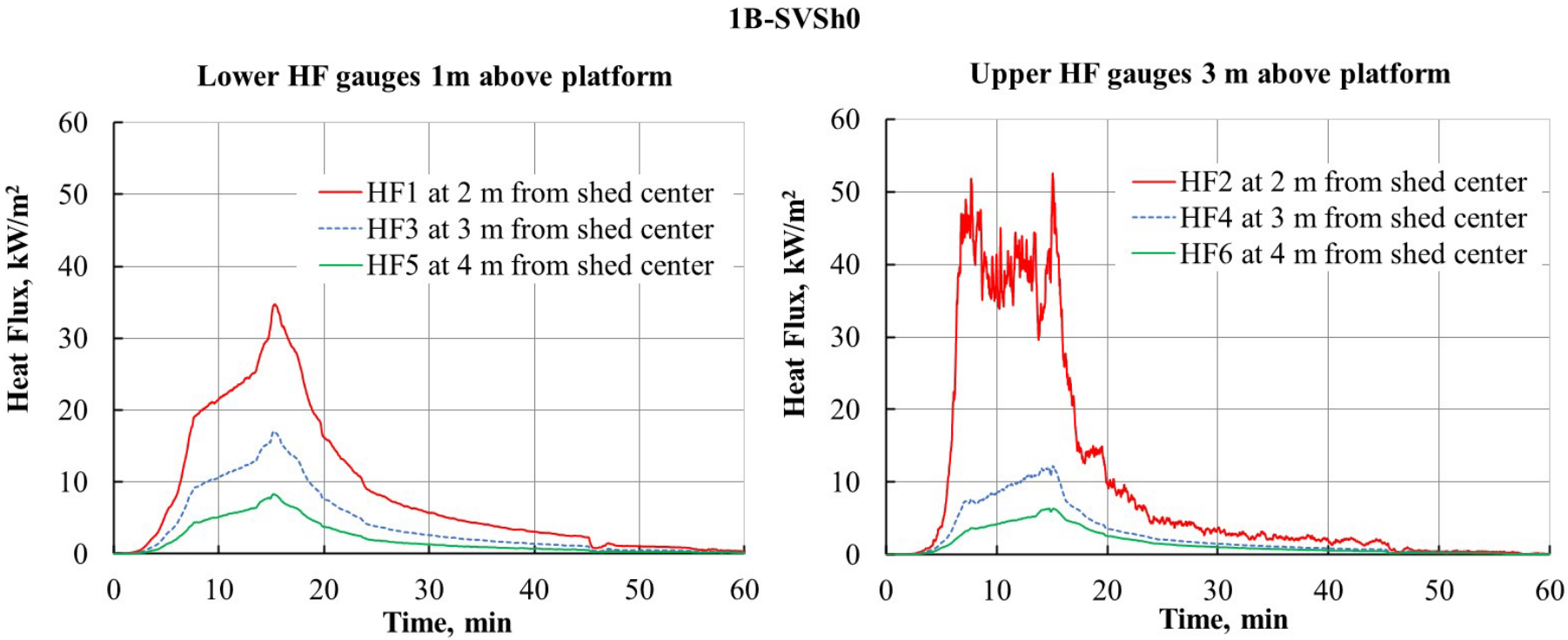

Fig. 44. Heat fluxes as a function of time recorded simultaneously by gauges located on the Rig1, Rig2, and Rig3 placed in the front of the Very Small shed in test 1B-SVSh0. Standard relative uncertainty is ±3 %.

4.3.5. Test: 1B-WCl0

4.3.5.1. Shed Specification

The wood Closet used in this test was the same as the one described in Section 4.3.1.1; however, this burn investigated a low fuel loading of only two wood cribs. The total mass of two wood cribs was 38 kg and that of the wood Closet was 49 kg. The resulting total combustible mass for this source structure was 87 kg.

Fig. 45. Photograph of wood Closet with low fuel loading of two 1-A cribs. Test 1B-WCl0.

4.3.5.2. Burn Overview

Figure 46 shows images of fire growth for a wood Closet with low fuel loading. Similar to the burning behavior observed in test 1B-WCh0, the HRR profile for the WCl0 test shows two characteristic peaks in (Fig**.** 47(a)). The first peak occurs when the roof of the Closet burns and exposes the wood cribs, while the second peak is noted when the walls of the Closet get involved in burning.

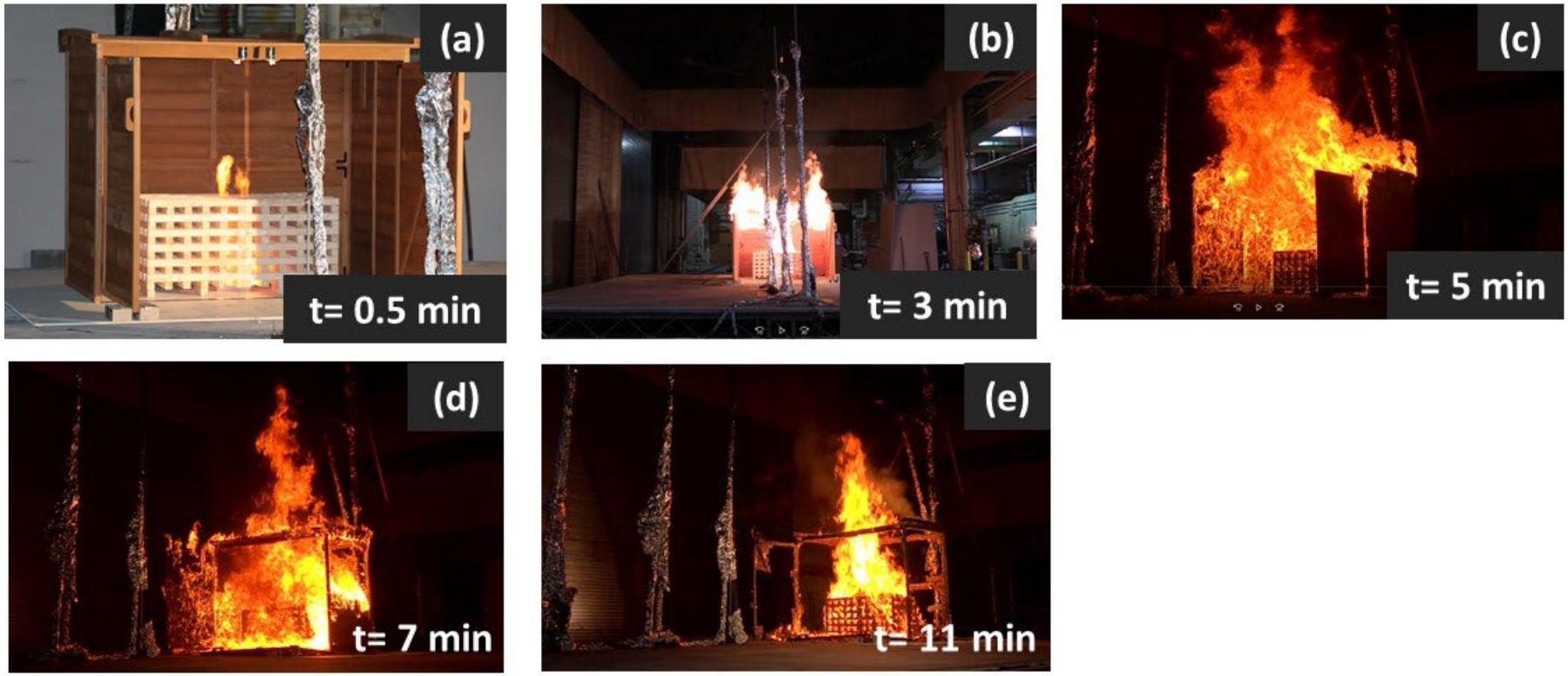

Fig. 46. Photographs captured from (a)still camera and from videos recorded by (b) Camera #1, (c), (d), and (e) Camera #2 showing ignition of wood cribs, flame spread to the roof, flame heights at the time of PHRRs, and burning of wood cribs after the Closet had burned down in test 1B-WCl0.

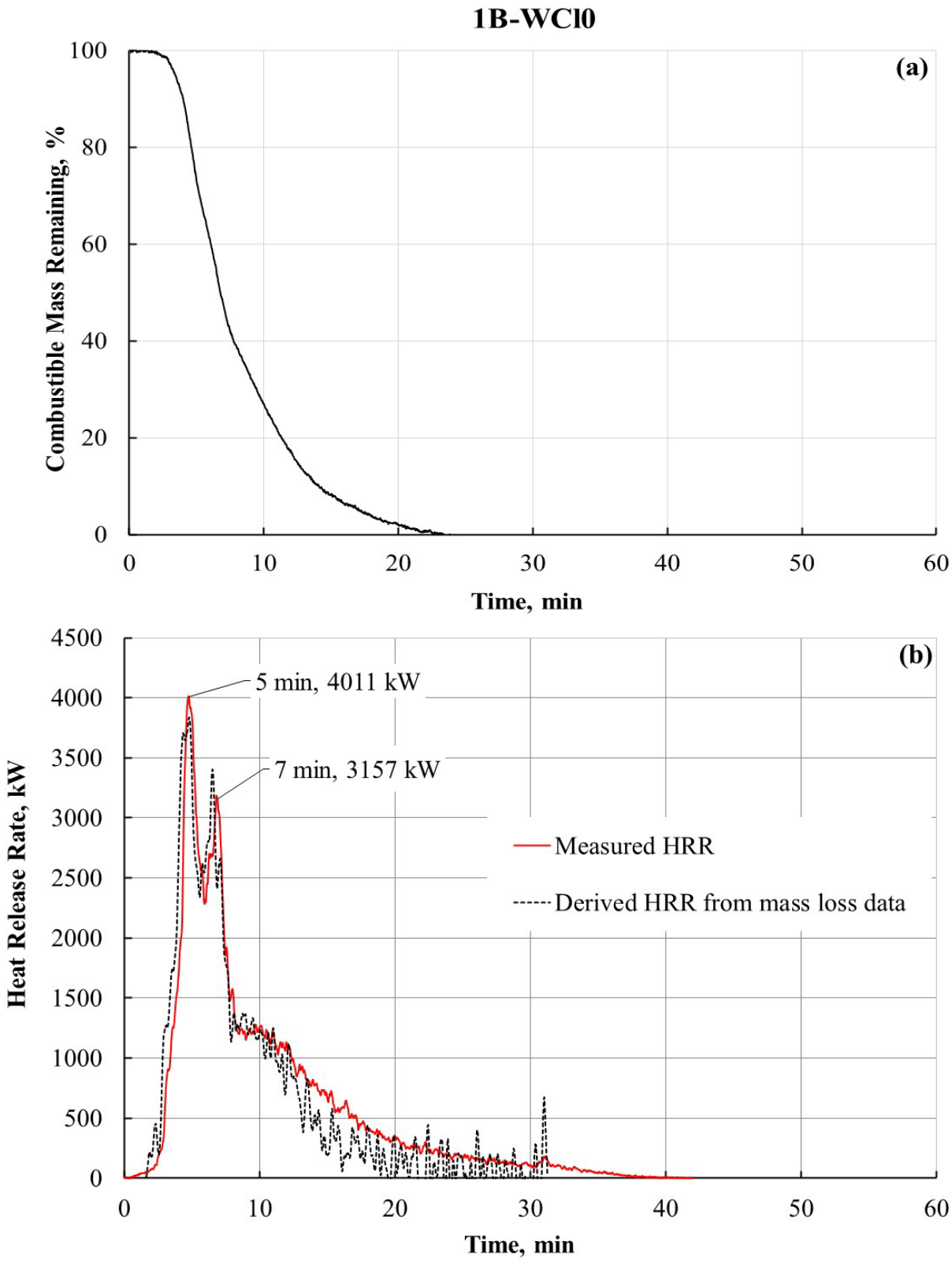

Fig. 47. Temporal plots of (a) percent mass of combustible fuel and (b) measured and calculated heat release from combustible fuel in test 1B-WCl0.

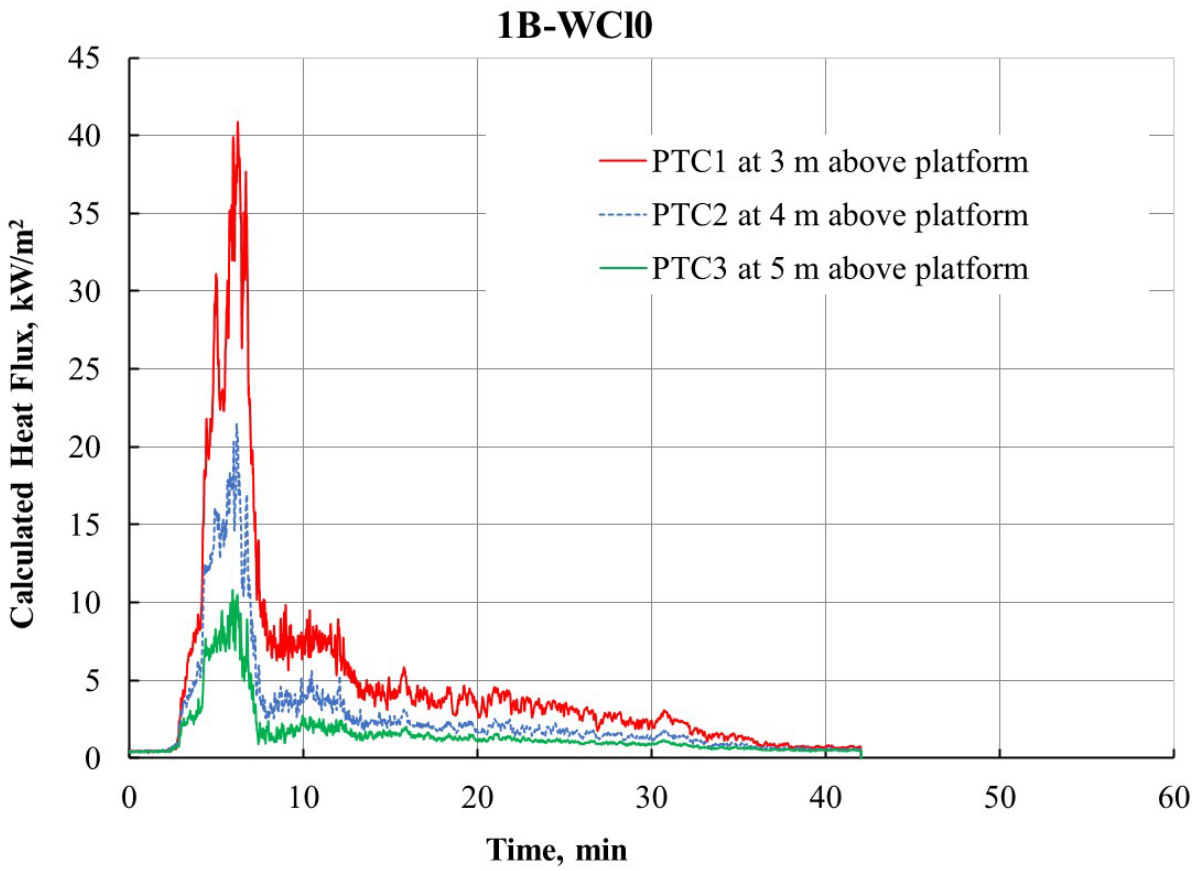

Fig. 48. Heat fluxes calculated from PTC1, PTC2, and PTC3 located above the Very Small shed in test1B-WCl0. Standard relative uncertainty is ± 5 %.

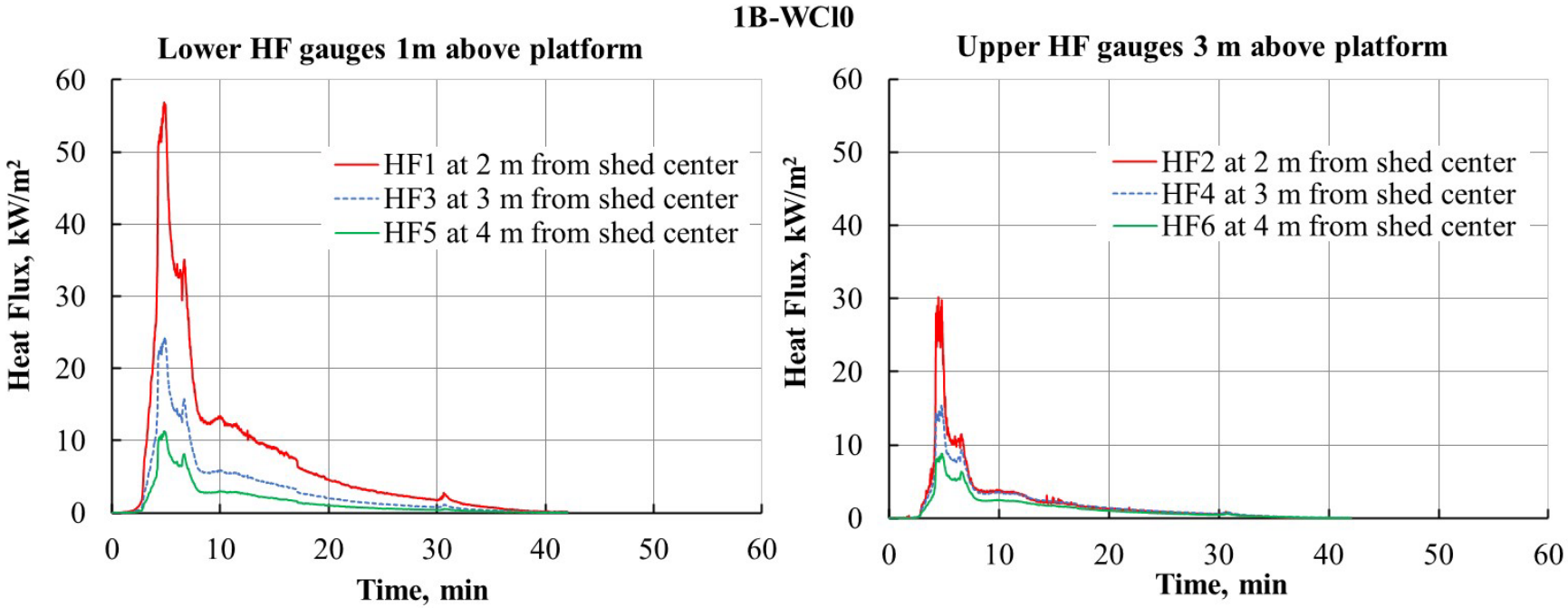

Fig. 49. Heat fluxes as a function of time recorded simultaneously by gauges located on the Rig1, Rig2, and Rig3 placed in the front of the Very Small shed in 1B-WCl0. Standard relative uncertainty is ±3 %.

4.3.6. Test: 1B-PCl0

4.3.6.1. Shed Specification

A photograph of a plastic Closet is shown in Fig. 25(a), and the low fuel loading of two 1-A wood cribs is shown in Fig. 25(b). This shed was made from high density polyethylene (HDPE) and had a footprint of 21 ft^2. The total mass of the two wood cribs was 39 kg and that of the plastic Closet was 38 kg. The resulting total combustible mass for this source structure was 67 kg. Similar to the test 1B-PVSh0, the plastic Closet was placed in sheet metal pan.

Fig. 50. Photograph of (a) plastic Closet (b) with low fuel loading of two 1-A cribs. Test 1B-PCl0.

4.3.6.2. Burn Overview

Photographs in Fig. 51 show the stages of fire growth within the plastic Closet. The flame from burning of wood cribs caused melting of the roof, and flames were seen penetrating out from the roof within 2 min after ignition of the wood cribs. The roof melted and collapsed within the next 2 min. At this time, the Closet walls had softened and deformed significantly. The source structure collapsed due to melting of plastic, and the polymer melt burned as a pool fire (see Fig. 51(d)). A PHRR of 3.2 MW was noted at 8 min from ignition due to the burning of polymer melt and wood cribs. The HRR profile and the mass loss data are plotted in Fig. 52.

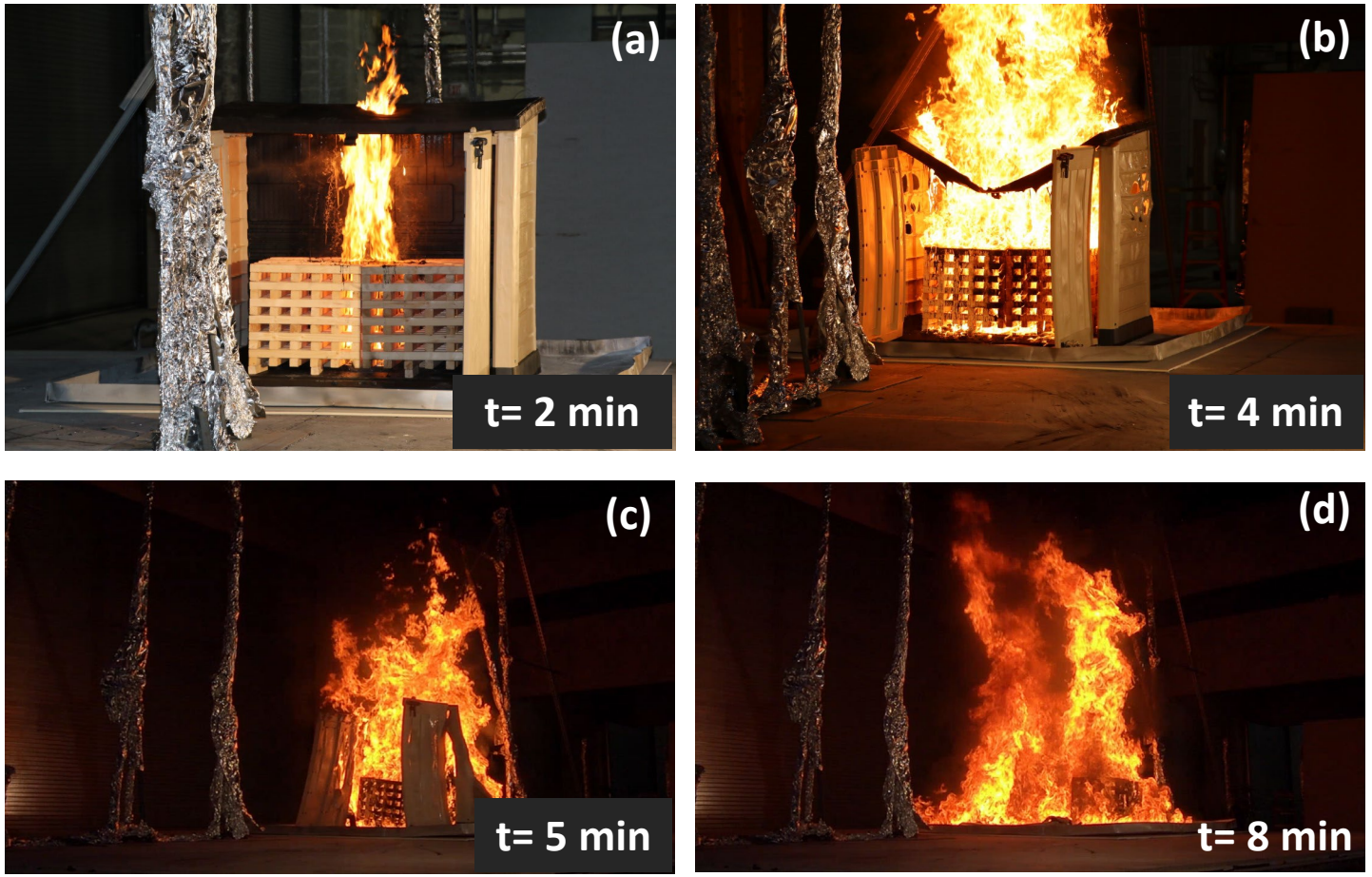

Fig. 51. Photographs captured from videos recorded by Camera #2, (b) Cameras #3, (c) Camera #2, (d) Camera #3, and (e) Camera #2 showing (a) flame spread to the roof, (b) roof collapse, (c) structure collapse due to melting of plastic, and (d) pool fire due to burning of polymer melt and burning of wood cribs in test 1B-PCl0.

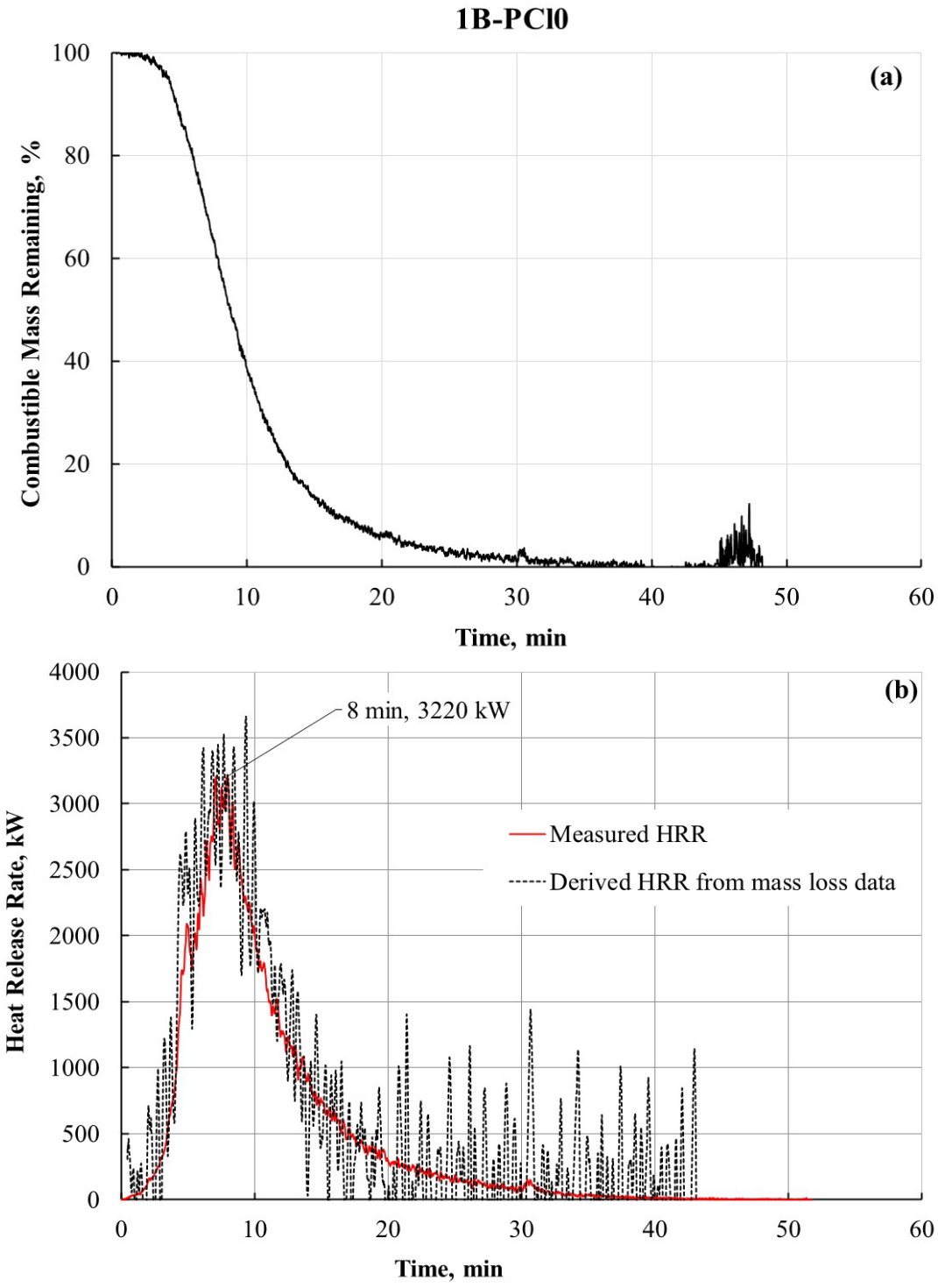

Fig. 52. Temporal plots of (a) percent mass of combustible fuel and (b) measured and calculated heat release from combustible fuel in test 1B-PCl0.

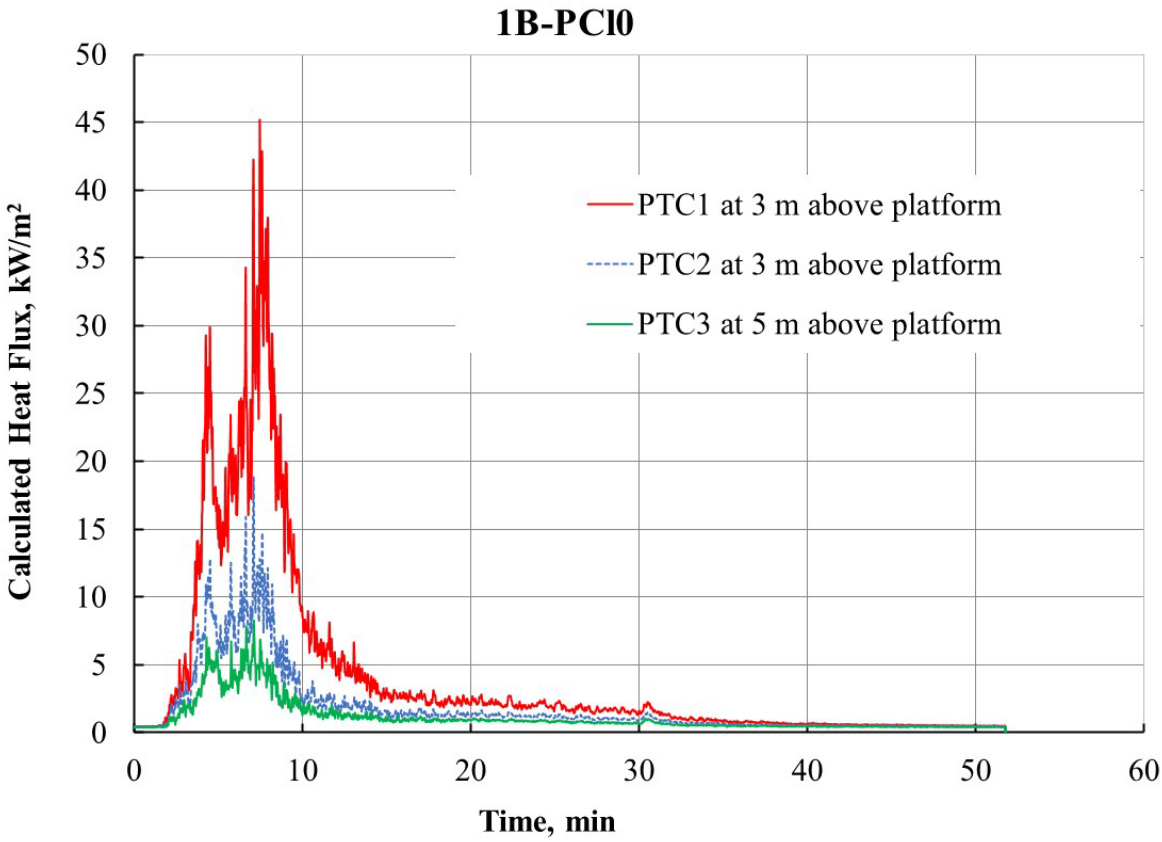

Fig. 53. Heat fluxes calculated from PTC1, PTC2, and PTC3 located above the Closet in test1 B-PCl0. Standard relative uncertainty is ± 5 %.

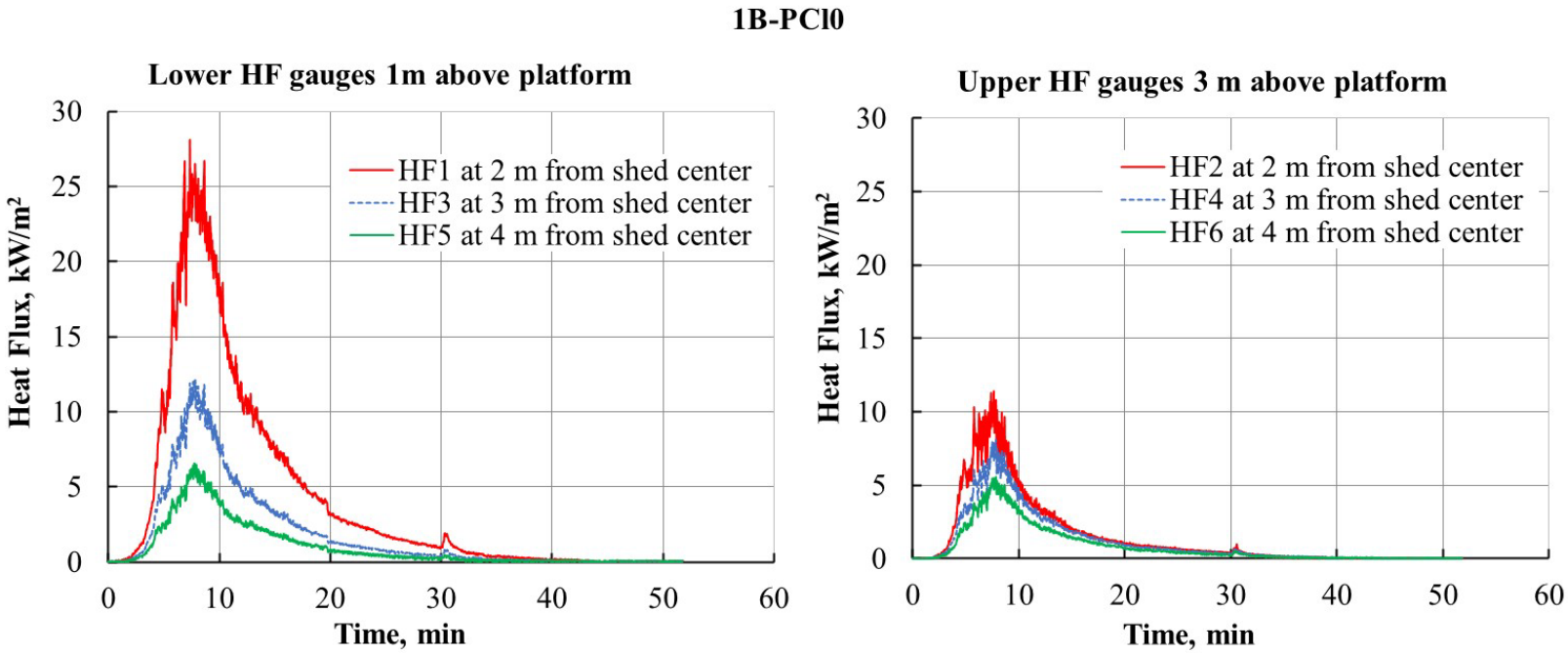

Fig. 54. Heat fluxes as a function of time recorded simultaneously by gauges located on the Rig1, Rig2, and Rig3 placed in the front of the Closet in test 1B-PCl0. Standard relative uncertainty is ±3 %.

4.3.7. Test: 1B-SCl0

4.3.7.1. Shed Specification

The source structure was a commercially available steel Closet with low fuel loading of two 1-A wood cribs. The Closet made from galvanized steel is shown in Fig. 55. The front door of the steel Closet was kept open; however, the top lid was placed in position without locking. The total mass of two wood cribs was 38 kg and that of the steel Closet was 24 kg. The total combustible mass for this source structure was 38 kg. The Closet was 53 in high and had a footprint of 15 ft^2.

Fig. 55. Photograph of steel Closet with low fuel loading of two 1-A cribs. Test 1B-SCl0.

4.3.7.2. Burn Overview

Images of flame spread to the roof, flames emerging out from the Closet, flame heights at the time of PHRR, and an intact Closet after the burn are shown in Fig. 56. The flame jetting from the burning fuel was significantly less compared to that noted in test 1B-SVSh0. This can be attributed to lower fuel loading and wider door opening in test 1B-SCl0. The corresponding HRR profile and mass loss profile for 1B-SCl0 are shown in Fig. 57.

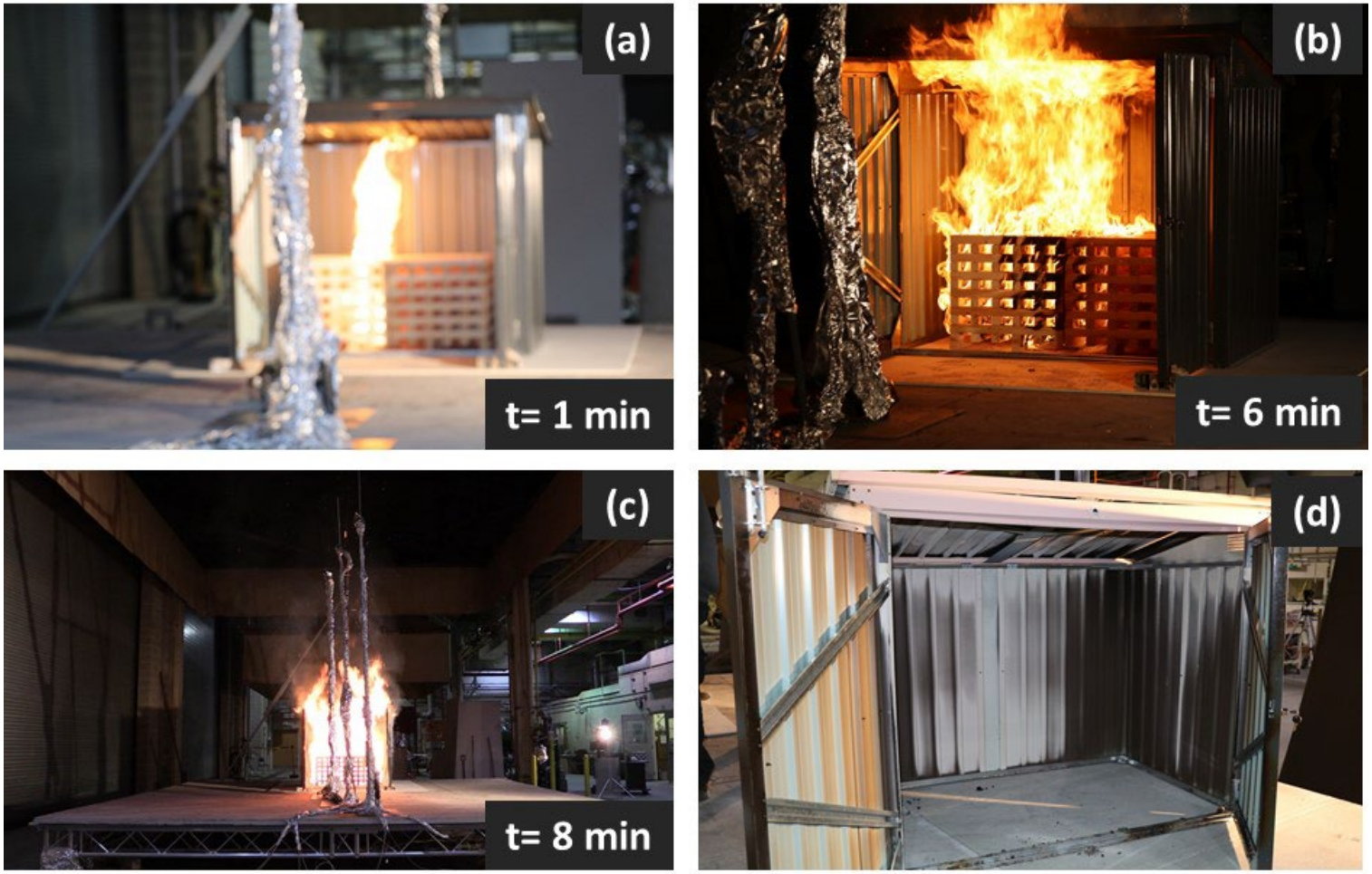

Fig. 56. Photographs captured from videos recorded by (a) and (b) Camera #2, (c) Cameras #1, and (d) still image showing flame spread to the roof, flames emerging out from the Closet, flame heights at the time of PHRR, and an intact Closet after the burn in test 1B-SCl0.

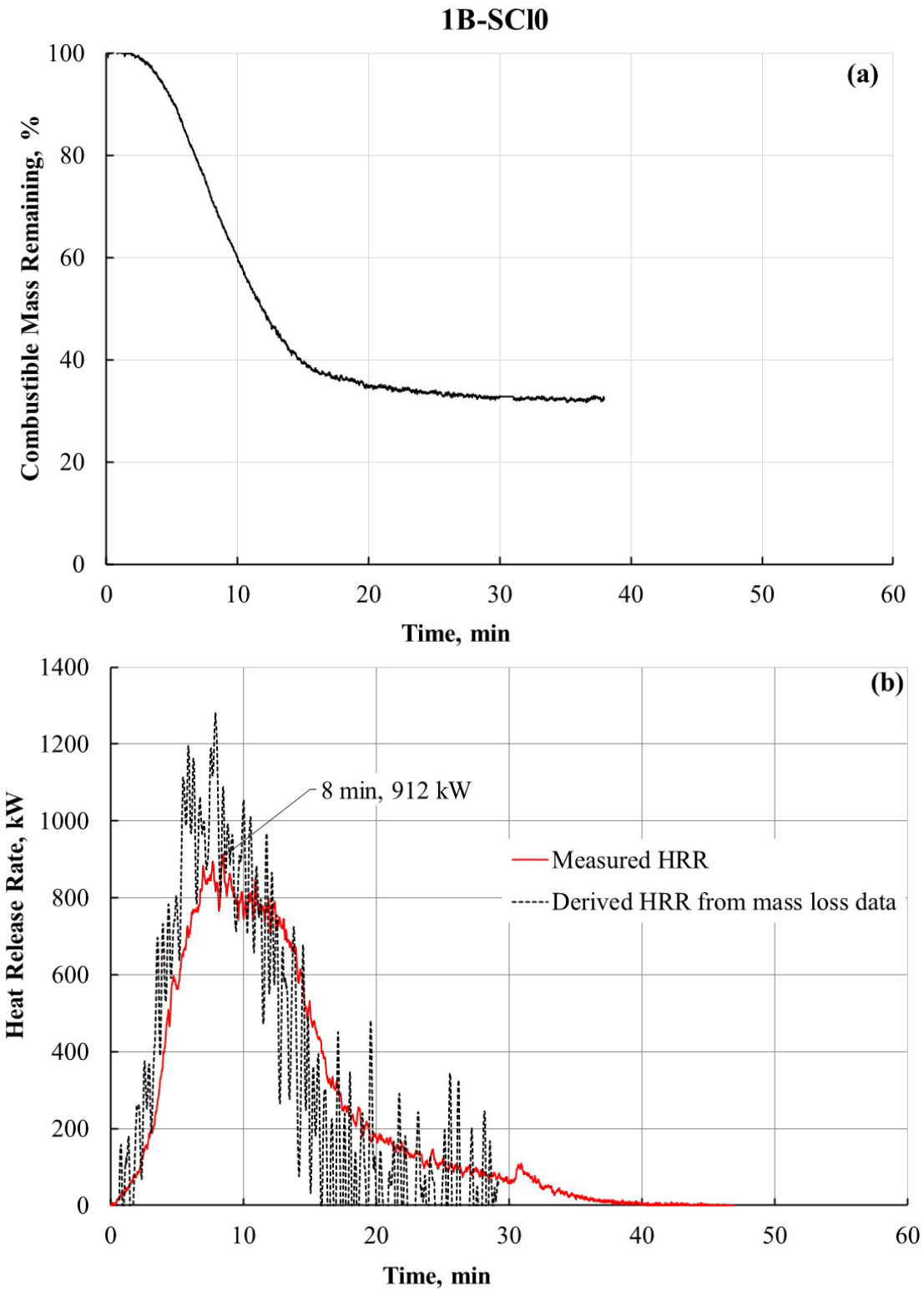

Fig. 57. Temporal plots of (a) percent mass of combustible fuel and (b) measured and calculated heat release from combustible fuel in test 1B-SCl0.

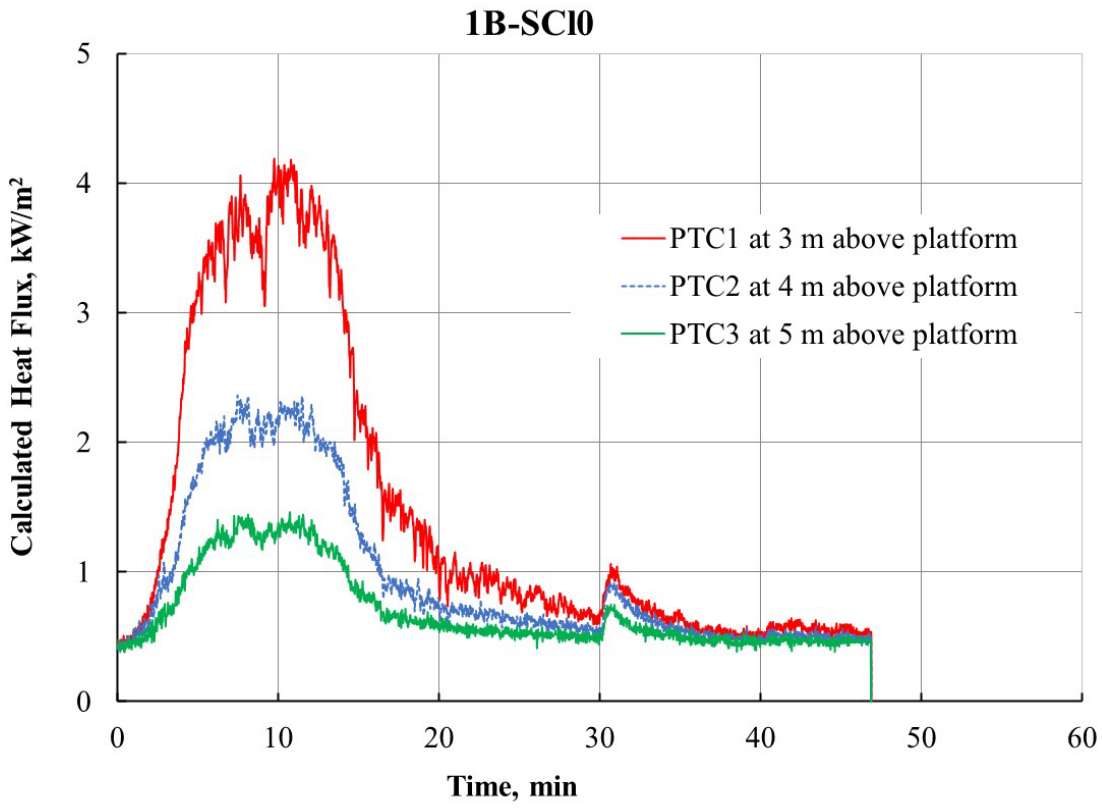

Fig. 58. Heat fluxes calculated from PTC1, PTC2, and PTC3 located above the Closet test1B-SCl0. Standard relative uncertainty is ± 5 %.

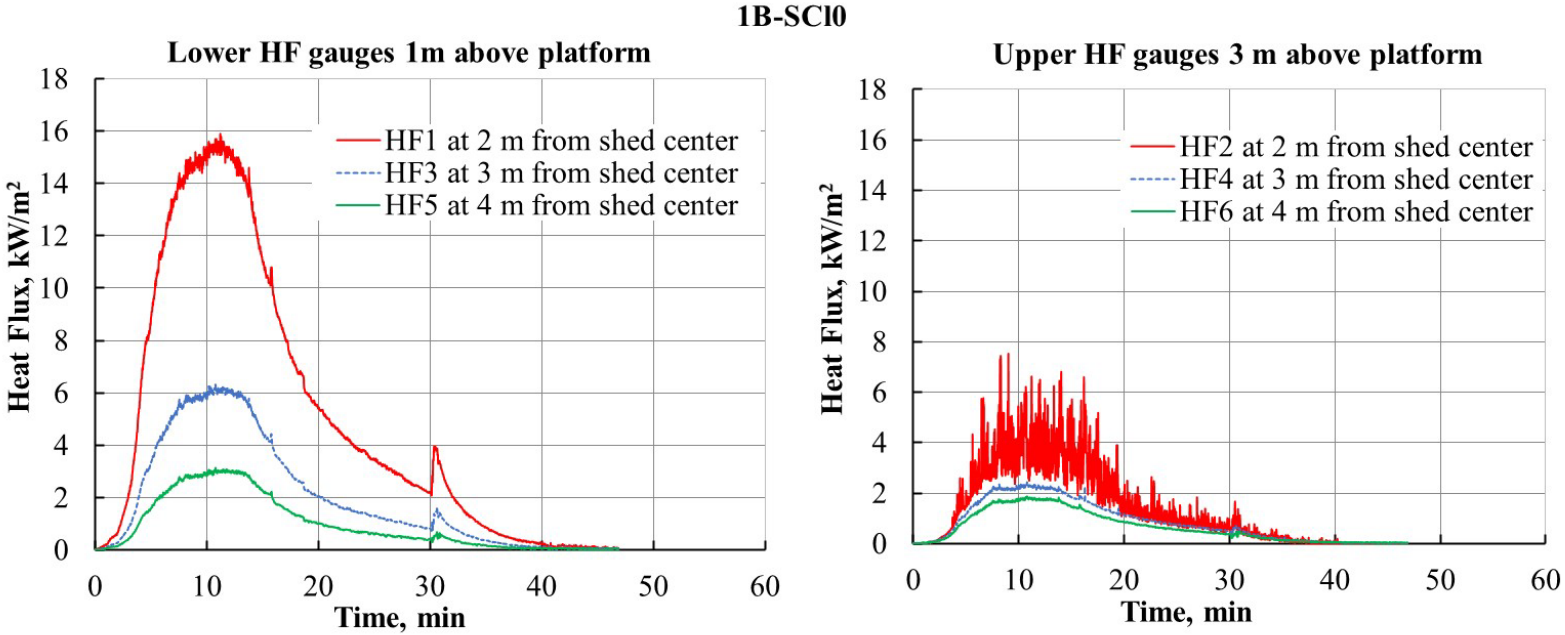

Fig. 59. Heat fluxes as a function of time recorded simultaneously by gauges located on the Rig1, Rig2, and Rig3 placed in the front of the Closet in test 1B-SCl0. Standard relative uncertainty is ±3 %.

4.4. Technical Findings

4.4.1. Reproducibility of Shed Burns

Comparisons of the HRR curves for 1B-WCh0, 1B-WCh0-R1, and 1B-WCh0-R2 showed that the results for repeated tests had similar shapes, magnitudes, and burning periods, as seen in Fig. 60. The HRR plots for all three tests have two characteristic peaks as discussed in Section 4.3.1.2. However, it is noted that the growth and peak HRR for 1B-WCh0 is slightly delayed relative to the other two tests. This was observed due to the top lid of the Closet being held in place by two small pneumatic liftgate cylinders. The pneumatic cylinders exploded in the fire, and the lid was automatically lifted. The flame spread in the wood cribs with the lifted lid was slower than that with the lids that were not held in place for 1B-WCh0-R1 and 1B-WCh0-R2.

The reproducibility of the measured quantities for repeated tests of 1B-WCh0 can be noted from Table 9. The average quantities with standard deviations from triplicate tests are provided in Table 9. These data show reproducibility of the measured quantities with PHRR variation of 5 % and THR variation of 2 %. The fire exposures (heat fluxes) to the surrogate targets varied between 4 % and 17 %. The reproducibility of these burns provides increased confidence in the measurements for the remainder of the shed burns.

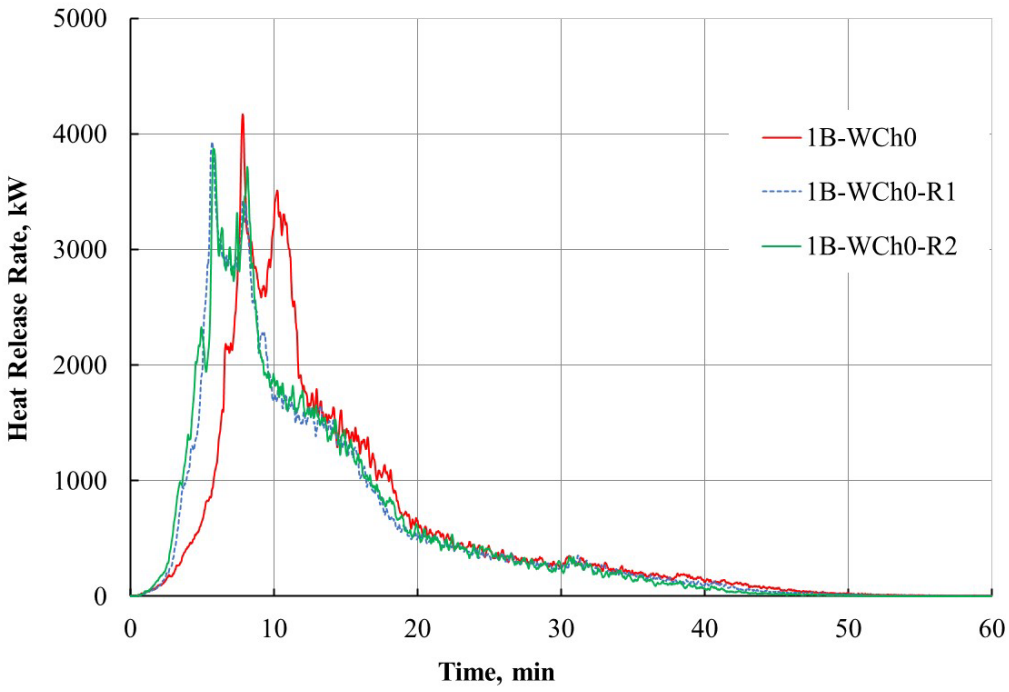

Fig. 60. Reproducibility of heat release rate data for WCh0.

Table 9. Reproducibility of experimental data for WCh0.

Test ID	Total combustible mass, kg	Total heat released, MJ	PHRR, MW	Calculated peak heat flux§, kW/m²			Measured peak heat flux‡, kW/m²					
				PTC1	PTC2	PTC3	2 m*		3 m*		4 m*	
							1m**	3m**	1m**	3m**	1m**	3m**
1B-WCh0	127	2104	4.2	76	53	24	47	27	21	15	10	9
1B-WCh0-R1	126	2059	3.9	83	48	23	45	25	19	14	9	8
1B-WCh0-R2	126	2029	3.9	72	23	19	43	20	19	13	9	8
Average	**126.3 ± 0.6**	**2064 ± 38**	**4.0 ± 0.2**	**77 ± 6**	**41 ± 16**	**22 ± 3**	**45 ± 2**	**24 ± 4**	**14 ± 1**	**14 ± 1**	**9 ± 1**	**8 ± 1**

*Distance from shed center, **height above the weighing platform.
§Standard relative uncertainty is ± 5 %.
‡ Standard relative uncertainty is ± 3 %.

4.4.2. Effect of Construction Materials on Heat Release from Source Structures

Two types of source structures, combustible and noncombustible, were examined in this study. The noncombustible shed does not contribute to the overall combustible mass of the source fire while combustible sheds contribute significantly towards the total combustible mass. The construction material for wood and plastic sheds (Closets and VS sheds) contributed approximately 40 % towards the total combustible mass and a 60 % increase in fuel load compared to the steel shed therefore producing the higher PHRR corresponding to higher fire hazard. The overall combustible mass of the source structure (shed + fuel) can be reduced by using a noncombustible shed.

Steel sheds were used in the current experiments and maintained their structural integrity throughout the burn. While a noncombustible aluminum shed will not add to the combustible mass, the aluminum will likely melt, deform, and form an opening due to the high temperatures if the contents ignite. Therefore, exposures from contents burning in an aluminum shed will be significantly higher than in a steel shed.

This section compares burning behaviors and thermal exposures from source structures with different construction materials. The indoor shed burn experiments were performed with open doors to capture potential exposures from noncombustible sheds. This is a realistic worst case scenario for steel sheds. Similar open-door configuration was used for wood and plastic sheds to provide additional oxygen entrainment. A comparison of peak HRR values for all the sheds tested in this series is provided in Fig. 61. Generally, and as expected, the PHRR and hence the fire hazard for combustible sheds is higher than that of noncombustible sheds. The effects of shed size and fuel loadings are discussed in sections below.

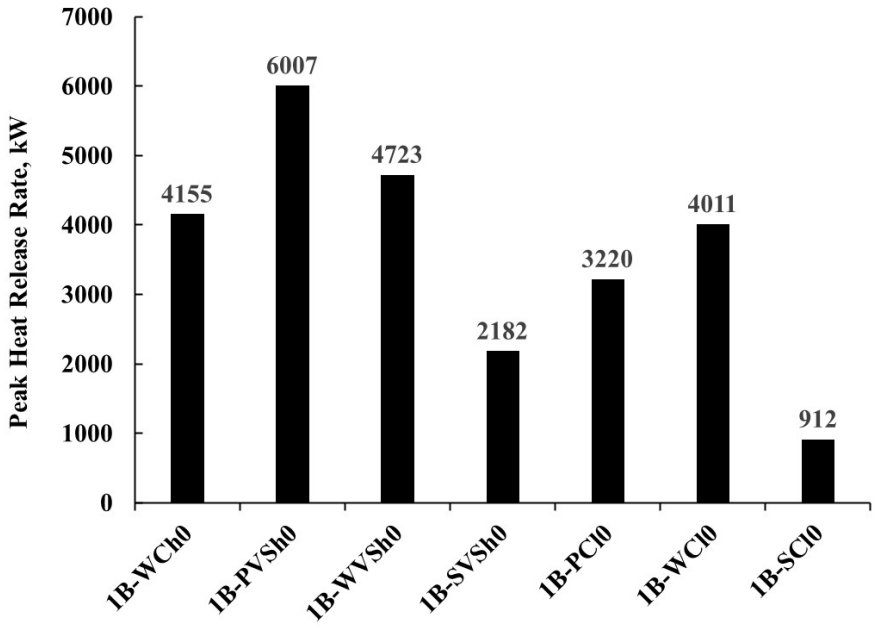

Fig. 61. Comparison of PHRR values for all the source structures tested.

Review of the HRR curves in Fig. 62 and Fig. 63 suggests that their shapes vary significantly with the material used in construction of the sheds. The observed differences exceed the uncertainties in the HRR measurements. With similar fuel loading of two 1-A cribs, the peak heat release rate for Closets with different construction materials varied from 0.9 MW to 4.0 MW. This four-fold increase in HRR resulted in significantly higher heat fluxes. The total heat release for the steel Closet registered the lowest value of 684 MJ while the measured total heat release for plastic and wood Closets was 1542 MJ and 1457 MJ, respectively. A similar trend was noted for Very Small sheds with different construction materials. The plastic Very Small shed particularly burned as a pool fire with very tall flames. Even if the plastic sheds are moved away from the primary residential structure, the molted pool can act as ladder fuel and ignite surrounding fuels.

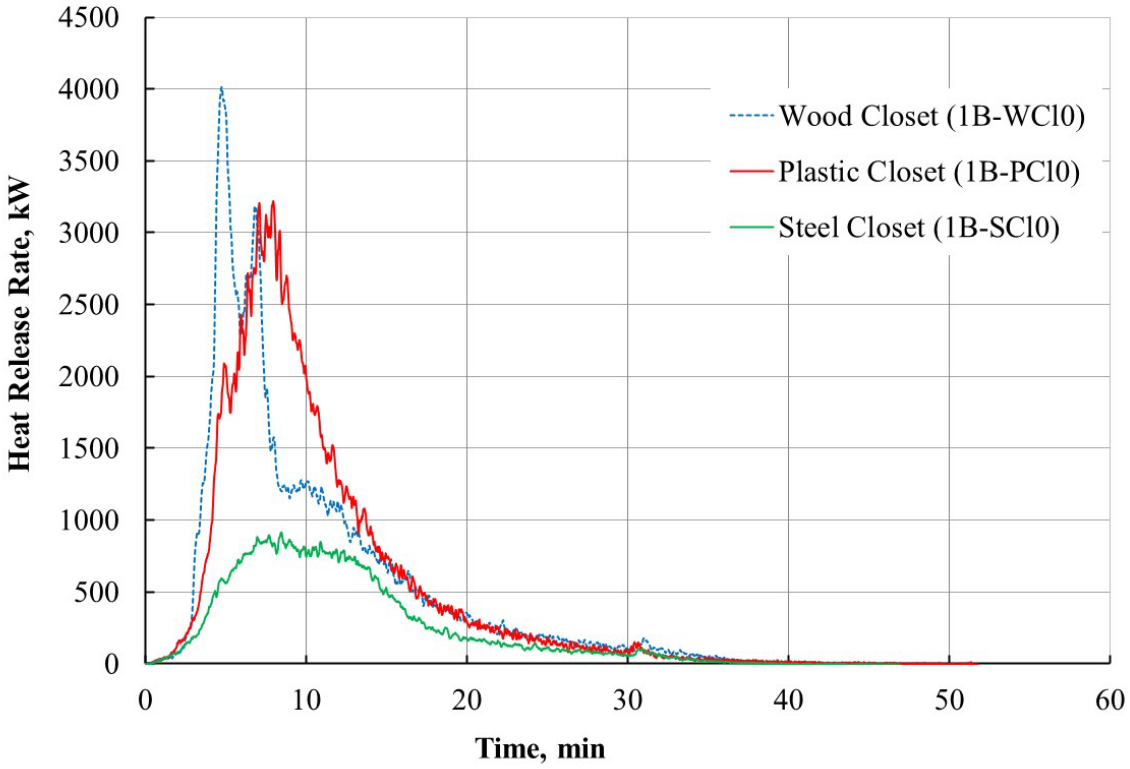

Fig. 62. Comparison of heat release rates for wood, plastic, and steel Closets with low fuel loading of two 1-A wood cribs.

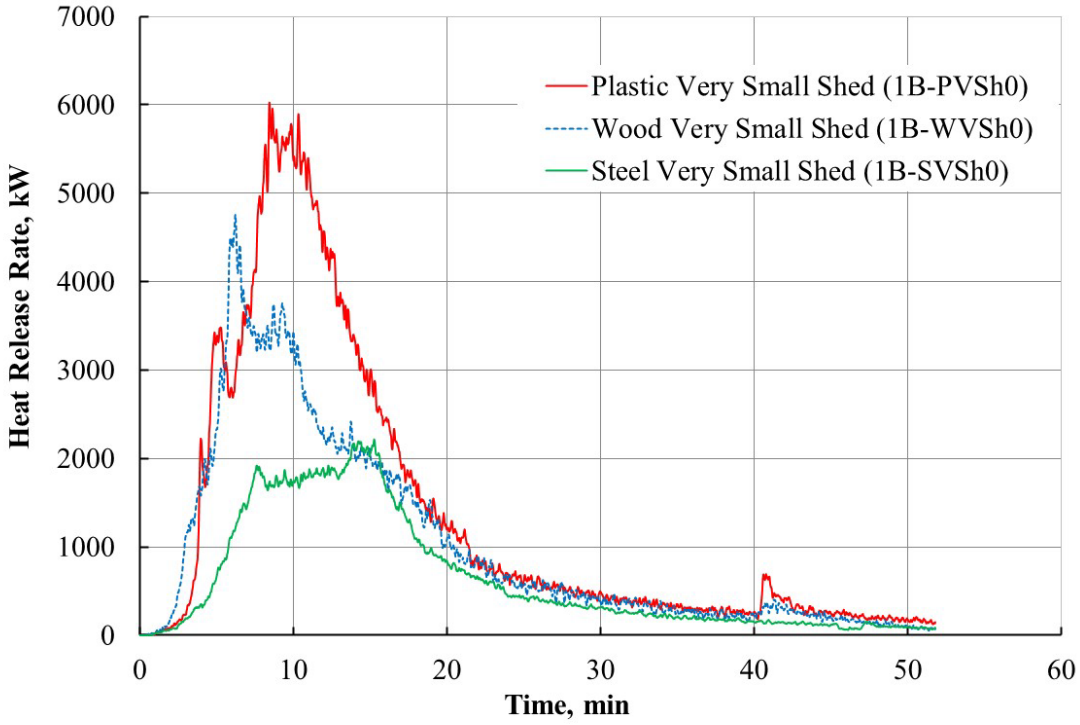

Fig. 63. Comparison of heat release rates for wood, plastic, and steel Very Small sheds with high fuel loading of six 1-A wood cribs.

A comparison of peak heat fluxes measured across the wood, plastic, and steel Very Small sheds with high fuel loading of six wood cribs is shown in Fig. 64. The peak heat flux varied with its distance from the source fire often showing an inverse relationship with squared radial distance. As discussed earlier, the lower HFGs recorded higher heat fluxes compared to the upper HFGs with an exception of HF2 for 1B-SVSh0 test. This pattern is due to their relative proximity to the source fire compared to the upper flux gauges. The higher peak heat flux value at HF2 for the steel Very Small shed was due to the plume "jetting" effect as discussed in Section 4.3.4.

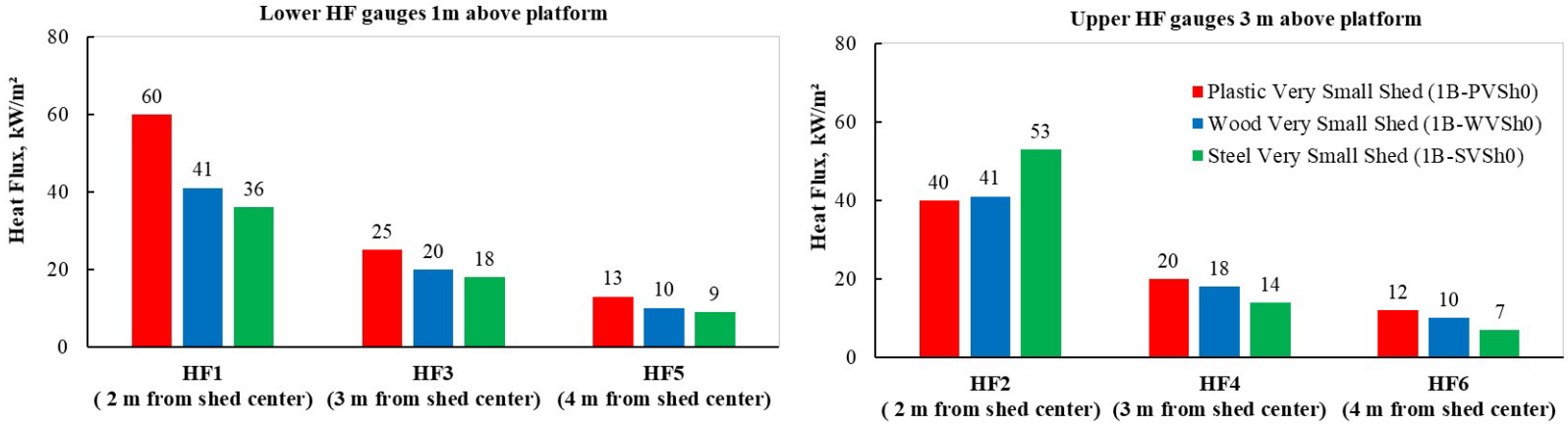

Fig. 64. Comparison of peak heat fluxes measured across the wood, plastic, and steel Very Small sheds with high fuel loading of six wood cribs. Standard expanded uncertainty is ±3 %.

4.4.3. Effect of Shed Size on Heat Release from Source Structures

Comparison of HRR profiles for 1B-WCh0 and 1B-WVSh0 in Fig. 65 shows the effects of shed size on HRR and THR. The fire growth rate for the wood Very Small shed is faster than that that for the Closet. This could be possibly attributed to the higher combustible mass of the shed, higher fuel loading, or lower fuel per unit area for the Very Small shed. The lower fuel per unit area could result in more re-radiation between the burning wood cribs and shed structure thereby causing faster pyrolysis. The THR for the wood Closet and the wood Very Small shed corresponded with their respective total combustible mass.

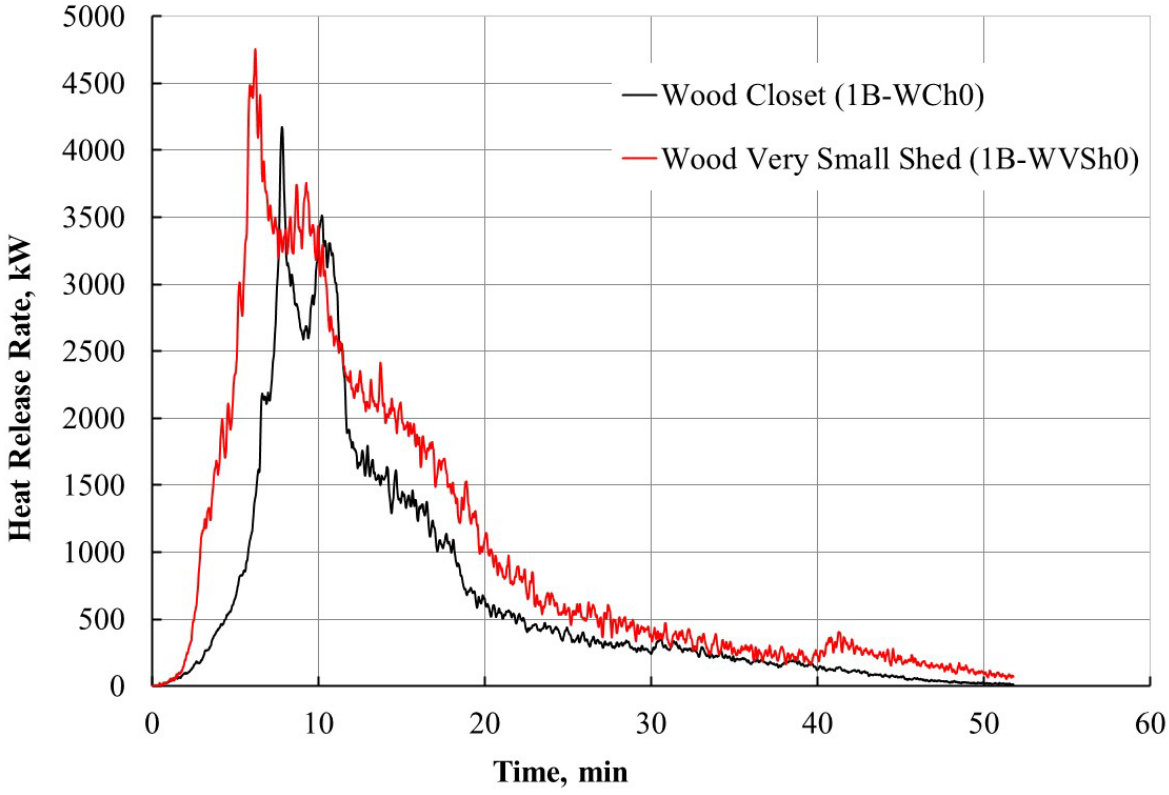

Fig. 65. Effect of shed size (Closet and Very Small shed) on heat release rate of wooden sheds with high fuel loadings.

4.4.4. Effect of Fuel Loading on Heat Release from Source Structures

A comparison of the heat release rate plots for 1B-WCl0 and 1B-WCh0 is shown in Fig. 66. For the low fuel loading (two 1-A wood cribs) the fuel loading density[3] is half of that for the wood Closet with high fuel loading (four 1-A wood cribs). The lower fuel loading density allows for higher oxygen availability and hence faster flame spread over the combustible fuel. The PHRR is not affected by the fuel loading; however, the time to reach peak is delayed by 3 min for 1B-WCh0. The total heat release increases with increase in fuel loading. The total heat released

[3] Fuel density is defined as energy per unit area of shed floor space and has units of MJ/m².

versus total combustible mass of the source structures plotted in Fig. 67 shows linear correlation except for the plastic sheds (represented in red dots) that burned with higher intensity compared to wood sheds. The heat of combustion for plastic (48 MJ/kg) is almost 2.6 times that of wood (18 MJ/kg).

The plot in Fig. 68 compares the total heat release, total combustible mass, and total mass of 1-A wood cribs (fuel loading) for all the source structures tested in this series. For noncombustible sheds, the combustible mass is the total mass of the wood cribs, i.e., the fuel loading, shown as solid black bars in Fig. 68. The hatched bars for combustible shed structures show the combustible mass of the shed material as a significant part of the overall fuel loading.

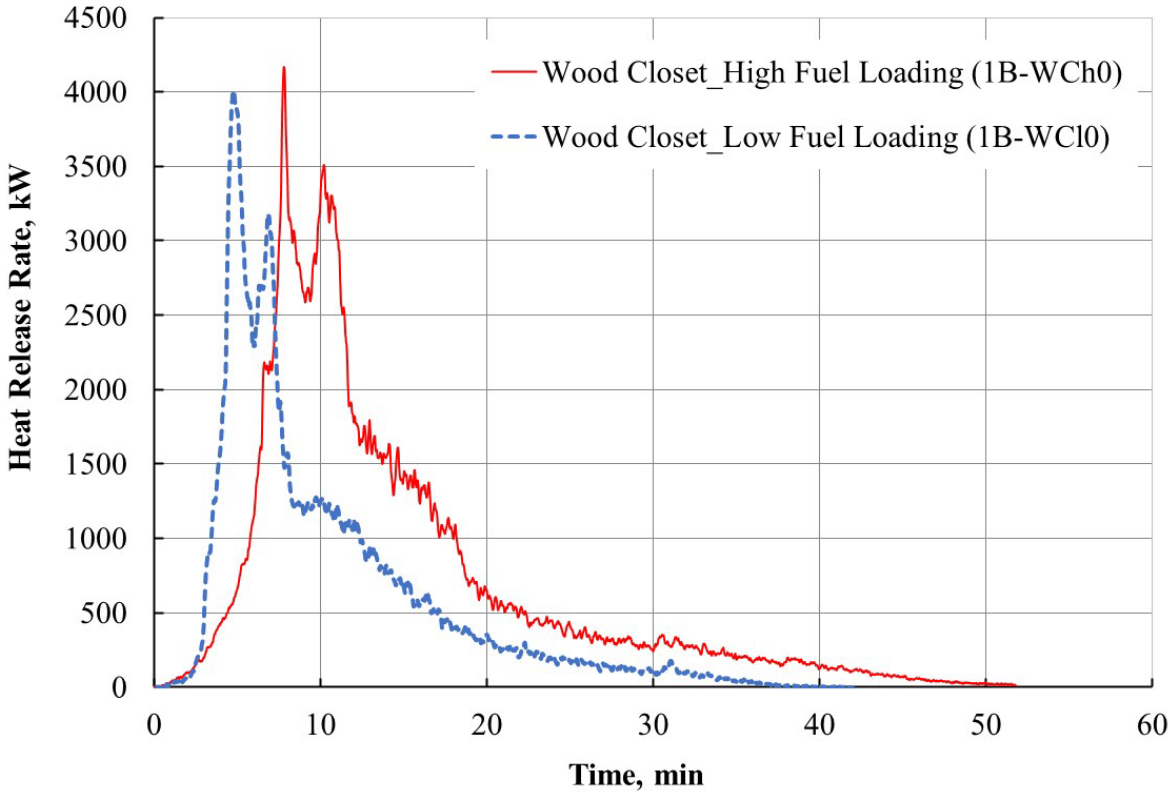

Fig. 66. Effect of fuel loading (low and high) on heat release rate of wood Closets.

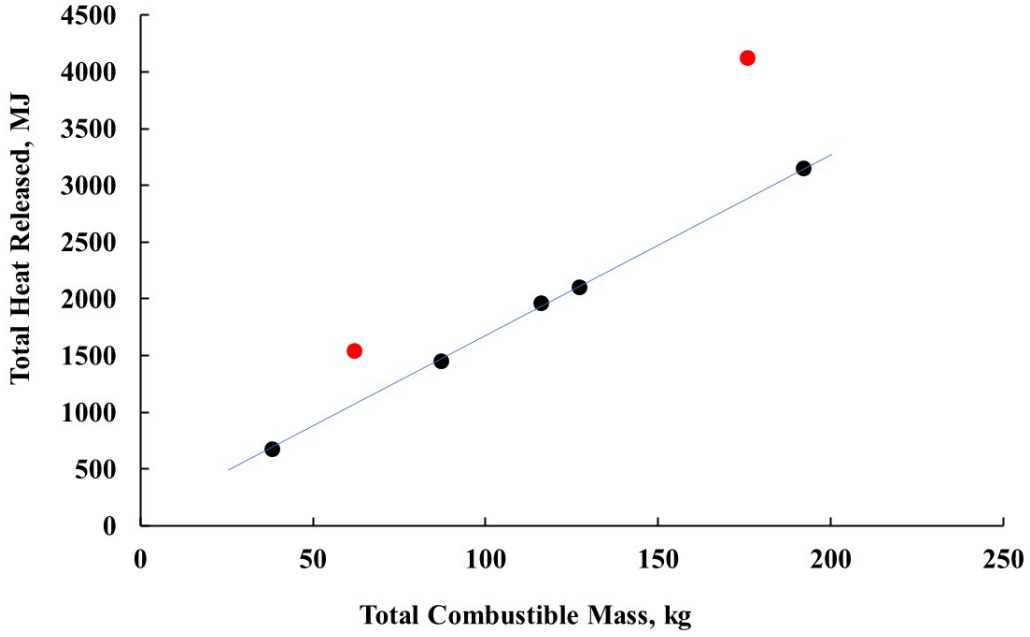

Fig. 67. Total heat released vs total combustible mass of the source structures tested. Note: Red dots indicate THR from plastic sheds.

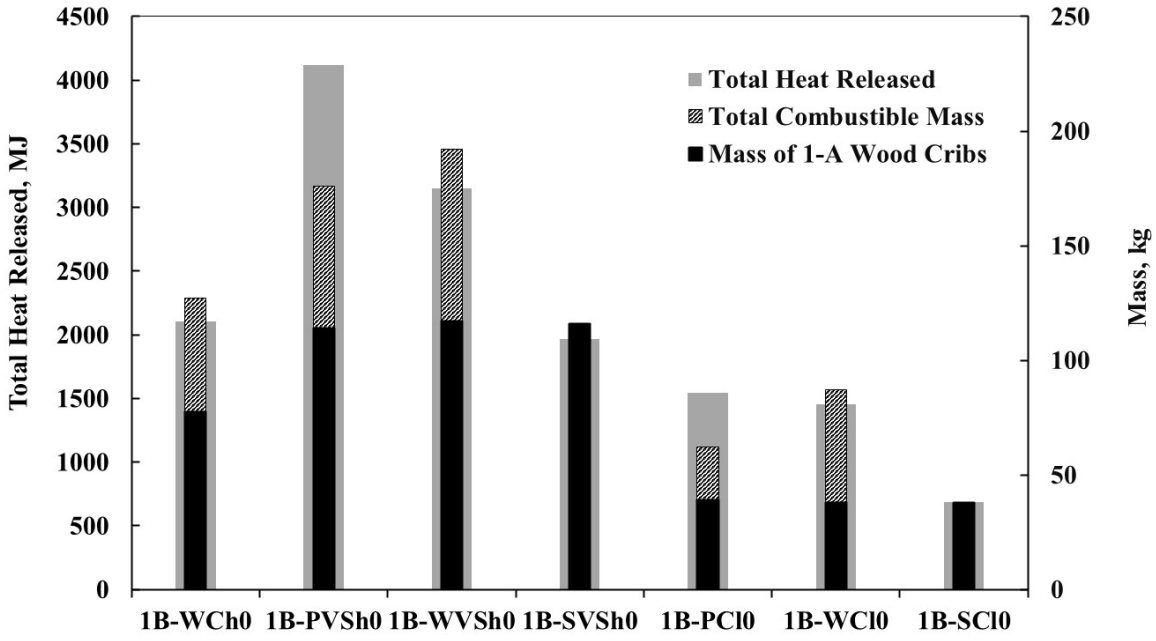

Fig. 68. Comparisons of total heat released, total combustible mass, and mass of the wood cribs (fuel loading).

4.4.5. Effects of Fire Size on Thermal Exposures to Surrogate Targets

Temporal responses for HFGs and the derived heat fluxes from PTCs are presented for each burn in the previous sections. Generally, comparisons of the heat flux and HRR plots suggest that the temporal profiles had similar time dependencies and that the measured heat fluxes were consistent with observed burning behaviors. In most cases, the lower HFGs recorded higher heat fluxes compared to the upper HFGs. This is due to their relative proximity to the burning fuel (source) compared to the upper flux gauges. The relative magnitudes of heat flux decreased with its distance from the source fire.

In this section the dependence of the fire size on the thermal exposures is examined by plotting the PHRR versus the peak heat fluxes recorded by the HFGs. The peak heat flux values recorded by lower and upper HFGs located in front of the source fire versus peak heat released for each test are plotted in Fig. 69 and Fig. 70, respectively. The peak flux values calculated from PTC measurements located above the source fire versus peak heat release rate for each test are plotted in Fig. 71.

Generally, there appears to be linear correlation between the peak heat flux and the PHRR values. The linear least squares curve fits were used to determine the best lines passing through the origins of the plots. The coefficient of determination, R^2, provide only qualitative indications for nonlinearity and fluctuations of the results about the line.

The data scatter along the lines in Fig. 69 and Fig. 70 can be attributed to several source structure characteristics including the size of door opening, the size of the shed, and the arrangement of wood cribs within the shed. The effects of the size of the door opening and arrangement of the wood cribs on heat flux measurements across the steel shed was demonstrated in test 1B-SVSh0. The fire plume from the wood cribs in test 1B-SVSh0 stretched through the door opening to reach the upper heat flux gauge (HF2) and registered the highest peak heat flux value encircled in Fig. 70 . This flame “jetting,” focusing the energy out of the door, can result in very high local exposures. In this case, heat fluxes over 50 kW/m^2 were recorded highlighting the need to have adequate spacing from other fuels even in the case of a noncombustible shed.

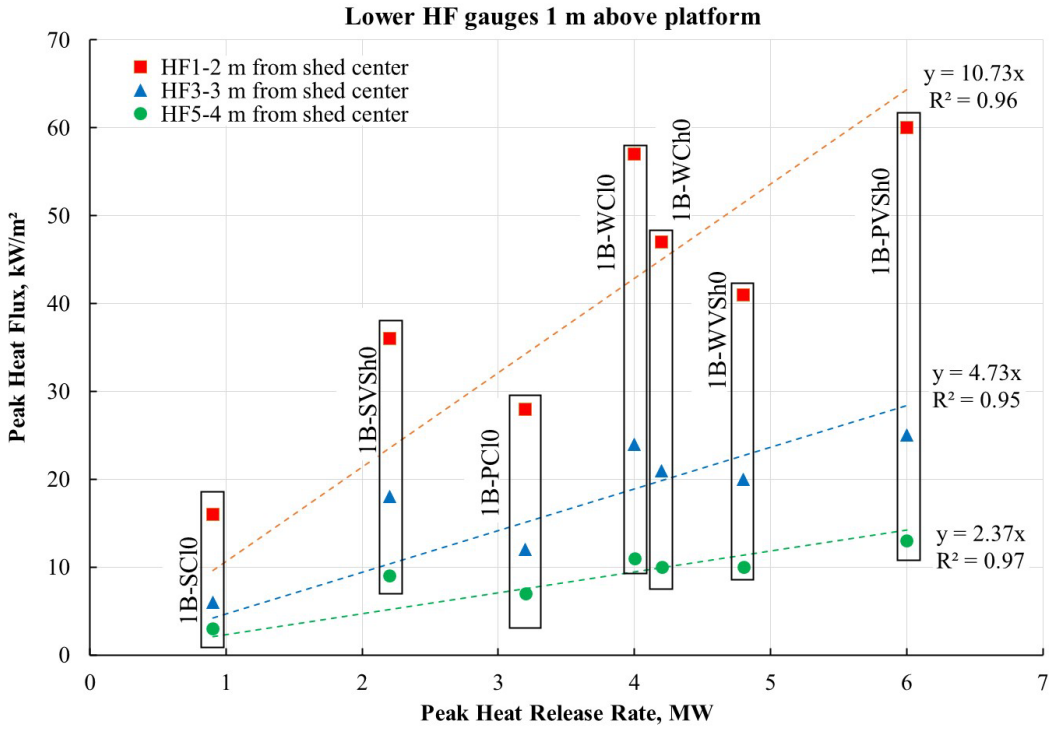

Fig. 69. Peak heat flux values recorded by lower HFGs located in front of the source fire versus peak heat release rate for each test.

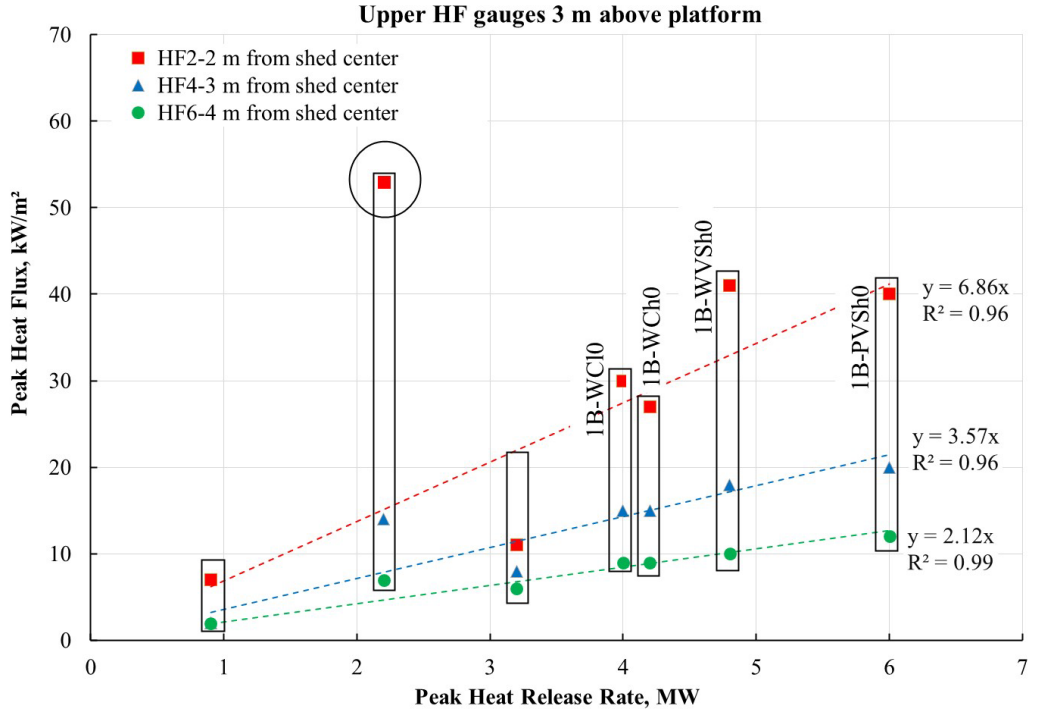

Fig. 70. Peak heat flux values recorded by upper HFGs located in front of the source fire versus peak heat release rate for each test.

The data scatter for peak heat fluxes estimated above the source fire can be attributed primarily to the structural integrity of the sheds during burning. The roof of the noncombustible steel Closet and Very Small shed remained intact and re-directed the convective heat. Very low thermal radiative heat fluxes estimated due to intense heating of the steel roof can be noted from Fig. 71. The PTC did not register high temperatures as they were not exposed to the flame/plume and hence lower heat flux values for steel source structures. The roof of the plastic Closet and the Very Small shed opened up due to melting of the plastic and the plate thermometers above the shed were exposed to radiant and convective heating from the burning of the wood cribs. High heat fluxes, in excess of 50 kW/m², were registered at the window height (PTC1) as shown in Section 4.3.2.

Despite the scatter and high fluctuations in the measured and estimated heat flux data, the results indicate that a reasonable estimate of the heat flux for a given PHRR at a given SSD is possible with R^2 varying from 0.95 to 0.99 for different spacings.

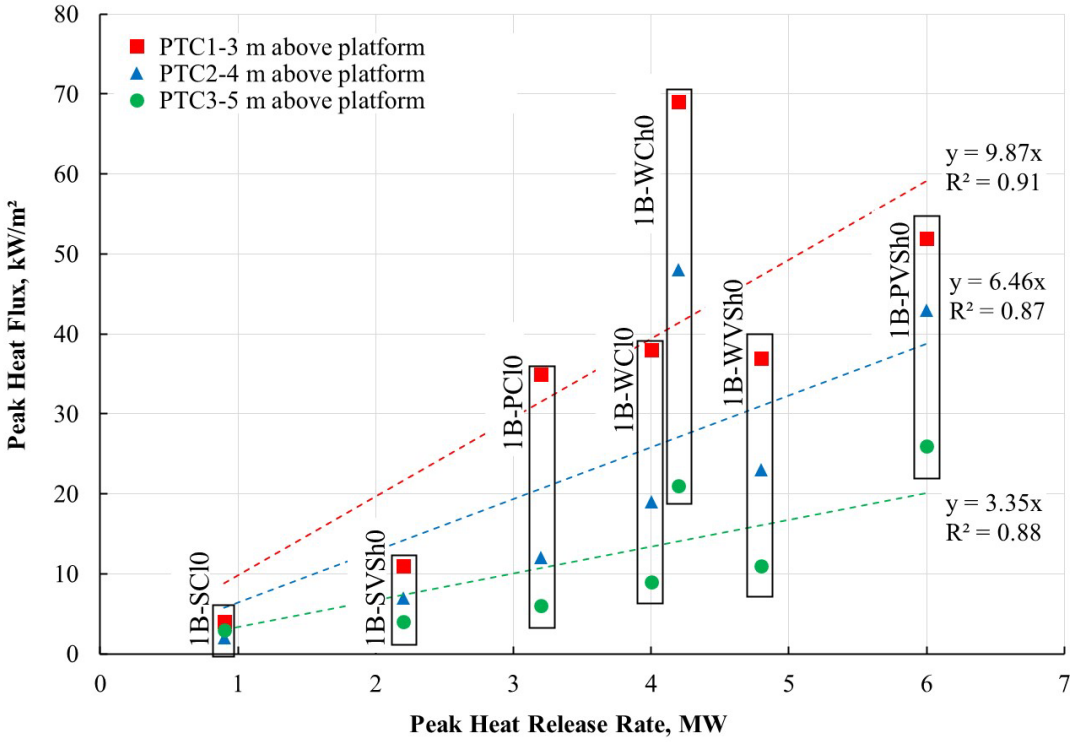

Fig. 71. Peak heat flux values calculated from PTC measurements located above the source fire versus peak heat released for each test.

5. Indoor Shed Burn Experiments with Target Structure

5.1. Test Objectives

The primary purpose of the experiments with a shed and target structure was to assess target performance for exposures from different sheds (construction, size, fuel loading) placed at different SSDs with no added wind field. The target structure performance was assessed in terms of window failures, vent performance, ignition of eaves, and structural integrity of the exterior layer of the target wall. The source term exposure was quantified in terms of heat release rate measurements. The mass loss measurements in these experiments were distorted due to the adjoining target structure and were discarded from the analysis. Thermal exposures to the nearby target structure were quantified by measuring heat fluxes at predetermined locations. For the last two tests, heat flux gauges were placed in the eave rafter bays to quantify thermal exposures at which ignition would occur.

5.2. Experimental Configuration

5.2.1. Target Structure Specifications

The target structure comprised of a wall-roof assembly with a double pane window, and a vented attic. Preliminary drawings and material specifications are provided in Ref. [3]. The target wall was designed to have nominal dimensions of 3.9 m (tall) × 4.87 m (wide) (13 ft × 16 ft) to accommodate the source structure (with a maximum height of 2.43 m (8 ft)) under the window. The asphalt shingle roof had a pitch of 5:12 and and open-eave configuration. The total height of the target structure including the foundation and the roof was approximately 5.28 m (17 ft 4 in). The wall was constructed with nominal 2-in × 4-in studs with 1-in-thick mineral fiber cavity insulation. A 5/8-in drywall was used as an interior layer, and the exterior wall had three layers, as shown in Fig. 72. A noncombustible board (DensGlass® sheathing) was sandwiched between a oriented strand board (OSB) and one layer of noncombustible cement board[4]. The main objective of this project was to assess the performance of eaves, but not wall. In order to achieve the main experimental objective and to prevent any potential ignition of the wall, an additional insulating layer of noncombustible gypsum panel lined with fiberglass mats was used in the construction of the target wall for this project. A fire established at a wall assembly has a high risk of spreading to the roof and eaves. The target wall was therefore thermally insulated using a sheathing to prevent ignition of wall assembly.

[4] Typically, an exterior non-combustible layer in the wall assembly would meet the requirements of SFM-12-7A-1.

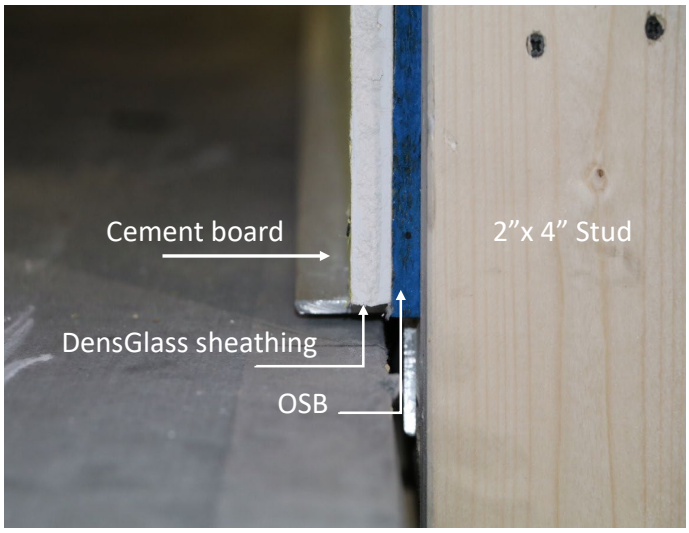

Fig. 72. Photograph showing a nominal 2-in × 4-in stud and the three exterior layers of the target wall.

A fire-resistant eave vent with an intumescent coating was installed in the central rafter bay. The core of the vent was made of aluminum honeycomb coated with a proprietary intumescent coating, encased within a galvanized metal casing. This eave vent is commonly recommended by California Building Code (Chapter 7A) for residential construction in wildland-urban interface (WUI) areas.

A horizontal sliding, double-pane window with a vinyl frame was placed 8 ft 6 ins (2.59 m) above the foundation and had nominal dimensions of 2 ft (high) × 3 ft (wide). Similar window configurations are commonly used in bathrooms, for example. Annealed glass with a low emissivity coating was used in the construction of the windows, typical of the non-fire hardened construction building stock that may be part of a retrofit hazard mitigation program. Window screens, typically required for WUI construction compliance, were also used. Metal or fiberglass screens are used to resist ember entry, and they are also known to reduce the amount of radiant heat transmitted to the glass.

A steel-plate window shutter (see Fig. 73) was placed on the unexposed side of the window and was closed after window failure to prevent flame penetration through the broken window causing unwanted ignition of the wall assembly from the unexposed side.

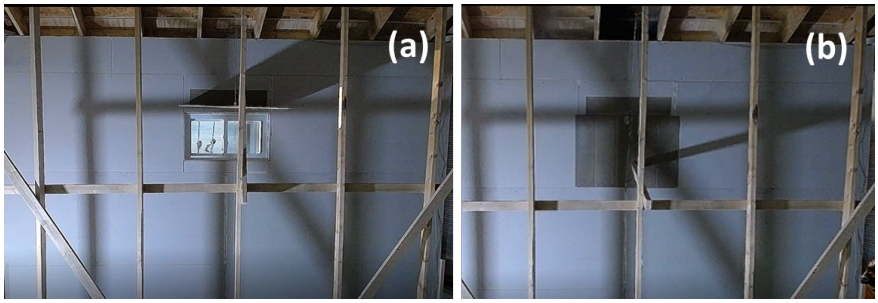

Fig. 73. Photographs showing window shutter at the back of target wall in (a) an open and (b) close configuration.

The schematics of the front and side views of the target structure and the shed are shown in Fig. 74 and Fig. 75, respectively. Also shown in Fig. 75 are the heat flux gauge rigs and the

placement of thermocouples in the vent. The locations and orientation of the instrumentation are provided in Table 10. The changes made to the instrumentation for subsequent tests are provided in Table 11 and Table 12. The uncertainties in distance measurements are discussed in Appendix C.

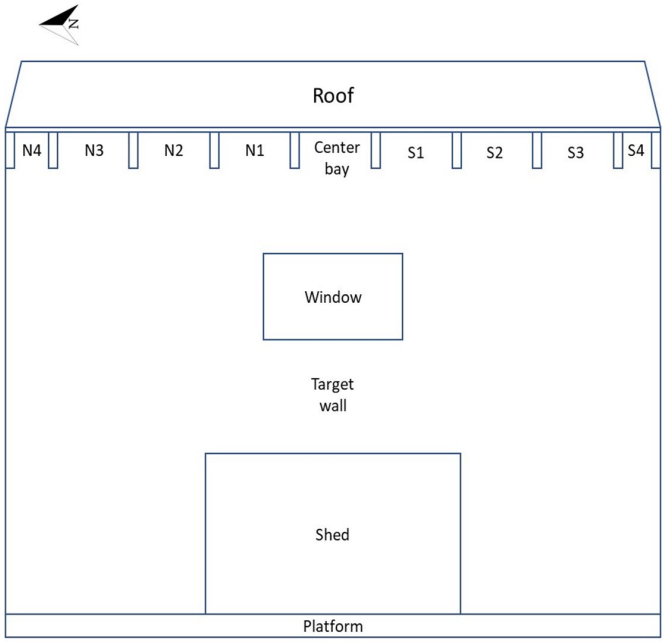

Fig. 74. Schematic showing placement of the shed and the target structure on the weighing platform.

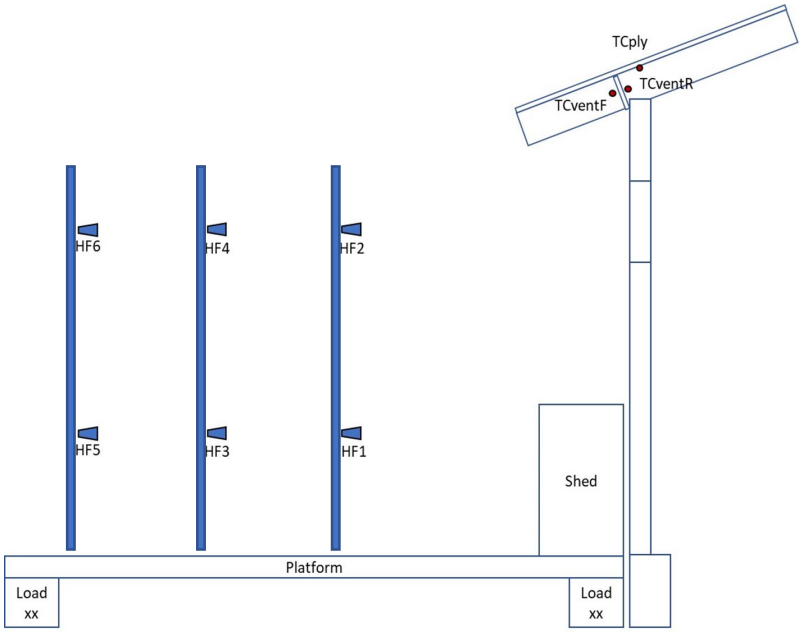

Fig. 75. Schematic showing the side view of the shed, target structure, weighing platform, and the placement of heat flux gauges and thermocouples. Note: Fig. not to scale.

In selected experiments, a plenum equipped with a negative pressure exhaust fan was situated behind the central eave vent and under the roof, simulating an attic area. The fan used to draw air

through the vent had a variable speed control adjustment to deliver an average speed of 0.9 m/s (2.0 mi/h). An inline centrifugal fan (115 V, maximum 84 W, and 0.74 A, nominal 2680 rev/min) specified in ASTM E 2886 [11] was used. Two Type K thermocouples were placed inside the plenum (Fig. 76) to measure the maximum temperature reached on the unexposed side of the target wall. Thermocouples were checked before the test to verify a response to known heat sources. As mentioned in the ASTM E 2886, a 100 % cotton batting with a density in the range of 20 kg/m^3 to 25 kg/m^3 was used as the combustible target material inside the plenum. Flame penetration through the vents and ignition of the combustible target material was monitored using a video camera. The thermal changes in the plenum were monitored using a FLIR camera.

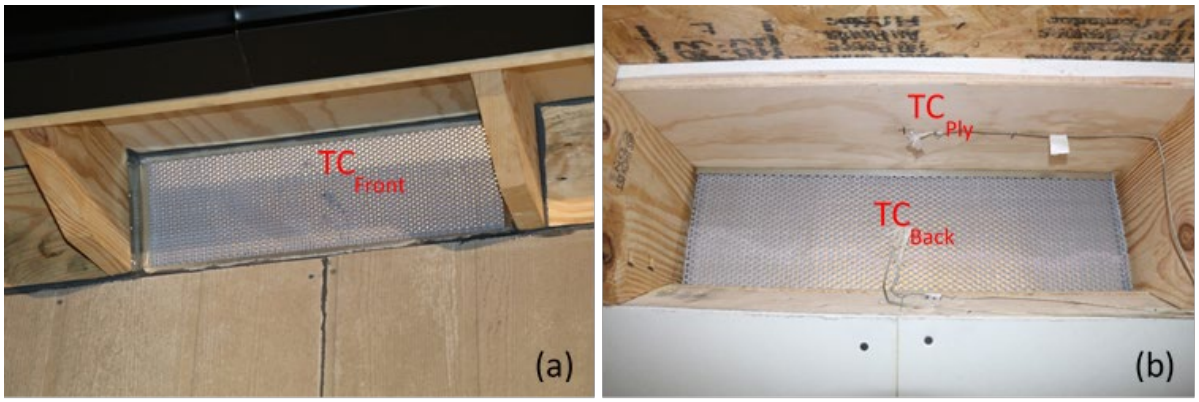

Fig. 76. Photographs showing eave vents with (a) front and (b) rear TCs.

Table 10. Location and orientation of instrumentation with reference to the target wall origin for tests 1B-WCl0-0, 1B-SCl0-0, and 1B-SCh0-0.

Device	ID	X East+ (cm)	Y North+ (cm)	Z Up + (cm)	Orientation
Heat flux gauge	HF1	−300	20	100	Facing shed
Heat flux gauge	HF2	−300	20	300	Facing shed
Heat flux gauge	HF3	−400	0	100	Facing shed
Heat flux gauge	HF4	−400	0	300	Facing shed
Heat flux gauge	HF5	−500	−20	100	Facing shed
Heat flux gauge	HF6	−500	−20	300	Facing shed
Thermocouple	TCventF	−4	0	416	Above shed center, facing down
Thermocouple	TCventR	0	0	416	Above shed center, facing down
Thermocouple	TCply	10	0	427	Above shed center, facing down
HDMI Camera #1	Front	—	—	—	Facing shed
HDMI Camera #2	Iso	—	—	—	Diagonally facing the shed
HDMI Camera #3	Side	—	—	—	Facing side of shed
HDMI Camera #4	Back	—	—	—	Facing rear side of shed

Table 11. Location and orientation of heat flux gauges with reference to the target wall origin for tests 1B-SVSh0-5.

Device	ID	X East+ (cm)	Y North+ (cm)	Z Up + (cm)	Orientation
Heat flux gauge	HF1	−500	20	100	On eave wall, facing shed rafter bay:S1
Heat flux gauge	HF2	−500	20	300	On eave roof, facing down rafter bay:S1
Heat flux gauge	HF3	−400	0	100	On eave wall, facing shed rafter bay: N1
Heat flux gauge	HF4	−400	0	300	On eave roof, facing down rafter bay: N1
Heat flux gauge	HF5	−500	−20	100	On eave wall, facing shed rafter bay: S3
Heat flux gauge	HF6	−500	−20	300	On eave roof, facing down rafter bay: S3

Table 12. Location and orientation of heat flux gauges with reference to the target wall origin for tests 1B-SVSh0-5-R1 and 1B-WC00-0.

Device	**ID**	**X East+ (cm)**	**Y North+ (cm)**	**Z Up + (cm)**	**Orientation**
Heat flux gauge	HF1	−300	20	100	On eave wall, facing shed rafter bay:S1
Heat flux gauge	HF2	−300	20	300	On eave roof, facing down rafter bay:S1
Heat flux gauge	HF3	−400	0	100	On eave wall, facing shed rafter bay: N1
Heat flux gauge	HF4	−400	0	300	On eave roof, facing down rafter bay: N1
Heat flux gauge	HF5	−500	−20	100	On eave wall, facing shed rafter bay: S3
Heat flux gauge	HF6	−500	−20	300	On eave roof, facing down rafter bay: S3
Thermocouple	TCeaveN	−26	60	418	Eave wall rafter bay: N1
Thermocouple	TCeaveS	−26	−60	418	Eave wall rafter bay: S1
Thermocouple	TCvent_Plenum	−30	0	400	Behind the vent

5.2.2. Test Procedure

The test protocol was similar to the one described in Section 4.2.2.

5.2.3. Test Matrix

The following conditional statements and flowchart in Fig. 77 were developed to facilitate the decision-making for the selection of follow-on tests based on the experimental results. The sequencing of the tests as prioritized using Fig. 77 is shown in Table 13.

IF C with heavy fuel loading (FL) fails, THEN Repeat C with heavy FL
IF C with heavy FL repeatably fails, THEN test C with low FL

IF C with heavy FL does not fail, THEN test VS with heavy FL
IF VS fails, THEN repeat VS
IF VS repeatably fails, THEN test VS with low FL

IF VS with low FL does not fail, THEN test S with heavy FL
IF S with heavy FL fails, THEN repeat S with heavy FL
IF S with heavy FL repeatedly fails, THEN test S with low FL

IF S with low FL does not fail, THEN test M with heavy FL
IF M with heavy FL fails, THEN repeat M with heavy FL
IF M with heavy FL repeatedly fails, THEN test M with low FL

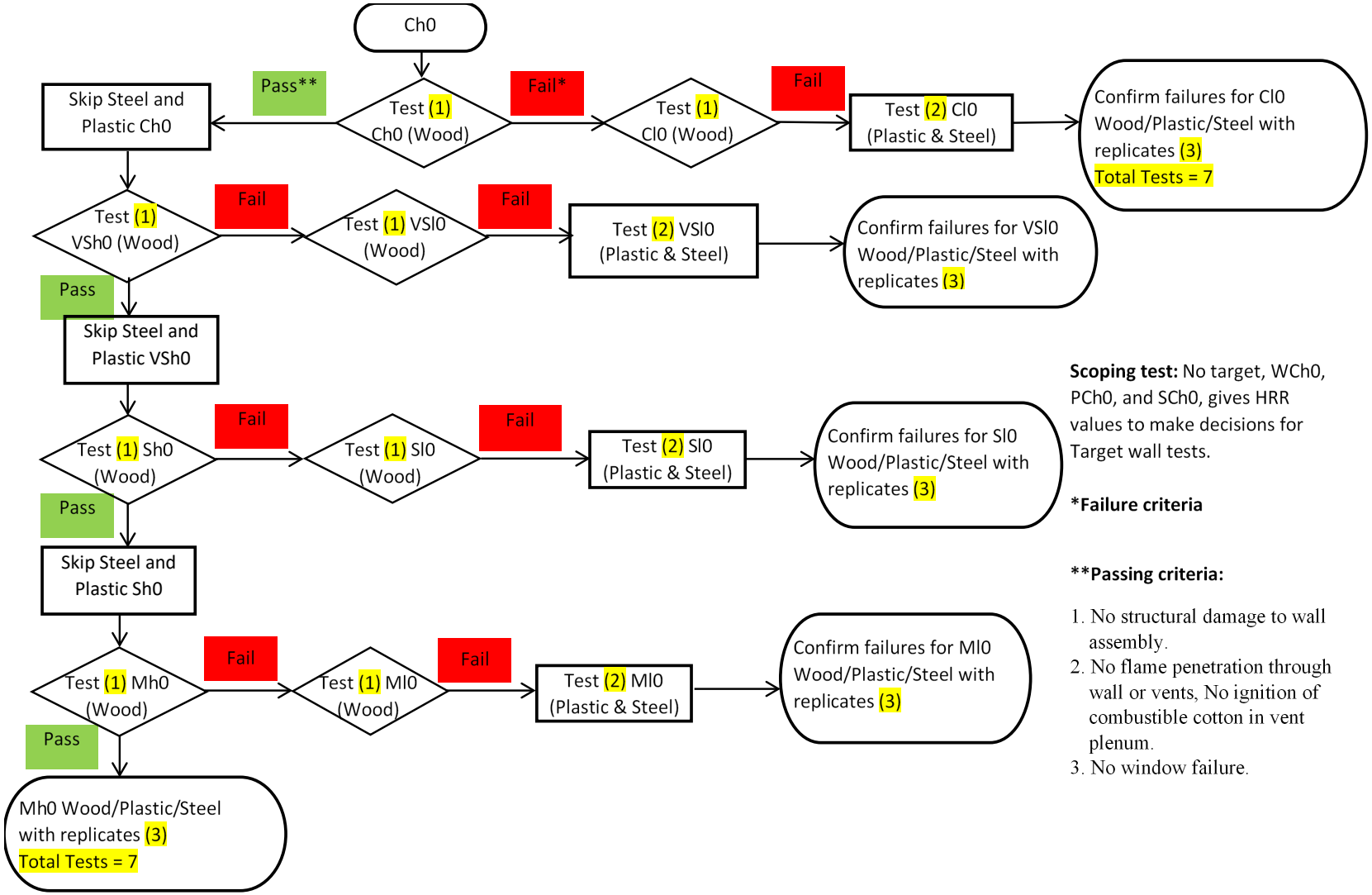

Fig. 77. Conditional flowchart used for developing shed plus target experiments.

Table 13. Shed and fuel loading specifications for the sheds tested with target structure.

#	Test ID	Shed type	Material	Fuel loading, (number of 1-A cribs)	SSD, ft	Mass, kg		
						Shed	Cribs	Total combustible
1	1B-WCl0-0	Closet	Wood	Low (2)	0	50	40	90
2	1B-SCl0-0	Closet	Steel	Low (2)	0	34	39	39
3	1B-SCh0-0	Closet	Steel	High (4)	0	32	77	77
4	1B-SVSh0-5	Very Small	Steel	High (4)	5	42	117	117
5	1B-SVSh0-5-R1	Very Small	Steel	High (4)	5	42	116	116
6	1B-WC00-0	Very Small	Wood	0	0	56	0	56

5.3. Data Analysis and Results

In this section, the results of each shed and target experiment are presented as: shed and target specifications, burn overview, and target structure performances. The burn overview is a detailed description of the flame spread using still images captured from the video recordings, and the burning behavior is quantified in terms of heat release rate data. The heat flux measurements are provided to quantify thermal exposures from the source structure to the surrogate target structures. The target structure performances are discussed qualitatively using still images captured following the experiment and quantitatively using thermocouple measurements located in the vent. In the last two experiments, heat fluxes were measured in the rafter bays to estimate the heat fluxes that led to ignition of the eaves and rafters. The target structure performances are discussed in terms of damage to the exterior layer of the target wall, window performance (frame melting and/or ignition, and breakage of the windowpane), vent failure (ember and/or flame penetration through the vent, temperature measurements using thermocouples located in the vent, and efficiency of intumescent coating in closing the vent cells), and ignition of rafters.

A summary of shed and target experiments is provided in Table 14.

Table 14. Summary of shed with target experiments.

Test ID	Material	Shed Size	Fuel Loading (1A cribs)	Total Combustible mass, kg	THR, MJ	PHRR, MW	Target Structure Fail ✗ or Pass ✓			
							Wall	Window	Vent	Eave Rafters
1B-WCl0-0	Wood	C	Low (2)	89	688	3.38	✗	✗	✗	✗
1B-SCl0-0	Steel	C	Low (2)	39	600	0.89	✓	✓	✓	✓
1B-SCh0-0	Steel	C	High (4)	77	1170	1.40	✗	✓	✓	✓
1B-SVSh0-5	Steel	VS	High (6)	117	780	2.71	✗	✗	✗	✗
1B-SVSh0-5-R1	Steel	VS	High (6)	116	956	3.11	✗	✗	✗	✗
1B-WC00-0	Wood	C	0	56	772	2.77	✗	✗	✗	✓

5.3.1. Test: 1B-WCl0-0

5.3.1.1. Shed and Target Specifications

The wood Closet and the fuel loading specifications are similar to the ones described in Section 4.3.5. The target specifications are as described in Section 5.2.1. The wood Closet was placed next to the target wall with SSD = 0 ft as shown in Fig. 78. The door was kept open and facing away from the target structure.

5.3.1.2. Burn Overview

The fire spread following the ignition of the wood cribs can be noted from the photographs in Fig. 78 while the heat release profile is shown in Fig. 79. The HRR plot shows two characteristic peaks as discussed in Section 1.1.1 and Section 4.3.5 for similar wood Closets. The ignition of the rafters occurred approximately 6 min after the ignition of wood cribs, while the peak in the HRR profile was registered at 8 min. The fire was extinguished immediately after the ignition of rafters.

Fig. 78. Photographs captured from videos recorded by (a) Cameras #2, (b) and (c) Camera #3, show ignition of cribs, burning of shed, and ignition of rafters, respectively, in test 1B-WCl0-0.

The temporal plots of heat fluxes recorded at a distance of 3 m (9 ft 10 in), 4 m (13 ft 1 in), and 5 m (1 ft 4 in) from the target wall are shown in Fig. 80. Comparison of heat flux data for lower and upper heat flux gauges clearly shows that the lower heat flux gauges (HF1, HF3, and HF5) recorded higher heat fluxes than the upper heat flux gauges (HF2, HF4, and HF6). As expected, the recorded heat fluxes dropped as a function of distance from the source structure (shed). A cursory analysis of the heat flux data suggests that heat fluxes in excess of 20 kW/m² recorded at a distance of 3 m (9 ft 10 in) for a period of 4 min can cause significant thermal damage to a nearby neighboring structure.

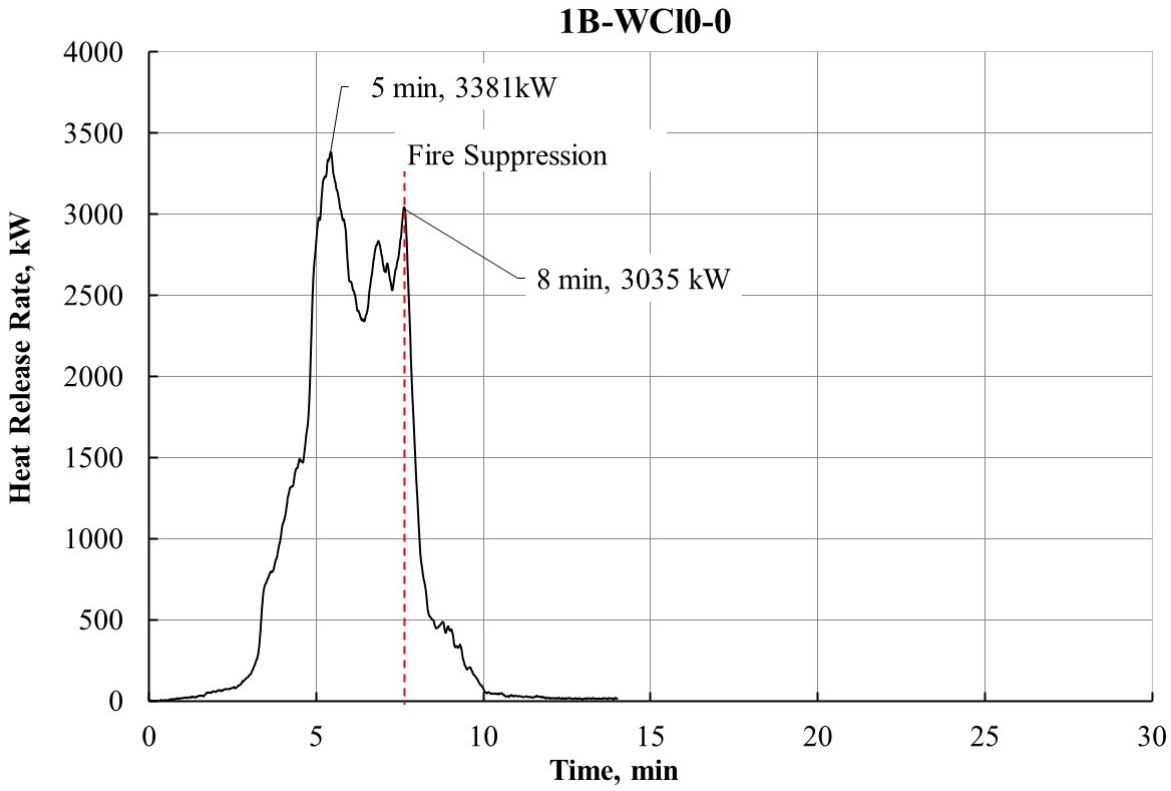

Fig. 79. Heat release rate of combustible mass in test 1B-WCl0-0.

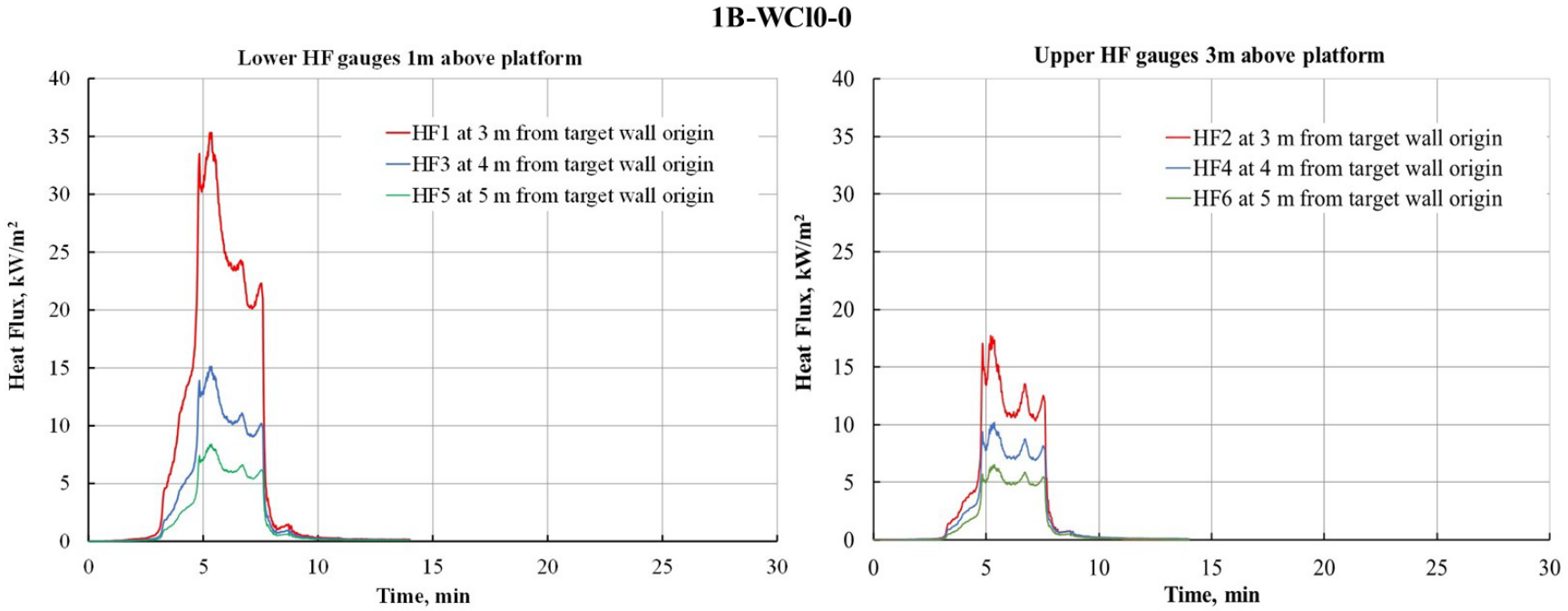

Fig. 80. Heat fluxes as a function of time recorded simultaneously by gauges located on the Rig1, Rig2, and Rig3 placed in the front of the shed in test 1B-WCl0-0. Standard relative uncertainty is ±3 %.

5.3.1.3. Target Structure Performance

The photographs of the target structure performance are shown in Fig. 81. The total heat released (688 MJ) from the burning of WCl0-0 for 8 min caused significant damage to the target structure. The central rafter bays ignited, and fire quickly spread along the eaves. Excessive spalling of the cement board was observed, and large pieces of cement board were expelled from the wall exterior. However, heat transfer through the cement board to the underlying layer of sheathing (DensGlass®) was limited such that no thermal damage to the gypsum panel was observed.

The exterior windowpane cracked 6 min after ignition of the cribs. The window screen fell off prior to the cracking of the windowpane. The vinyl frame melted and deformed; however, the broken glass remained in place. Such cracked-but-still-in-place phenomena occurred after approximately 7 min of exposure to radiant heat. Similar observations have been previously reported by Quarles et al. [12]. Although the broken glass remained in place during these experiments without wind, such a phenomenon is considered a window failure since the broken glass could possibly be displaced in presence of wind.

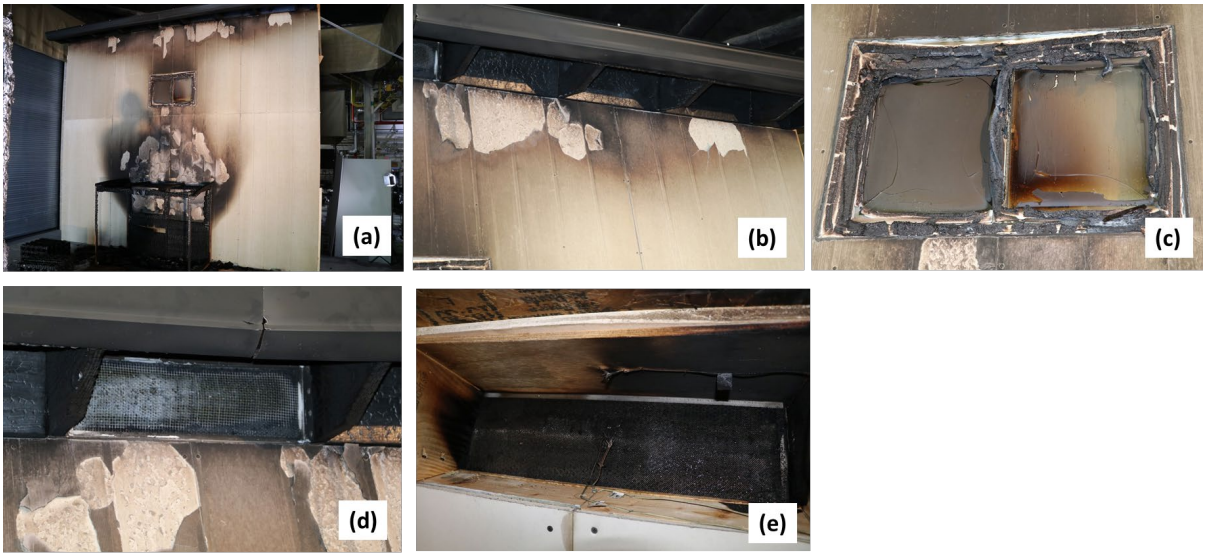

Fig. 81. Photographs showing (a) spalling of exterior layer (cement board), (b) charring of the rafters, (c) windowpane cracking and melting of the vinyl frame, (d) partial intumescence in the vent (front), and (e) partial intumescence in the vent (rear) in test 1B-WCl0-0.
Note: No vent plenum was used for this test.

Partial intumescence in the vents from the exposed and unexposed sides can be seen in Fig. 81(d) and Fig. 81(e), respectively. The performance of the vent is clearly depicted by the temperature-time plots in Fig. 82. The temperature-time profile recorded by the TC in front of the vent (TCventF) shows a steep rise in temperature until the ignition of the rafters. The temperature-time profile recorded by the TC behind the vent (TCventR) shows a rise in temperature up to 390 ºC. At this temperature, the intumescent coating on the vent is supposed to activate and close the vent openings. A significant drop in the temperature recorded by the TCventR suggested closing of the vent cells during the experiment. However, the intumescent coating was not

effective at very high temperatures. Note the peak temperature (941 ºC) recorded by TCventF at the time (7 min) when the intumescent coating failed, and the temperature recorded by TCventR begins to rise. The failure of the intumesced coating resulted in temperature rise behind the vent until the fire suppression began. The temperature-time profile for the TC on the plywood behind the vent (TCply) shows lower temperatures compared to those recorded by TCventR but generally followed the same trend.

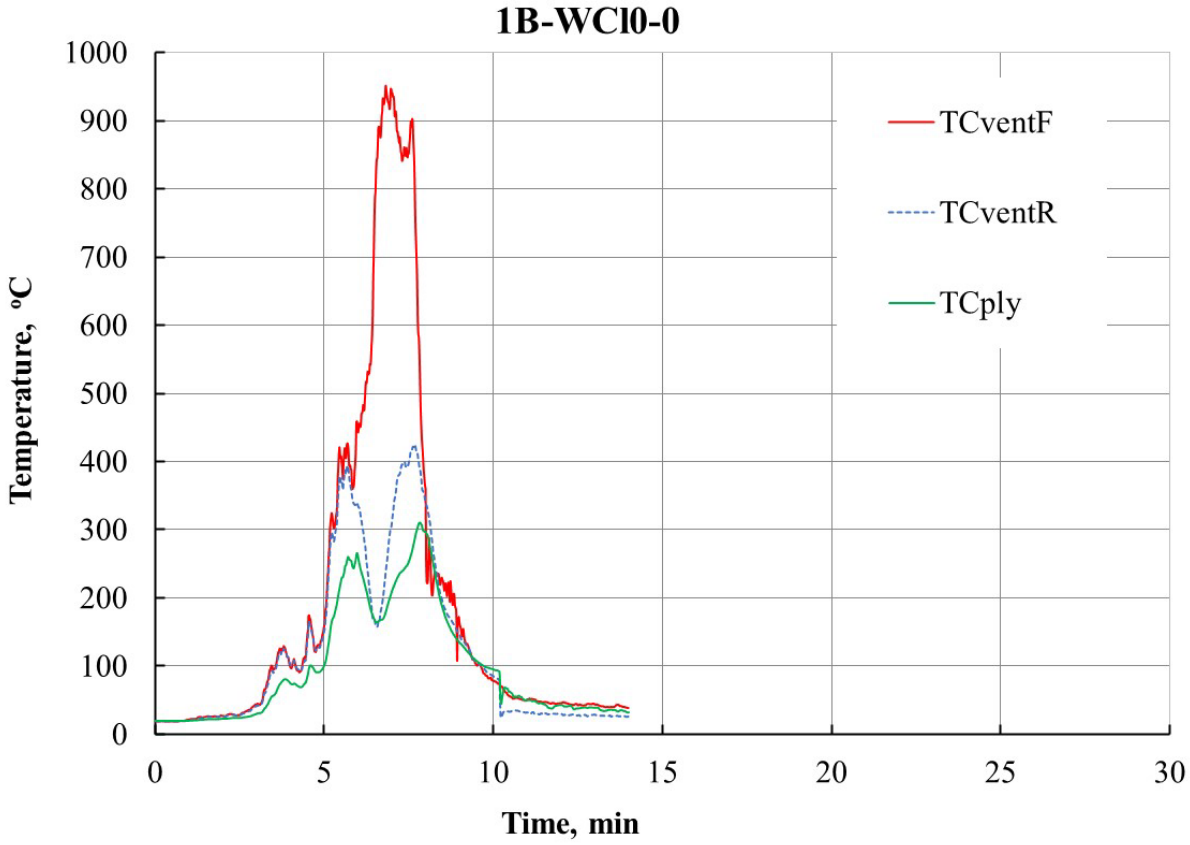

Fig. 82. Temperature-time profiles recorded by TCs in front of the vent (TCventF), behind the vent (TCventR), and on the plywood (TCply) behind the vent in test 1B-WCl0-0. Standard relative uncertainty is ± 0.75 %.

5.3.2. Test: 1B-SCl0-0

5.3.2.1. Shed and Target Specifications

The steel Closet and the fuel loading specifications are similar to those described in Section 4.3.7. The target specifications are as described in Section 5.2.1. The steel Closet was placed next to the target wall with SSD = 0 ft. The shed door was kept open and was facing away from the target structure, as shown in Fig. 83.

5.3.2.2. Burn Overview

The burning of the wood cribs within the noncombustible steel Closet can be noted from the photographs in Fig. 83, while the heat release profile is shown in Fig. 84. As noted in Fig. 83(c), the flames from burning wood cribs were deflected away from the target structure by the steel shed roof in this no-wind experiment. The burning behavior of the wood cribs and the associated measured quantities, including HRR and heat fluxes, are comparable to those reported for the free burning steel Closet without the target wall in Section 4.3.7. As mentioned earlier, the heat fluxes recorded by the lower heat flux gauges are significantly higher than those recorded by the upper heat flux gauges on the HFG rigs (Fig. 85). However, the measured heat fluxes are significantly lower than those recorded in test 1B-WCl0-0,

Fig. 83. Photographs captured from videos recorded by (a), (b) Camera #2, and (c) Camera #3, show steel Closet with low fuel loading, ignition of cribs, and flames coming out of the Closet in test 1B-SCl0-0.

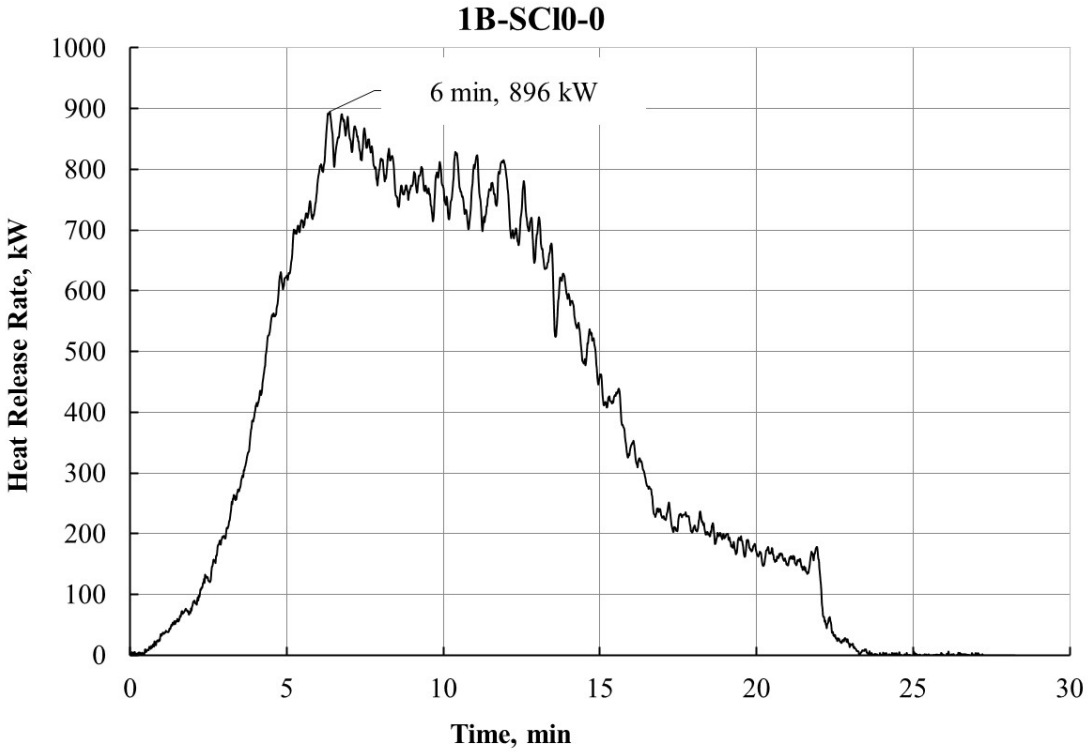

Fig. 84. Heat release rate of combustible mass in test 1B-SCl0-0.

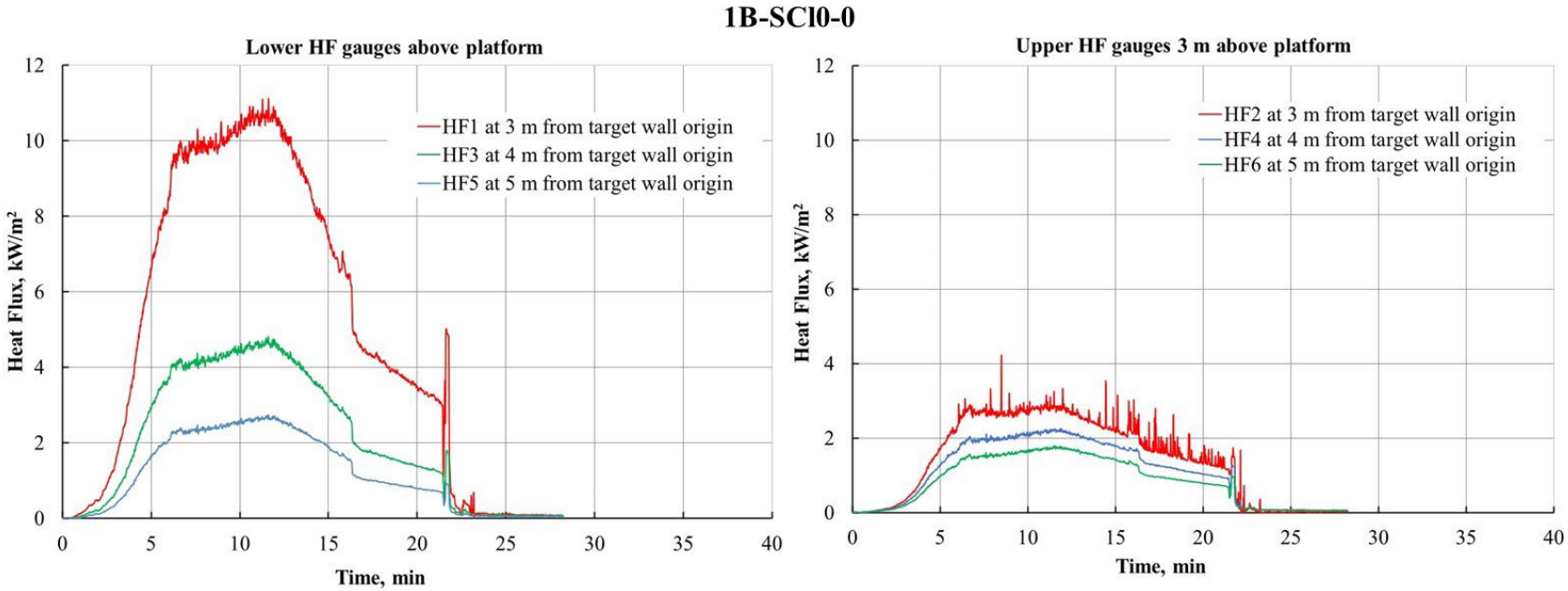

Fig. 85. Heat fluxes as a function of time recorded simultaneously by gauges located on the Rig1, Rig2, and Rig3 placed in the front of the shed in test 1B-SCl0-0. Standard relative uncertainty is ±3 %.

5.3.2.3. Target Structure Performance

The associated target structure performances due to thermal exposure from the burning of the wood cribs within the noncombustible steel Closet are shown in Fig. 86. It is evident from the photographs in Fig. 86 that the thermal damage to the target structure was localized in the area where the steel Closet was placed. The exterior cement board cracked due to excessive heat exposure for a prolonged duration of about 20 min. However, the removal of the cement board revealed that there was no thermal damage to the DensGlass® layer of the target wall. There was no damage to the windowpane or the window frame. The temperatures recorded at the vent remained well below 60 ºC as seen in Fig. 87.

Fig. 86. Photographs of target structure showing (a) overall marginal damage to the exterior wall, (b) some cracking of cement board, and (c) some discoloration of DensGlass® seen after removal of cement board in test 1B-SCl0-0.

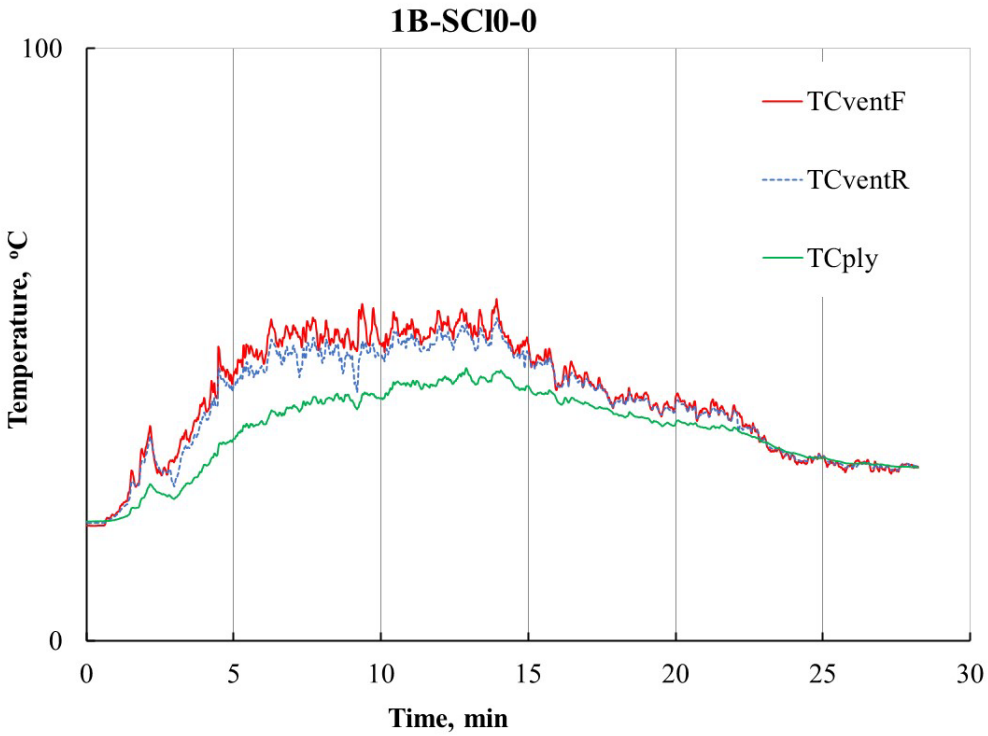

Fig. 87. Temperature-time profiles recorded by TCs in front of the vent (TCventF), behind the vent (TCventR), and on the plywood (TCply) behind the vent in test 1B-SCl0-0. Standard relative uncertainty is ± 0.75 %.

5.3.3. Test: 1B-SCh0-0

5.3.3.1. Shed and Target Specifications

The steel Closet specifications are similar to the one described in Section 4.3.7. The steel Closet had high fuel loading of 4 wood cribs. The target specifications were the same as described in Section 5.2.1. The steel Closet was placed next to the target wall with SSD = 0 ft. The shed door was facing away from the target wall as shown in Fig. 88.

5.3.3.2. Burn Overview

The burning behavior of 1B-SCh0-0 was similar to 1B-SCl0-0 except that the total heat released in case of the 1B-SCh0-0 was almost twice as that recorded for 1B-SCl0-0 due to higher fuel loading compared to 1B-SCl0-0. Visual observations suggests that the flame lengths were significantly longer in case of 1B-SCh0-0. The temporal profile of the HRR is shown in Fig. 89, and heat flux data for the lower and upper heat flux gauges on the HFG rigs are plotted in Fig. 90. The fire was extinguished at 30 min.

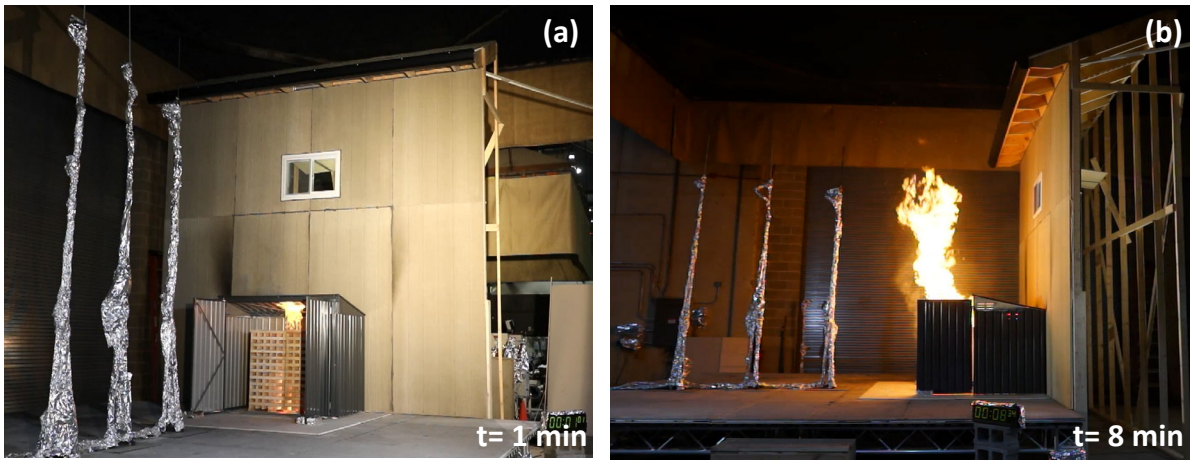

Fig. 88. Photographs captured from videos recorded by (a) Camera #2 and (b) Camera #3 show the ignition of cribs and flames emerging from the shed, respectively, in test 1B-SCh0-0.

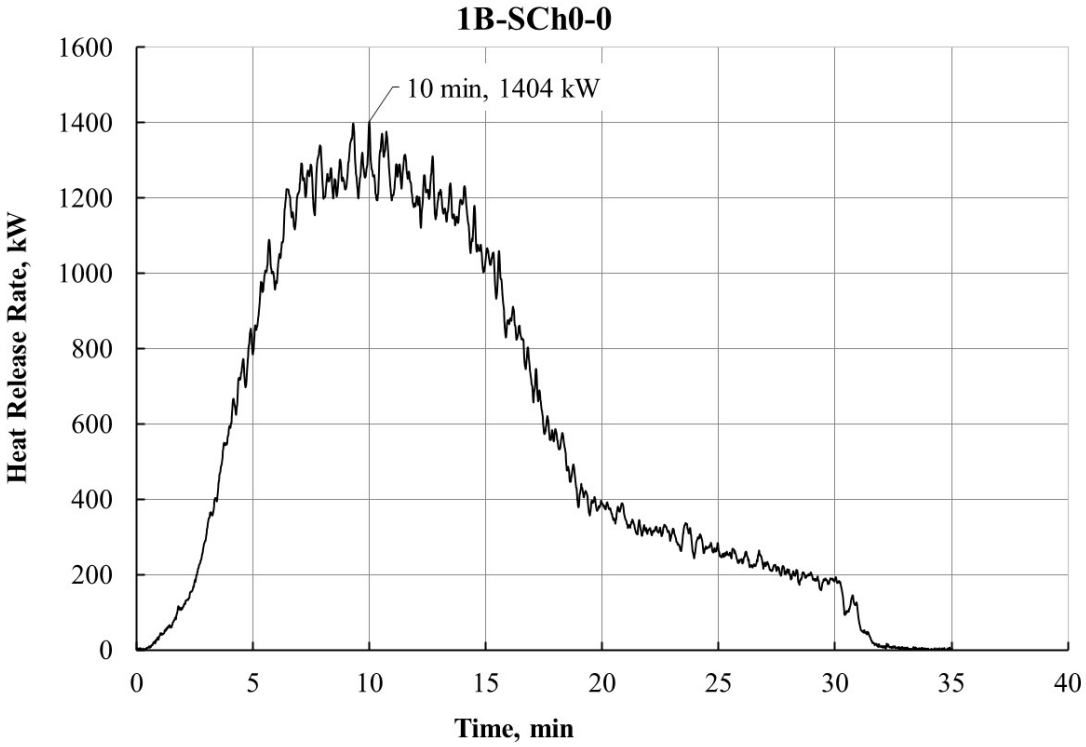

Fig. 89. Heat release rate of combustible mass in test 1B-SCh0-0.

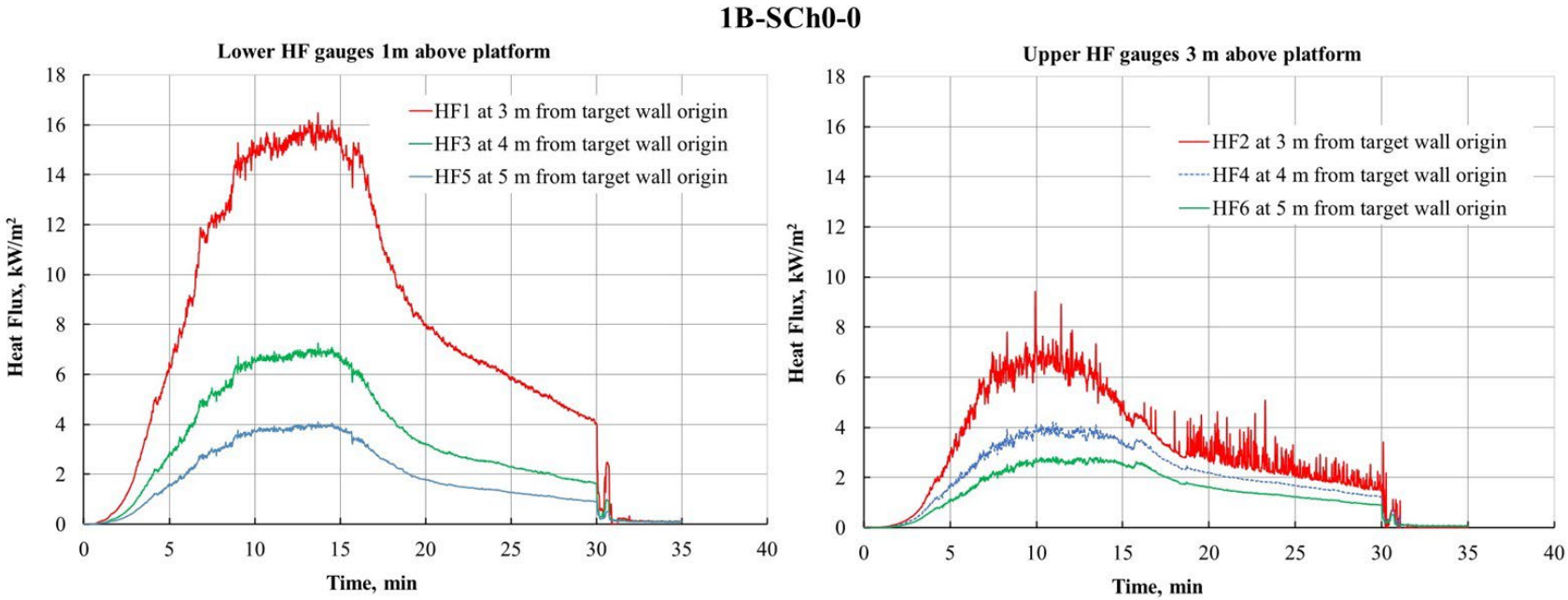

Fig. 90. Heat fluxes as a function of time recorded simultaneously by gauges located on the Rig1, Rig2, and Rig3 placed in the front of the shed in test 1B-SCh0-0. Relative expanded uncertainty is ±3 %.

5.3.3.3. Target Structure Performance

The photograph in Fig. 91(a) shows thermal damage to the target wall. The cracks in the cement board were localized in the area where the steel Closet was close to the wall. Otherwise, the target structure was not affected since the flames were jetting out of the source structure and away from the target structure. The window, the vent, and the eaves were unaffected by the limited radiant heat exposure, as shown in Fig. 91. There was no visible impact of the fire on the insulation board.

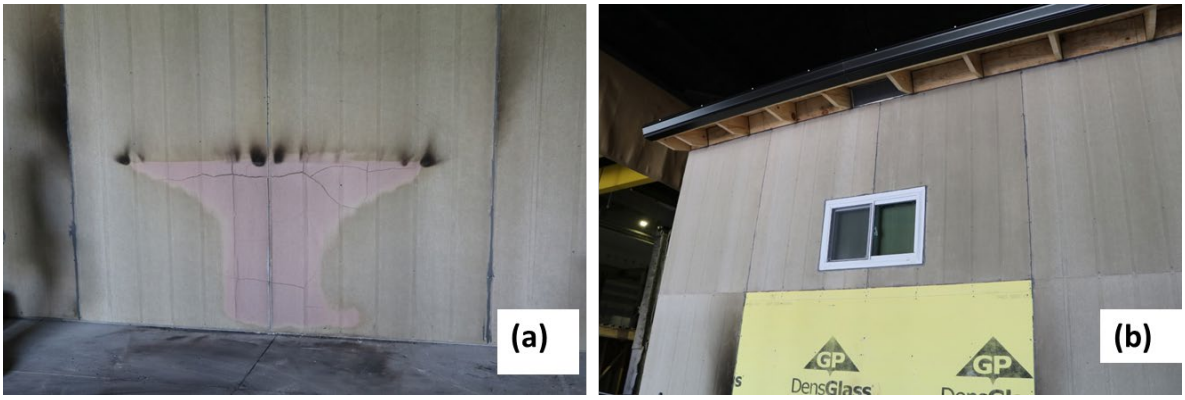

Fig. 91. Photographs of target structure showing (a) cracking of cement board due to thermal exposure and (b) undamaged window and eaves in test 1B-SCh0-0.

The temperature-time plots for the TCs located in the vent area are presented in Fig. 92. The temperature recorded by TCventF and TCventR generally remained under 80 ºC with the exception of two higher spikes in the temperature-time plots. Inspection of videos recorded during the test indicated that the flames occasionally leaned towards the vent, causing spikes in the temperature profiles.

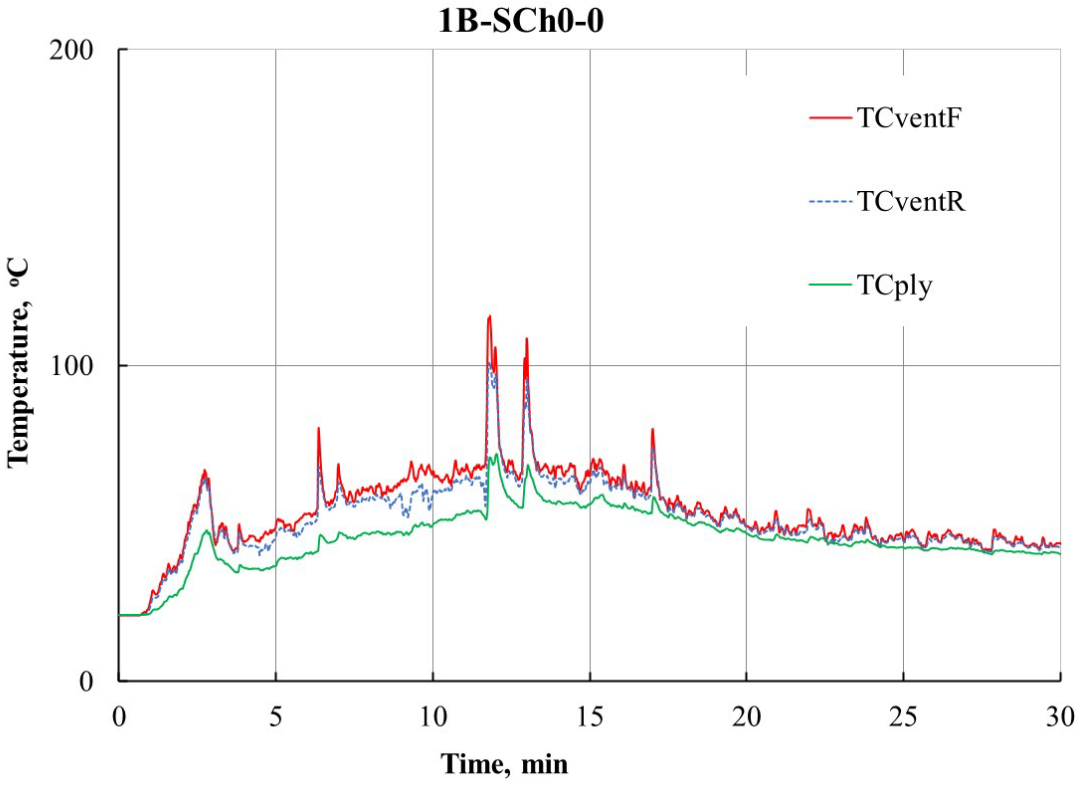

Fig. 92. Temperature-time profiles recorded by TCs in front of the vent (TCventF), behind the vent (TCventR), and on the plywood (TCply) behind the vent in test 1B-SCh0-0. Standard relative uncertainty is ± 0.75 %.

5.3.4. Test: 1B-SVSh0-5

5.3.4.1. Shed and Target Specifications

The steel Very Small shed specifications and the fuel loading specifications were the same as described in Section 4.3.4. The target specifications are as described in Section 5.2.1. For this test, a window shutter and a vent plenum with cotton batting was added to the target structure. An additional video camera was placed behind the target structure to record embers or flame penetration through the vent.

The steel Very Small shed was placed 5 ft away from the target wall and with the door facing the target wall as seen in Fig. 93. The arrangement of the heat flux gauge rigs was altered for this test by placing them in a triangular pattern. The positions of the heat flux gauges on Cartesian coordinates (x, y, z), where the origin O is the wall origin and z is the distance up from the weighing platform, are provided in Table 11.

5.3.4.2. Burn Overview

The photographs in Fig. 93 show the progression of flames from the interior the noncombustible steel shed. The plume length was short at first, with most flames contained within the shed (4 min from the ignition of wood cribs). Once the wood cribs were fully involved in the fire, the plume length increased significantly such that flame impingement on the target structure occurred within 7 min from ignition. First, the window frame ignited, followed by rafter ignition. The HRR plot for this test is shown in Fig. 94. The temporal plot in Fig. 94 is very similar to that of the test 1B-SVSh0, with two characteristic peaks. In the HRR plot for the test 1B-SVSh0, the second peak was attributed to excessive burning of the wood cribs after they collapsed. The second peak in the HRR plot for test 1B-SVSh0-5 at 11 min suggests contribution of heat released from the flaming ignition of rafters. The intense burning of the wood cribs, along with the rafters and the roof, is also reflected in the temporal plots of heat flux measurements with sharp peaks in the profiles. The heat fluxes recorded on the heat flux gauge rigs were significantly lower than those recorded for the test 1B-SCh0 despite the higher fuel loading. This is primarily due to the fact that heat flux gauge rigs were placed behind the source structure. The fire was extinguished at 11 min after ignition of the target structure.

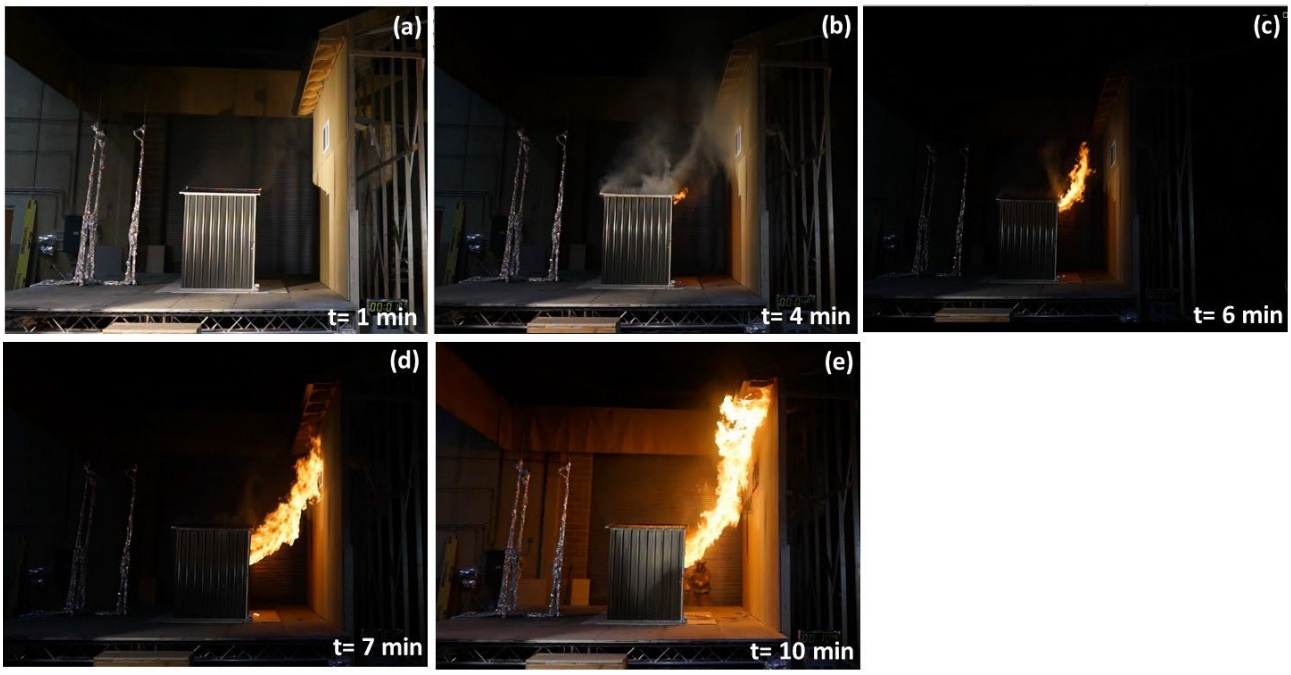

Fig. 93. Photographs captured from videos recorded by Camera #3 showing (a) steel Very Small shed with door opening facing the target structure and HFG rigs behind the shed, (b) short flames emerging from the shed door, (c) increased flame length, (d) flames from burning of cribs impinging on the target structure, and (c) ignition of rafters in test 1B-SVSh0-5.

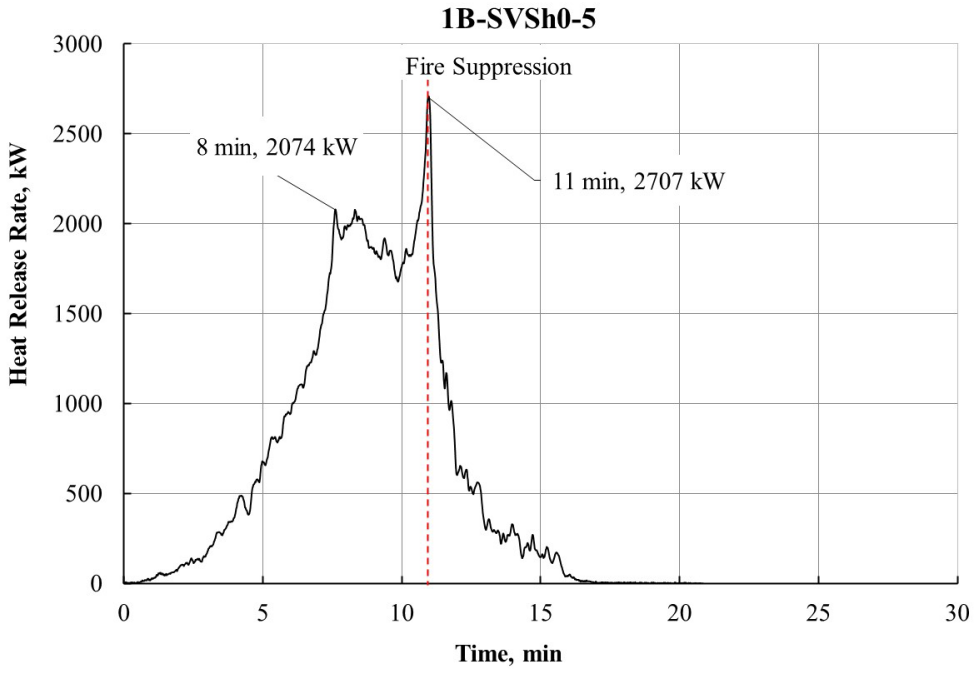

Fig. 94. Temporal profile of heat release rate of combustible mass in test 1B-SVSh0-5.

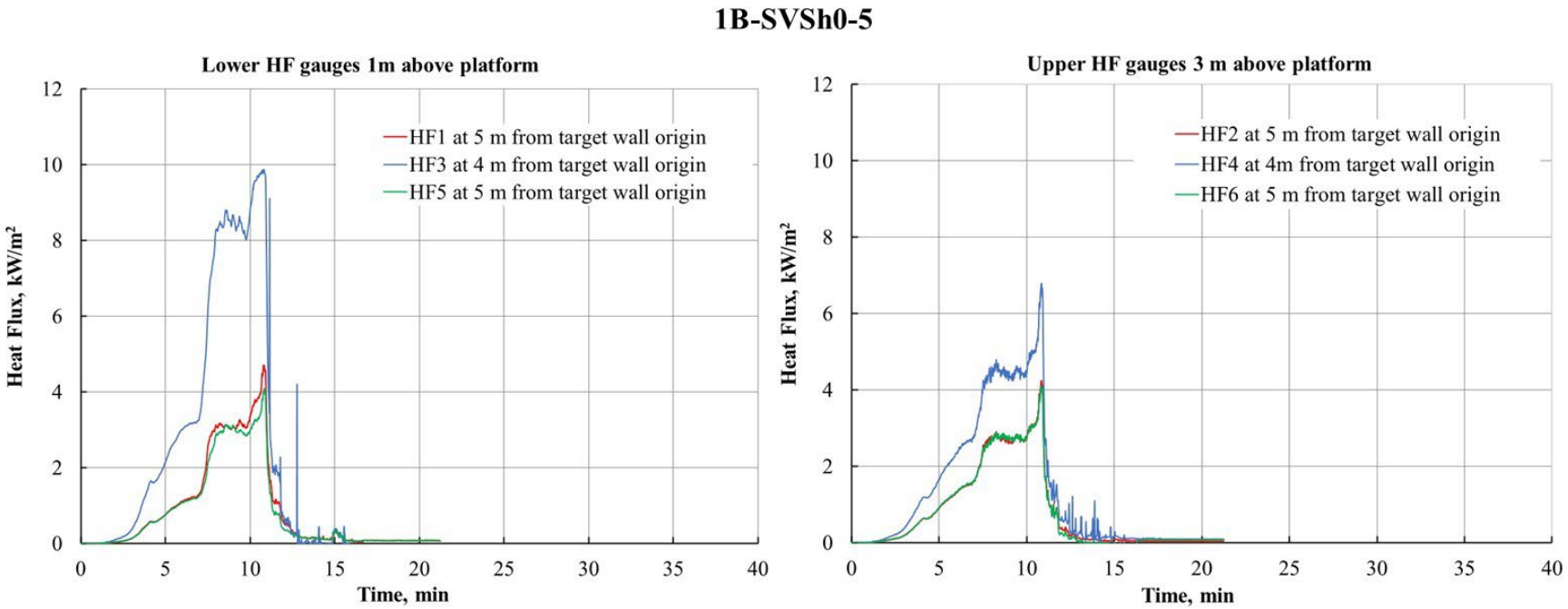

Fig. 95. Heat fluxes as a function of time recorded simultaneously by gauges located on the HFG Rig1, HFG Rig2, and HFG Rig3 placed in the front of the shed in test 1B-SVSh0-5. Standard relative uncertainty is ±3 %.

5.3.4.3. Target Structure Performance

The target structure performance when exposed to radiant and convective heat exposure from a steel Very Small shed with a high fuel loading of 6 wood cribs is shown in Fig. 96. Significant damage to the target structure was observed to be caused by convective flaming exposure as opposed to radiant heating. However, the windowpane cracked due to radiant heating before the flames had contacted the target structure. Ignition of the vinyl window frame followed window cracking, and hot gases and flames were seen penetrating through the broken window. The ignition of the window frame occurred approximately 7 min after the wood crib ignition. The window shutter at the back of the target wall was deployed, and the window shutter was closed to prevent the target wall from igniting on the unexposed side. At this point, the HRR from the burning of the wood cribs approached a peak value of 2 MW. The rafters ignited nominally 10 min after the ignition of the wood cribs, and flame penetration through the vent was noticed at the back of the vent (Fig. 96(b)). The non-flame retardant caulking surrounding the vent failed forming an opening for flame penetration. The intumesced vent and charred cotton batting situated in the vent plenum can be noted from the photograph in Fig. 96(c).

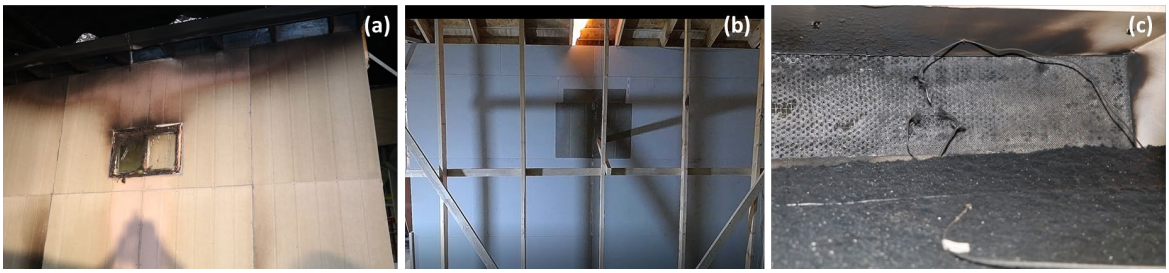

Fig. 96. Photographs showing (a) significant thermal damage to the window frame, cracking of the windowpane, charring of the rafters, (b) flames penetrating through the vent, (c) significant intumescence in the vent (rear), and thermal degradation of cotton batting in the plenum in test 1B-SVSh0-5.

The mechanism of vent operation is discussed based on the temperature-time plot in Fig. 97. The thermocouples located in the front of the vent (TCventF) and at the back of the vent (TCventR) registered nominal temperatures of 400 ºC at about 6.6 min from the ignition of wood cribs. Following such high temperature exposure, the vent cells closed due to intumescence of the coating. Note the significant difference in temperatures recorded by TCventF and TCventR for the period between 7.5 min and 10.2 min in Fig. 97, suggesting that the intumescent coating was effective during this brief period. However, once the rafters ignited, the temperature increased until the suppression of the roof fire began. The temperatures recorded by TCventF began to decrease following the intumescence in the vent, and this could be due to a short circuit in the TC wiring caused by the flames and/or due to the activation of intumescent in the vent. The TCventF temperatures would not be expected to drop during the fire, and the measured peak temperature during the ignition of the rafters is significantly lower than expected in a flaming fire and as measured in previous test (Fig. 82).

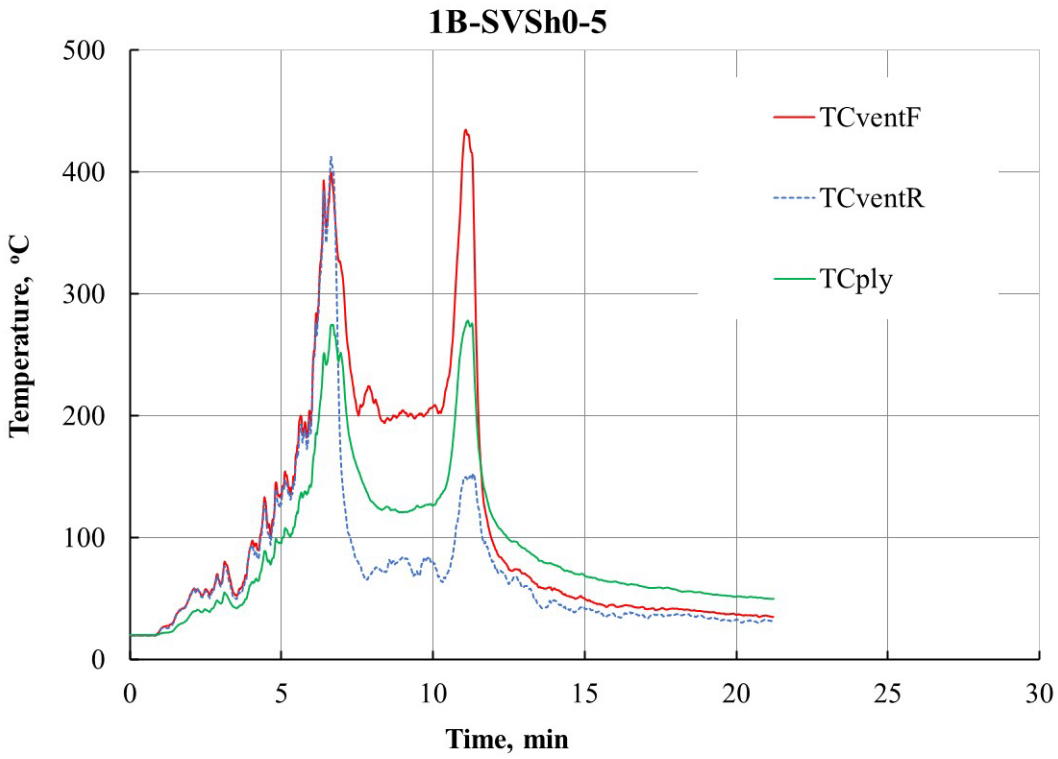

Fig. 97. Temperature-time profiles recorded by TCs in front of the vent (TCventF), behind the vent (TCventR), and on the plywood (TCply) behind the vent in test 1BSVSh-5. Standard relative uncertainty is ± 0.75 %.

5.3.5. Test: 1B-SVSh0-5-R1

5.3.5.1. Shed and Target Specification

The shed, the fuel loading specifications, and the SSD for this test were exactly the same as that used in test 1B-SVSh0-5 described above. However, the target structure was significantly modified in terms of instrumentation. The heat flux gauge rigs were not used in this test. Instead, heat flux gauges were located in the rafter bays as shown in the schematic (Fig. 98) and in the image (Fig. 99) below. One TC was placed near the heat flux gauge in the eave roof in rafter bays N1 and S1, and a TC was added in the vent plenum. The plenum situated behind the central eave vent and under the roof, simulating an attic area, was equipped with negative pressure exhaust fan. A flame retardant caulking was used for installation of the eave vent.

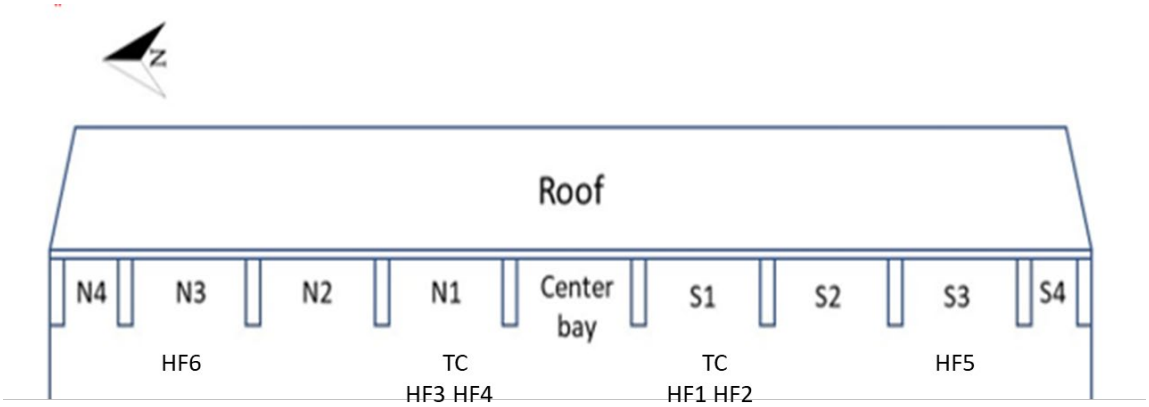

Fig. 98. Schematic showing location of heat flux gauges and TCs in the eaves.

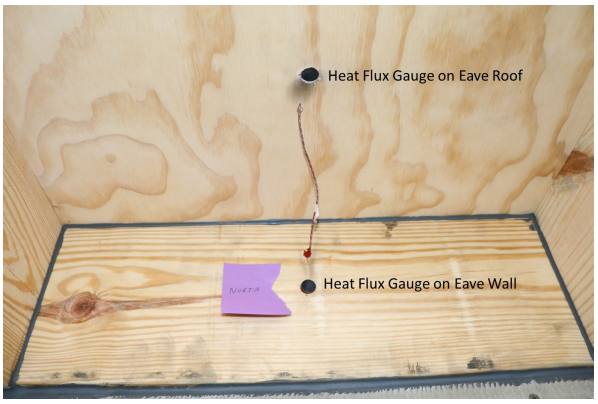

Fig. 99. Photograph showing location of heat flux gauges and a TC in the eave.

5.3.5.2. Burn Overview

The photographs in Fig. 100 show the shed configuration with respect to the target structure and were captured at the times during which the peaks were registered in the temporal plots of the HRR shown in Fig. 101. The burning behavior of the wood cribs within the Very Small steel shed for tests 1B-SVSh0-5 and 1B-SVSh0-5-R1 was very similar except that the ignition of

rafters in the case of 1B-SVSh0-5-R1 was delayed by about 3 min. The comparison of HRR plots of tests 1B-SVSh0-5 and 1B-SVSh0-5-R1 are shown in Fig. 102. The delayed ignition of rafters could be partly attributed to a change in airflow and resultant cooling at the central bay in the presence of a fan in the plenum. Potential differences in the moisture content of the rafters (not measured in this study) on the different days of testing could also result in delayed ignition of the rafters.

The measured heat fluxes in the rafter bays are plotted in Fig. 103 and Fig. 104. Since the door opening of the shed was aligned with the central vent bay, the heat fluxes measured by the gauges located in bays N1 and S1 on either side of central bay recorded higher values (nominally 20 kW/m^2) compared to those recorded in rafter bays N3 and S3 (nominally 10 kW/m^2). However, once the flaming ignition occurred in the rafters, the peak fluxes recorded across the width of the wall were comparable (> 80 kW/m^2). Comparison of heat fluxes measured on the eave wall versus those in the eave roof is shown in Fig. 104. The heat fluxes recorded by the gauges on the wall and on the roof were typically the same.

Fig. 100. Photographs captured from videos recorded by Camera #3 showing (a) steel Very Small shed with door opening facing the target structure, (b) flames from burning of cribs impinging on the target structure, and (c) ignition of rafters in test 1B-SVSh0-5-R1.

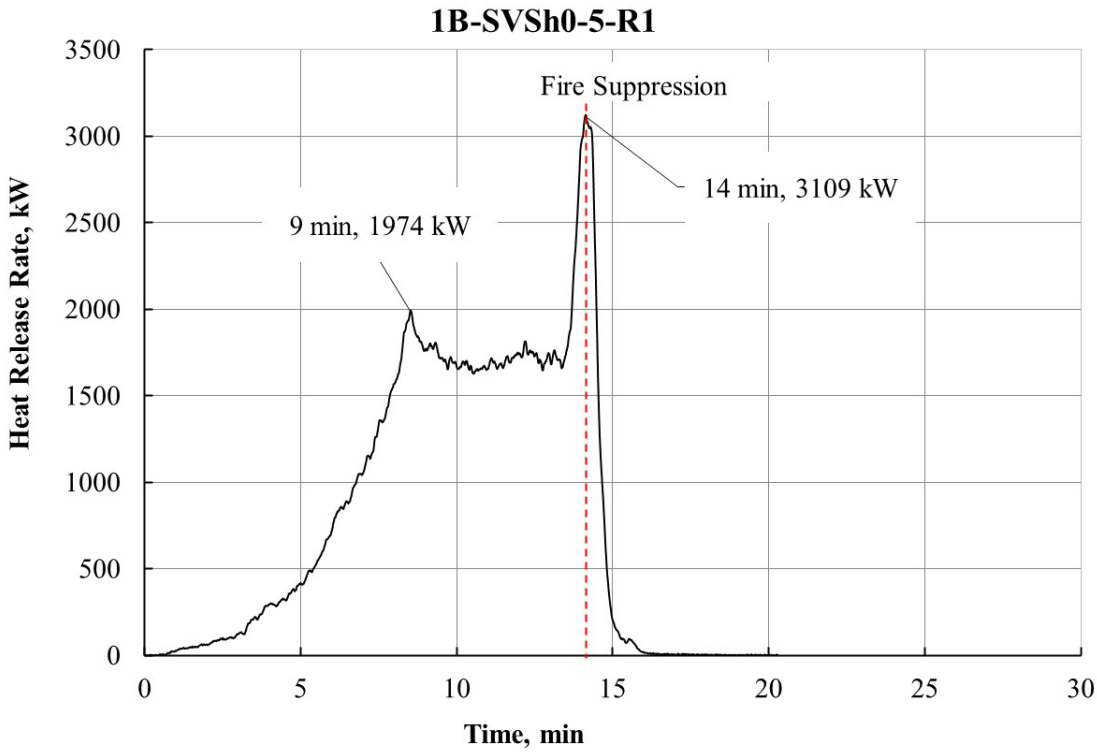

Fig. 101. Temporal profile of heat release rate of combustible mass in test1B-SVSh0-5-R1.

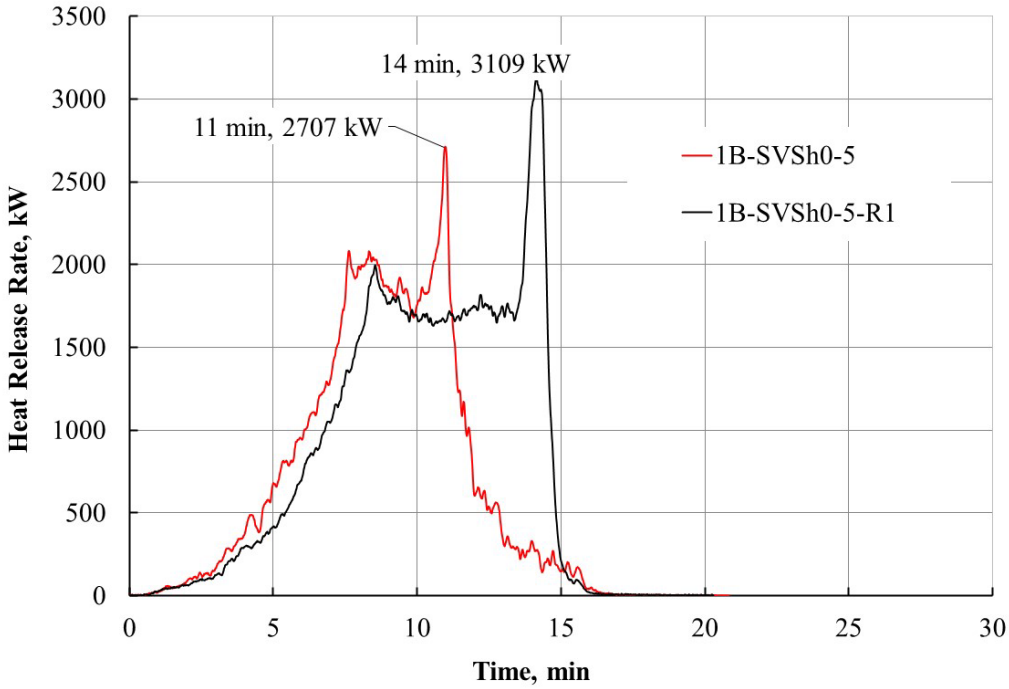

Fig. 102. Comparison of HRR data for test 1B-SVSh0-5 and test 1B-SVSh0-5-R1.

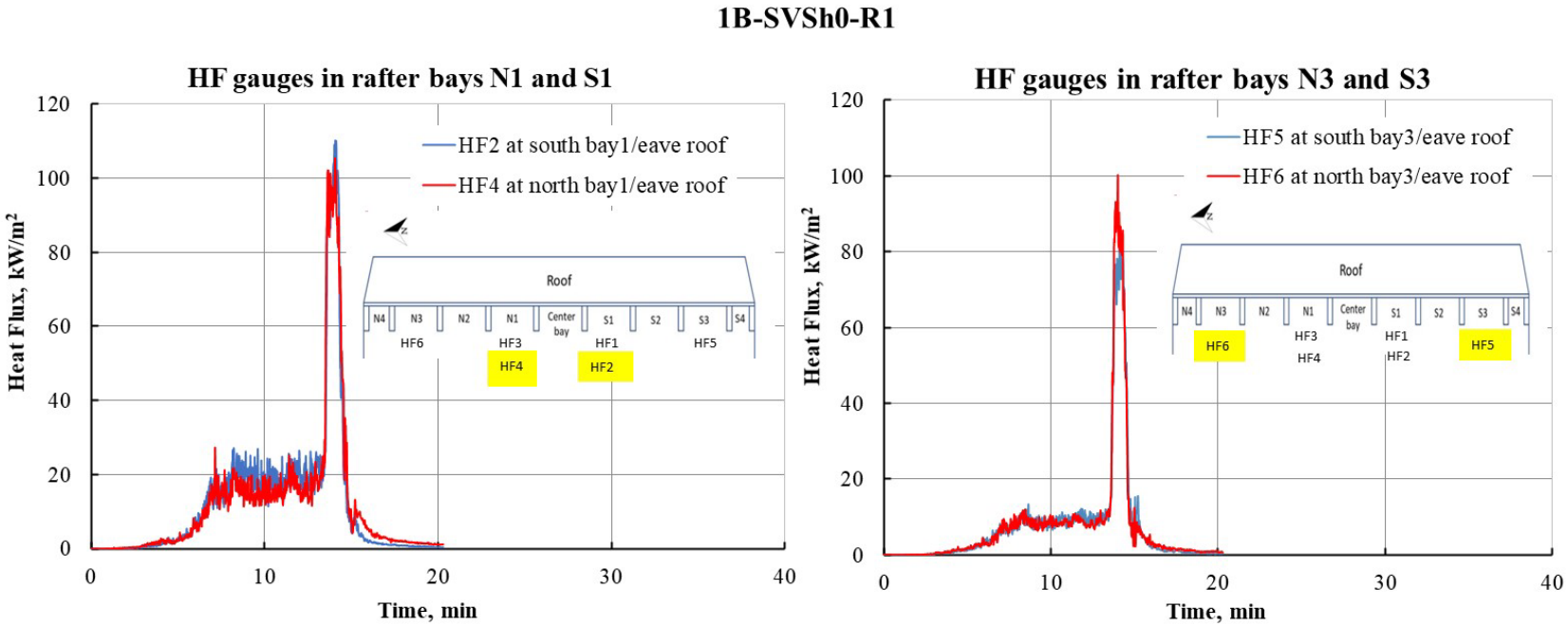

Fig. 103. Heat fluxes as a function of time recorded simultaneously by gauges located on the eave roof of the target structure in test 1B-SVSh0-5-R1. Note: Measurements from the highlighted HF gauges in the insert are plotted. Standard relative uncertainty is ±3 %.

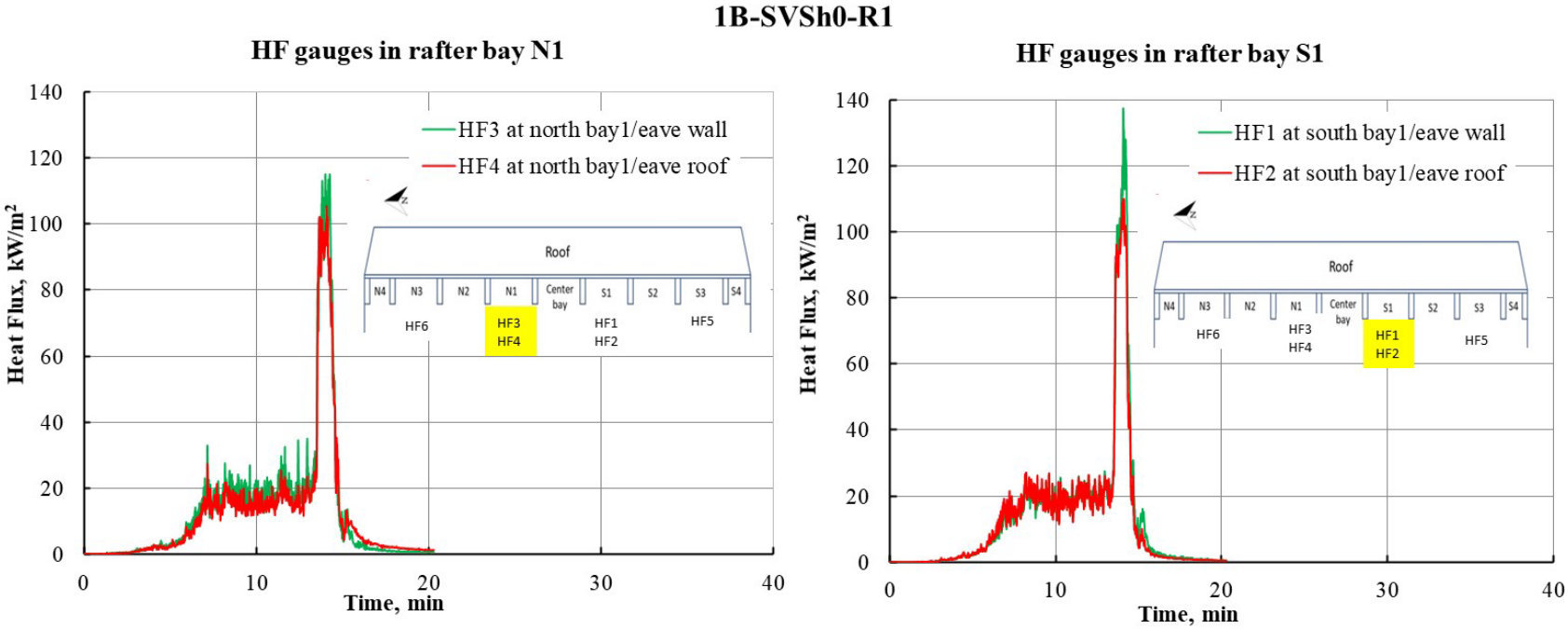

Fig. 104. Heat fluxes as a function of time recorded simultaneously by gauges located on eave wall and eave roof of the target structure in test 1B-SVSh0-R1. Note: Measurements from the highlighted HF gauges in the insert are plotted. Standard relative uncertainty is ±3 %.

5.3.5.3. Target Structure Performance

The performance of the target structure observed during the repeat experiment of test 1B-SVSh0-5-R1 was similar to that noted during test 1B-SVSh0-5. Photographs of target structure damages are shown in Fig. 105. The cracked cement board, charred rafters, and the window failure can be noted in Fig. 105(a), Fig. 105(b), and Fig. 105(c), respectively.

The vent performance, however, was noticeably different from those observed in previous shed and target burn experiments. The performance of the vent when exposed to flaming fire for test 1B-SVSh0-5-R1 can be noted from Fig. 106. The temperature at the front of the vent (TCventF) increased rapidly as the flames from the burning wood cribs started impinging on the target structure. The temperatures on the exposed side of the vent averaged over 350 ºC while average temperatures of 320 ºC were recorded on the unexposed (simulated attic area) side of the vent.

This indicates that intumescent coating did not activate fully as the temperatures on the unexposed side were similar to the front side. Peak temperatures up to 845 ºC were recorded on the exposed side of the vent while temperatures peaked at about 700 ºC on the unexposed side of the vent. According to the ASTM E 2886, the temperatures in excess of 360 ºC on the unexposed side of the vent indicate vent failure. However, partially opened vent cells above the activation temperature of 176 ºC and charred cotton batting seen in Fig. 106 suggest compromised vent performance.

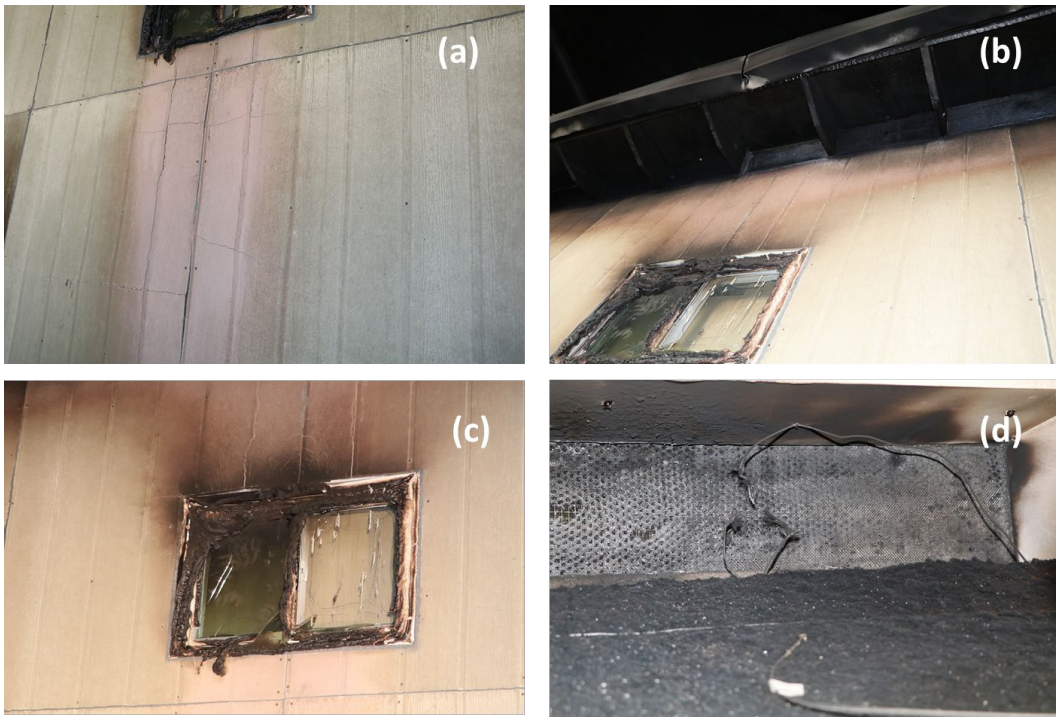

Fig. 105. Photographs showing (a) cracks in cement board due to thermal expansion, (b) significant charring of rafters, (c) significant thermal damage to the window frame, cracking of the windowpane, and (d) significant intumescence in the vent (rear), and thermal degradation of cotton batting in the plenum in test 1B-SVSh0-5-R1.

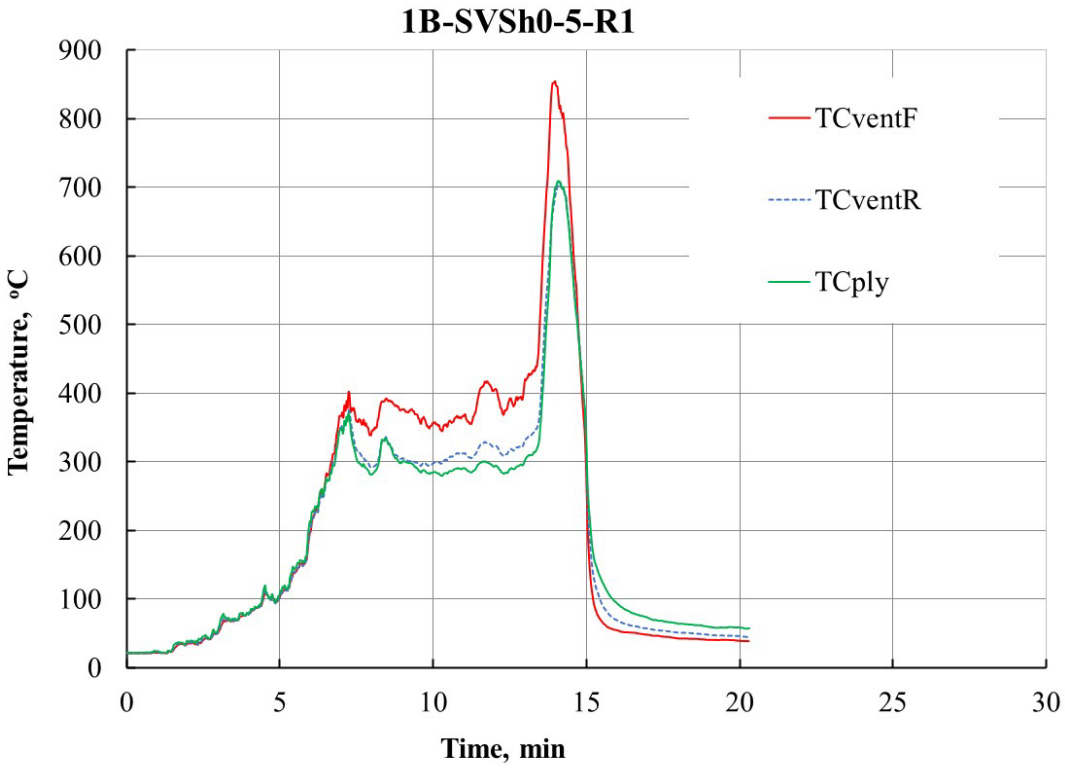

Fig. 106. Temperature-time profiles recorded by TCs in front of the vent (TCventF), behind the vent (TCventR), and on the plywood (TCply) behind the vent in test 1B-SVSh0-0-R1. Standard relative uncertainty is ± 0.75 %.

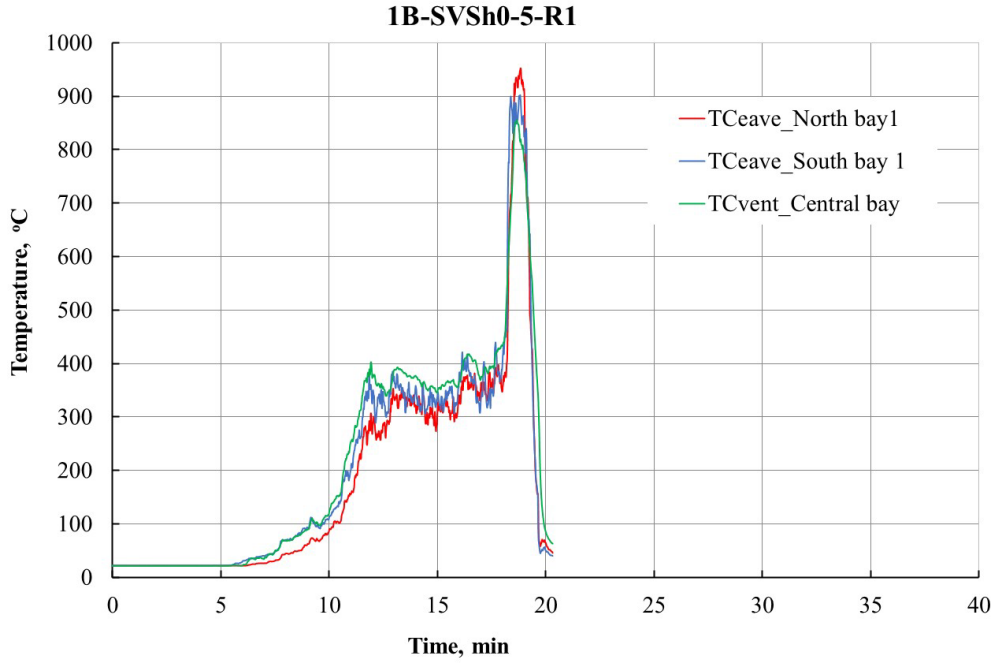

Fig. 107. Temperature-time profiles recorded by TCs in the north, central and south bays in test 1B-SVSh0-0-R1. Standard relative uncertainty is ± 0.75 %.

Temperature-time profiles plotted in Fig. 107 suggests that the temperatures in the north, central, and south bays were very similar and followed the same time dependencies.

5.3.6. Test: 1B-WC00-0

5.3.6.1. Shed and Target Specification

The wood Closet used in this test was slightly different from the one used in test 1B-WCl0-0. The mass of the Closets varied by 5 kg, and the Closet in this test had a ventilated partition at the center. No wood cribs were used in this test. The Closet was ignited using two pans with 300 mL of heptane, one on each side of the partition.

The target structure specifications were similar to the test 1B-SVSh0-5-R1, except that the DensGlass® sheathing was not used in the wall assembly to see if the OSB would ignite.

5.3.6.2. Burn Overview

The wood Closet with zero fuel loading exhibited rapid fire spread within the source structure and to the target structure. The stages of flame spread are shown in Fig. 108, and the temporal plot of HRR for the wood Closet is shown in Fig. 109. Following the ignition of heptane, the rapid flame spread within the source structure led to flashover (see Fig. 108 (b)) at approximately 2.5 min, giving a PHRR of 2772 kW (see Fig. 109). During peak burning the flame lengths were sufficiently high to reach above the window. Subsequently, the burning of the Closet subsided as shown in Fig. 108(c), and the HRR dropped significantly. However, as the flames travelled to the outer surfaces of the Closet, the HRR began to rise. At this time, the source structure began to collapse, and burning of the remainder of the Closet became intense due to availability of excess oxygen. This intense burning resulted in the second peak (1519 kW) in the HRR curve as shown in Fig. 109.

The Closet was allowed to burn completely, and no suppression was required as the target structure did not ignite. A comparison of HRR profiles for wood Closet with low fuel loading and no fuel loading is shown in Fig. 110. WCl0-0 was extinguished so there cannot be comparison between the curves after 8 min.

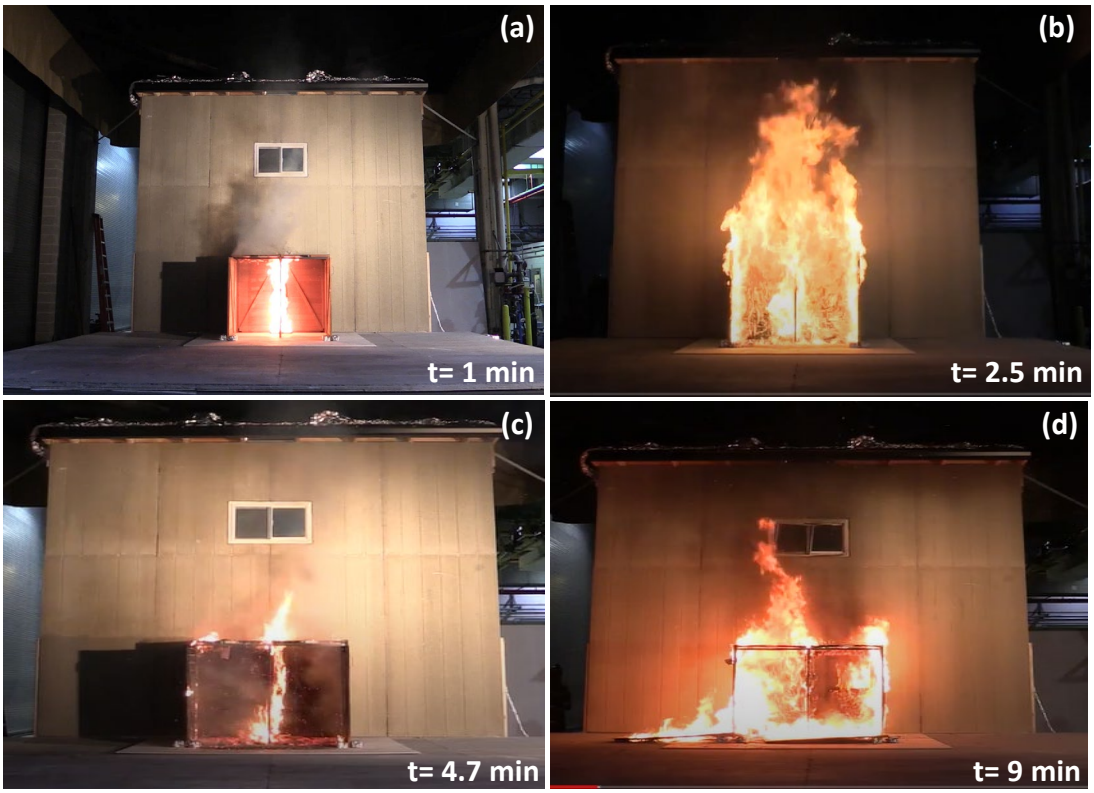

Fig. 108. Photographs captured from videos recorded by Camera #1 showing (a) heptane burning within the wood Closet with door opening facing away from the target structure, (b) intense burning of wood Closet at the time of 1st peak HRR, (c) marginal burning of the Closet after interior flashover, (d) flame spread to the side walls and the door panels in test 1B-WC00-0.

The measurements from the heat flux gauges in the rafter bays is plotted in Fig. 111 and Fig. 112. The heat fluxes recorded for the wood Closet with a total combustible mass of 56 kg were significantly lower than that recorded for test1B-SVSh0-5-R1 which had a total combustible mass of 116 kg. The heat flux gauges in the eave wall and eave roof recorded similar heat fluxes.

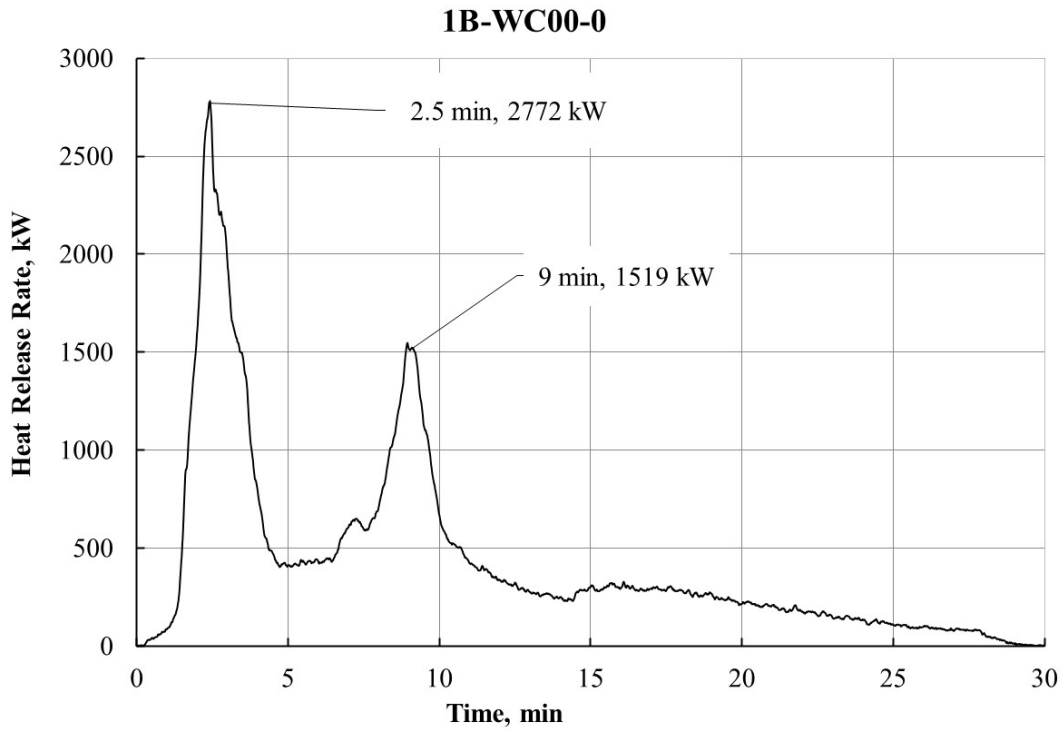

Fig. 109. Temporal profile of heat release rate of combustible mass in test 1B- WC00-0.

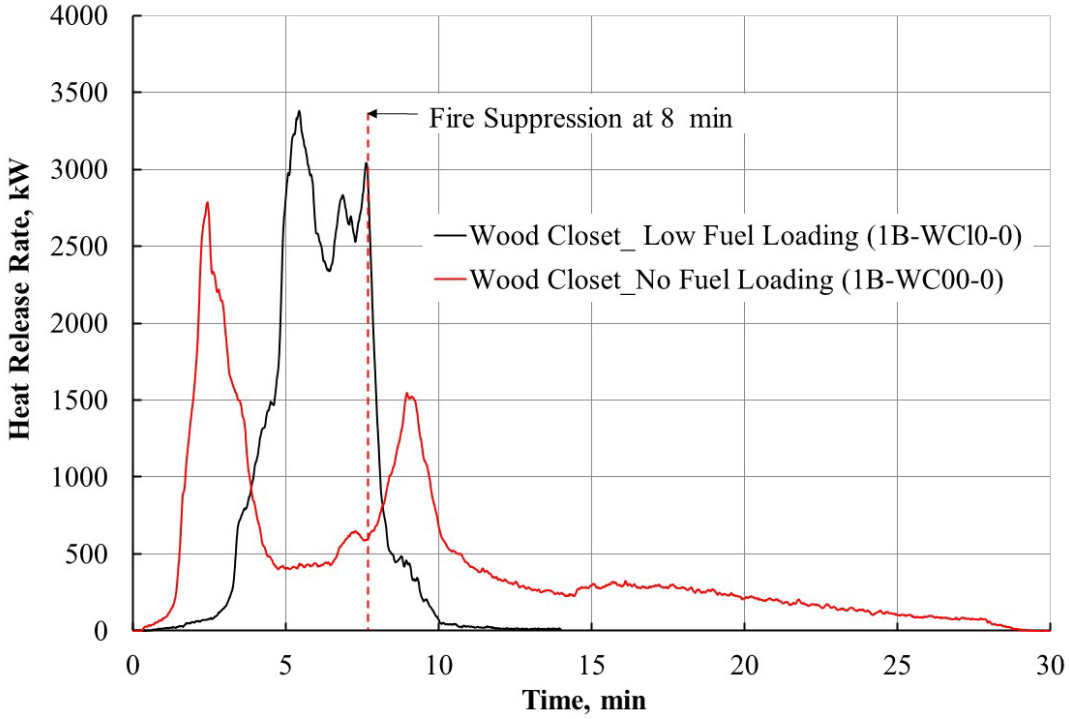

Fig. 110. Comparison of HRR plots for test 1B-WCl0-0 and test 1B-WC00-0. Note: Suppression occurred at 8 min in test 1B-WCl0-0

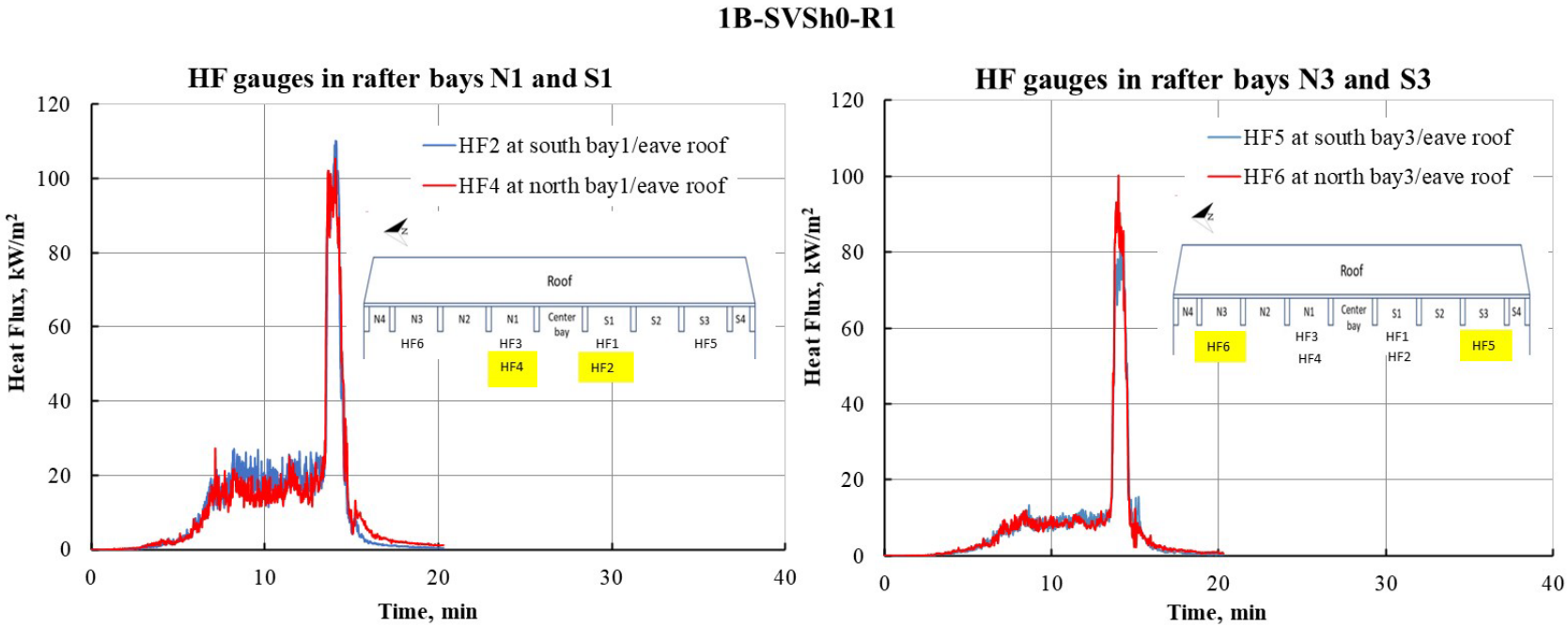

Fig. 111. Heat fluxes as a function of time recorded simultaneously by gauges located on eave roof of the target structure in test1B-WC00-0. Standard relative uncertainty is ±3 %.

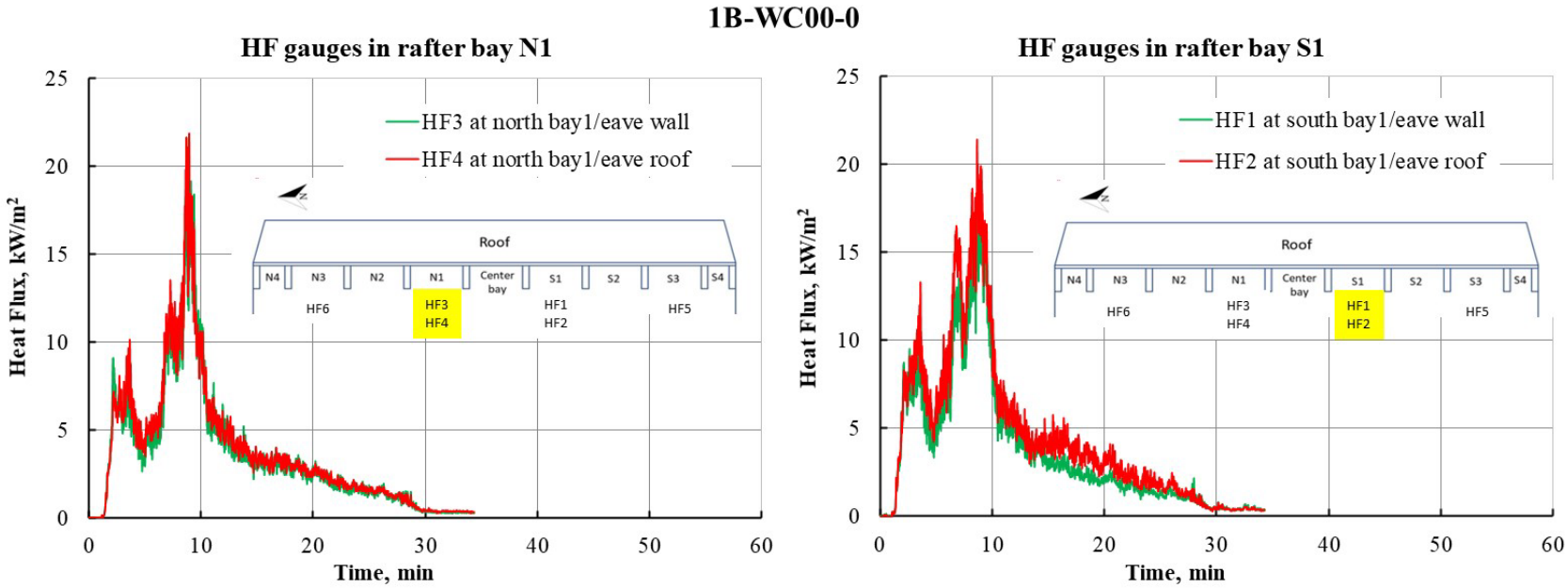

Fig. 112. Heat fluxes as a function of time recorded simultaneously by gauges located on eave wall the target structure in test 1B-WC00-0. Standard relative uncertainty is ±3 %.

5.3.6.3. Target Structure Performance

The photographs of the target structure performance are shown in Fig. 113. The damage to the exterior cement board was localized where the Closet was in close proximity to the target structure. The cracking of the cement board is shown in Fig. 113(a). Removal of the exterior cement board revealed significant charring of the OSB (Fig. 113(b)). The window frame melted and charred due to excessive heating, and the screen from the window fell off. However, there was no cracking of the windowpane. Deformation of the window frame due to melting and charring is shown in Fig. 113(c).

The performance of the vent can be noted from the images in Fig. 113(d) and Fig. 113(e). It is evident (d) that the intumescent coating was activated and that the vent cells partially closed. The cotton batting placed in the simulated attic area remained undamaged and very little, if any, thermal damage to the cotton batting can be noted from the photograph in Fig. 113(e). Temperature-time profiles provided in Fig. 114 show similar temperature data recorded by all three TCs in the vent, suggesting that the vent cells did not close efficiently. A comparison of temperature-time profiles for the north, central, and south bays in Fig. 115 also shows similar temperature data.

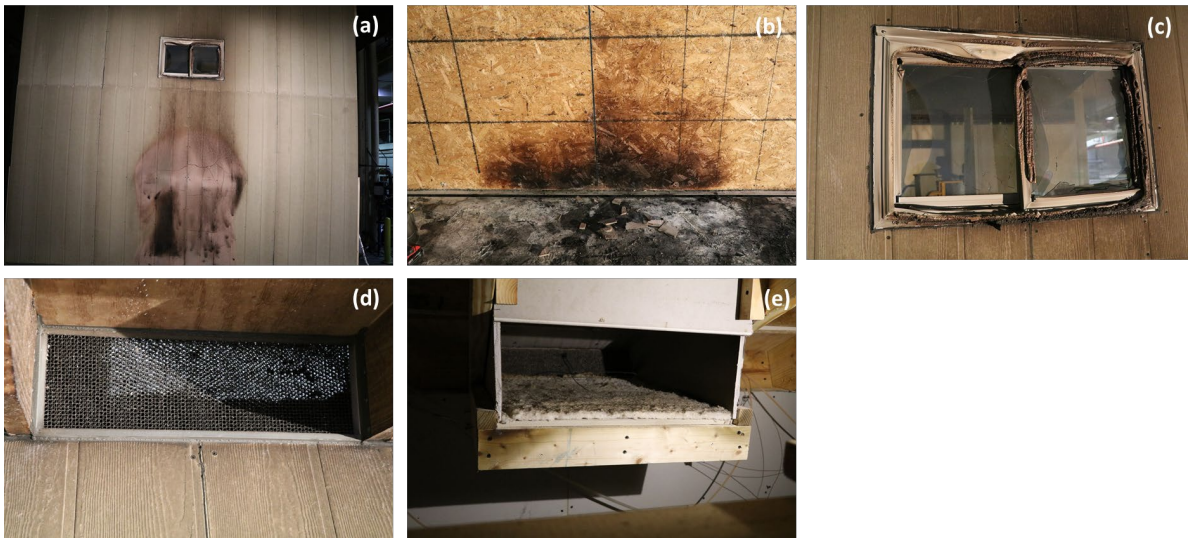

Fig. 113. Photographs showing (a) thermal damage to the exterior layer (cement board), (b) charring of OSB, (c) windowpane cracking and melting of vinyl frame, (d) partial intumescence in the vent (front), and (e) partial discoloration of cotton batting in the plenum during test 1B-WC00-0.

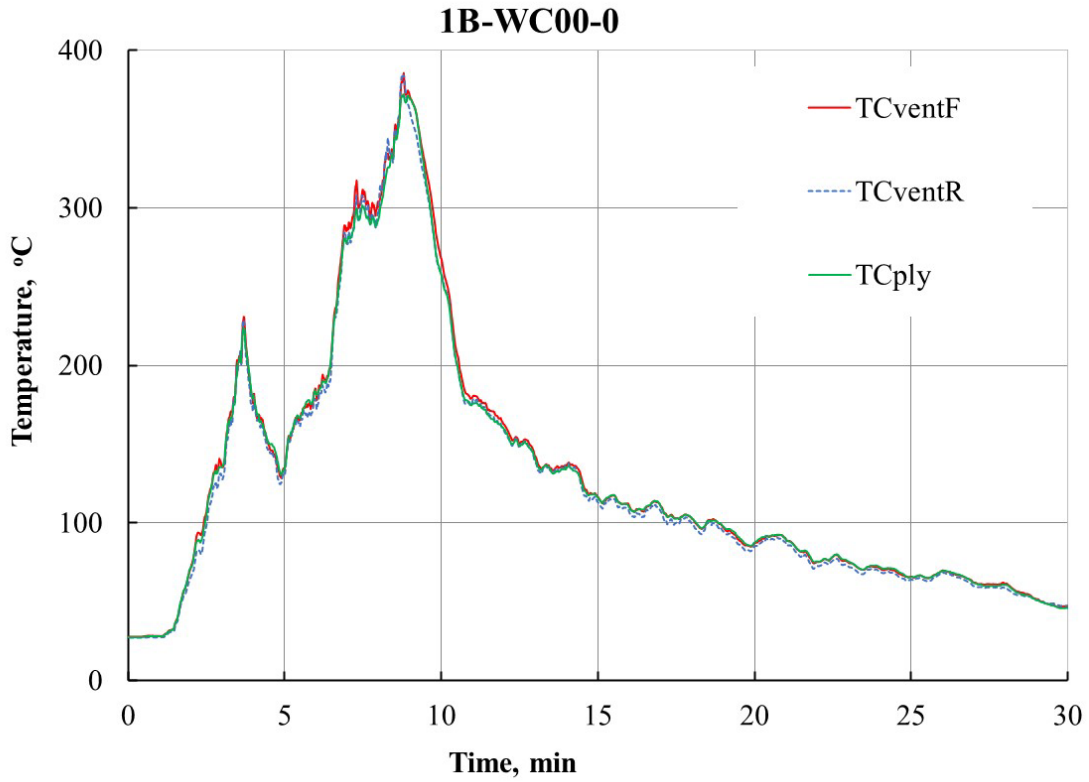

Fig. 114. Temperature-time profiles recorded by TCs in front of the vent (TCventF), behind the vent (TCventR), and on the plywood (TCply) behind the vent in test 1B- WC00-0. Standard relative uncertainty is ± 0.75 %.

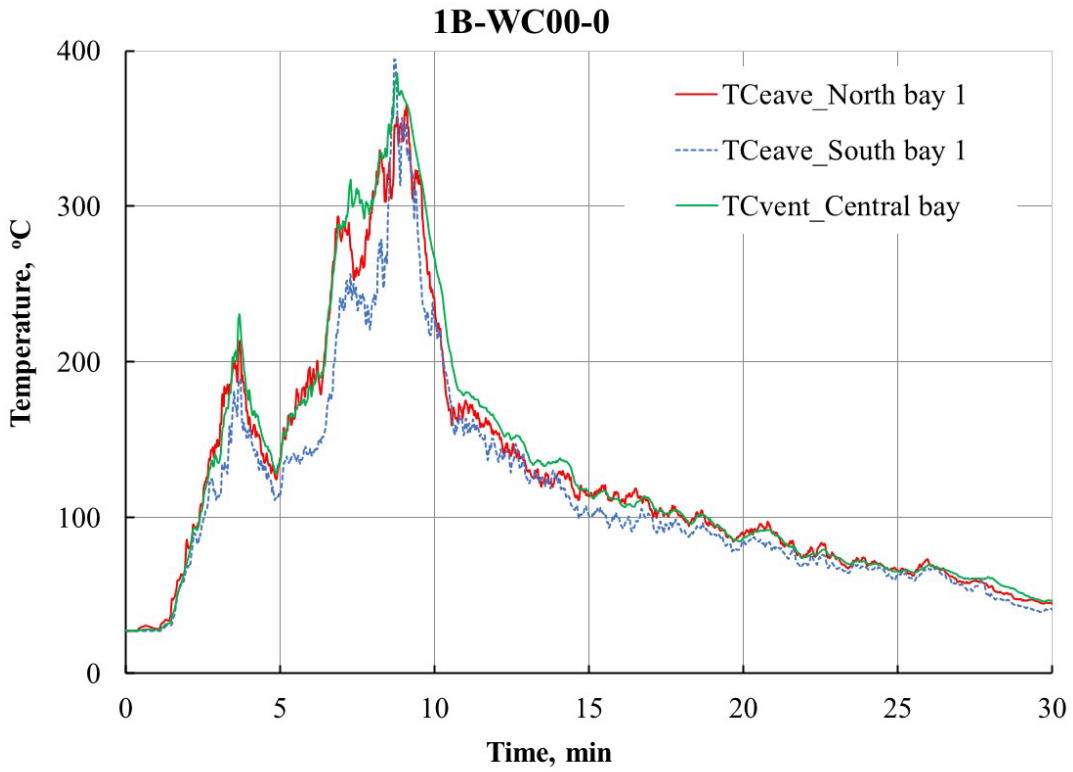

Fig. 115. Temperature-time profiles recorded by TCs in the north, central and south bays in test1B-WC00-0. Standard relative uncertainty is ± 0.75 %.

5.4. Technical Findings

5.4.1. Eave Performance

Eaves are protruding parts of the roof that are vulnerable to radiant heat and flame impingement. Open eaves (see Fig. 116) made from combustible materials have been consistently reported as a weak link that leads to structural losses in WUI communities [13]. It is important to prevent structure ignitions as unattended ignitions can result in complete structure destruction. This study used open eaves construction made from combustible wood as a worst-case scenario to assess the effects of radiative and convective heat exposures from the source structure.

Fig. 116. Photograph of a target structure showing eaves, eave vent, and window.

In this experimental series, the heat fluxes in the rafter bays were measured in the last two tests to determine the critical heat flux at which the eaves would ignite. Heat flux gauges were placed on the sides of the central bay where the eave vent was located. This was done so that the performance of the eave vent assembly was not affected. Since the HF data was collected on either side of the central bay, the heat flux values are likely lower than the incident peak heat fluxes at the center. The limited data in these tests suggests that heat fluxes of approximately 15 kW/m² for at least 5 min resulted in the ignition of eaves (Fig. 103 and Fig. 104). These conditions were observed in test 1B-SVSh0-5-R1. In test 1B-WC00-0, a wood Closet with an SSD of 0 ft and no fuel loading, the heat fluxes in the rafter bays peaked at 20 kW/m² but only for a short duration of 5 s (see Fig. 111 and Fig. 112) and was not sufficient to cause ignition of the eaves.

5.4.2. Wall Performance

As described in Section 5.2.1, the target wall was constructed well above the minimum requirements specified by the California Building Code. Chapter 7A of the California Building Code specifies a test method (SFM-12-7A-1) for assessing the performance of exterior wall assemblies exposed to direct flames. Assessing wall performance was not a primary objective of this study. Nonetheless, according to test method SFM-12-7A-1, a wall assembly meets test

requirements if no flame penetration is observed through the wall assembly and there is no evidence of glowing combustion on the unexposed side of the assembly.

Local damage to the cement board was observed, and the intensity of cracking and/or spalling was a function of shed construction, fuel loading, shed orientation and SSD. In the presence of the gypsum sheathing, no thermal damage to the OSB was observed. However, for test 1B-WC00-0 without panel sheathing and zero fuel loading in the wooden shed, significant charring of the OSB (see Fig. 113b) behind the cement board was observed. This wall damage occurred with the smallest fuel package of the experimental series (wood closet without any fuel loading). This finding suggests that the extra layer of panel sheathing included in the exterior wall construction is necessary to prevent the ignition of OSB given the exposures from the source structures with combustible fuel in the SSD configuration evaluated (i.e. SSD = 0). While sheathing provides protection to the wall, other vulnerabilities remain as identified in these experiments.

5.4.3. Window Performance

As mentioned earlier, the annealed glass windows used in this study represent pre- Chapter 7A construction. Window failures from exposure to radiant and convective heat can be clearly noted from Fig. 117. In all four tests where the flames from the source structure were in contact with the window frames, melting and thermal deformation of the frames can be noted. Cracking of the glass occurred, but the broken glass remained in place. Glass was broken in bigger pieces which is characteristic of annealed glass breakages. Window failures were observed in experiments with wood Closets with zero structure separation distance (SSD = 0) and for Very Small steel sheds with high fuel loadings. The Very Small steel shed door opening was facing the target wall with a structure separation distance of 5 ft (SSD = 5 ft). No visible damage to the windows was observed for tests 1B-SCL0-0 and 1B-SCh0-0 where the door opening of the noncombustible source structure was facing away from the target structure.

Window failures in this limited test series indicate that with given exposure from the source structure, the primary structure would be compromised. The broken glass would likely be displaced in the presence of wind, thereby forming an opening for embers and flames to enter the structure.

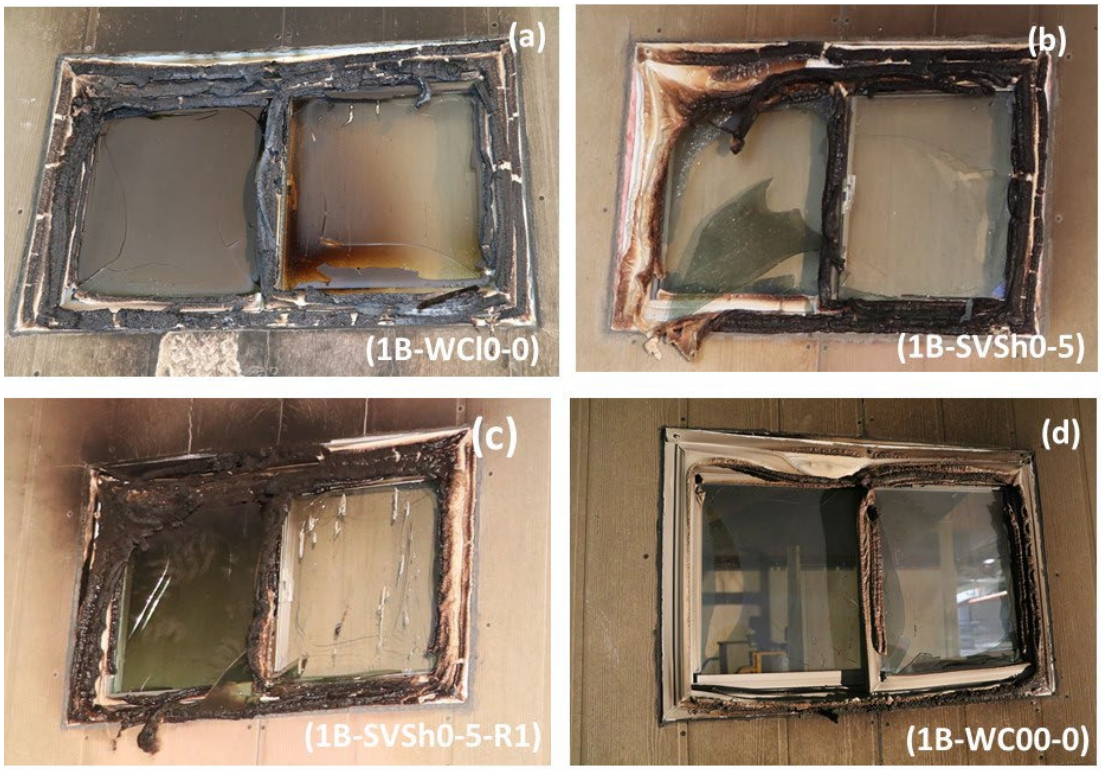

Fig. 117. Window performance during tests (a) 1B-WCl0-0, (b) 1B-SVSh0-5, (c) 1B-SVSh0-5-R1, and (d) 1B-WC00-0.

5.4.4. Vent Performance

This limited test series assessed the performance of attic vents when exposed to combustible and noncombustible Closets and Very Small sheds with varying fuel loads under no wind conditions. The post-fire images of the vents are shown in Fig. 118, and the maximum temperatures recorded at the vent for different exposure conditions are provided in Table 15. Highlighted in Table 15 are the peak temperatures on the unexposed side of the vent indicating vent failures per ASTM E 2886.

For combustible wood Closets (test 1B-WCl0-0 and test 1B-WC00-0), the radiant and convective heat exposure was sufficient to raise the gas temperature at the vent above 176 ºC and activate the intumescent coating on the honeycomb core. However, the intumescent coating was not effective to block the heat; temperatures in excess of 380 ºC were recorded on the unexposed side of the vent. The temperature of the plywood in the simulated attic space exceeded the ignition temperature of wood (260 ºC) [5], suggesting that the glowing ignition of plywood may occur with prolonged exposures.

[5] Ignition temperature of wood as measured by ASTM D1929.

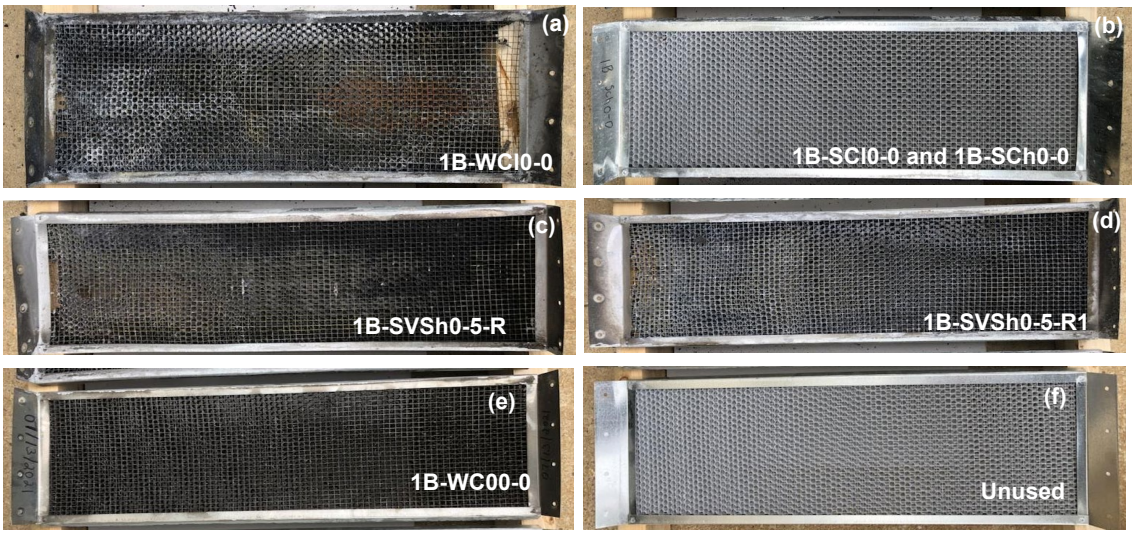

Fig. 118. Photographs of vents showing effects of thermal exposure compared to the unused vent in (f).

The radiant and convective heat exposure were significantly lower with noncombustible Closets (test 1B-SCl0-0 and test 1B-SCh0-0), with the door-opening facing away from the target wall, keeping the temperatures in the vent area well below the activation temperature of the intumescent coating. However, for the Very Small steel shed with door-opening facing towards the target wall and with an SSD = 5 ft (test 1B-SVSh0-5 and test 1B- SVSh0-5-R1), the vents were exposed to significant radiant and convective heat. While the intumescence mechanism activated during such high heat exposures, the protective barrier thus formed was not effective for a longer duration of exposures. The performance of these vents cannot be interpreted as failures with respect to the standard test method (ASTM E 2886) as the thermal exposures to the vents were significantly different than those specified in the standard. The standard test method (ASTM E 2886) specifies exposure of vents to flaming fire with HRR of 300 kW ± 10 kW for 10 min.

Table 15. Maximum measured temperatures at the vent during thermal exposures from burning sheds.

Test ID	Material	PHRR, MW	Maximum measured temperature at the vent[§], ºC					
			TCventFront		TCventBack		TCplyBack	
			Peak 1	Peak 2	Peak 1	Peak 2	Peak 1	Peak 2
1B-WCl0-0	Wood	3.38	952	—	394	425	265	310
1B-SCl0-0	Steel	0.89	58	—	55	—	46	—
1B-SCh0-0	Steel	1.40	116	—	101	—	72	—
1B-SVSh0-5	Steel	2.71	400	434	153	413	275	278
1B-SVSh0-5-R1	Steel	3.11	403	855	376	704	371	709
1B-WC00-0	Wood	2.77	386	—	384		372	—

[§]Standard relative uncertainty is ± 0.75 %.

When subjected to high heat exposures as those seen in this test series, the vent performance is likely related to 1) the intensity of source fire, 2) local fire plume velocities, and 3) airflow through the vent. The intensity of the source fire is a function of construction material, fuel loading, source structure orientation, and SSD. The airflow through the vent is impacted by specific attic venting system. This requires further investigation and specific experiments are planned to assess vent performance for varying back-pressure conditions (attic pressure).

5.4.5. Summary of Shed and Target Structure Technical Findings

This experimental series investigated the effects of thermal exposures from combustible (wood) and noncombustible (steel) sheds on a target structure in the absence of wind. Generally, the factors contributing to the fire hazard of the sheds include:

1. Construction material of the shed,
2. Fuel loading,
3. Shed orientation (door opening), and
4. Structure separation distance.

Based on the construction materials, the sheds can be primarily classified into combustible and noncombustible sheds. If the contents of the combustible shed ignite, as frequently occurs in WUI fire events, the fire can spread and consume the shed as shown in test 1B-WCl0-0. Furthermore, the thermal exposure from such a source fire ignited the eaves of a nearby primary structure, and the fire subsequently spread to the roof. The eave vent failed to prevent flames from penetrating to the unexposed (interior) side. The window frame melted and deformed while the annealed glass cracked. Thus, significant damage to the target structure was noticed. A noncombustible steel Closet with similar size and fuel loading in test 1B-SCl0-0 contained the fire within the source structure, and the damage to the target structure was negligible.

The construction materials contribute significantly towards the total combustible fuel. Fuel loading is particularly critical for combustible sheds. As shown in test 1B-WCl0-0 and test 1B-WC00-0, additional low fuel loading (of two 1-A cribs) resulted in thermal exposures that led to target structure ignition. With a zero SSD, a combustible Closet with no contents can cause significant damage to the target structure (1B-WC00-0). On the contrary, increased fuel loading in case of a noncombustible steel Closet from two 1-A cribs (1B-SCl0-0) to four 1-A cribs (1B-SCh0-0) did not affect the target structure noticeably. However, shed orientation and door opening are critical. The door opening for the noncombustible steel sheds in test 1B-SCh0-0 and test 1B-SCl0-0 was facing away from the target structure resulting in less thermal exposure to the target structure. The effect of shed orientation and the door opening was further assessed in test 1B-SVSh0-5. The door opening of the Very Small shed was facing the target structure with an SSD of 5 ft. In the open-door configuration, the thermal exposure from the wood crib fire was significant and resulted in fire spread to the target structure. The observations from the indoor shed burn experiments, test 1B-WC00 suggests that combustible sheds pose a significant fire hazard even if they have no combustible contents.

For noncombustible steel sheds, which maintain structural integrity throughout the burn, the fire plume jets out from the opening (door), thereby channeling radiant and convective heat in a certain direction. This jetting effect has a high potential to spread fire and is particularly hazardous in high density communities or areas with low SSDs. The plume length and incident heat fluxes on the target structure will depend on the fuel loading and size of door opening. The particular hazard of the noncombustible steel shed (test 1B-SVSh0-5) in a high-density housing area is illustrated in Fig. 119. The arrow in Fig. 119 indicates direction of plume jetting out from the noncombustible steel shed.

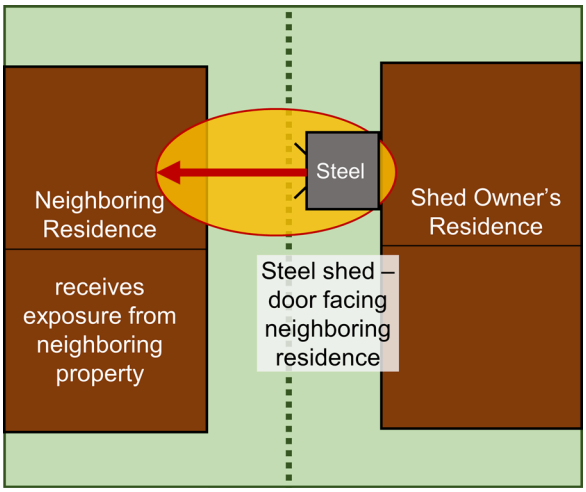

Fig. 119. Schematic illustrating fire hazard from a noncombustible steel shed in a high-density housing.

6. Outdoor Shed Burn Experiments without Wind

6.1. Test Objectives

The main objective of the outdoor shed burn experiments was to estimate HRR of larger sheds that could not be tested under the 10 MW calorimeter at the NFRL. The HRR of burning Medium (M), Large (L), and Very Large (VL) sheds was estimated from the mass loss rate using a large weighing platform specifically designed and constructed for this project. These outdoor shed burn experiments measuring mass loss rate were performed without an artificially generated wind field, similar to the indoor shed burn experiments. However, it was very difficult to achieve zero ambient air movement during the outdoor shed burn experiments. Generally, ambient wind conditions < 3 m/s (6.7 mi/h) were recorded. Thermal exposures from the source structure (shed) to potential nearby target structures were quantified by measuring heat fluxes at heights, orientations, and distances representative of components of a target structure (i.e., single-family residence). The locations of the heat flux sensors represented the fascia board, under-eave, and a window on the target structure.

6.2. Experimental Configuration

The outdoor free shed burn experiments were conducted at IBHS on the concrete pad outside the test cell. The aerial view of the test area with the placement of the weighing platform and the source structure (shed) is shown in Fig. 120. Fig. 121 shows the photograph of the experimental setup for the outdoor free shed burn experiment. The shed openings were oriented to face north.

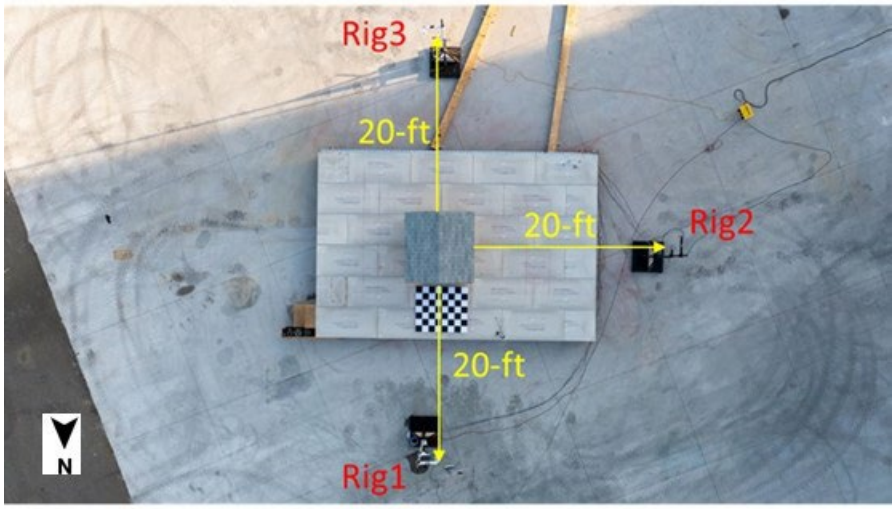

Fig. 120. Aerial view of test area, outside of the IBHS test chamber showing a shed on the weighing platform and heat flux sensor rig placement relative to the shed.

Fig. 121. Photograph showing experimental setup for outdoor free shed burn testing at the IBHS test facility. The photograph shows a shed on the weighing platform and the heat flux gauge rigs.

6.2.1. Data Acquisition and Instrumentation

The section below provides a detailed description of the instrumentation used for the outdoor free shed burn experiments at the IBHS test facility.

6.2.1.1. Weighing Platform

In order to measure the mass loss rate of a shed during combustion, a weighing platform with nominal dimensions of 24 ft × 36 ft × 2 ft was designed and fabricated at IBHS. The construction details of the weighing platform are shown in Fig. 122. Two 36 ft (11 m) long steel I-beams were placed 24 ft apart and connected with steel joists. Each end of the steel joist was hung from a steel I-beam with a S-shaped tension and compression load cell. The top ends of the load cell were attached to the steel I-beam, and the lower ends were attached to the steel joists. A total of 38 load cells were used. Aluminum tubes with rectangular cross-section were placed on the framework of cold-formed steel joists to form a base for the weighing platform. Type B metal decking was placed on rectangular aluminum tubes. The B-decking was covered with two layers of drywall and a top layer of cement board.

The weighing platform was calibrated using NIST-certified weights in steps of 50 lb and 500 lb. The weights were placed at the center of the platform, nominally in the area that the shed would be placed during the experiments. The calibration curves provided in Appendix B show the relationship between actual mass and measured mass.

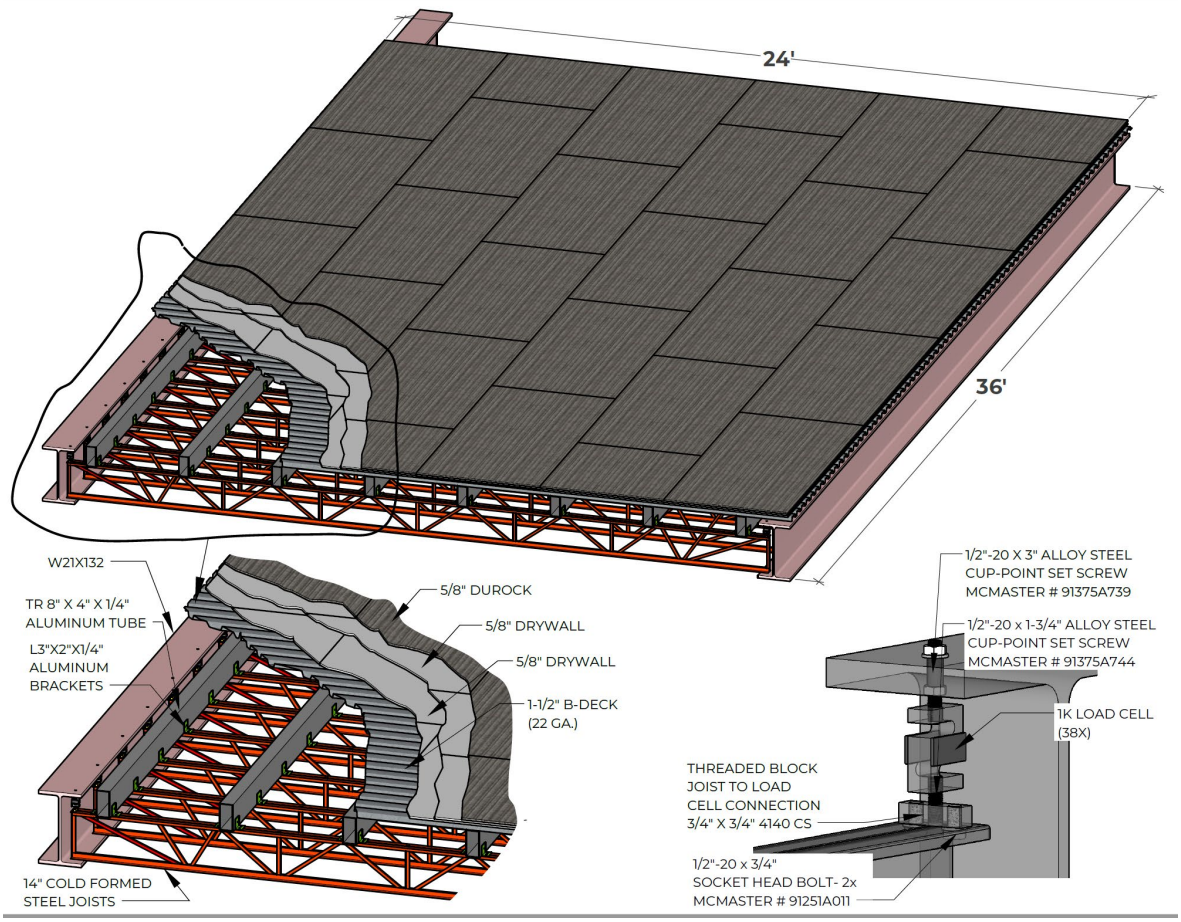

Fig. 122. Weighing platform construction details.

6.2.1.2. Surrogate Target Structure (Heat Flux Rig) Specifications

Water-cooled heat flux gauges with combined Gordon and Schmidt–Boelter configurations were used for measuring incident heat fluxes in a measurement range of up to 200 kW/m^2. Three rigs (Rig1, Rig2, and Rig3) were each equipped with three heat flux gauges positioned to represent surrogate target structures. HF1 was positioned at eave height oriented to face the shed, representing fascia material. HF2 was at eave height oriented to face the ground, representing exposed under-eave. HF3 was at window height oriented to face the shed, representing window glass. The design of the surrogate target structure was based on the dimensions of the single-story residential structure shown in Fig. 123.

The schematic in Fig. 124 shows the placement of the surrogate target structure with respect to the shed and the weighing platform. Fig. 120 shows an aerial image of the experimental setup with the placement of heat flux gauge rigs with respect to the source structure. The rigs were placed at a distance of 20 ft from the outer surface of the shed wall. Rig1 was situated in front of the primary door, Rig2 was on the side, and Rig3 was at the rear end of the shed.

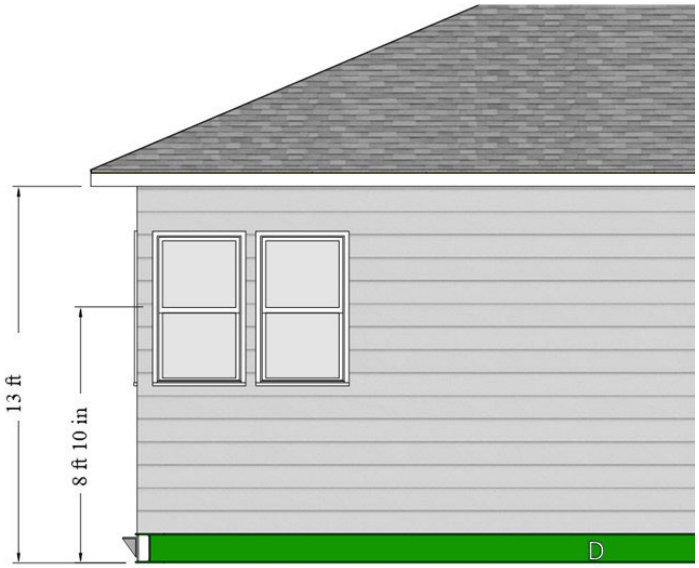

Fig. 123. Drawing showing window and eave heights for a single-story residential structure.

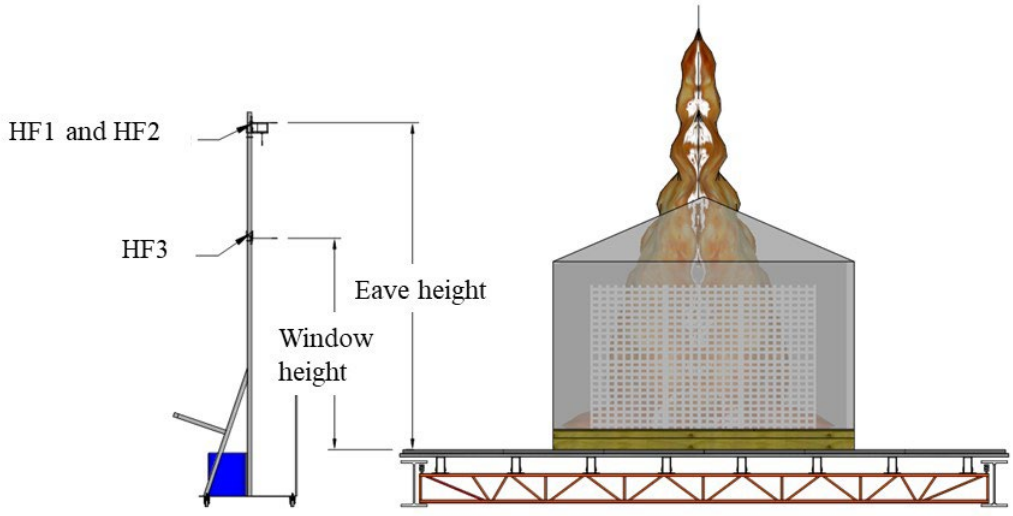

Fig. 124. Schematic showing shed placement on weighing platform and surrogate targets corresponding to the fascia board, under-eave, and window heights for a single-story residential structure.

6.2.1.3. Video cameras

Four high-speed video cameras (Sony CX405) were placed around the shed at a distance of 70 ft to record the fire development. A drone also recorded the shed burn experiment from different heights and positions depending on the wind and fire plume conditions.

6.2.1.4. Crib Specifications

Larger-sized cribs (6-A cribs) were used for the outdoor shed burn experiments compared to 1-A cribs used for indoor shed burn experiments. The crib specification was based on UL 711 (Standard for Safety Rating and Fire Testing of Fire Extinguishers) type 6-A cribs. The cribs were assembled at IBHS with pre-cut (3 ft long) 2 in × 2 in members. Each crib was constructed using 230 members, 23 layers with 10 members each. The nominal exterior dimensions of the crib were 3 ft × 3 ft × 2 ft 10 ½ in. The nominal mass of each crib was 144 kg ± 6 kg (318 lb ± 14 lb).

6.2.1.5. Test Procedure

The test procedure for each of the six experiments was nominally the same. On the day of the experiment, the weighing platform was zeroed for the baseline static weight of the platform. The shed was placed on the platform, followed by the specified number of cribs. Wood cribs were arranged inside the shed to capture the steady-state mass by the weighing platform. The total number of cribs was based on the desired fuel loading (low, medium, or high) and the size of each shed. The shed doors were fully open and secured in this position for the test duration.

An acoustic resonance wind sensor (FT technologies FT742) recorded ambient wind velocity throughout the experiments. The sensor was mounted on a tripod placed on the grass field, away from all obstructions, and sampled at 3 Hz throughout the experiment.

The procedure of igniting wood cribs using 300 mL of heptane was similar to procedures described in Section 4.2.2. Since the sheds were larger than those used in the indoor shed burn experiments, and to ensure uniform flame spread over the wood cribs, a crib farthest from the door opening was ignited using heptane (Fig. 125).

Following the experimental setup and safety briefing, the data acquisition was started prior to the ignition of heptane to record baseline heat flux and mass data. Test time (t=0) started at the ignition of heptane.

The sheds were allowed to burn freely with no suppression or intervention. The end of the test and data acquisition occurred when substantial flaming combustion had ceased. Typical test durations ranged from 45 min for Medium sheds to over 2 h for Very Large sheds with high fuel loadings.

Fig. 125. An example of an ignition method using 300 mL of heptane in an aluminum pan placed underneath the back-middle crib.

6.2.2. Test Matrix

The shed dimensions, storage capacity, and door opening dimensions for the sheds tested at the IBHS test facility are provided in Table 16. The shed and fuel loading specifications are provided in Table 17.

Table 16. Dimensions and storage capacity of the sheds tested at IBHS test facility.

Shed Type	**Measured shed dimensions, ft**			**Measured door dimensions, ft**		**Area of door opening, ft^2**	**Measured footprint, ft^2**	**Nominal shed storage capacity*, ft^3**
	Height	Width	Depth	Height	Width			
Wood Medium	9	8	8	6	4	24	64	384
Steel Large	6.5	12	10	5.4	4.6	25	120	693
Plastic Large	8.3	11	9	5.8	4.8	28	99	100
Steel Very Large	8.5	24	12	6.8	7.9	54	278	2037
Wood Very Large	9.75	24	12	6	5	30	288	2020

Table 17. Shed and fuel loading specifications for the sheds tested outdoors at IBHS test facility.

Serial number	Test ID	Shed type	Material	Fuel loading, (number of 6-A cribs)	Mass, kg		
					Shed	Cribs	Total combustible
1	1B-WMh0	Medium	Wood	High (4)	595	546	1141
2	1B-WMh0-R1	Medium	Wood	High (4)	620	515	1135
3	1B-SLh0	Large	Steel	High (6)	133	855	1040[1]
4	1B-PLh0	Large	Plastic	High (6)	127	870	1134[2]
5	1B-SVLh0	Very Large	Steel	High (15)	346	2138	2920[3]
6	1B-WVLh0	Very Large	Wood	High (15)	1839	2193	4032

[1]A 185 kg wood floor was added, [2]A 127 kg wood floor was added, [3]A 782 kg wood floor was added.

6.3. Data Analysis and Results

Mass loss rate (MLR) data was used to quantify the burning behavior of source structures. Temporal profiles of the mass loss data and MLR are provided for each outdoor shed burn experiment. As anticipated, the derivatives of experimental measurements were very sensitive to sudden variations in the mass signal, which could result from electrical noise, variations in the ambient wind velocity, and structural collapse. High frequency noise in the mass loss and heat flux data was reduced using a data smoothing process. The method implemented was a Gaussian-weighted moving average filter using a heuristically fixed window length (i.e., the number of elements over which the average is computed). Due to the sensitivity of the MLR to the fluctuations of the mass loss data, a larger window length was used to filter them compared to the window length used for the heat flux data.

For the mass loss data, the window length was defined as the number of elements that corresponds to 2.5% of the data where 80% of the mass loss occurred. Meanwhile, the window length for the heat flux data was defined as the number of elements that corresponds only to 1% of the data where 80% of the mass consumption occurred. For example, if 80% of the mass consumption happens in the first 100 s which at a 90 Hz sample frequency means 9000 data points, the window length for the mass loss data filter would be 225 data points (i.e., 2.5% of 9000), and the window length for the heat flux data filter would be 90 data points (i.e., 1% of 9000). The smoothed mass loss data was used to derive the HRR considering a heat of combustion of 18 MJ/kg. Finally, a 30-point moving and a decrease in sampling frequency by a factor of ten was applied to the data.

In addition to the derived HRR, visual observations were used to characterize fire growth. Images captured from various video cameras were used to provide burn overview of each experiment.

Measurements of radiative heat fluxes at surrogate target structures were obtained from three locations surrounding the source structure. The heat flux data recorded at the three HF rigs placed around the shed are plotted as a function of time for each experiment. Generally, it was observed that the lower HF gauges (HF3) recorded higher heat fluxes compared to the upper gauges (HF1 and HF2) at the eave height. This can be attributed to their relative view of the burning fuel compared to the upper flux gauges which primarily viewed the flames/plume. HF1 and HF3, facing the source structure, recorded higher heat fluxes compared to HF2 facing the ground.

The ambient wind was measured using an ultrasonic probe located at about 150 ft northwest of the weighing platform.

A summary of measured and derived quantities for the outdoor shed burn experiments is provide in Table 18.

Table 18. Summary of measured and derived quantities for the outdoor shed burn experiments.

Serial number	Test ID	Total combustible mass, kg	Derived parameters			Peak heat flux, kW/m²								
			PHRR, (MW)	TTPHRR*, (min)	MLR, (kg/s)	Rig1			Rig2			Rig3		
						HF1	HF2	HF3	HF1	HF2	HF3	HF1	HF2	HF3
1	1B-WMh0	1141	22.6	17	1.3	7	3	7	5	2	5	2	6	5
2	1B-WMh0-R1	1135	17.9	19	1.0	7	2	6	6	3	7	4	1	4
3	1B-SLh0	1040	5.97	21	0.3	3	1	2	0.8	0.5	1	1	0.5	1
4	1B-PLh0	1134	29.8	14	1.7	11	5	11	4	2	4	5	2	5
5	1B-SVLh0	2920	16.6	10	0.9	3	1	2	2	2	3	4	2	4
6	1B-WVLh0	4032	66.5	22	3.7	14	3	11	7	3	8	29	18	22

*TTPHRR = time to PHRR, HF1- represents fascia board facing the source structure, HF2-represents under-eaves facing down, and HF3- represents window.

6.3.1. Test:1B-WMh0

6.3.1.1. Shed Specifications

The source structure was a commercially available wooden shed with a high fuel loading of four 6-A wood cribs. The shed was constructed with 24 in, over the center (O.C.) wall studs, 3/8 in, composite wood siding with 8 in, center grooves, and a 7/16 in, OSB roof sheathing. The OSB sheathing was covered with a felt underlayment and asphalt-composite shingles. Photographs in Fig. 126 show an experimental setup with a medium-sized wooden shed and an interior view of the shed with four 6-A wood cribs stacked in a "C" pattern. The double doors of the shed were kept fully open and secured in place using screws, thereby creating an opening of 24 ft^2 (4 ft × 6 ft). The shed was nominally 9 ft tall and had a footprint of 64 ft^2. The mass of the shed was 595 kg, and the mass of four wood cribs was 546 kg. The resulting total combustible mass for this source structure was 1141 kg.

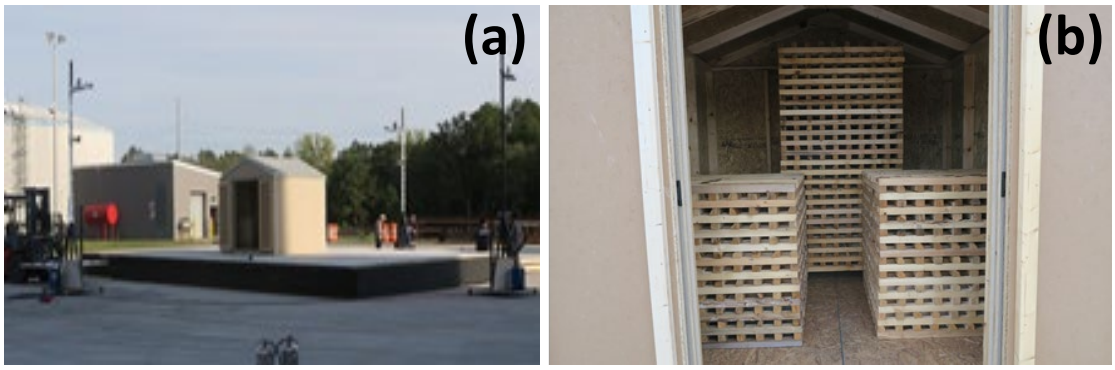

Fig. 126. Photographs of experimental setup showing (a) wood medium shed (b) with high fuel loading of four 6-A cribs.

6.3.1.2. Burn Overview

The average ambient wind speed on the test site was 0.65 m/s ± 0.13 m/s (1.46 mi/h ± 0.30 mi/h) blowing from the southwest. Fig. 127(a) shows the wood cribs igniting following the ignition of heptane. The wood cribs were fully engulfed in flames approximately 7 min into the test, and flames emerged from the door opening (Fig. 127(b)). About 15 min from the ignition of heptane, burning of the shed roof and walls was noted.

The temporal profiles of the mass loss, mass loss rate (MLR), and the derived HRR are shown in Fig. 128. Intense burning behavior coincided with the measured maximum MLR of 1.3 kg/s and a derived PHRR of 22.6 MW around 17 min (Fig. 128). The shed and wood cribs had fully collapsed within 40 min of the heptane ignition, with only a pile of glowing, and occasionally flaming, debris seen at this time (Fig. 127(d)).

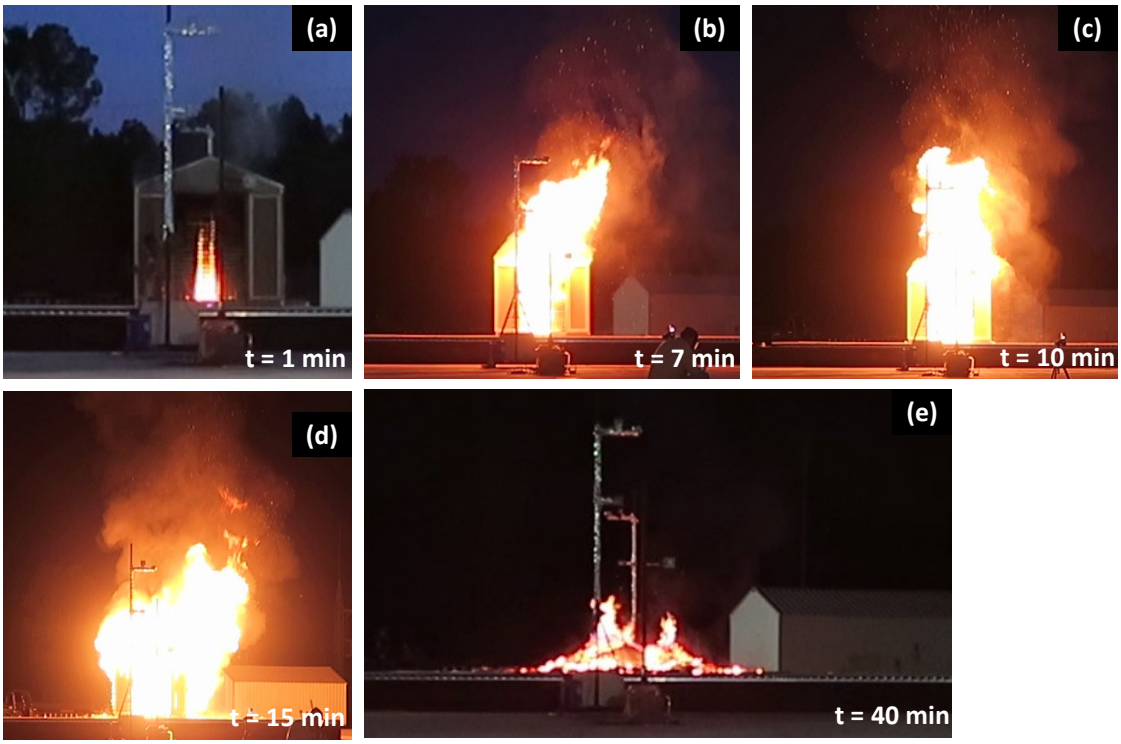

Fig. 127. Photographs captured from the video of the shed burn show (a) ignition of wood cribs, (b) intense burning of wood cribs, (c) burning of shed, (d) flashover, and (e) collapse of shed structure in test 1B-WMh0.

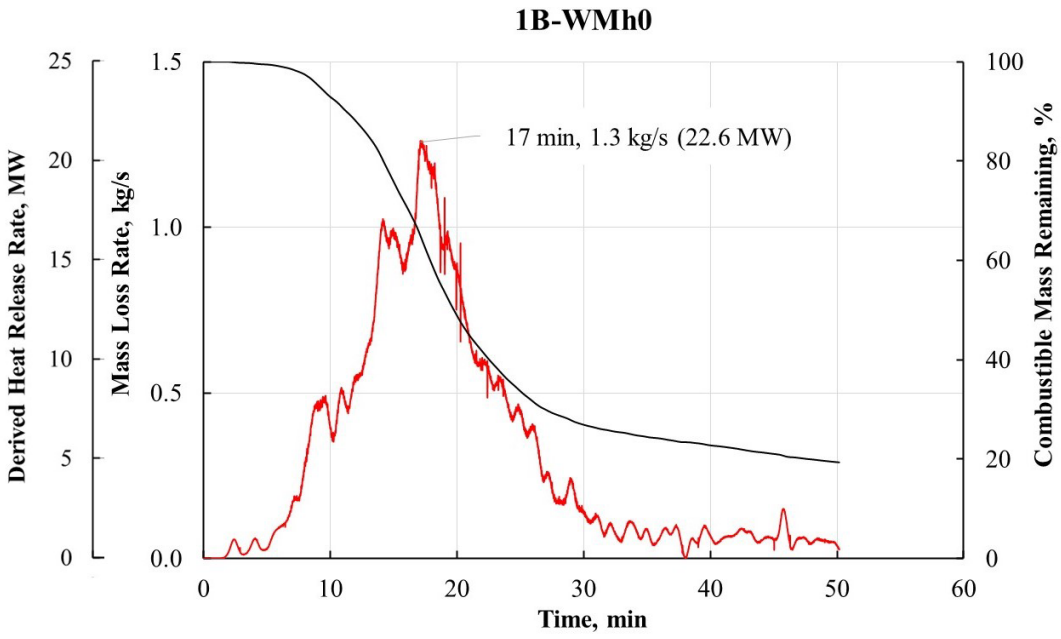

Fig. 128. Percent mass loss, mass loss rate, and derived HRR of combustible fuel in test 1B-WMh0.

Temporal profiles of heat flux data measured at surrogate target structures (Rig1, Rig2, and Rig3) located at a separation distance of 20 ft are provided in Fig. 129. Of all three rigs, HF2, which faced the ground, recorded the lowest heat flux values, with HF2 on Rig1 registering a peak heat flux of approximately 5 kW/m^2. The incident heat fluxes at the fascia board and at the window on a given rig were similar and corresponds with the shape of the HRR curves. Heat flux gauges on all three rigs recorded peak heat fluxes between 5 kW/m^2 and 8 kW/m^2 at the fascia board and the window.

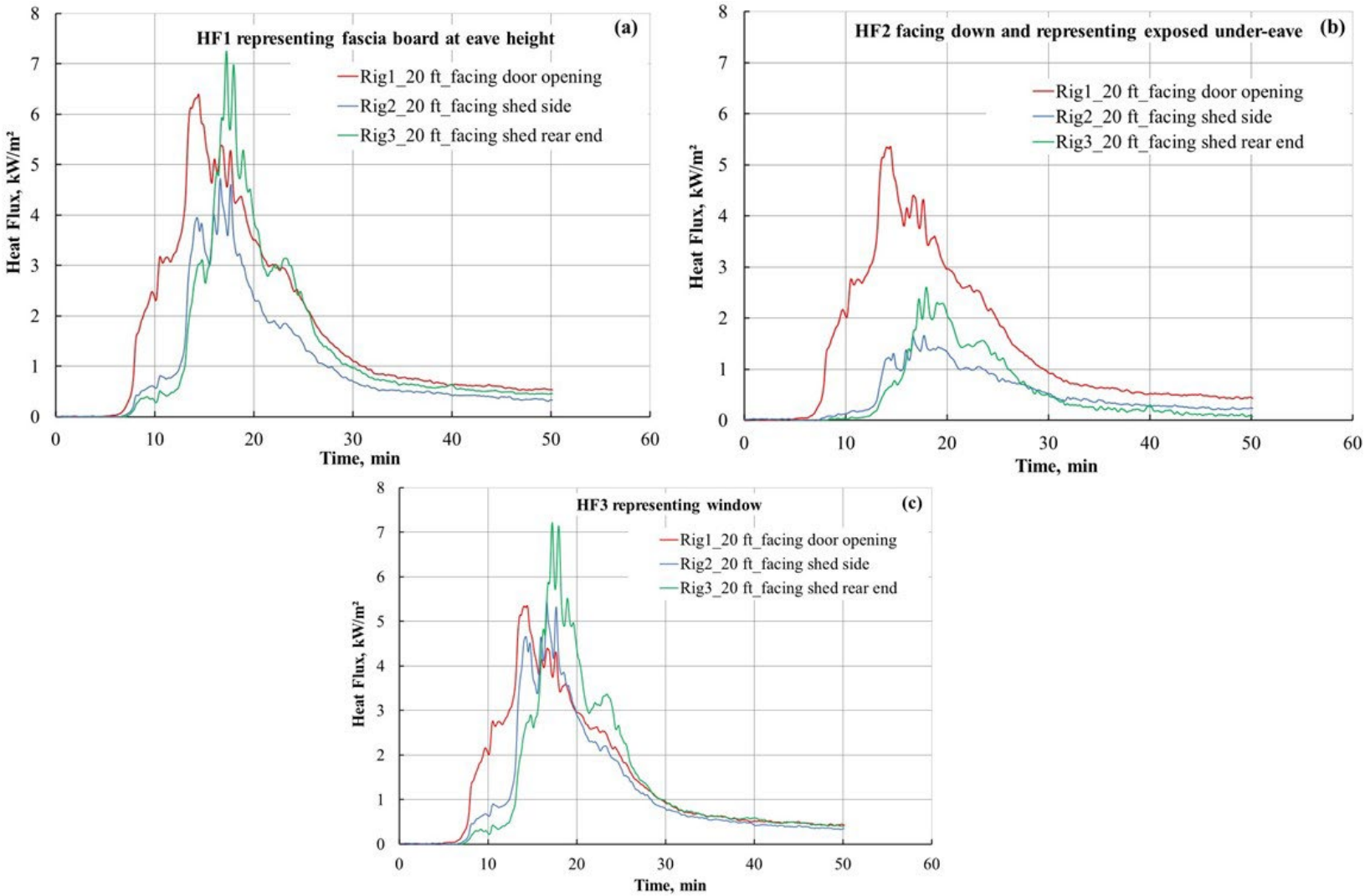

Fig. 129. Heat fluxes at (a) HF1-fascia board, (b) HF2- exposed under eaves, and (c) HF3-window, recorded simultaneously by gauges located on Rig1, Rig2, and Rig3 in test 1B-WMh0.

6.3.2. Test:1B- WMh0-R1

6.3.2.1. Shed Specifications

The specifications for the shed used in this test were similar to the one used in test 1B-WMh0. The fuel load and its placement were also the same. The shed was built in-house due to long lead times on delivering a commercially available shed. The construction materials and design specifications were the same for the in-house built shed. The photographs in Fig. 130 shows the in-house built shed placed on the weighing platform and the wood crib arrangement inside the shed. The shed was nominally 9 ft tall and had a footprint of 64 ft^2. The mass of the shed was 620 kg, and the mass of the four wood cribs was 515 kg. The resulting total combustible mass for this source structure was 1135 kg.

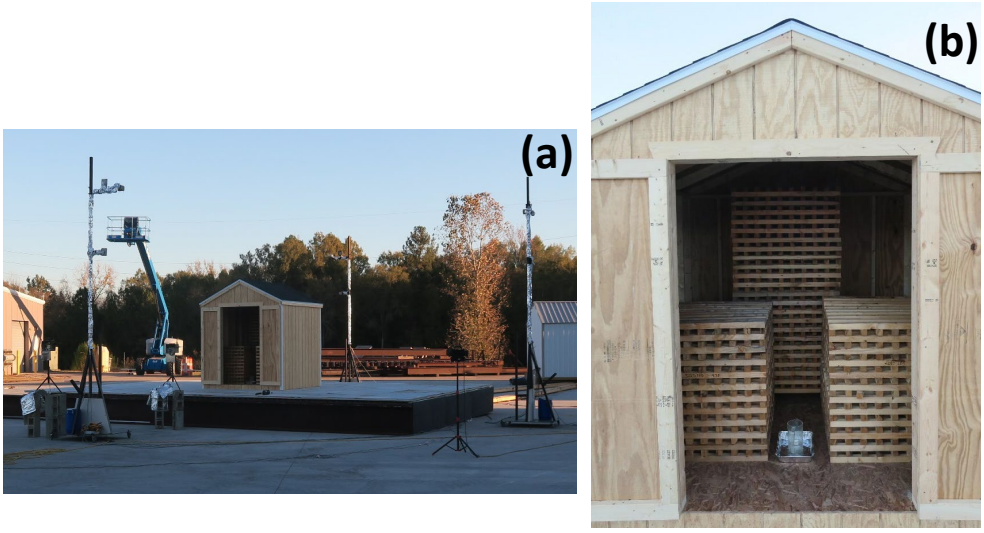

Fig. 130. Photographs of experimental setup showing (a) in-house built wood medium shed (b) with high fuel loading of four 6-A cribs.

6.3.2.2. Burn Overview

The key events during the shed burn experiment can be noted from the images provided in Fig. 131. The temporal profiles of the mass loss, MLR, and the derived HRR are shown in Fig. 132. Fig. 131 (a) shows ignition of the wood cribs following the ignition of heptane. The wood cribs were fully engulfed in flames approximately 6 min after the heptane ignition (Fig. 131(b)). Flames (heights estimated at 20 ft) emerged from the door opening at around 6 min (Fig. 131 (b)). Flashover and partial roof collapse occurred at 19 min (Fig. 131 (c)). At the same time, peak MLR of 1.0 kg/s was registered (Fig. 132). The PHRR of about 18 MW at 19 min into the test was estimated from the derived HRR plot in Fig. 132. Fire consumed the walls and roof, exposing the wood cribs to excess ambient oxygen at 28 min (Fig. 131 (d)). At 45 min into the test, the shed and wood cribs had collapsed (Fig. 131 (e)).

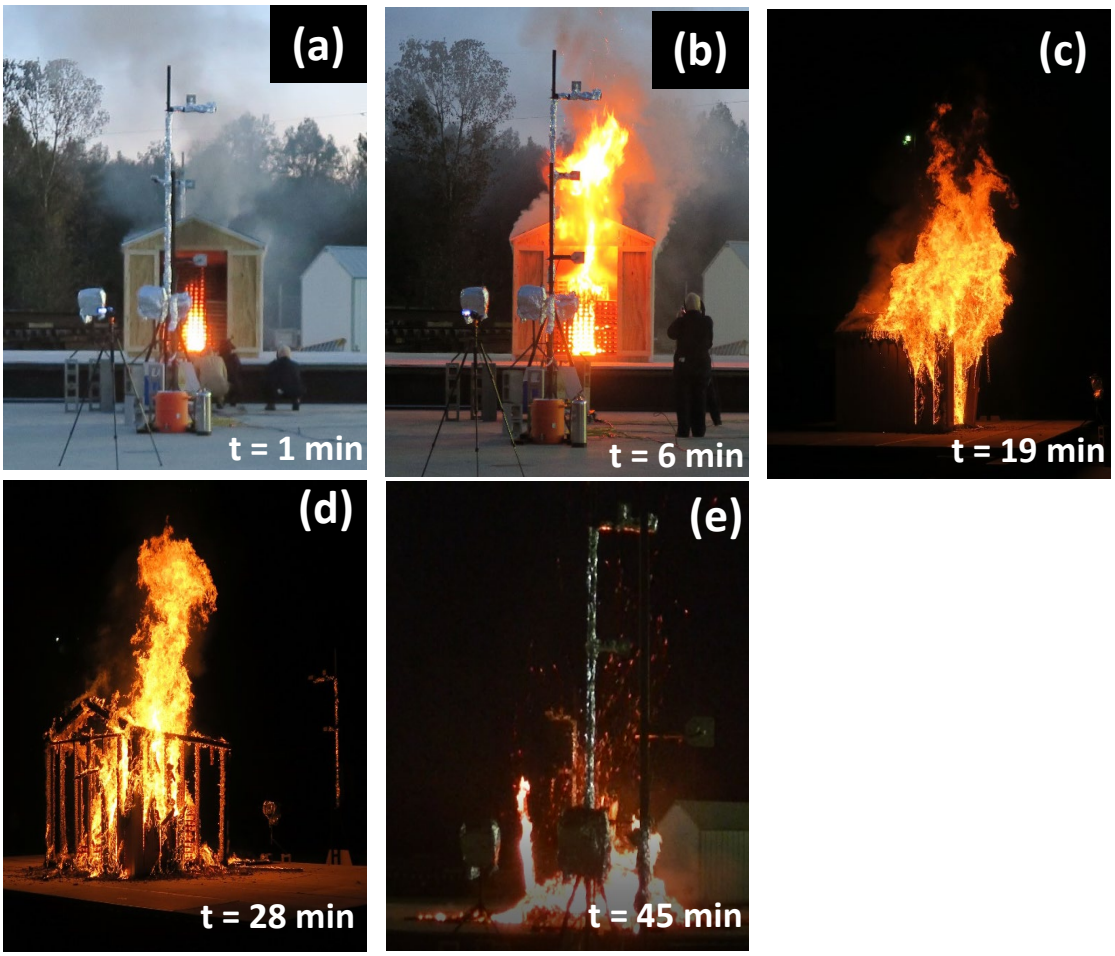

Fig. 131. Photographs captured from video recording of the shed burn showing (a) ignition of wood cribs, (b) intense burning of wood cribs, (c) flashover, (d) and (e) collapse of shed structure and wood cribs in test 1B-WMh0-R1.

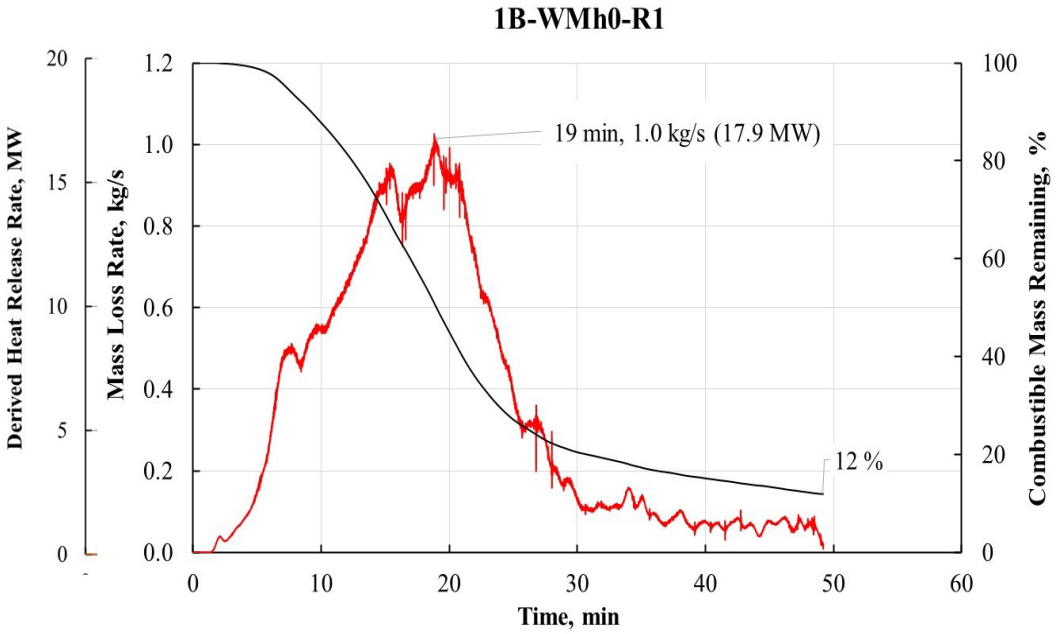

Fig. 132. Percent mass loss, mass loss rate, and derived HRR of combustible fuel in test 1B-WMh0-R1.

A comparison of temporal profiles of the HRR for tests 1B-WMh0 and 1B-WMh0-R1 is shown in Fig. 133. The PHRR for 1B-WMh0-R1 is 20 % lower than that of 1B-WMh0; however, the shapes of the heat release curves are similar and shows good repeatability.

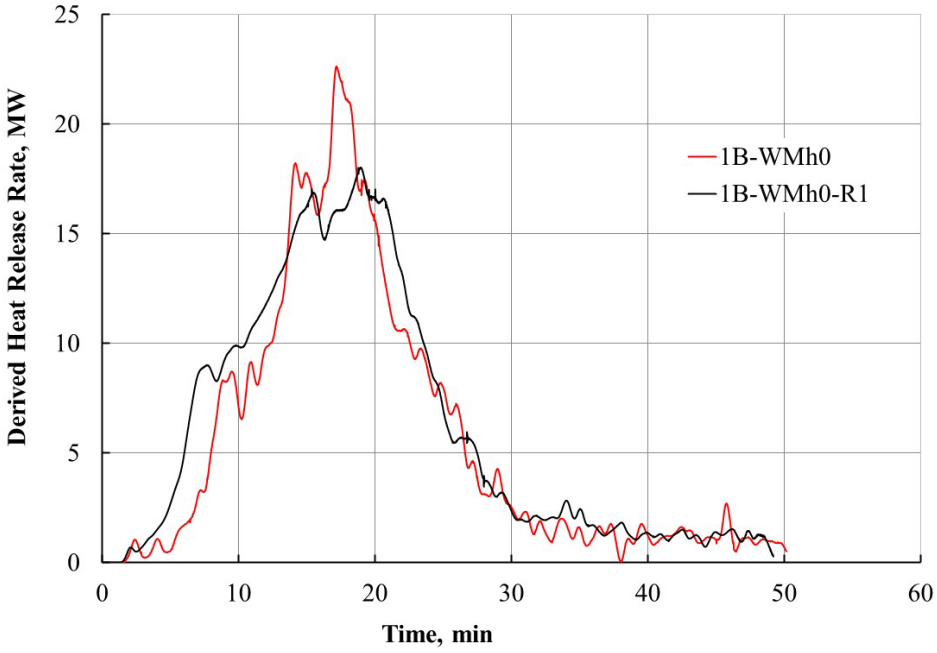

Fig. 133. Comparison of derived heat release rate curves for 1B-WMh0 and 1B-WMh0-R1.

The temporal profiles of heat flux data recorded by the heat flux gauges on the three rigs are plotted in Fig. 134. A comparison of heat fluxes recorded by HF3 on Rig1, Rig2, and Rig3 for tests 1B-WMh0 and 1B-WMh0-R1 is shown in Fig. 135.The peak heat flux values recorded for 1B-WMh0 by HF3 at Rig1 and Rig2 are 20 % lower than those recorded for 1B-WMh0-R1. The peak heat fluxes registered at Rig3 were 80 % higher than the repeat shed burn.

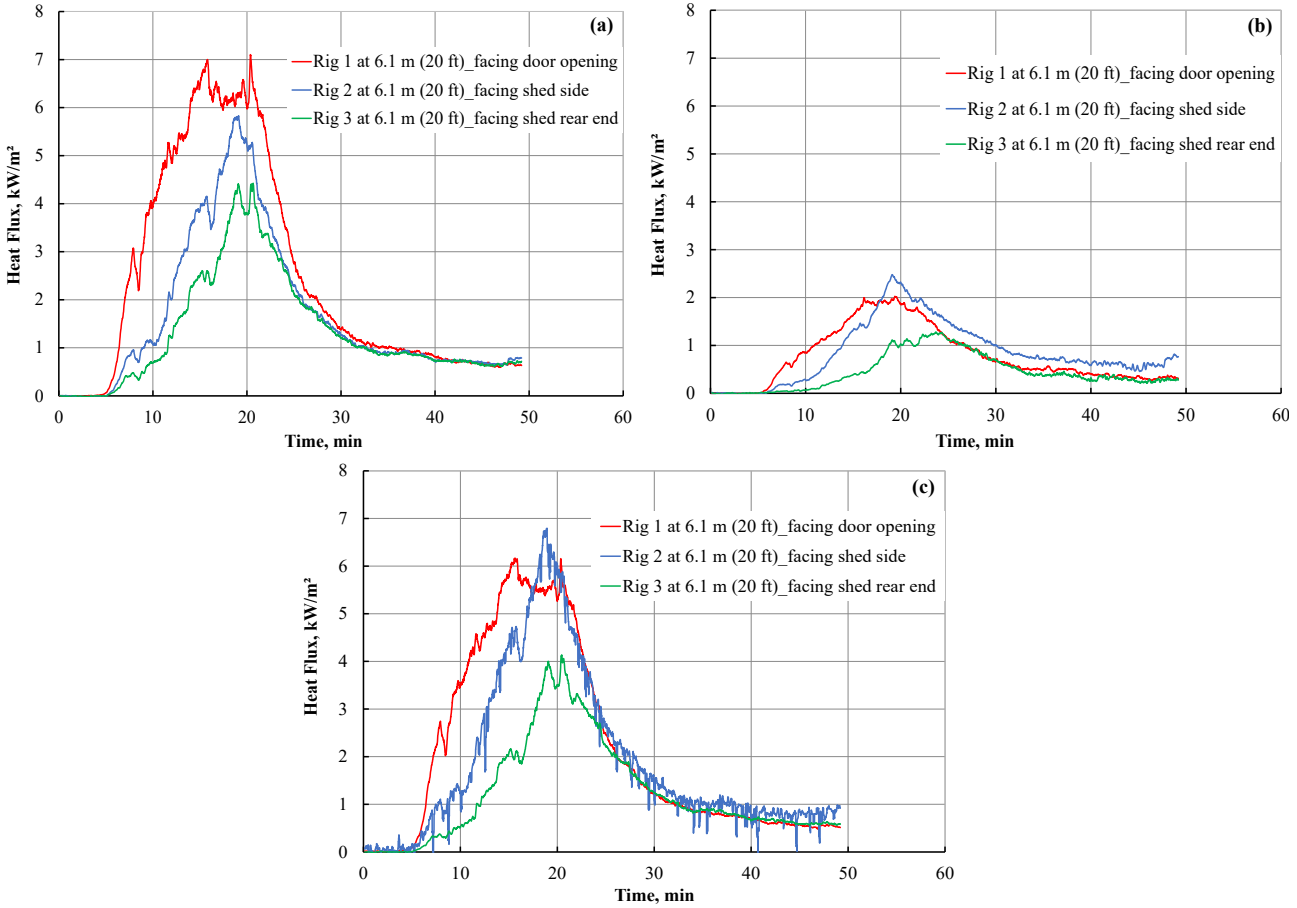

Fig. 134. Heat fluxes at (a) HF1-fascia board, (b) HF2- exposed under eaves, and (c) HF3-window, recorded simultaneously by gauges located on Rig1, Rig2, and Rig3 in test 1B-WMh0-R1.

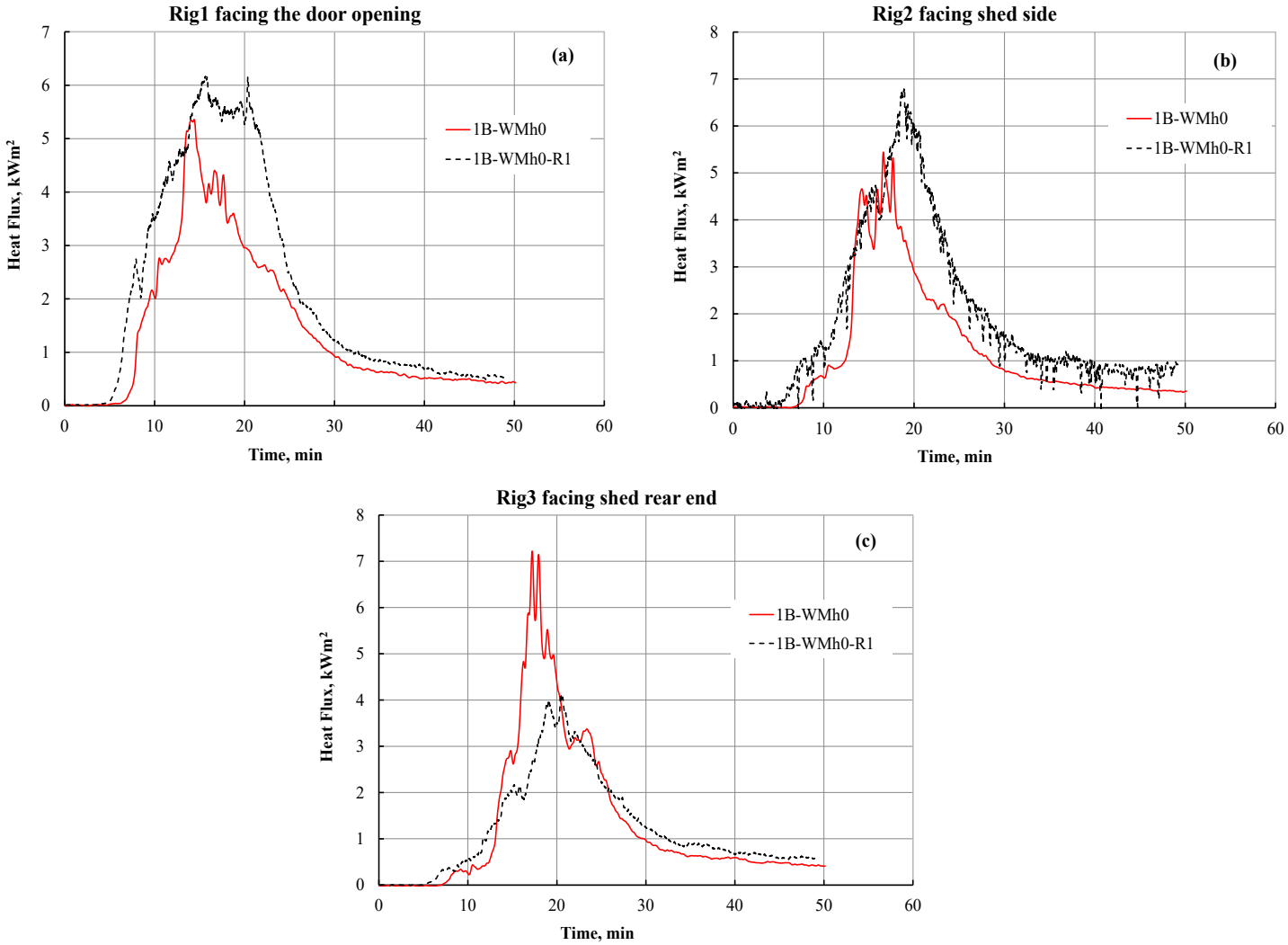

Fig. 135. Comparison of heat fluxes measured by HF3 (window height) at (a) Rig1-facing the door opening, (b) Rig2-facing the shed side, and (c) Rig3-facing the rear end of the shed.

6.3.3. Test: 1B- SLh0

6.3.3.1. Shed Specifications

The source structure was a commercially available galvanized metal shed with a sliding lockable door. The shed was attached to a wooden floor assembly, consisting of OSB and wood framing. Photographs of the steel Large shed and six 6-A wood cribs stacked in a "C" pattern are shown in Fig. 136(a) and Fig. 136(b), respectively. The fully opened sliding doors created an opening of approximately 24.8 ft^2 (4.6 ft × 5.4 ft). The shed was 10 ft tall and had a footprint of 120 ft^2. The mass of the steel shed was 133 kg, the wooden floor assembly was 185 kg, and the mass of six wood cribs was 855 kg. The resulting total combustible mass for this source structure was 1040 kg.

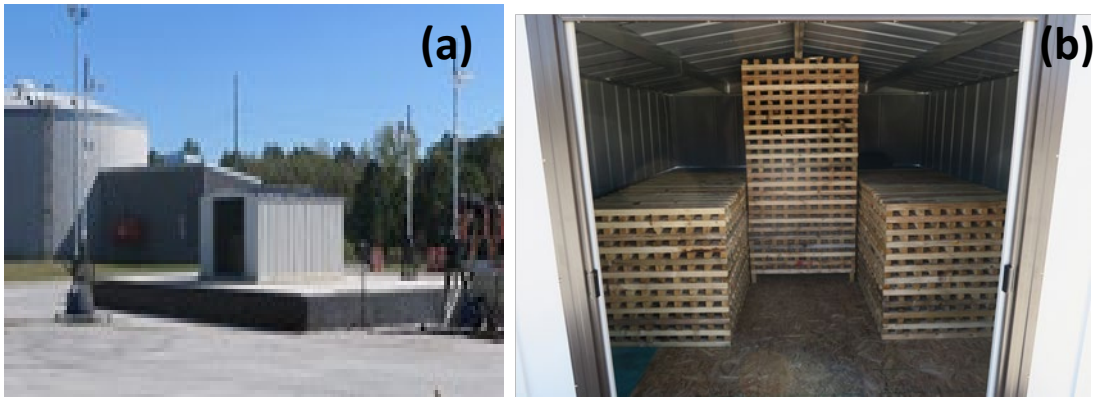

Fig. 136. Photograph of (a) steel Large shed setup and (b) the steel Large shed with high fuel loading of six 6-A cribs.

6.3.3.2. Burn Overview

The average ambient wind speed during test 1B-SLh0 was about 1.35 mi/h± 0.70 mi/h, blowing from the southwest (from the right rear of the shed). The photographs in Fig. 137 show the fire progression during test 1B-SLh0, while the general burning behavior of the combustible mass can be noted from the measured mass loss and derived MLR and HRR plotted in Fig. 138.

The initial burning of the wood cribs using a 300 mL heptane pool fire (Fig. 137(a)) was the same as described earlier. Approximately 15 min from the ignition of heptane, the cribs were burning vigorously as shown in Fig. 137(b). Visual observations suggests that approximately 20 min into the test, the floor assembly began to burn. A maximum MLR of 0.3 kg/m^2 was registered during this time (Fig. 138). The derived HRR plotted in Fig. 138 shows a PHRR of 5.9 MW at 22 min. The burning intensity slowly decayed following the PHRR. The burning conditions at 30 min are seen in Fig. 137(c). The metal shed mostly contained the fire with flames extending out from the door opening. Mean flame lengths of approximately 4 ft to 5 ft were observed jetting out from the door opening (Fig. 137(d)). The metal shed was manually lifted from the platform approximately 70 min after the start of the test leading to another period of increased burning, seen as a slight rise in HRR in Fig. 138.

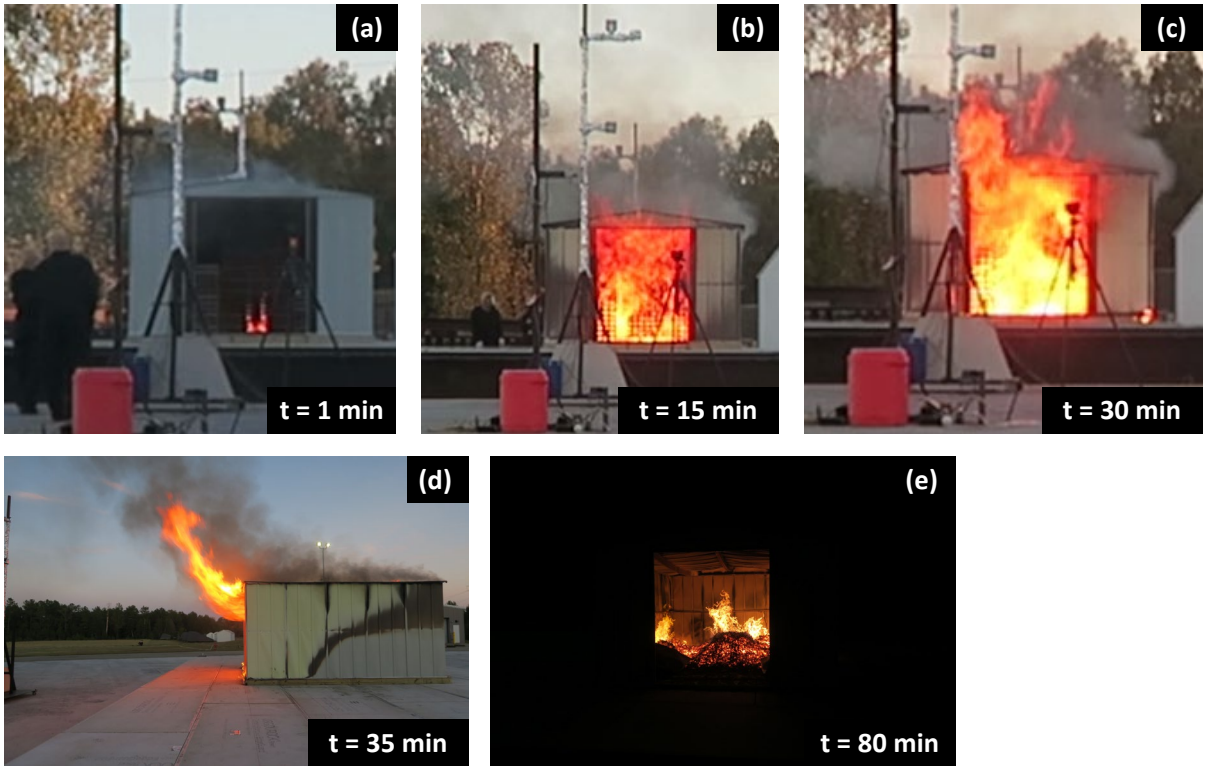

Fig. 137. Photographs captured from video recording of the shed burn showing (a) ignition of the wood crib, (b) and (c) burning of all wood cribs, (d) flames jetting out from the door opening, and (e) residual burning of the collapsed wood cribs in test 1B-SLh0.

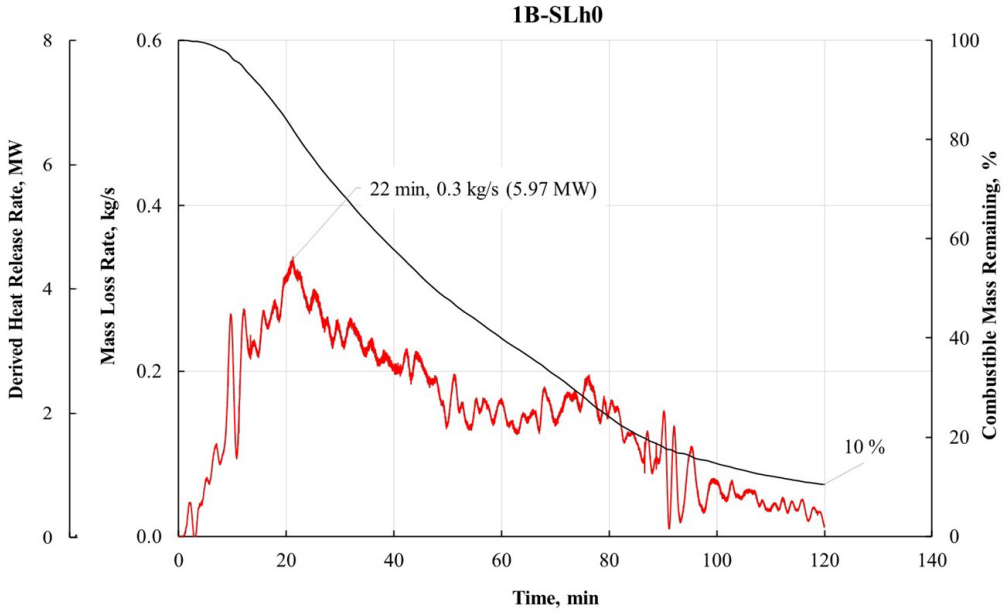

Fig. 138. Percent mass loss, mass loss rate, and derived HRR of combustible fuel in test 1B-SLh0.

The large fluctuations in the MLR and the derived HRR curves in Fig. 138 could be due to the effects of ambient wind load on the weighing platform, or the buoyancy forces of the hot gases trapped inside the metal shed.

The heat flux plots for HF1, HF2, and HF3 on Rig1 facing the door opening of the metal shed (Fig. 139) correspond with the HRR curve. The metal shed kept its integrity throughout the experiment and aside from the flame extension from the door, contained the fire inside. Only the heat flux sensors on Rig1 facing the shed door opening were exposed to the fire and recorded values above 1 kW/m^2. Heat flux gauges on Rig2 and Rig3 registered heat fluxes lower than 1 kW/m^2 due to shielding from the shed structure itself. The rise in heat fluxes on these rigs peaking around 80 min (Fig. 139) corresponded with lifting of the metal shed and exposing the heat flux gauges to the burning wood cribs.

Despite the higher fuel load compared to 1B-WMh0, the heat fluxes registered at the surrogate target structures for 1B-SLh0 were significantly lower than those recorded for 1B-WMh0. These lower heat fluxes are primarily due to the containment of the fire within the metal shed, while the heat flux gauges in test 1B-WMh0 were exposed to a large flaming fire.

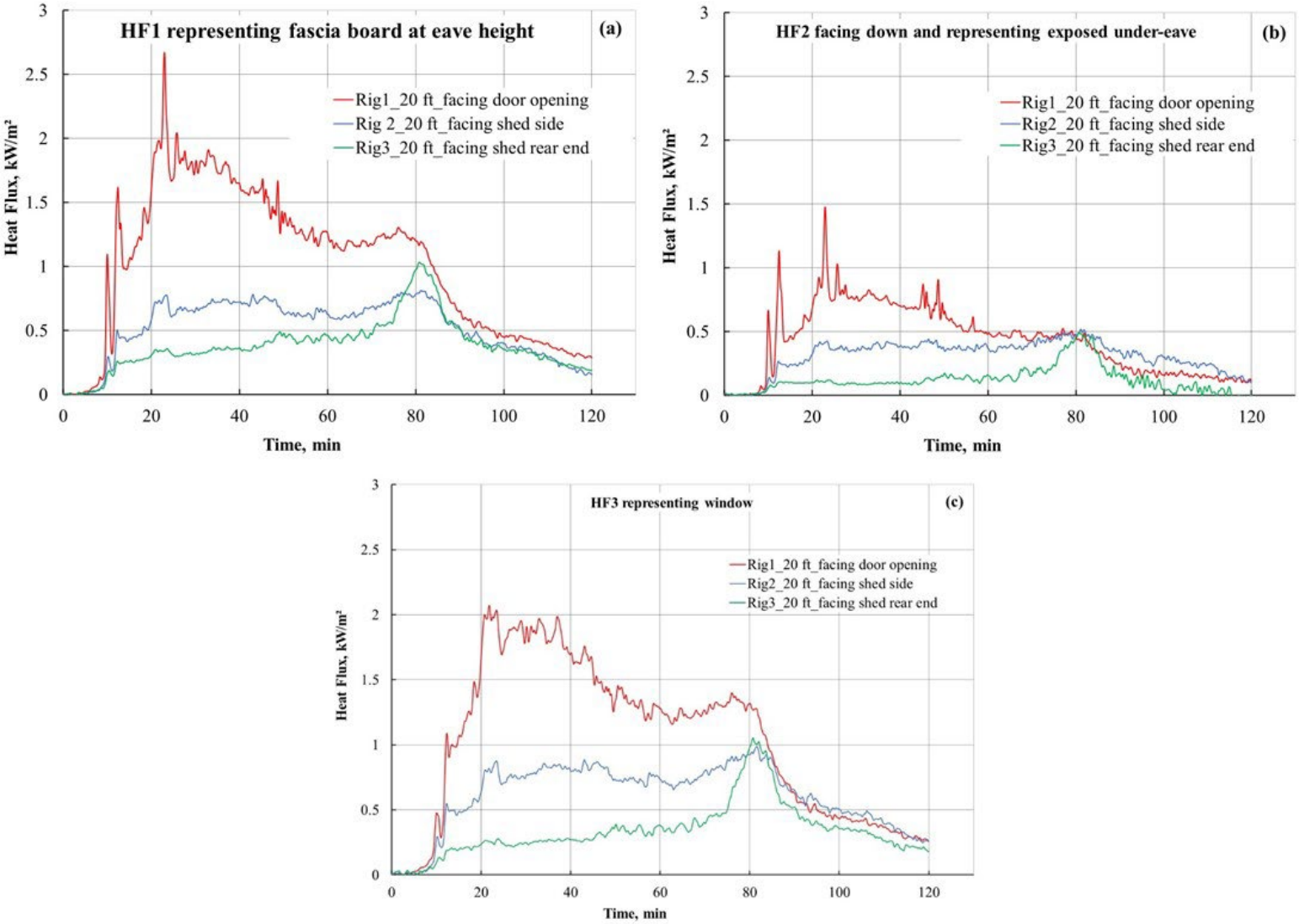

Fig. 139. Heat fluxes at (a) HF1-fascia board, (b) HF2- exposed under eaves, and (c) HF3-window, recorded simultaneously by gauges located on Rig1, Rig2, and Rig3 in test 1B-SLh0.

6.3.4. Test:1B- PLh0

6.3.4.1. Shed Specifications

The source structure was a commercially available composite shed with an aluminum frame, polycarbonate wall panels, and wood flooring. The shed was attached to the wood floor assembly consisting of OSB and wood framing. Photographs of the large plastic shed and wood crib fuel load are shown in Fig. 140(a) and Fig. 140(b), respectively. The shed doors were kept open creating an opening of 27.8 ft^2 (4.8 ft ×5.8 ft). The shed was nominally 8.3 ft tall with a footprint of 99 ft^2. The mass of the composite shed assembly was 127 kg, the wooden floor assembly was 127 kg, and the mass of six wood cribs was 870 kg. The resulting total combustible mass for this source structure was 1134 kg[6].

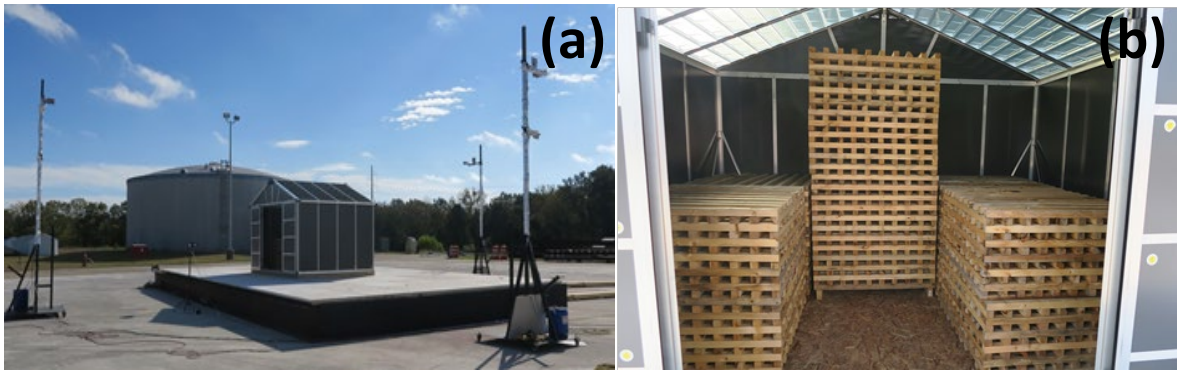

Fig. 140. Photograph of experimental setup showing (a) plastic large shed and (b) crib assembly inside the shed.

6.3.4.2. Burn Overview

The average ambient wind velocity prior to ignition was less than 1 m/s (2.2 mi/h). During the shed burn, the local wind velocity gradually increased, and the anemometer recorded an average ambient wind speed of 2.8 m/s ± 1 m/s (6.35 mi/h ± 2.2 mi/h) from the west. The general burning behavior of the Large plastic shed with high fuel loading can be noted from Fig. 141. Following the ignition of heptane, the burning of the wood cribs occurred fairly rapidly. Within 10 min of ignition, the fire had spread to multiple cribs, and polycarbonate panels on the roof and the walls had melted. The melting of polycarbonate panels created large openings in the structure as seen in Fig. 141(b). The wood cribs were exposed to excess ambient air, and intense burning of the cribs was observed. The aluminum framing began to collapse at around 12 min as shown in Fig. 141(d). As mentioned previously, the wind speed increased during the burn, and flames were near-parallel with the ground (see Fig. 141(e)), driven by winds from the west. Most fuels were consumed within 45 min from the ignition of heptane.

The burning behavior of the plastic Large shed can be quantified from the measured mass loss, MLR, and the derived HRR plotted in Fig. 142. Also plotted in Fig. 143 is the wind speed during the shed burn. The measured mass loss, and therefore the derived HRR, was affected by the

[6] Mass of the aluminum frame was considered negligible.

ambient wind. The large fluctuations in the MLR correspond with the temporal plot of wind velocity in Fig. 143. Due to large fluctuations in the mass measurements, the derived HRR data often fell below zero, i.e., a non-physical quantity. However, general burning behavior is evident in Fig. 142. The HRR should only be used as an estimate to assess the fire hazard of the source structure. The PHRR of 30 MW was estimated for 1B-PLh0 at 14 min following ignition of heptane. This experiment illustrated that event relatively low wind speeds of less than 10 mph can have significant effect on plume orientation.

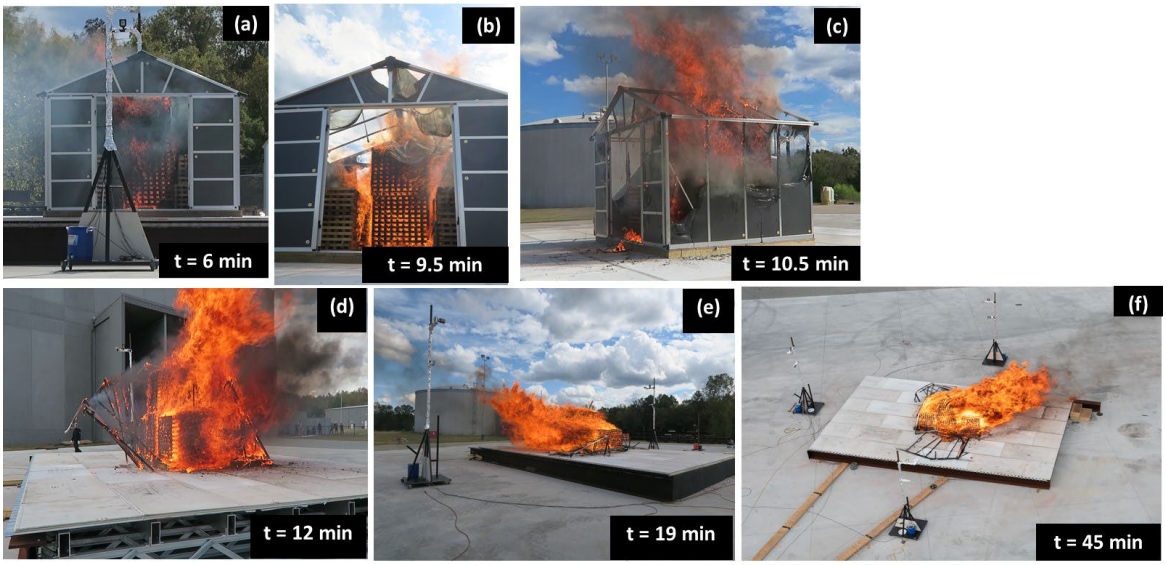

Fig. 141. Photographs showing (a) ignition of cribs, (b) and (c) melting of polycarbonate sheets, (d) collapse of shed structure, (e) effect of wind on plume direction, and (f) aerial view of wood crib burning in test 1B-PLh0.

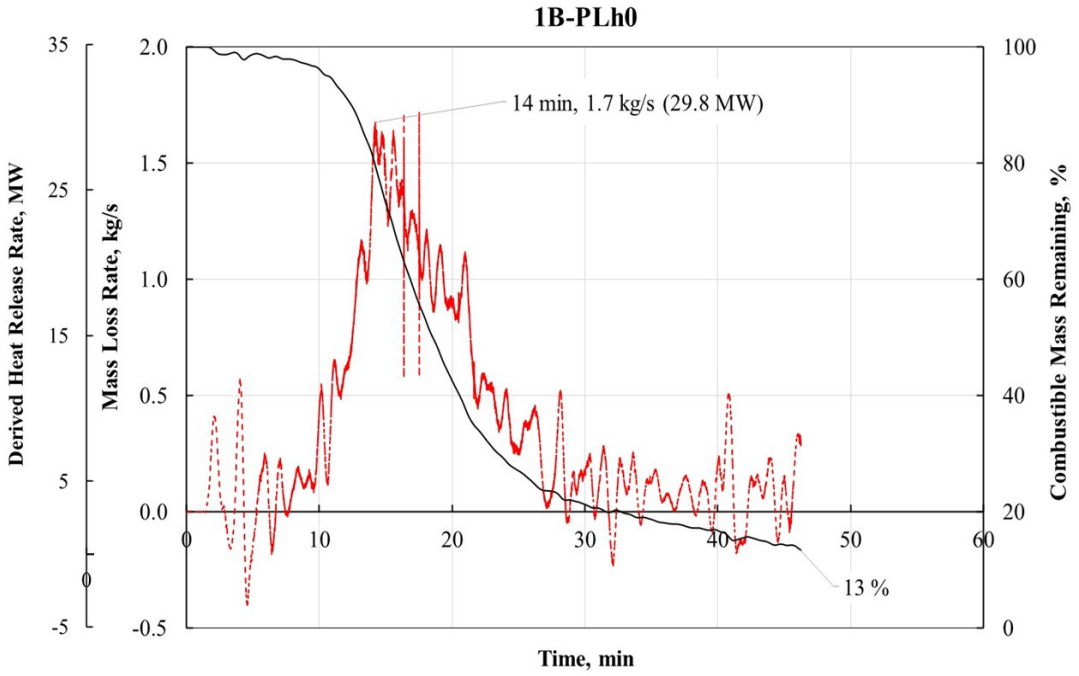

Fig. 142. Percent mass loss, mass loss rate, and derived HRR of combustible fuel in test 1B-PLh0.

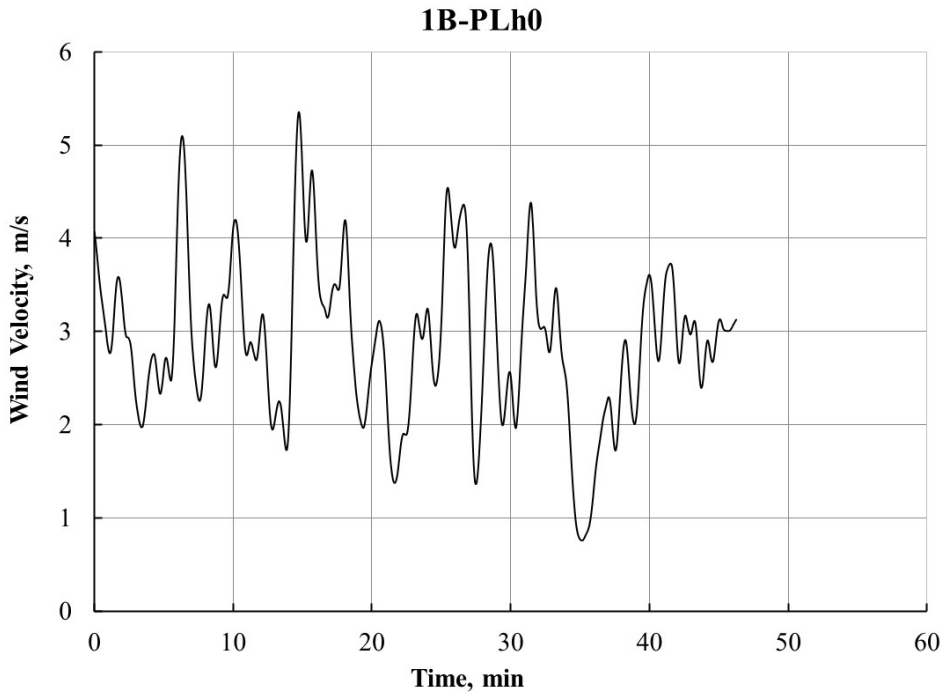

Fig. 143. Wind velocity measured during the shed burn in test 1B-PLh0.

The temporal plots of heat flux measurements at the eaves and at the window height of a surrogate target structures located around the shed are provided in Fig. 144. The heat fluxes recorded by HF1, HF2, and HF3 on Rig1 are significantly higher than those recorded at Rig2 and

Rig3. It can be clearly noted from Fig. 141(e) that flames are jetting towards Rig1 located in front of the shed door. The peak heat fluxes at Rig1 were recorded approximately at the same time as time to PHRR (14 min). The HF gauges on Rig2 and Rig3 registered steady heat fluxes once the shed structure had melted and exposed the wood cribs. The peak heat fluxes estimated from the heat flux data shown in Fig. 144 are provided in Table 18.

On a given surrogate structure, the HF3 representing the window recorded the highest heat flux followed by the HF1 representing the fascia board while HF2 registered lowest heat fluxes.

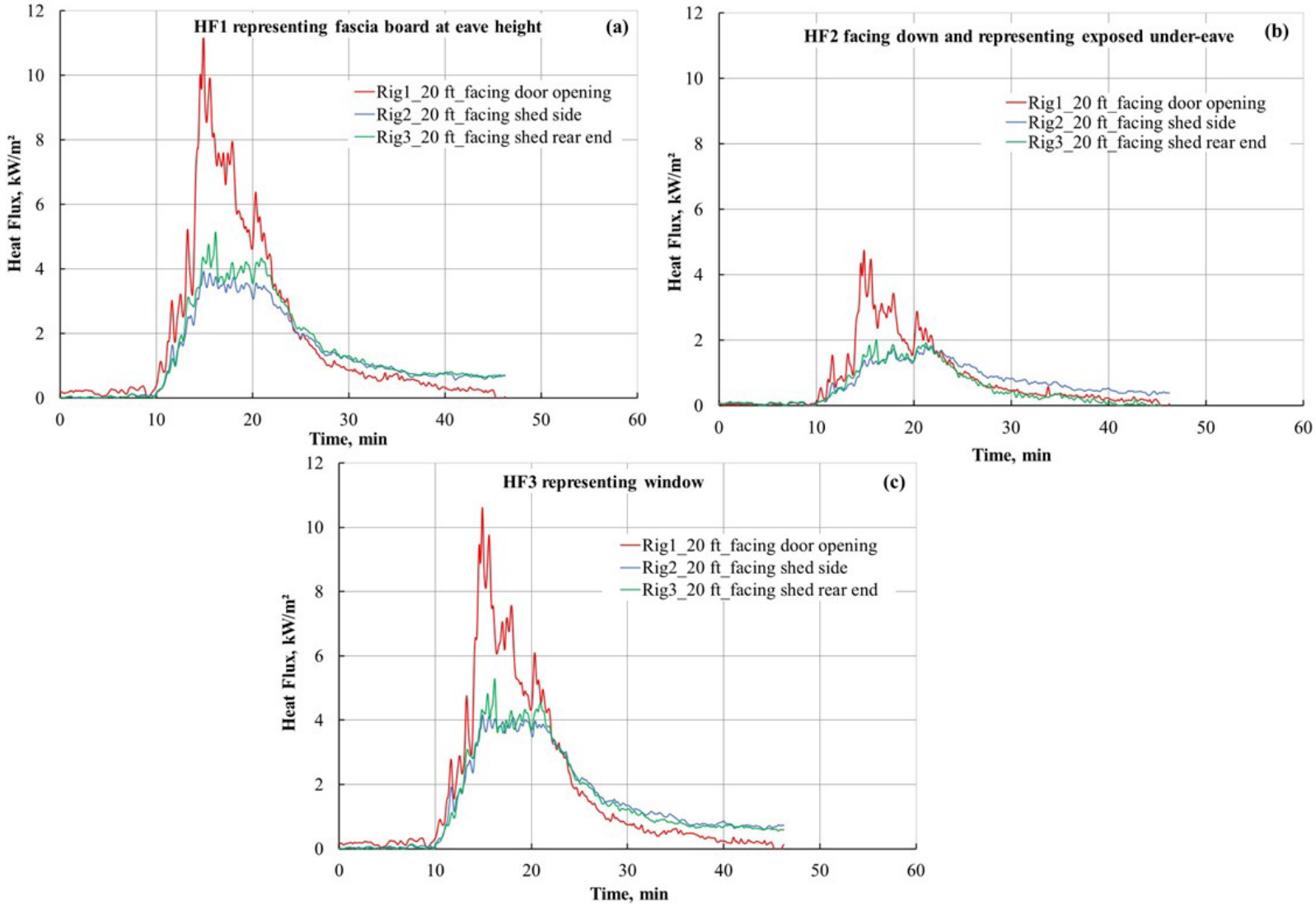

Fig. 144. Heat fluxes at (a) HF1-fascia board, (b) HF2- exposed under eaves, and (c) HF3-window, recorded simultaneously by gauges located on Rig1, Rig2, and Rig3 in test 1B-PLh0.

6.3.5. Test:1B-SVLh0

6.3.5.1. Shed Specifications

A commercially available, steel Very Large shed is shown in Fig. 145. The shed was nominally 8.5 ft tall with a footprint of 278 ft^2. Based on the observations in test 1B-SLh0, it was decided to block the side door and create a "garage door" type of opening on the shorter side of the shed. The newly formed door opening had a nominal area of 27.8 ft^2 (4.8 ft ×5.8 ft). The mass of the metal shed was 346 kg, and the combustible mass of 15 wood cribs was 2138 kg.

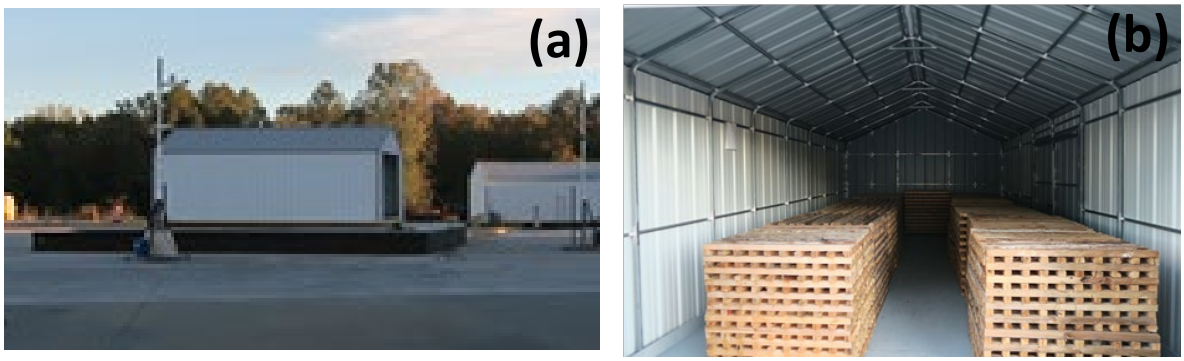

Fig. 145. Photograph of (a) steel Very Large shed setup with (b) high fuel loading of 15 wood cribs.

6.3.5.2. Burn Overview

The average local wind speed at the start of the shed burn was below 1 mi/h. For this Very Large shed, an aluminum pan filled with 500 mL of ethanol was used as an ignition source. The aluminum pan was placed under the middle crib situated at the end of the shed. The fire spread following the ignition of ethanol is shown in Fig. 146. The ignition of the wood crib at the rear end of the shed can be noted from Fig. 146(a). The fire spread to the adjacent cribs placed at the rear end of the shed (see Fig. 146(b)) generated intense smoke and heat. The severe heating of the metal components led to melting of the sealant material used in the construction of the shed; small flames jetting through the resulting gaps can be noted in Fig. 146(c). About 10 min following the ignition of ethanol, all wood cribs were burning, and flame lengths of approximately 5 ft were seen jetting out from the door opening. A maximum MLR of 0.9 kg/s was registered at this time as shown in Fig. 147. The estimated PHRR for this burn was 16.6 MW. The temporal plot of HRR in Fig. 147 shows steep increase in HRR during the flame spread over the wood cribs. The HRR dropped significantly following the peak and remained steady for 40 min until the shed structure collapsed. Fig. 146(e) and Fig. 146(f) show the collapse of the roof and walls, respectively. The collapse of the roof suppressed the flames while the collapse of the walls exposed the burning wood cribs to excess oxygen. This caused more intense burning and damaging the back wall of the shed more severely leading to complete collapse of the structure. The second peak in the HRR plot at 67 min corresponds to the collapse of the walls shown in Fig. 146(f). The effect of structural collapse significantly affected the heat flux measurements, as discussed below.

Generally, the burning behavior was steady and was not much affected by the wind, which remained stable throughout the burn. The temporal profile of the measured wind velocity is shown in Fig. 148.

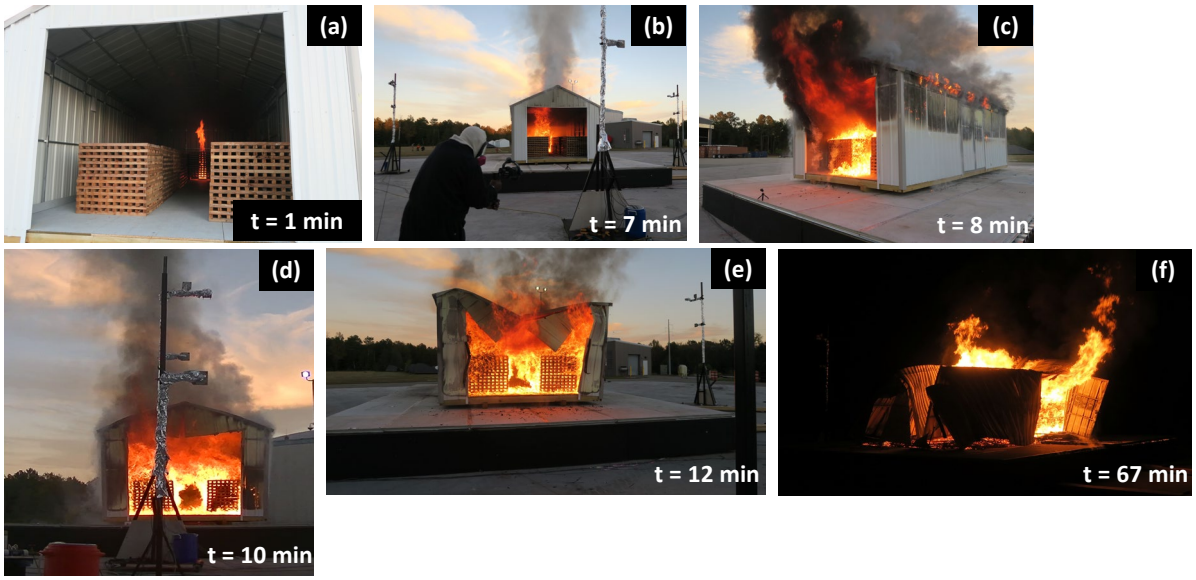

Fig. 146. Photographs showing (a) ignition of the wood crib, (b) flame spread to adjacent wood cribs, (c) flames jetting out from door opening, (d) flashover, (e) roof collapse, and (f) shed structure collapse in test 1B-SVLh0.

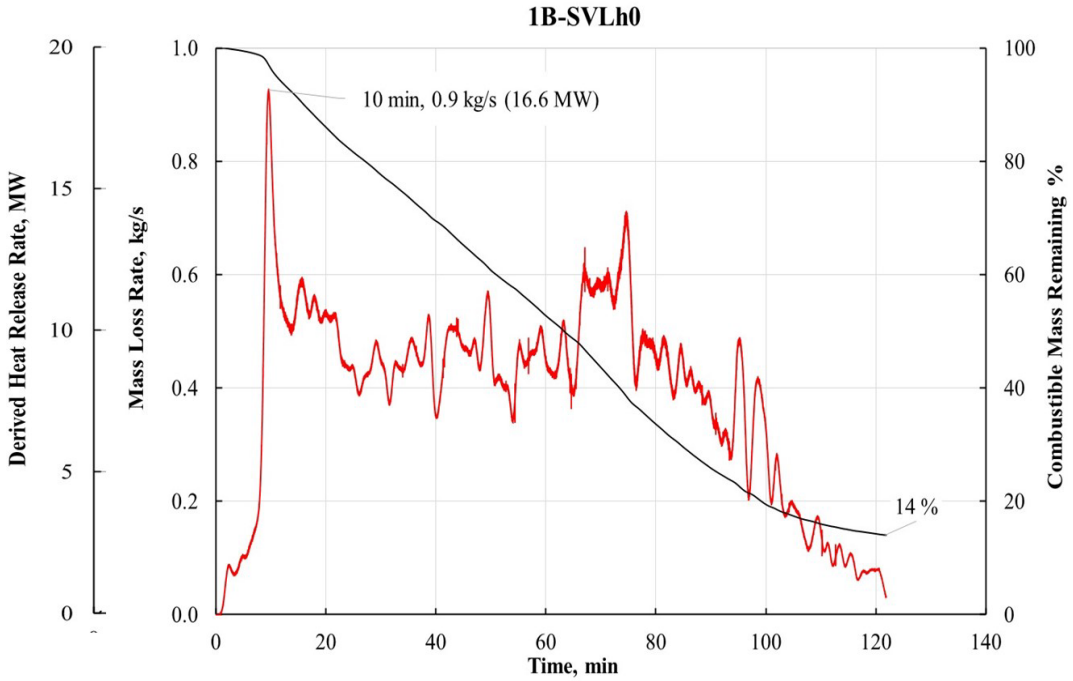

Fig. 147. Percent mass loss, mass loss rate, and derived HRR of combustible fuel in test 1B-SVLh0.

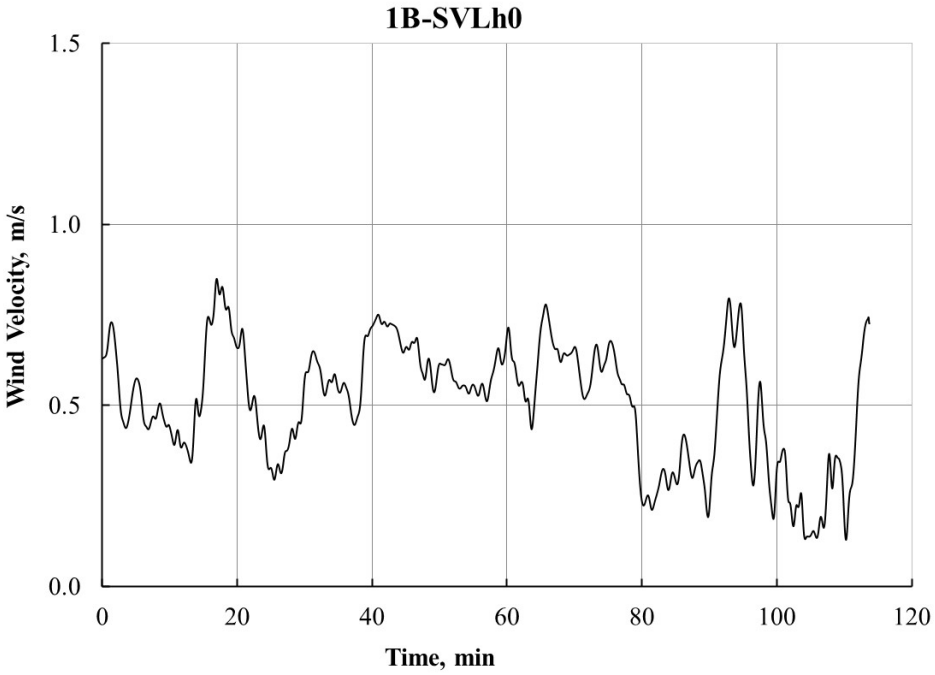

Fig. 148. Wind velocity measured during the shed burn in test 1B-SVLh0.

The heat flux data recorded at the three rigs located in front (Rig1), side (Rig2), and behind the shed (Rig3) are plotted in Fig. 149. Fig. 149(a) compares the heat fluxes measured at the fascia board height at all three rigs, and it can be noted that the heat fluxes recorded at Rig1 are higher than those registered at Rig2 and Rig3. This is primarily due to the fact that Rig1 was located in front of the door opening and the heat flux gauges were exposed to the radiant and convective heating while the heat flux gauges on Rig2 and Rig3 were not directly exposed to the flames while the structure was intact. As the fire progressed and the structure collapsed, the heat flux gauges on Rig2 and Rig3 registered heat fluxes up to 3.5 kW/m². Similar trends can be noted for heat flux data recorded at the under-eave position and at window height in Fig. 149(b) and Fig. 149(c), respectively.

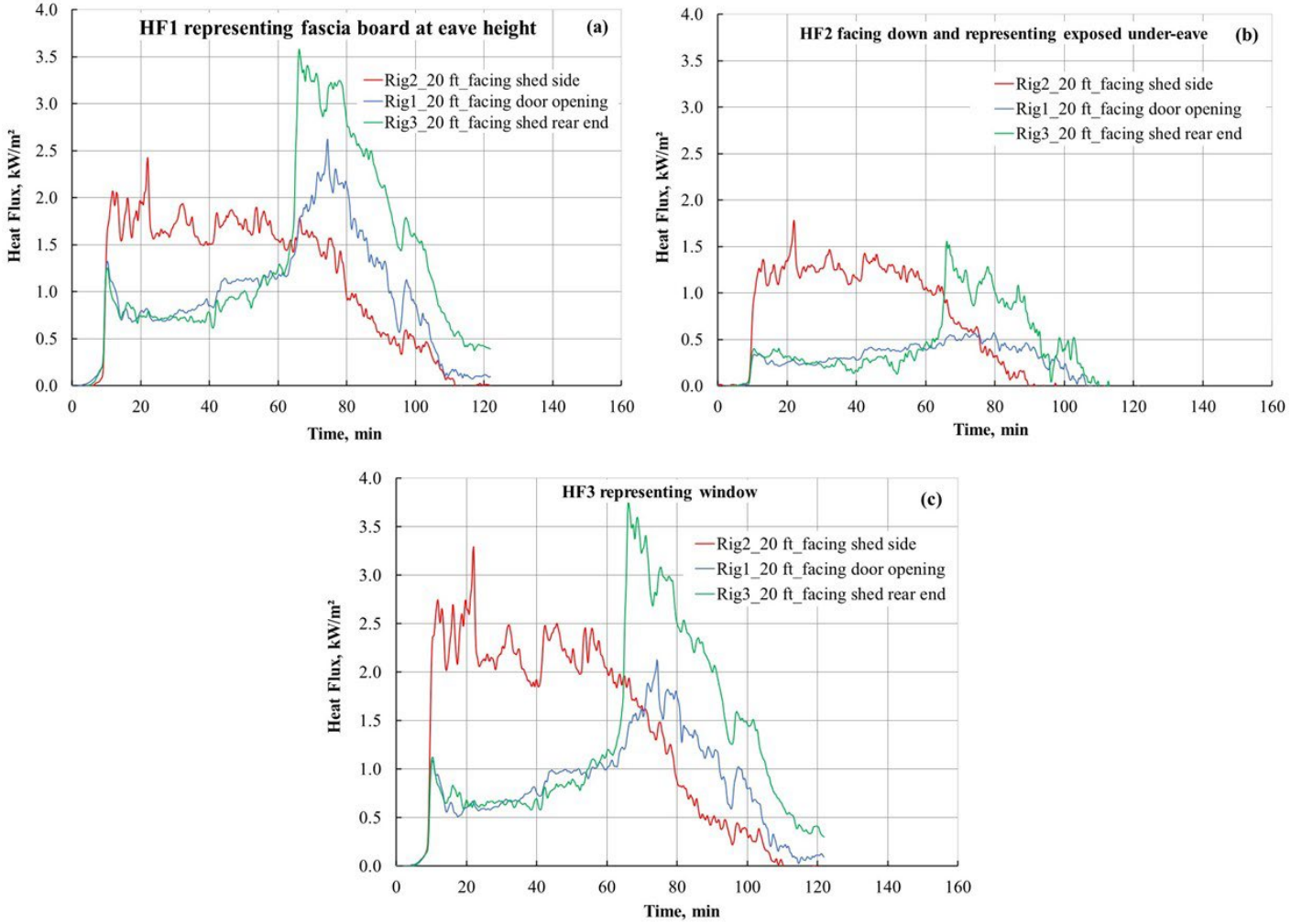

Fig. 149. Heat fluxes at (a) HF1-fascia board, (b) HF2- exposed under eaves, and (c) HF3-window, recorded simultaneously by gauges located on Rig1, Rig2, and Rig3 in test 1B-SVLh0.

6.3.6. Test:1B-WVLh0

6.3.6.1. Shed Specifications

The Very Large wooden shed is shown in Fig. 150(a) while the crib arrangement inside the shed is shown in Fig. 150(b) and (c). The double doors, located on the long side of the shed, were kept fully open and secured using screws, thereby creating an opening of 30 ft^2 (5 ft × 6 ft). The shed had two windows with nominal dimensions of 18 in × 22 in. The shed was nominally 10 ft tall and had a footprint of 288 ft^2. The combined mass of the shed and 15× 6-A wood cribs was about 4032 kg.

Fig. 150. Photograph of (a) wood Very Large shed setup with (b, c) high fuel loading of fifteen 6-A wood cribs.

6.3.6.2. Burn Overview

The average wind speed recorded on site just before ignition was about 1.6 mi/h ± 0.75 mi/h from the west. Due to the size of the shed and the amount of fuel loading, the ignition of the wood cribs for this test was carried out using 500 mL ethanol. To achieve uniform fire spread, the ignition source (aluminum tray filled with ethanol) was placed under the central crib within the shed.

Flame spread for this Very Large wooden shed was rapid, compared to the previously described shed burns. The key events during the Very Large shed burn are shown in Fig. 151. The entire fuel load and some parts of the shed were burning intensely about 10 min after ethanol ignition.

Flames of about 15 ft length jetting out from the door opening can be noted from Fig. 151(b). At about 13 min from the ignition of ethanol, the roof, windows, and some sections of the siding were consumed by the flames. Fig. 151(d) shows collapse of the roof. The total duration of the burn was 100 min.

The burning behavior was quantified by mass loss measurements, and the temporal profiles of percent mass loss, MLR, and the derived HRR are shown in Fig. 152. The peak MLR of 3.7 kg/s was recorded at 22 min into the test (see Fig. 152). The MLR profile from 12 min up to 25 min shows significant spikes suggesting noise in the measured mass loss data. This noise in the measured data corresponds to the flashover, collapse of the structural components, and the effect of the wind. The PHRR derived from the mass loss measurements was estimated to be 66.3 MW.

Peak heat fluxes between 20 kW/m² and 30 kW/m² were recorded at HF1 and HF3. The higher heat fluxes registered by HFGs located on Rig3 can be attributed to the plume leaning towards Rig3 (see Fig. 151 (e)).

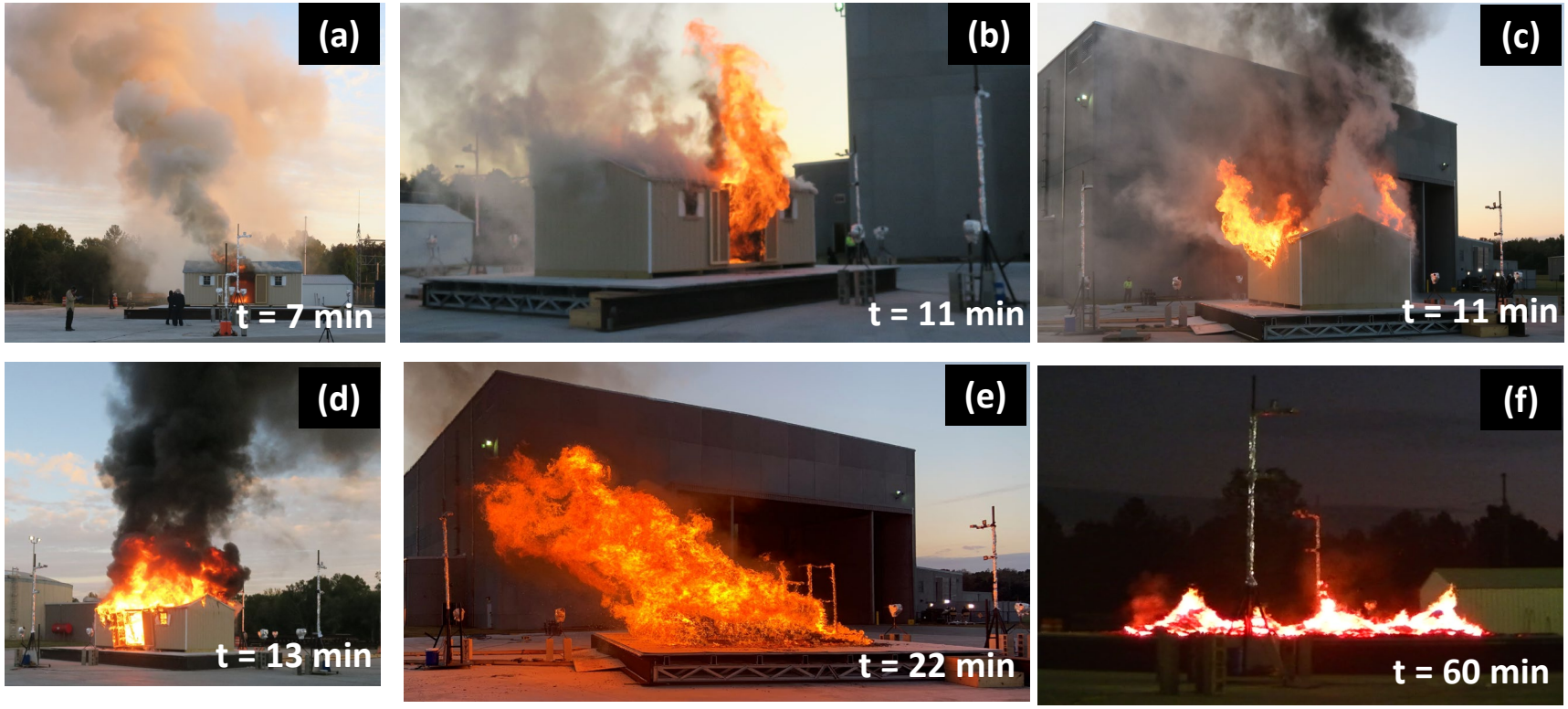

Fig. 151. Photographs showing (a) ignition of the wood crib and release of moisture and combustion products, (b) flames jetting out from door opening, (c) flame spread to the roof and the walls, (d) consumption of roof in the fire, (e) collapse of shed structure, and (f) residual burning of collapsed structure and wood cribs in test 1B-WVLh0.

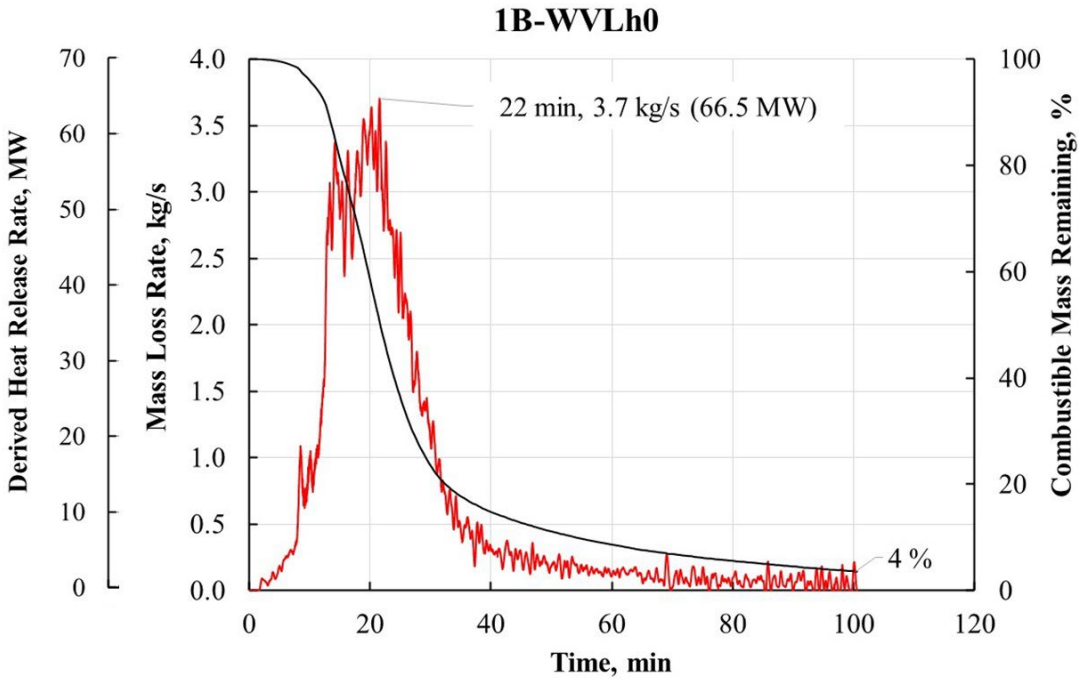

Fig. 152. Percent mass loss, mass loss rate, and derived HRR of combustible fuel in test 1B-WVLh0.

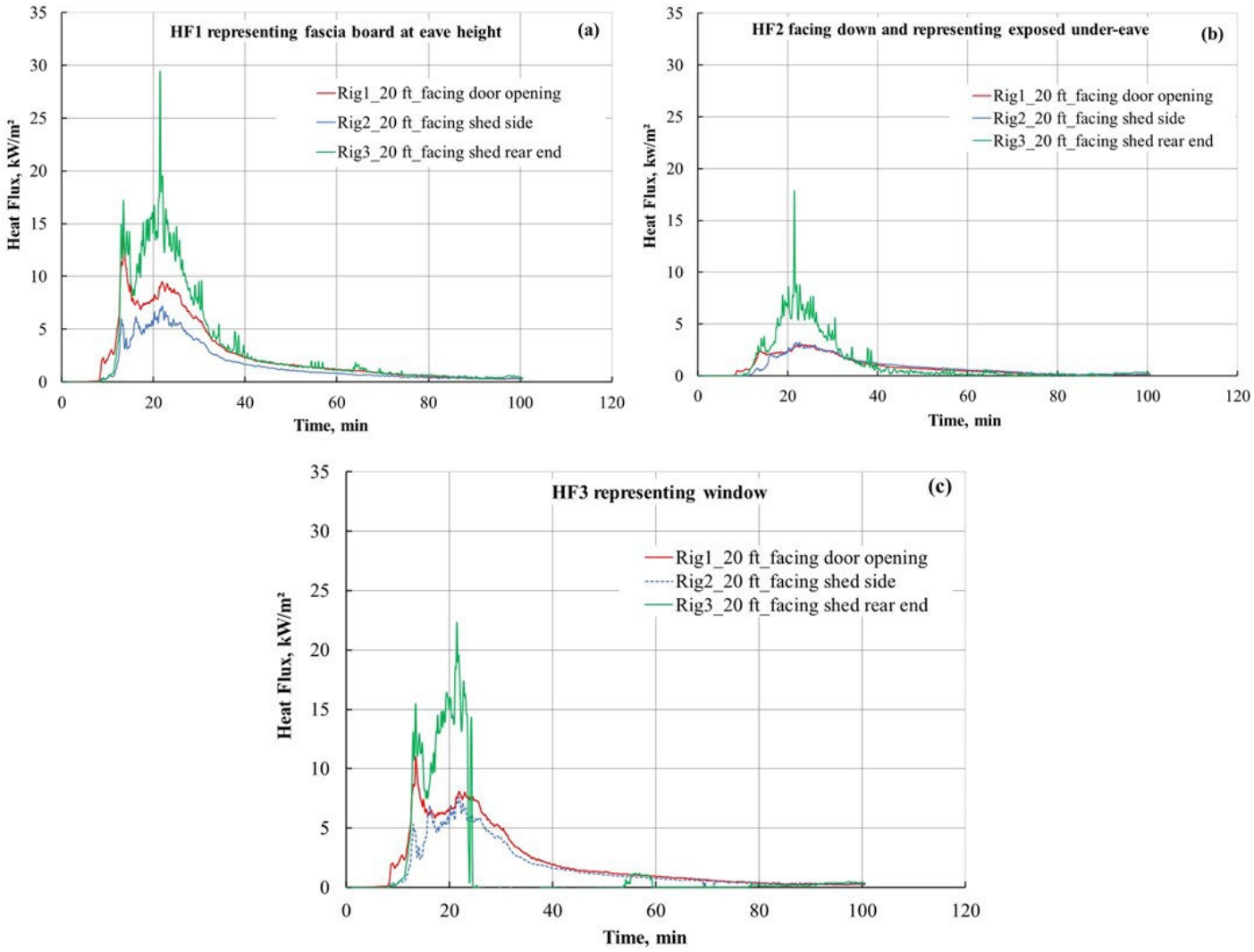

Fig. 153. Heat fluxes at (a) HF1-fascia board, (b) HF2- exposed under eaves, and (c) HF3-window, recorded simultaneously by gauges located on Rig1, Rig2, and Rig3 in test 1B-WVLh0.

6.4. Technical Findings

6.4.1. Mass Loss Method

Based on the successful estimation of HRR from mass loss measurements in the indoor shed burn experiments, the same method for estimating HRR was used for Medium, Large and Very Large sheds. Given that the maximum portion of combustible material was wood cribs, the heat of combustion of wood was used to estimate the HRR of the source structures. The primary findings are:

- The wind, the turbulence of hot gases during flashover, and the collapse of the structural components during the fire affected mass loss measurements.
- The derived HRR was generally noisy due to large fluctuations in mass loss data.
- The derived HRR should only be used as an estimate to assess the fire hazard of the source structure. The PHRR values should be used as general guidance because of the uncertainties in measuring mass loss and the assumed heat of combustion.

6.4.2. Effects of Construction Materials on Burning of Sheds

The effects of construction materials on the burning behavior of the Large and Very Large sheds can be noted from Fig. 154, comparing HRR measurements of combustible versus noncombustible shed constructions. The HRR plots for Large plastic and steel sheds with high fuel loading of six 6-A wood cribs shown in Fig. 154(a) show rapid burning of the plastic shed with an estimated PHRR of 29.8 MW. The walls and the roof of the plastic shed melted within 10 min of heptane ignition and opened the structure, exposing the wood cribs to excess ambient oxygen. All the combustible contents were consumed in the fire within 45 min. The steel structure remained intact throughout the burn (80 min), and the PHRR was reduced by a factor of 5.

Fig. 154(b) compares the temporal plots of Very Large sheds with high fuel loading of 15 6-A cribs. The PHRR for the Very Large wooden shed was significantly higher than that of the steel Very Large shed. The flames from the burning wood cribs consumed the wooden shed within 15 min with measured PHRR of 66.3 MW whereas the steel shed was intact for a longer duration of about 60 min. The PHRR for the steel shed registered at 10 min was lower than that of the wooden shed, with similar fuel loading, by a factor of 4.

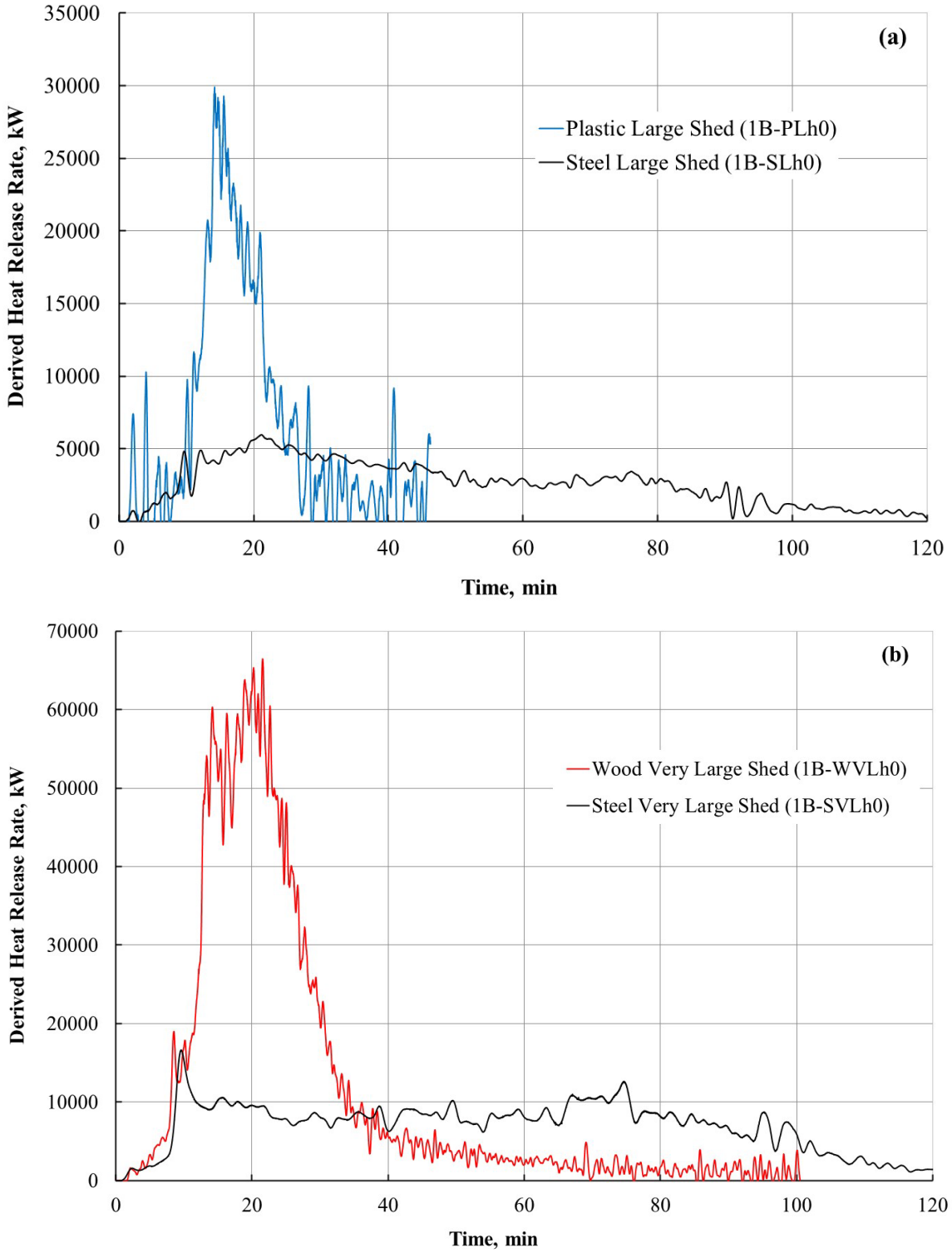

Fig. 154. Effects of shed construction materials on HRR for (a) Large sheds and (b) Very Large sheds.

6.4.3. Effects of Shed Size and Fuel Loading on Burning of Sheds

The effects of shed size and fuel loading on the HRR of the source structures can be noted from Fig. 155. Fig. 155(a) compares HRR plots for steel sheds of two different sizes (Large and Very Large), each with high fuel loading. The average HRR was 6911 kW for test 1B-SVLh0, while the average HRR for test 1B-SLh0 was 2626 kW. The duration of fuel burning was almost the same for both source terms. However, the severity of the fire is higher in the case of 1B-SVLh0. Similar trends can be noted (see Fig. 155(b)) for wooden sheds of different sizes with high fuel loading.

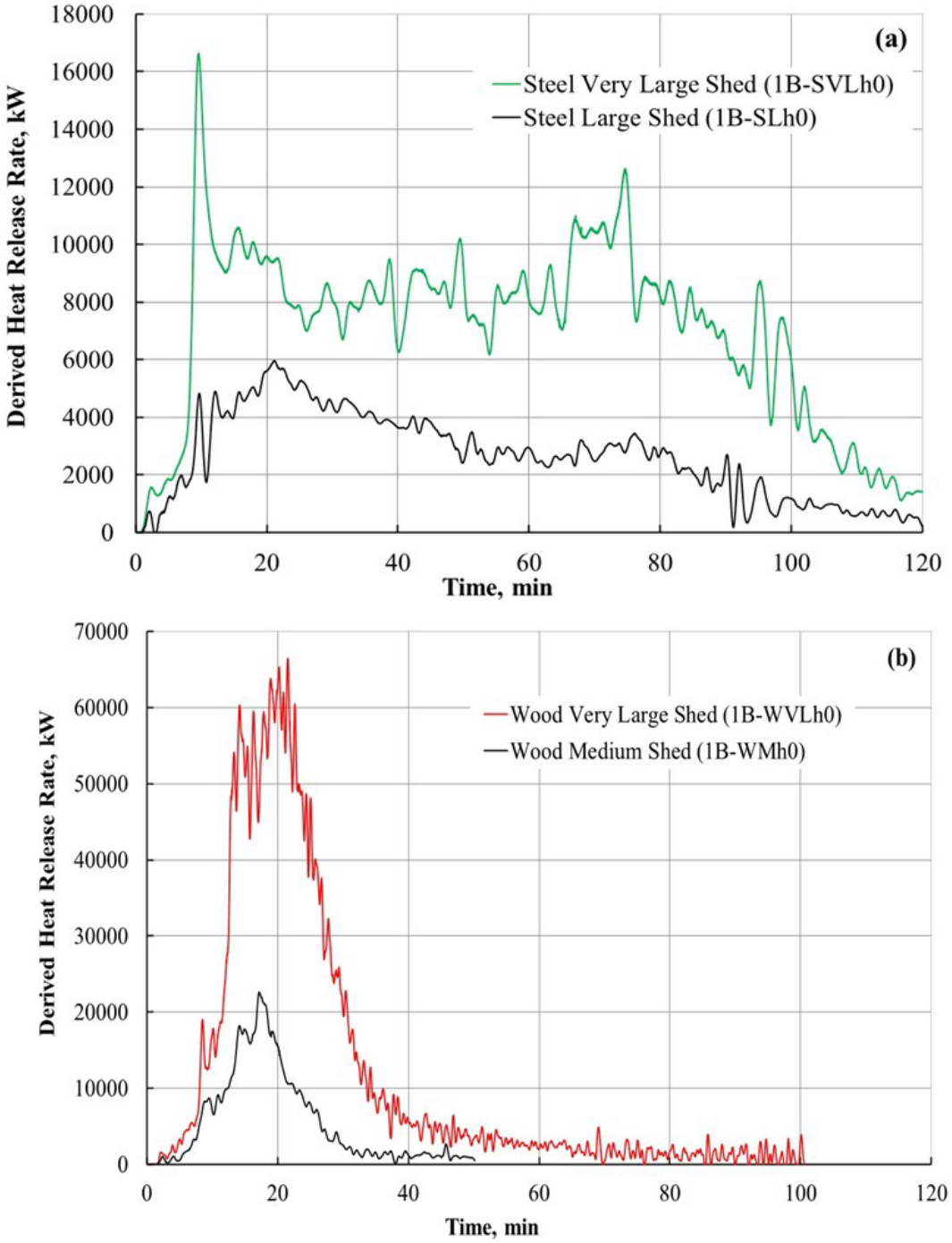

Fig. 155. Effects of shed sizes and fuel loadings on HRR for (a) steel and (b) wooden sheds.

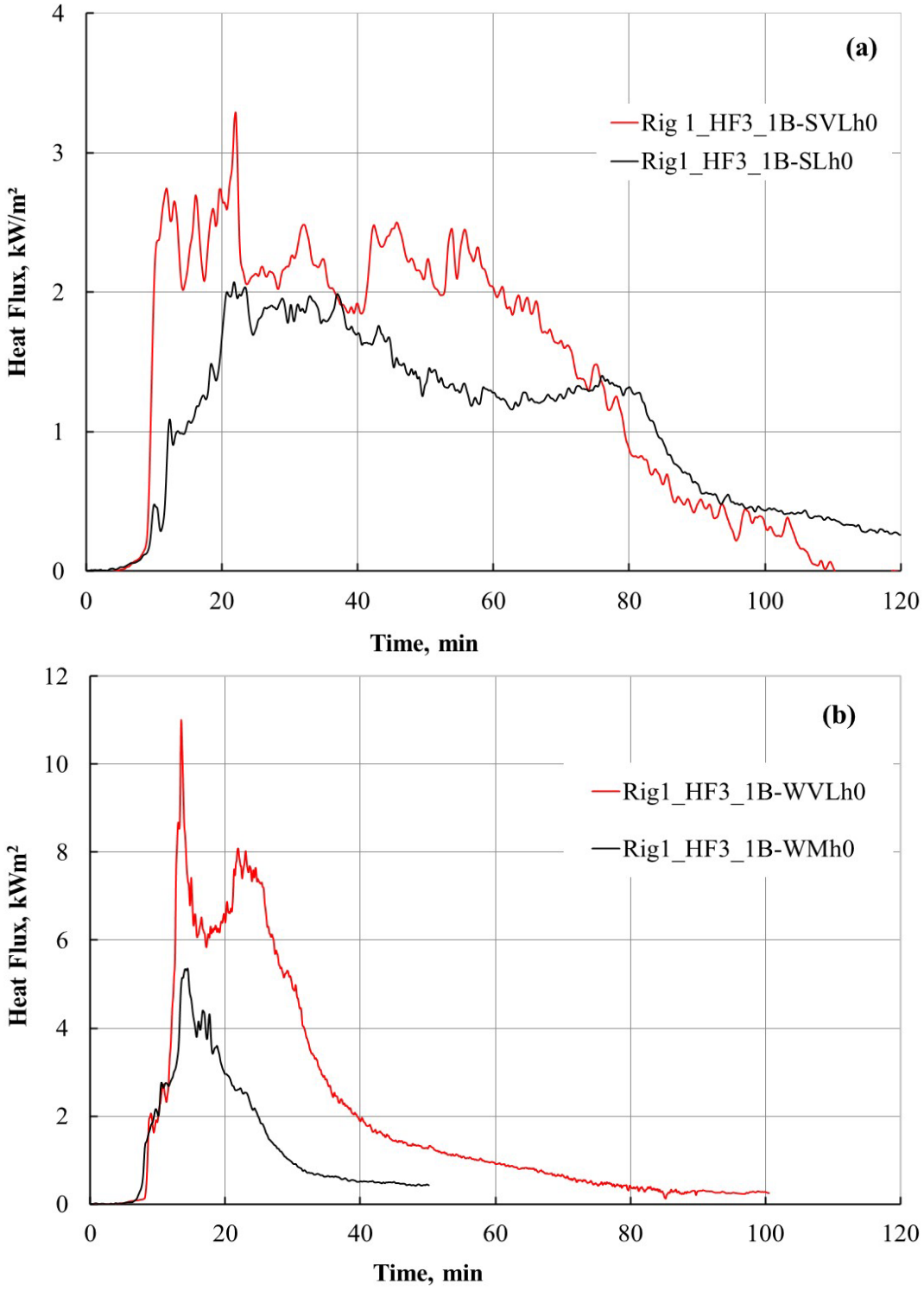

Fig. 156. Effects of shed sizes and fuel loadings on thermal exposures at window height (HF3) at Rig1 facing the door opening (SSD = 20 ft) for (a) steel and (b) wooden sheds.

6.4.4. Effects of Combustible and Noncombustible Sheds on Exposure Potential

The effects of shed construction materials on fire hazard can be assessed by measuring and comparing the heat fluxes at selected locations from sheds with similar fuel loading. This information can be used to inform SSD and fire source placement for future experiments with wind and provide preliminary guidance for implementation in hazard mitigation for no-wind scenarios.

Comparison of temporal profiles of heat fluxes measured at window height at a distance of 20 ft are shown in Fig. 157. The heat fluxes from the plastic Large shed are significantly higher than those from the steel Large shed as shown in Fig. 157(a); however, the duration of exposure is significantly shorter. The surrogate target structures were exposed to radiant and convective heat from burning wood cribs after the plastic melted, while the fire was contained within the steel shed resulting in a reduced amount of radiant heat to the surrogate targets. Similar trend can be noted from Fig. 157(b) which compares heat fluxes from steel and wood Very Large sheds with similar fuel loading of 12 6-A wood cribs. The duration of heat exposure from steel sheds is much longer compared to combustible plastic and wooden sheds with similar fuel loads. The steel sheds are much more capable of protecting surrounding target structures or fuels from radiant and convective heating. However, as was seen in the indoor experiments, significant "jetting" of the fire was observed outside the door opening, reaching the target structure at 5 ft even in cases with no wind. Any directionality of the flames would influence the heat flux; therefore, the true maximum exposure is expected to be greater than measured in these experiments.

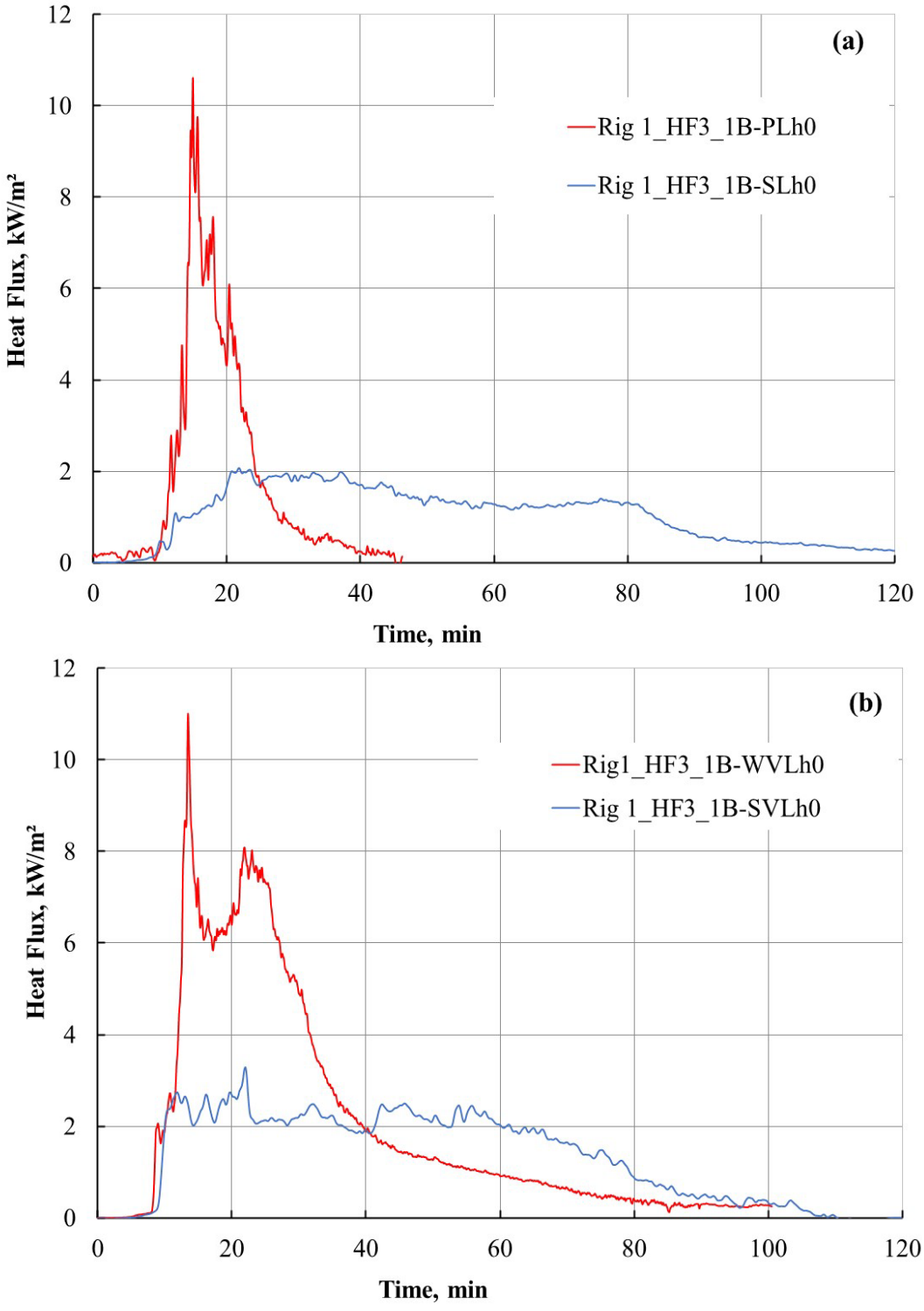

Fig. 157. Comparison of temporal profiles of heat flux data measured at window height (HF3) on Rig1 facing the door opening for (a) plastic and steel sheds and (b) wood and steel sheds of similar sizes and fuel loadings with an SSD of 20 ft.

7. Overall Summary of Technical Findings and Implementation Guidance

If ignited, auxiliary structures can become a source of high thermal exposure to a primary residential structure. Structures of this type that have a floor area of less than 120ft^2 are often unregulated and placed against or near primary structures. The fire hazard from auxiliary structures is particularly critical in high-density housing areas where structures are closely spaced, and structure-to-structure fire spread can exponentially increase the impacts of a WUI fire event. Fire exposures from a range of auxiliary structures (sheds) were quantified in this study; however, the effects of wind and terrain on the exposures and fire spread were not included.

The fire hazard and exposure possibilities from different shed construction materials in the absence of wind are illustrated in Fig. 158. The noncombustible steel shed with an open door has a directional high hazard while the combustible wood shed can generate uniform thermal exposure. The combustible plastic shed melts and burns as a pool fire, and the melted polymer can flow downhill and spread the fire significantly.

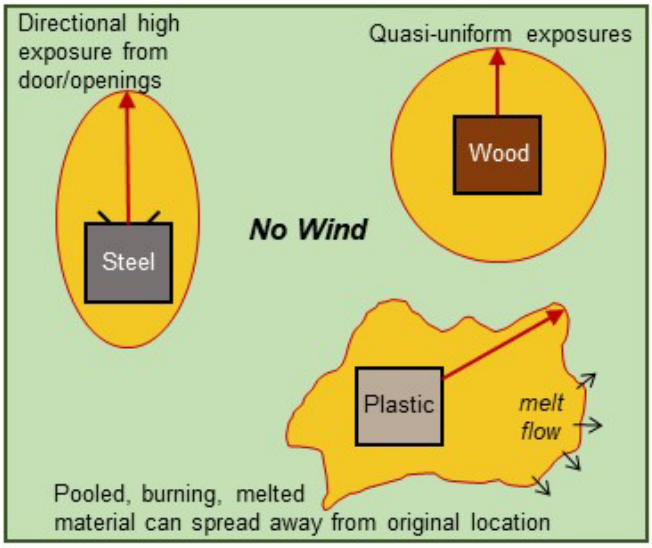

Fig. 158. Schematic showing possible fire spread hazards from sheds with different construction materials and door orientation.

The fire hazard from combustible and noncombustible sheds to the primary and the neighboring residential structure is shown in Fig. 159(a) and Fig. 159(b), respectively. The combustible wood Closet without any combustible contents (fuel loading) is a direct fire threat to the primary residence, as was shown in test 1B-WCl0-0. The noncombustible steel shed (Very Small shed) with high fuel loading, on the contrary, is not much of fire threat to the primary residence, but it poses significant fire threat to the neighboring residence as was demonstrated in test 1B-SVSh0-5.

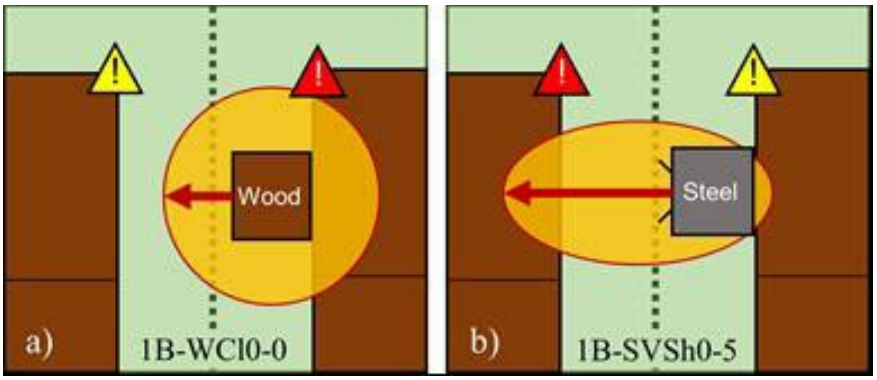

Fig. 159. Schematic showing fire hazard to the primary residence and residence on the neighboring lot from (a) combustible and (b) noncombustible sheds.

Wind and topography impact the fire exposure from auxiliary structures to nearby combustibles. Neither of these parameters were assessed in this initial SSD study. The findings of this study apply for hardened construction as described in Section 5.2.1; SSDs will need to be increased for non-hardened constructions. Overall findings of this study are listed below :

- The fire hazard of auxiliary structures (storage sheds) is a function of construction material used, the contents within the structure (fuel loading), structure orientation with respect to the primary structure, the size of door opening, and the structure separation distance (SSD).
- The construction material for wood and plastic sheds (Closets and Very Small sheds) contributed approximately 40 % towards total combustible mass, and hence higher PHRR, corresponding to higher fire hazard.
- The contents of noncombustible sheds can pose a fire hazard even if the shed itself does not contribute to the fire hazard.
- Non-flame retarded plastic sheds burn more intensely compared to wooden sheds evaluated in this study.
- Structural integrity of plastic sheds is compromised in the event of a fire. The plastic melts and burns as a pool fire, posing greater fire hazard due to fire spread.
- High heat fluxes in excess of 15 kW/m² were recorded at SSD = 20 ft for Very Large wooden shed with high fuel loading.
- Structure construction vulnerabilities to such exposures were studied for 1) non-tempered windows, 2) eave vents, 3) rafters and open eave assembly, and 4) wall assembly.
    - Vinyl window frames melt and distorted.
    - The limited data from the shed and target structure experiments suggests that heat fluxes of approximately 15 kW/m² for at least 5 min resulted in the ignition of open eaves.
    - Eave vents failed to prevent flame penetration when the eaves and rafters ignited. The performance of these vents cannot be interpreted as failures with respect to the standard test method (ASTM D 2886) as the thermal exposures to the vents were significantly different than those specified in the standard. However, when exposed to realistic hazards as in burning sheds, the eave vents failed to perform.

- Under flaming conditions, the non-flame retarded caulking around the eave vent degraded and formed an opening for flame penetration while flame retarded caulking stayed intact and prevented flame penetration in the vent attic.
- An extra layer of gypsum panel sheathing in the exterior wall construction (underneath the noncombustible cladding) was necessary to prevent the ignition of OSB from the combustible source structures.

The minimum SSD is defined as the shortest distance between the source and the target structure to prevent ignition and flame spread. The implementation of the SSD can be achieved through best practices and/or regulation at the national, state, or community level. Given the limitations in regulating the contents (fuel loading) and orientations of auxiliary structures, structure-to-structure fire spread within high-density housing areas can be mitigated by implementing the identified structure separation distance (SSD), using the Remove, Relocate, Reduce (RRR) fuel management principles outlined in the HMM and hardening the residential structures against ember exposures. Considerations should be given to the effects of wind and slope on SSD. The effects of wind as assessed during the NIST Outdoor Structure Separation Experiments (NOSSE) on Closet, Very Small and Small Sheds are being documented in the upcoming SSE NIST Technical Note. A future NIST technical note will describe the experiments and results from the Very Large sheds with wind conducted at IBHS.

Recommendations

Presence of wind can significantly affect the flame spread within WUI communities; the SSDs identified in this study with no wind conditions bounds the fire exposures with minimum distances. Larger SSDs may be needed if the wind and terrain are factored in. Based on the key findings of this study, the following recommendations can be made.

Shed Usage

- ✓ Consider Remove, Relocate, Reduce (RRR) as specified in the HMM to reduce fire exposures.
  - Minimum SSD[7,8] = 10 ft for Closet and Very Small sheds (< 26 ft^2).
  - Minimum SSD = 20 ft for Large and Very Large sheds (< 288 ft^2).
- ✓ Choose construction materials to reduce exposures; however, this alone cannot substitute for RRR and SSD
  - Consider relative position of neighboring residence for door orientation of noncombustible steel shed.
  - Keep doors closed.
  - Avoid placing plastic sheds on sloped terrain and/or where pool fires can spread and ignite nearby combustibles.

Target Hardening

- ✓ Replace annealed glass windows with tempered glass where fire exposures are expected on the structure. This should be done in conjunction with window screens and other necessary structure hardening for embers and fire (HMM).
- ✓ Use flame-retardant caulking around windows and eave vents.
- ✓ Additional gypsum panel sheathing similar to DensGlass® may be used to prevent ignition of combustible layers of the exterior wall assembly.

Further Research

- ✓ The standard test method for assessing performance of eave vents needs to be further assessed for realistic thermal exposures. **N**IST **E**ave **V**ent **E**xperiments (NEVE) have been planned to assess vent performance exposed to flaming fires.
- ✓ Assess the performance of fire caulking for extended exterior use. Work is planned at NIST to assess the fire performance of flame retarded caulking that has been exposed to accelerated weathering.

[7] Minimum SSD applies for hardened construction as described in Section 5.2.1; SSD will need to be increased for non-hardened constructions.
[8] Minimum SSD listed here does not account for effects of wind and slope

References

[1] Maranghides A., Link ED., et al. (2021) A Case Study of the Camp Fire - Fire Progression Timeline. NIST Technical Note 2135. National Institute of Standards and Technology, Gaithersburg, MD. https://doi.org/10.6028/NIST.TN.2135

[2] Maranghides, A., Link ED., et. al. (2022) WUI Structure/Parcel/Community Fire Hazard Mitigation Methodology. NIST Technical Note 2205. National Institute of Standards and Technology, Gaithersburg, MD. https://doi.org/10.6028/NIST.TN.2205

[3] Maranghides, A., Nazare S., et al. (2021) Structure Separation Experiments Phase 1 Preliminary Test Plan. NIST Technical Note 2161. National Institute of Standards and Technology, Gaithersburg, MD. https://doi.org/10.6028/NIST.TN.2161

[4] ASTM E 2957- Standard Test Method for Resistance to Wildfire Penetration of Eaves, Soffits and Other Projections.

[5] Bryant RA. and. Bundy MF. (2019) The NIST 20 MW Calorimetry Measurement System for Large-Fire Research. NIST Technical Note 2077. National Institute of Standards and Technology, Gaithersburg, MD. https://doi.org/10.6028/NIST.TN.2077

[6] NIST Fire Calorimetry Database (FCD) https://doi.org/10.18434/mds2-2314

[7] Putorti A, Melly NB, Bareham S, Praydis Jr J (2015) Characterizing the Thermal Effects of High Energy Arc Faults. *23th International Conference on Structural Mechanics in Reactor Technology (SMiRT 23)-14th International Post Conference Seminar on Fire Safety in Nuclear Power Plants and Installations*.

[8] Ingason H. and Wickström U. (2007) Measuring incident radiant heat flux using the plate thermometer. *Fire Safety Journal* 42(2):161-166.

[9] ANSI/UL 711, Standard for Rating and Fire Testing of Fire Extinguishers, 2013.

[10] Walton W. (1988) Suppression of Wood Crib Fires with Sprinkler Sprays: Test Results. NBSIR 88-3696, National Bureau of Standards, U.S. Department of Commerce.

[11] ASTM E 2886- Standard Test Method for Evaluating the Ability of Exterior Vents to Resist the Entry of Embers and Direct Flame Impingement.

[12] Quarles SL and Sindelar M. (2011) Wildfire Ignition Resistant Home Design (WIRHD) Program: Full-scale Testing and Demonstration Final Report. https://doi.org/10.2172/1032503

[13] Vacca P., Caballero D., et al (2020) WUI fire risk mitigation in Europe: A performance-based design approach at home-owner level. Journal of Safety Science and Resilience 1(2), 97-105 https://doi.org/10.1016/j.jnlssr.2020.08.001

[14] Taylor BN , Kuyatt CE (1994) Guidelines for evaluating and expressing the uncertainty of NIST measurement results. NIST Technical Note 1297. National Institute of Standards and Technology, Gaithersburg, MD.

[15] Maranghides A and Johnsson EL (2008) Residential Structure Separation Fire Experiments, NIST Technical Note 1600. National Institute of Standards and Technology, Gaithersburg, MD.

Appendix A. Calibration of Heat Flux Gauges

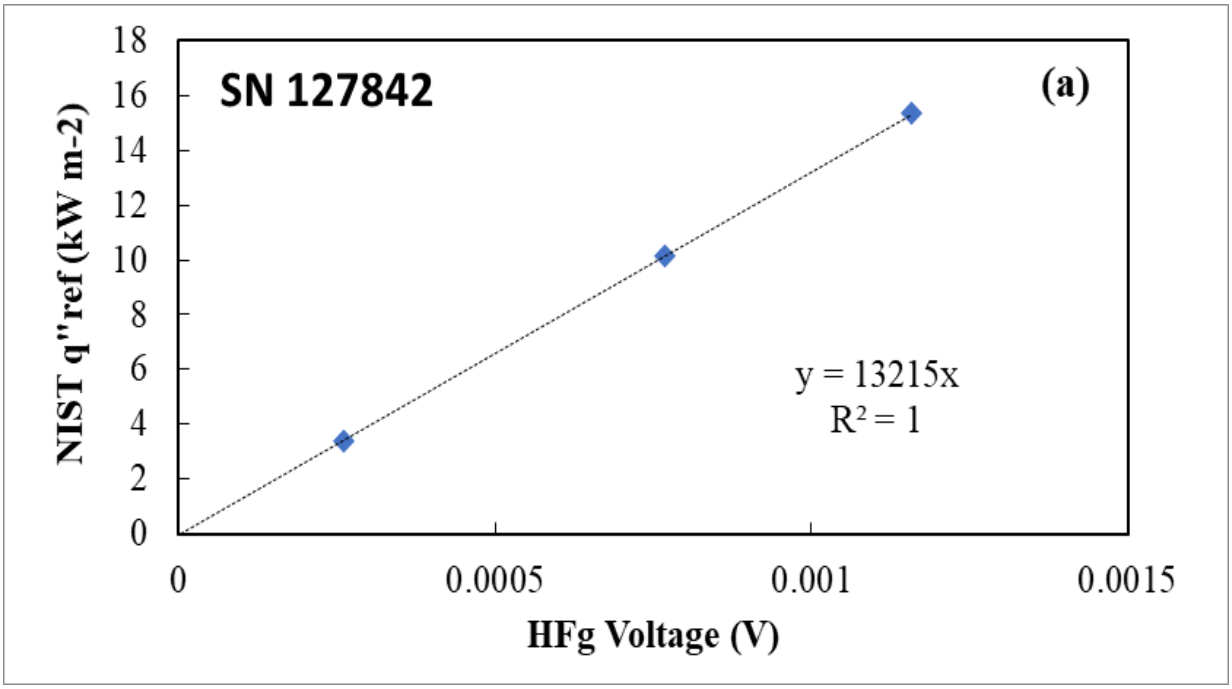

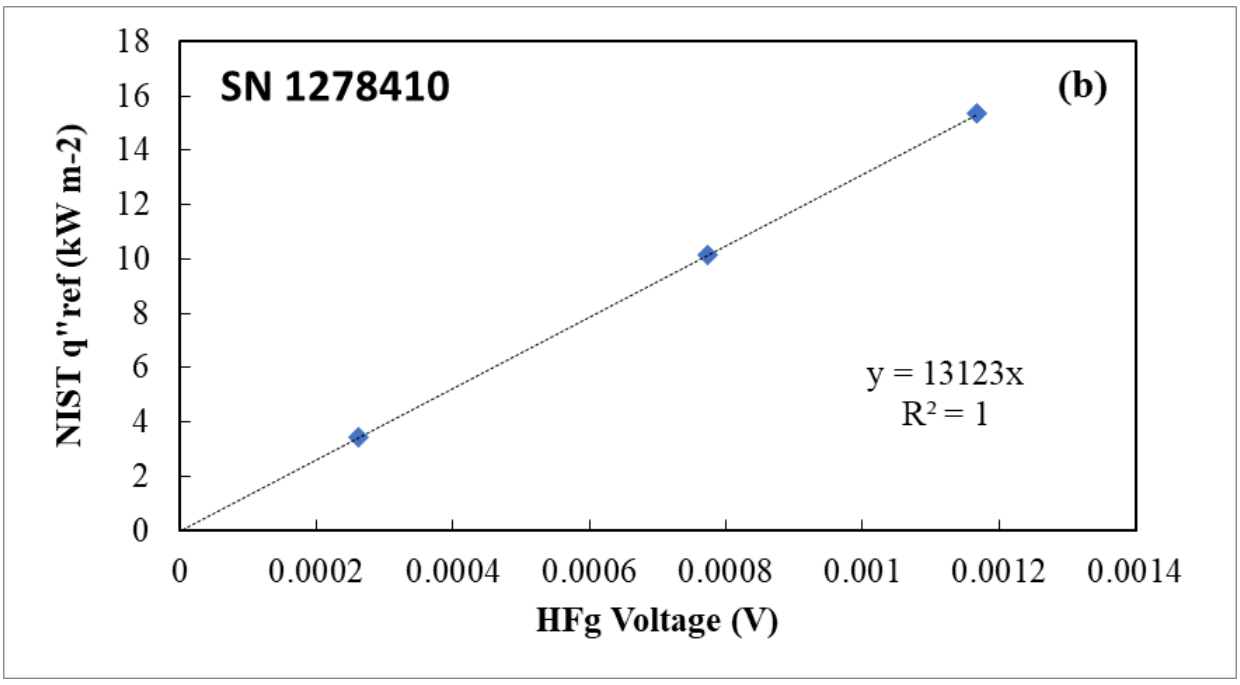

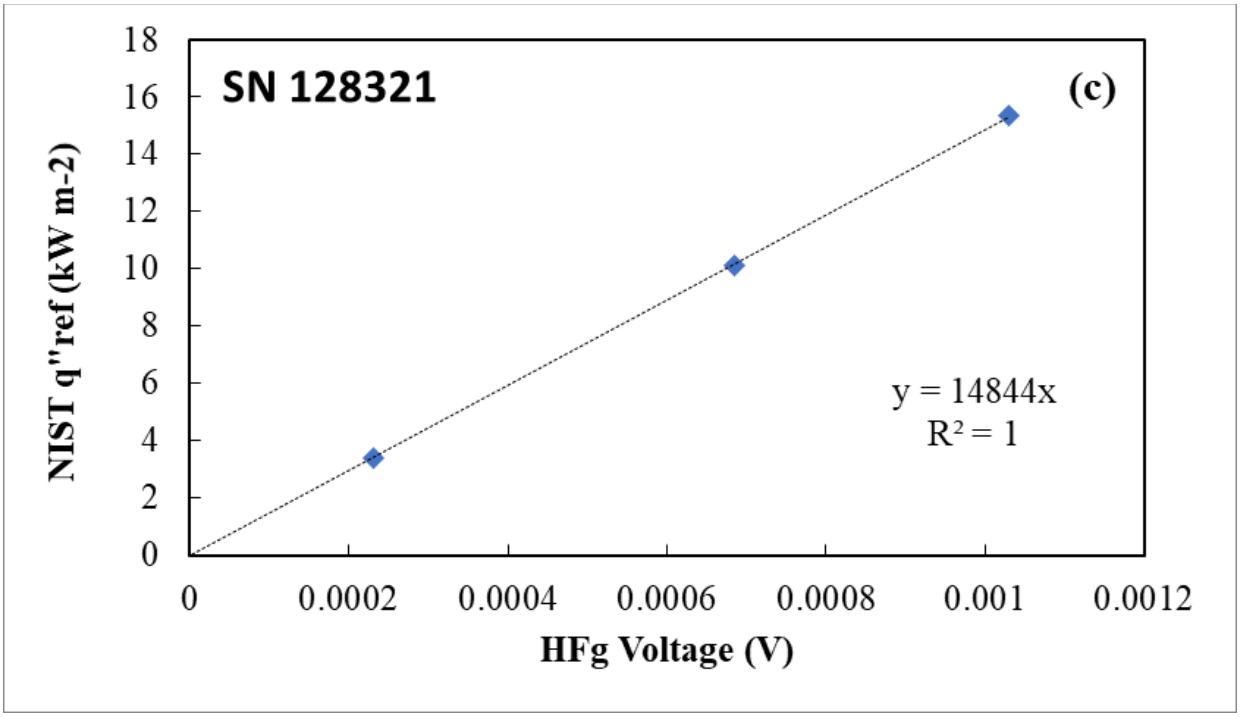
SN 128321
(c)
NIST q''ref (kW m-2)
HFg Voltage (V)
y = 14844x
R² = 1
0
2
4
6
8
10
12
14
16
18
0
0.0002
0.0004
0.0006
0.0008
0.001
0.0012

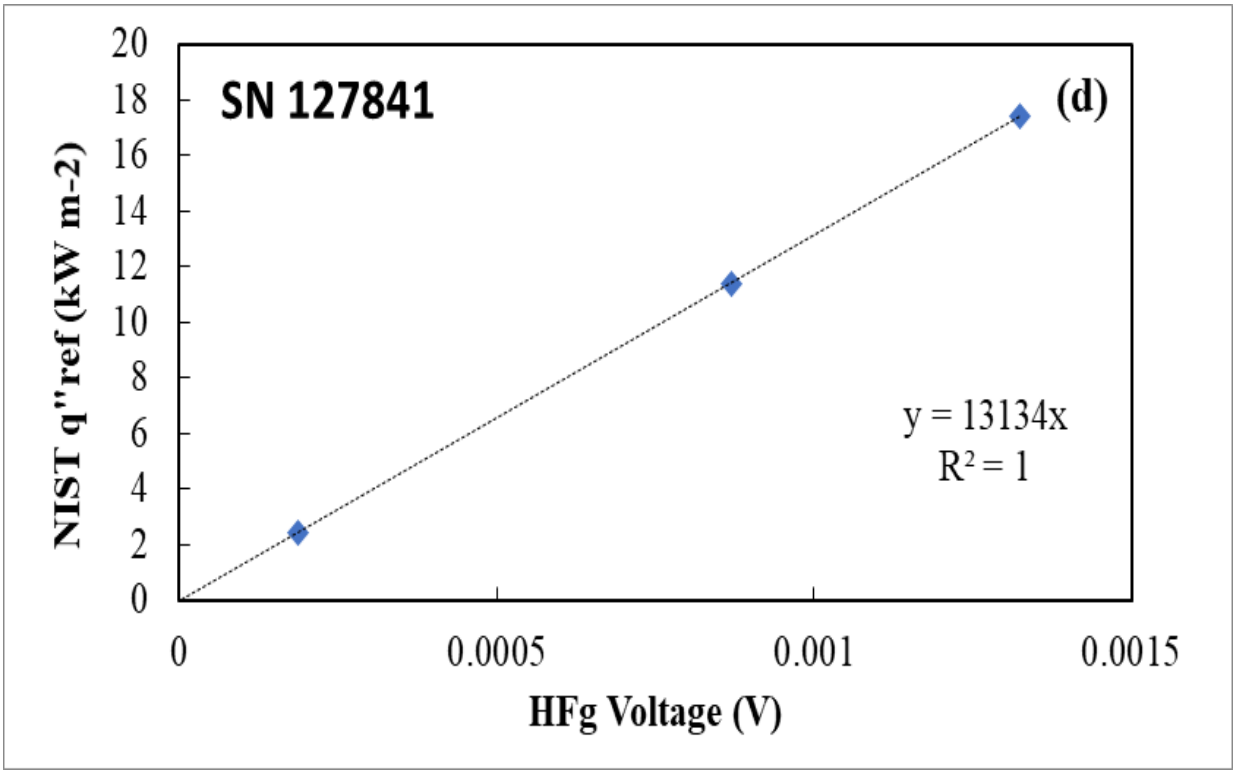
SN 127841
(d)
NIST q''ref (kW m-2)
HFg Voltage (V)
y = 13134x
R² = 1
0
2
4
6
8
10
12
14
16
18
20
0
0.0005
0.001
0.0015

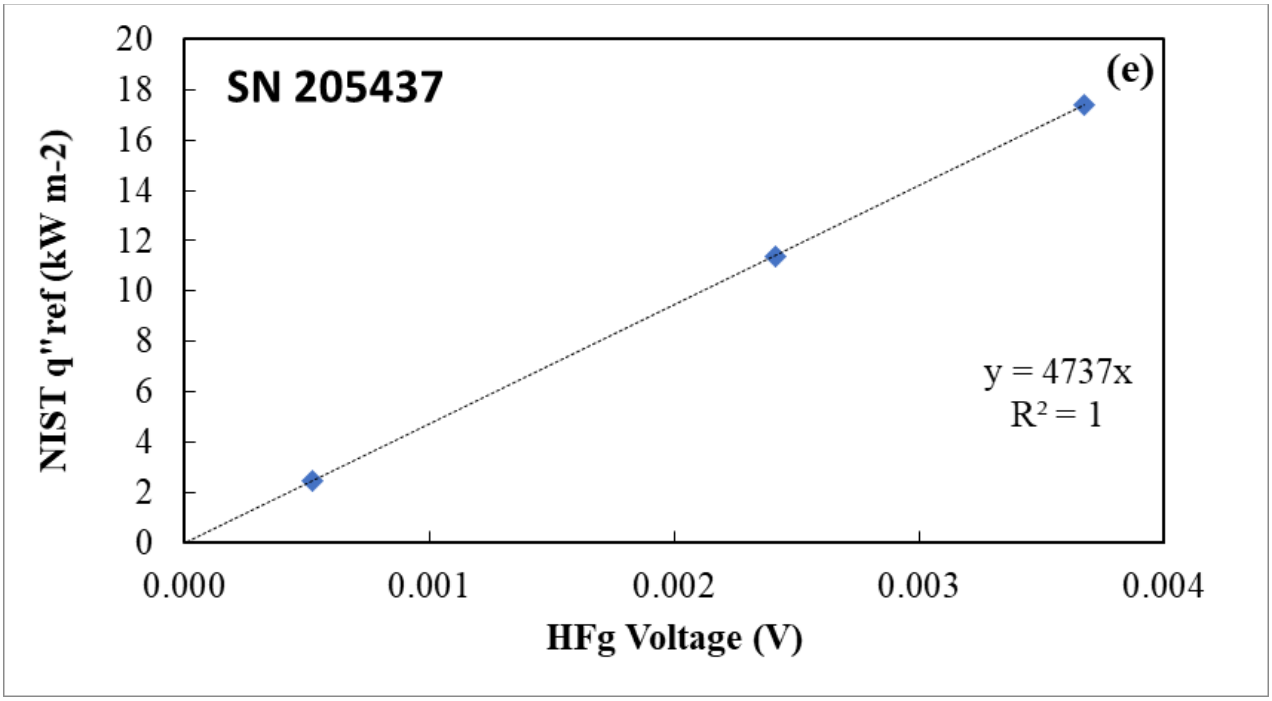

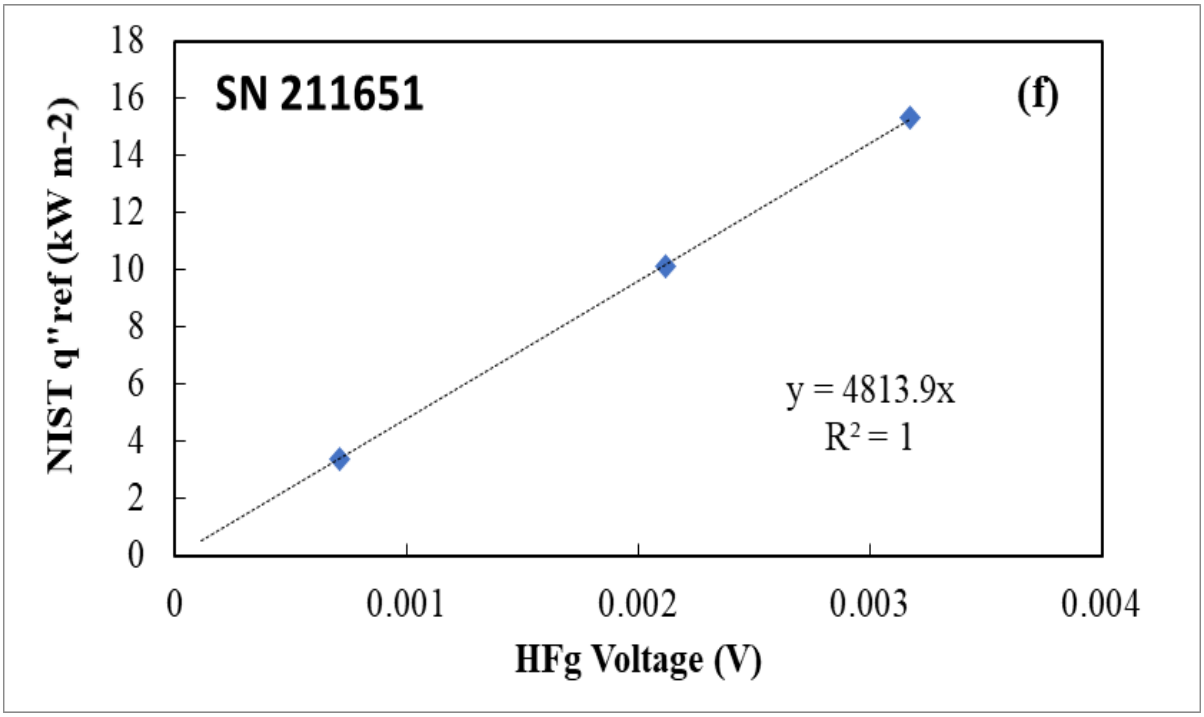

Fig. A- 1. Calibration plots for (a) HF1, (b) HF2, (c) HF3, (d) HF4, (e) HF5, and (f) HF6.

Table A- 1. Heat flux sensor and calibration specifications for heat flux gauges used in indoor shed burn experiments.

ID	Manufacturer	Serial Number	Calibration Constant, (kW/m2 /mV)
HF1	Medtherm	127842	13.215
HF2	Medtherm	1278410	13.123
HF3	Medtherm	128321	14.844
HF4	Medtherm	127841	13.134
HF5	Medtherm	205437	4.373
HF6	Medtherm	211651	4.813

Heat Flux Sensor Calibrations

A total of ten (10) heat flux sensors were used for IBHS no wind experiments. Seven (7) were HukseFlux heat flux sensors model SBG01-200, 180-degree field of view and measurement range up to 200 kW/m2. Three (3) were Medtherm heat flux transducers model 64-10SB-18.

These sensors were calibrated in October 2021 prior to the start of this experimental series with a Mikron M300 blackbody calibration source.

Table A- 2. Calibration specifications for heat flux gauges used in outdoor shed burn experiments

Sensor ID	**Serial Number**	**Manufacturer**	**Model**	**Calibration Slope**	**Calibration Y-intercept**	**R-squared value**
R1_HF1	13234	Hukseflux	SBG01-200	6162	0.1003	0.9955
R1_HF2	13233	Hukseflux	SBG01-200	6680	1.8561	0.9923
R1_HF3	13230	Hukseflux	SBG01-200	7008	1.564	0.9922
R2_HF1	13232	Hukseflux	SBG01-200	6846	0.1902	0.9945
R2_HF2	105462	Medtherm	64-10SB-18	10735	11.788	0.9998
R2_HF3	13235	Hukseflux	SBG01-200	6012	2.0339	0.9935
R3_HF1	13227	Hukseflux	SBG01-200	10391	10.6420	0.9999
R3_HF2	172104	Medtherm	64-10SB-18	5464	1.4362	0.9963
R3_HF3	13231	Hukseflux	SBG01-200	10463	11.7060	0.9998

Appendix B. Calibration of IBHS Weighing Platform

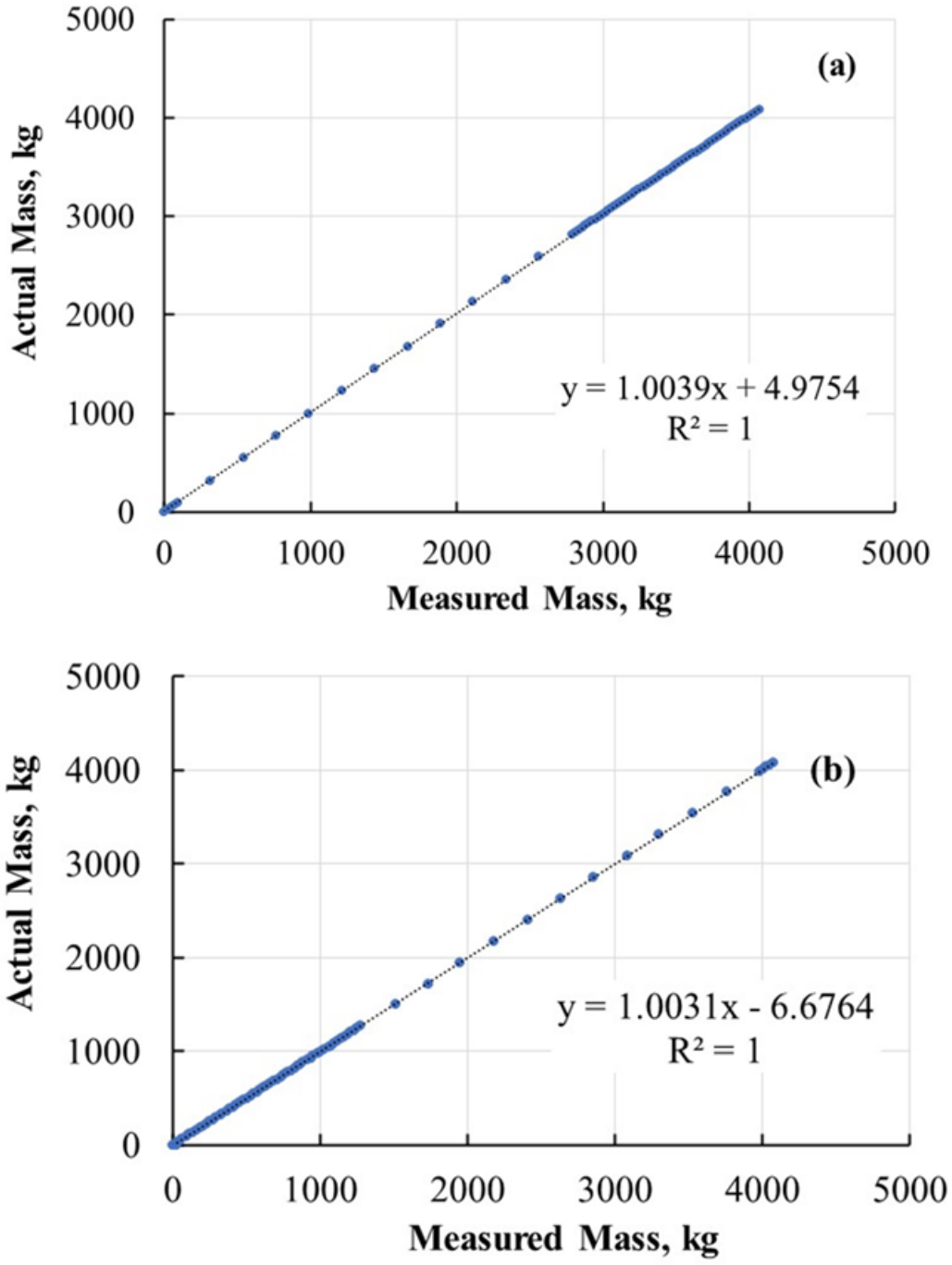

Fig. B- 1. Calibration plots for (a) loading and (b) unloading of the IBHS weighing platform.

Appendix C. Uncertainty of Measurements

The measurements of heat release rate, heat fluxes, temperatures, times, airflow, mass, and distances have uncertainties. Measurement uncertainties have several components typically grouped into two categories based on the method used to estimate their value. Type A uncertainties are evaluated by statistical methods, and Type B uncertainties are evaluated by other means, often based on scientific judgment using all available relevant information [14]. The component standard uncertainty includes resolution, calibration, installation, and random errors. The resolution is the minimum change in the data measurement the instrument can exhibit. Calibration error includes uncertainties from sensor calibration. The resolution and calibration uncertainties were derived from instrument specifications (Type B). Uncertainty due to the installation method was estimated based on engineering judgment (Type B) considering misalignment, quality of the sensor mounting method, and previous data.

Given the nature of experiments and hence the singular measurements in this study, the evaluation of Type A uncertainties was not feasible for majority of measurements. Most uncertainties reported herein are Type B uncertainties, either estimated through scientific judgment or obtained from the literature.

Airflow measurements: No statistical analysis was performed on the airflow measurements in this study.

Temperature measurements: Type K thermocouples used in this test series have an inherent standard uncertainty of the standard relative uncertainty in temperature measurements reported by the manufacturer was ± 0.75 %.

Additional uncertainties in measured temperature are primarily due to radiative heating and cooling of the thermocouple bead that causes it to respond to phenomena other than the surrounding gas temperature. Due to the nature of fire testing, the thermal environment surrounding a given thermocouple is difficult to characterize. These uncertainties will overwhelm the inherent uncertainties in the thermocouple described earlier.

The FLIR camera has standard uncertainty of 2 °C (4 °F) or 2% of the measured temperature. The uncertainties in temperature measurement using IR camera may result from emissivity value employed, reflected temperature, distance between the camera lens and the target surface, ambient temperature, transmittance, and calibration accuracy. The FLIR temperature measurements were used qualitatively and these additional factors were not quantified.

Heat release rate measurements: The average expanded uncertainty in measuring the HRR in the normal operating range of the 10 MW (8.4 m × 12.4 m) hood for generic combustible fuels is 8.7 %. This uncertainty is valid for near steady state fires. Transient events (less than 30 s) may have more significant uncertainty because of system response time. The range of expanded uncertainty for the natural gas (fuel consumption) verification burners is 1.4 % to 1.8 %. Bryant and Bundy [5] provide detailed information on the NFRL calorimetry measurement system.

Heat flux measurements: The relative expanded uncertainty reported by the manufacturer is ± 3 % of the gauge sensitivity (the slope of the calibration curve) with a coverage factor of 2. This would result in an uncertainty of about 4 kW/m^2 for a nominal reading of 140 kW/m^2. The main sources of uncertainty about the total heat flux measurements are: (1) the uncertainty of the A/D conversion, (2) uncertainty in the calibration, and (3) uncertainty due to soot deposition on the sensing surface of the gauge [15]. The uncertainty in A/D conversion is inherent to the data

acquisition system. It is system-specific and is associated with the digitization of the analog signals from the gauge. This type of uncertainty is negligible. The uncertainty due to soot deposition is more challenging to quantify. The amount of soot deposition depends on many parameters, such as the location of the gauge, the flow field and temperature fields near the gauge, the duration of an experiment, and the soot volume fraction. No attempt was made to quantify this soot effect for these experiments. Additional uncertainty due to flame impingement on the gauges is considered negligible.

The expanded uncertainty in steady-state heat flux under ideal conditions measured by the plate thermometers is 5 % at 75 kW/m^2.

Distance measurements: The structure separation distances (SSDs) between the target wall and the source structure and the distance between the source structure and instrumentation including the heat flux gauge rigs (surrogate target structures) were determined using a tape measure. Sources of uncertainty include the placement of the tape measure and the ability to adjust the positions of the source structure and the HFG rigs accurately. The construction dimensions are rounded to the nearest tenth. The expanded uncertainty for engineering measurements with a confidence level of 95 % was estimated as ½ inch (1.2 cm). For longer tape measures, the expanded uncertainty was ±1 in (±2.54 cm).

The users of this report are advised to be informed that the experimental results presented in this report are either raw data or the statistics of raw data acquired by the measurement systems. Incorporating the measurement uncertainty reported herein into the validation of predictive models is highly recommended.

Appendix D. List of Symbols, Abbreviations, and Acronyms

AHJ	Authorities Having Jurisdiction
CBIA	California Building Industry Association
CAL FIRE	California Department of Forestry and Fire Protection
CO	Carbon Monoxide
DAQ	Data Acquisition
ECS	Emissions Control System
FDS	Fire Dynamics Simulator
FLIR	Forward-Looking InfraRed
HDPE	High Density Polyethylene
HF	Heat Flux
HFG	Heat Flux Sensor
HMM	Hazard Mitigation Methodology
HRR	Heat Release Rate
IBHS	Insurance Institute for Business & Home Safety
MIDAS	Modular In-situ Data Acquisition System
ML	Mass Loss
MLR	Mass Loss Rate
NFPA	National Fire Protection Association
NI	National Instruments
NIST	National Institute of Standards and Technology
NFRL	National Fire Research Laboratory
OSB	Oriented Strand Board
PHRR	Peak Heat Release Rate
PTC	Plate Thermometer
SFM	State Fire Marshal
SI	International System of Units
SSD	Structure Separation Distance

SSE	Structure Separation Experiments
SPE	Steel Plate Eave
TC	Thermocouple
THR	Total Heat Released
TTPHRR	Time To Peak Heat Release Rate
USFS	United States Forest Service
WUI	Wildland-Urban Interface
AHJ	Authorities Having Jurisdiction
CBIA	California Building Industry Association
CAL FIRE	California Department of Forestry and Fire Protection
CO	Carbon Monoxide
DAQ	Data Acquisition
ECS	Emissions Control System
FDS	Fire Dynamics Simulator
FLIR	Forward-Looking InfraRed
HDPE	High Density Polyethylene
HF	Heat Flux
HFG	Heat Flux Sensor
HMM	Hazard Mitigation Methodology
HRR	Heat Release Rate
IBHS	Insurance Institute for Business & Home Safety
MIDAS	Modular In-situ Data Acquisition System
ML	Mass Loss
MLR	Mass Loss Rate
NFPA	National Fire Protection Association
NI	National Instruments
NIST	National Institute of Standards and Technology
NFRL	National Fire Research Laboratory

OSB	Oriented Strand Board
PHRR	Peak Heat Release Rate
PTC	Plate Thermometer
SFM	State Fire Marshal
SI	International System of Units
SSD	Structure Separation Distance
SSE	Structure Separation Experiments
SPE	Steel Plate Eave
TC	Thermocouple
THR	Total Heat Released
TTPHRR	Time To Peak Heat Release Rate
USFS	United States Forest Service
WUI	Wildland-Urban Interface